(NASA-CR-158753) COMPARISON OF THEORETICAL PREDICTED LONGITUDINAL AERODYNAMIC CHARACTERISTICS WITH FULL-SCALE WIND TUNNEL DATA ON THE ATLIT AIRPLANE (Kansas Univ. Center for Research, Inc.) 365 p HC A16/MF A01 CSCL 01C

N79-26018

Unclas

G3/02 27879

THE UNIVERSITY OF KANSAS CENTER FOR RESEARCH, INC.
2291 Irving Hill Drive—Campus West
Lawrence, Kansas 66045

COMPARISON OF THEORETICAL PREDICTED LONGITUDINAL AERODYNAMIC CHARACTERISTICS WITH FULL-SCALE WIND TUNNEL DATA ON THE ATLIT AIRPLANE

KU-FRL-399-1

This work was performed under
NASA Grant NSG-1574

Prepared by: Cornelis P. G. van Dam
Michael Griswold

Principal Investigator: J. Roskam

University of Kansas
Lawrence, Kansas

July 1979

SUMMARY

In this report an analytical method is presented for predicting the lift coefficient, C_L, the pitching moment coefficient, C_m, and the drag coefficient, C_D, of light, twin-engine, propeller-driven airplanes.

The method is applied to the Advanced Technology Light Twin-Engine (ATLIT) airplane. The calculated characteristics are correlated against full-scale wind tunnel data.

In addition, results obtained with the "thick wing" lifting surface program of Reference 6 and the "thin wing" lifting surface program of Reference 5 are used in the correlation.

The method described in this report predicts the drag and pitching moment fairly well. The lift prediction, however, is rather poor and needs improvement. In the case of lift prediction the lifting surface methods of References 5 and 6 show better agreement with the wind tunnel results of Reference 2.

TABLE OF CONTENTS

TABLE OF CONTENTS (continued)

TABLE OF CONTENTS (continued)

TABLE OF CONTENTS (continued)

TABLE OF CONTENTS (continued)

LIST OF TABLES

LIST OF TABLES (continued)

LIST OF TABLES (continued)

LIST OF TABLES (continued)

LIST OF FIGURES

LIST OF FIGURES (continued)

LIST OF FIGURES (continued)

LIST OF FIGURES (continued)

LIST OF FIGURES (continued)

LIST OF FIGURES (continued)

LIST OF FIGURES (continued)

LIST OF FIGURES (continued)

LIST OF SYMBOLS

Symbol	Definition	Dimension
A	Aspect ratio	
A_i	Aspect ratio of the portion of the wing immersed in the slipstream of one propeller	
$A_{w_{eff}}$	Effective aspect ratio of the wing	
a	Vertical position of the horizontal tail quarter chord relative to the vortex core	m (in, ft)
ac	Aerodynamic center, fraction or percent of mean aerodynamic chord	
$(ac)_{w_s}$	Average value of the aerodynamic center of the wing in the non-linear range of the wing lift curve slope to stall, fraction of wing mean aerodynamic chord	
b	Span	m (in, ft)
b_i	Span of the total portion of the wing immersed in the slipstream of the propeller	m (in, ft)
b_p	Blade width of the propeller	m (in, ft)
b_{ru}	Span of the completely rolled up tip vortices	m (in, ft)
b_{vor}	Span of the tip vortices at the longitudinal location of the quarter chord of the horizontal tail mean aerodynamic chord	m (in, ft)
$b_{w_{eff}}$	Effective span of the wing	m (in, ft)
C_1, C_2	1) Factors used in determining the propeller downwash, ε_p (Section 5.1) 2) Factors used in determining wing lift distribution (Section 4.2)	

Symbol	Definition	Dimension
C_3, C_4	Factors used in determining wing lift distribution	
C_B	Equivalent circular perimeter of the maximum frontal area of the body	m (in, ft)
C_b	Equivalent circular perimeter of the base area	m (in, ft)
C_D	Drag coefficient	
C_{D_b}	Base drag coefficient	
C_{D_f}	1) Wing zero-lift drag coefficient of total wing (Section 4.9) 2) Skin friction and pressure drag coefficient of the body (Section 4.12)	
C_{D_i}	Induced drag coefficient	
C_{D_o}	Zero-lift drag coefficient	
$(C_{D_o})_{f(w)}$	Zero-lift drag coefficient of the fuselage with fuselage interference accounted for	
$(\overline{C_{D_o}})_h$	Zero-lift drag coefficient of the horizontal tail with interference effects accounted for	
$(\overline{C_{D_o}})_{n(w)}$	Net zero-lift drag coefficient of the nacelles in presence of the wing	
$(\overline{C_{D_o}})_v$	Net contribution of the vertical tail to the zero-lift drag coefficient with interference effects accounted for	

Symbol	Definition	Dimension
$(\overline{C_{D_o}})_{wf}$	Net zero-lift drag coefficient of the wing-fuselage combination with interference effects accounted for	
C_f	Skin-friction coefficient of a flat plate	
C_L	Lift coefficient	
C_L''	Lift coefficient of an isolated wing including the increments of lift due to the normal force of one propeller and due to the lift component of one propeller	
$C_{L_{h(hf)}}$	Lift coefficient of the horizontal tail with tail-fuselage interaction effects included, referred to wing area and free-stream dynamic pressure	
$\overline{C}_{L_{h(hf)}}$	Lift coefficient of the horizontal tail, referenced to the tail area (unless noted otherwise), with tail-fuselage interaction effects, angle of attack, stabilizer deflection, and tab deflection accounted for	
$(C_{L_{h(hf)}})' \; S_h, \frac{\bar{q}_h}{\bar{q}_\infty} = 1.0$	Net lift coefficient of the horizontal tail due to α_h, i_h, and δ_{tab}, with tail-fuselage interaction effects included, referenced to the horizontal tail area and a dynamic pressure-ratio at the tail equal to one	
$(C_{L_{i_h}})_{\delta_{tab}} = 0$	Stabilizer effectiveness, $\partial C_L/\partial i_h$, with tab fixed at zero setting	deg^{-1}
$C_{L_{i_h}}$	Stabilizer effectiveness, $(C_{L_{i_h}})_{\delta_{tab}=0} + C_{L_{\delta_{tab}}} (\frac{\delta_{tab}}{i_h})$, with the tab geared to the stabilizer to deflect in the ratio of δ_{tab}/i_h	deg^{-1}

LIST OF SYMBOLS (continued)

Symbol	Definition	Dimension
$C_{L_{max}}$	Maximum lift coefficient	
$C_{L_{w(f)+f(w)}}$	Lift coefficient of the wing including mutual wing-fuselage interference effects.	
C_{L_α}	Lift-curve slope	deg^{-1}, rad^{-1}
$(C_{L_\alpha})_{h(f)}$	Lift-curve slope of the horizontal tail alone with fuselage effects on the tail accounted for	deg^{-1}
$(C_{L_\alpha})_{h(hf)}$	Lift-curve slope of the horizontal tail with interacting tail-fuselage effects accounted for.	deg^{-1}
$(C_{L_\alpha})_{Pol}$	Wing lift-curve slope according to Polhamus	rad^{-1}
$C_{L_{\delta_{tab}}}$	Tab effectiveness, $\partial C_L/\partial \delta_{tab}$	deg^{-1}
C_m	Pitching moment coefficient	
$C_{m_{h(hf)}}$	Horizontal tail contribution to the pitching moment coefficient based on $C_{L_{h(hf)}}$	
$\overline{C}_{m_{h(hf)}}$	Contribution of $\overline{C}_{L_{h(hf)}}$ to pitching moment coefficient	
$C_{m_{i_h}}$	Stabilizer effectiveness in pitch with the tab geared to the stabilizer to deflect in the ratio of δ_{tab}/i_h	deg^{-1}
C_{m_o}	Zero-lift pitching moment coefficient	
C_{m_α}	Variation of the pitching moment coefficient with angle of attack	deg^{-1}

Symbol	Definition	Dimension
$(C_{m_\alpha})_{B(\varepsilon)}$	Slope of the "free moment" coefficient of the body	deg^{-1}
$(C_{m_\alpha})_{f(\varepsilon)+n(\varepsilon)}$	Sum of the "free moment" slopes of the fuselage and nacelles	deg^{-1}
$(C_{m_\alpha})_{w(D)}$	Slope of the pitching moment coefficient due to wing drag	deg^{-1}
$(C_{m_\alpha})_{w(f)+f(w)}$	Slope of the pitching moment coefficient about the leading edge of the wing mean aerodynamic chord due to the effective wing lift, including the effects of fuselage upwash on the wing and wing lift carryover onto the fuselage	deg^{-1}
$(C_{m_\alpha})_{w_s}$	Average slope of the wing pitching moment coefficient about the leading edge of the wing mean aerodynamic chord in the non-linear lift range to stall	deg^{-1}
$(C_{N_\alpha})_p$	Normal-force derivative of the propeller based on the propeller disk area	rad^{-1}
$[(C_{N_\alpha})_p]_{K_N = 80.7}$	Reference normal-force derivative of a propeller having a normal force factor, K_N, equal to 80.7	rad^{-1}
C_x	Circumference of cross-section of body at distance x from the nose	m (in, ft)
c	Chord	m (in, ft)
$\bar{c}$	Mean aerodynamic chord	m (in, ft)
c_2	Taper-ratio correction factor	
c_{d_c}	Steady-state crossflow drag coefficient	
c_g	Standard mean chord, $(c_r + c_t)/2$	m (in, ft)

LIST OF SYMBOLS (continued)

Symbol	Definition	Dimension
$\bar{c}_i$	Mean aerodynamic chord of the portion of the wing immersed in the propeller slipstream	m (in, ft)
c_{int}	Chord at the intersection of the vertical and horizontal tail	m (in, ft)
c_ℓ	Section lift coefficient	
c_{ℓ_a}	"Additional" lift coefficient	
c_{ℓ_b}	"Basic" lift coefficient	
$c_{\ell_{max}}$	Maximum section lift coefficient	
c_{ℓ_α}	Section lift-curve slope at low Mach number ($M \leq 0.2$)	deg^{-1}, rad^{-1}
$c_{\ell_{\delta_{tab}}}$	Section effectiveness of the tab, $\partial c_\ell / \partial \delta_{tab}$	deg^{-1}, rad^{-1}
c_m	Section pitching moment coefficient	
c_{m_o}	Section pitching moment coefficient at zero lift	
c_n	Chord of the wing at the centerline of the nacelle	m (in, ft)
c_w	Wing chord	m (in, ft)
d	Fuselage width at the wing	m (in, ft)
d_B	Diameter of the equivalent circular perimeter of the maximum frontal area of the body (fuselage or nacelle)	m (in, ft)
d_b	Diameter of the equivalent circular perimeter of the base area	m (in, ft)
$-(dC_m/dC_L)_{cg}$	Static margin relative to the center of gravity as a fraction of the wing mean aerodynamic chord	

Symbol	Definition	Dimension
$(d_f)_h$	Fuselage width at the horizontal tail	m (in, ft)
d_{max}	Maximum diameter of an equivalent circular body	m (in, ft)
e	Oswald span efficiency factor used in the induced drag equation	
f	1) Propeller inflow factor, ratio of the propeller normal force coefficient at power-on to power-off ($T_c' = 0$) conditions (section 5.1) 2) Lift distribution function (Section 4.2)	
i_h	Incidence of the horizontal tail	deg
i_w	Wing incidence at the root, angle between wing chord and X-body axis	deg
$(i_w)_o$	Incidence of the zero-lift line of the wing relative to the X-body axis, $i_w - \alpha_{o_w}$	deg, rad
i_T	Incidence of the thrust axis relative to X-body axis	deg
K	Correction factor for maximum lift due to power	
K'	Correction factor for the lift effectiveness of the tab at large tab deflections	
K_1	Correlation parameter for additional wing lift due to power effects on the wing	
K_b	Span factor for inboard flaps or tabs	
K_D	Propeller drag factor	
$K_{f(h)}$	Ratio of the tail-lift carryover onto the fuselage to the tail alone	

Symbol	Definition	Dimension
$K_{f(w)}$	Ratio of wing lift carryover on the fuselage to the wing alone	
$K_{h(f)}$	Ratio of the lift on the tail in the presence of the fuselage to the tail alone	
K_N	Propeller normal force factor	
K_{Pol}	Error in Polhamus formula when compared with lifting surface method	
$K_{w(f)}$	Ratio of the lift on the wing in the presence of the fuselage to the wing alone	
K_Λ	Correction factor to account for the effects of the wing planform on the increment of maximum lift coefficient due to tab position	
k	1) $c_{\ell_\alpha}/2\pi$ (Section 4.2) 2) d/b (Section 4.8) 3) Equivalent sand roughness of a surface (Section 4.12)	m (in, ft)
$k_2 - k_1$	Reduced mass factor	
k_1	Correction factor to account for c_{tab}/c other than 0.25	
k_2	Correction factor to account for tab deflection other than 60 degrees	
k_3	Correction factor to account for chord extension due to tab deflection	
$k_{f(h)}$	Ratio of the lift carryover, due to stabilizer deflection, onto the fuselage to the lift of the stabilizer alone	
$k_{h(f)}$	Ratio of the lift on the stabilizer, due to stabilizer deflection, in the presence of the fuselage to stabilizer alone	

Symbol	Definition	Dimension
LER	Leading edge radius as a fraction of the chord	
ℓ	Reference length, for lifting surfaces, equal to the mean aerodynamic chord of the surface, for bodies, equal to the length of the body	m (in, ft)
ℓ_B	Length of body (fuselage or nacelle)	m (in, ft)
ℓ_{eff}	Distance, in the wing root-chord plane, from the tip vortex at the quarter chord of $b_{w_{eff}}$ to the quarter chord of the horizontal-tail mean aerodynamic chord	m (in, ft)
ℓ_f	Length of fuselage	m (in, ft)
$\bar{\ell}_f$	Distance from the nose of the fuselage to the quarter chord of the wing mean aerodynamic chord	m (in, ft)
ℓ_h	1) Distance from the wing trailing edge to the centroid of the last aft Δx segment of the fuselage (Section 4.8)	m (in, ft)
	2) Distance from the center of gravity to the quarter chord of the horizontal tail mean aerodynamic chord (Section 5.1)	m (in, ft)
ℓ_h'	Distance from the quarter chord of the mean aerodynamic chord of the immersed portion of the wing to the quarter chord of the horizontal tail mean aerodynamic chord	m (in, ft)
ℓ_n	Nacelle length	m (in, ft)
ℓ_{ru}	Distance required for the complete rollup of the wing-tip vortices	m (in, ft)
ℓ_2	Tail length in the wing-root chord plane from the root-chord trailing edge to the quarter chord of the horizontal tail mean aerodynamic chord	m (in, ft)

LIST OF SYMBOLS (continued)

Symbol	Definition	Dimension
ℓ_3	Distance from the leading edge of the wing mean aerodynamic chord to the trailing edge of the wing root chord	m (in, ft)
M	Mach number	
M_c	$M \sin\alpha_{B_{eff}}$	
N_{Re}	Reynolds number	
n	Number of propellers	
n_1	Number of junctures of the tail surface with the fuselage	
n_2	Number of corners in the juncture of the vertical tail with the horizontal tail (cruciform intersection would have four corners)	
prop	Propeller	
$\bar{q}_h/\bar{q}_\infty$	Dynamic pressure ratio at the horizontal tail	
$\bar{q}_\infty$	Free stream dynamic pressure	N/m^2 (lb/ft^2)
R	Leading-edge suction parameter	
R_p	Propeller radius	m (ft)
R_{wf}	Ratio of the wing-fuselage to the fuselage-alone zero-lift drag with the base drag omitted	
r	Cross-section radius of equivalent circular body	m (in, ft)
S	Area	m^2 (in^2, ft^2)
S_B	Maximum frontal area of the body (fuselage or nacelle)	m^2 (in^2, ft^2)
S_f	Planform area of the fuselage	m^2 (in^2, ft^2)

Symbol	Definition	Dimension
$\bar{S}_f$	Planform area of the fuselage forward of the quarter chord of the wing mean aerodynamic chord	m^2 (in^2, ft^2)
S_{h_i}	Area of the horizontal tail immersed in the propeller slipstreams	m^2 (in^2, ft^2)
$(S_h)_{tab}$	Horizontal tail area in front of and including the tab	m^2 (in^2, ft^2)
S_i	Wing area immersed in the slipstream of the propellers	m^2 (in^2, ft^2)
$S_{\ell s_e}$	Area of the exposed panels of a lifting surface	m^2 (in^2, ft^2)
S_o	Cross-section area of an equivalent circular body.	m^2 (in^2, ft^2)
S_p	Disk area of propellers (total)	m^2 (in^2, ft^2)
S_x	Cross-section area of an equivalent circular body at the foregoing station being considered	m^2 (in^2, ft^2)
S_{wet}	Wetted area	m^2 (in^2, ft^2)
T	Thrust of the propellers (total)	N (lb)
T_c'	$T/(\bar{q}_\infty S_w)$	
t/c	Maximum thickness ratio	
$(t/c)_{int}$	Average maximum thickness ratio of intersecting vertical-and horizontal tail surfaces	
v	Induced drag factor due to linear twist	
w	1) Width (diameter) of an equivalent circular body at the foregoing station being considered (Section 4.7) 2) Zero-lift drag factor due to linear twist (Section 4.12)	m (in, ft)

Symbol	Definition	Dimension
w_B	Mean width of the body planform segment, Δx	m (in, ft)
x	1) Distance from nose of body to the centroid of ΔS_x for the forebody, and to the centroid of Δx of the afterbody (Section 4.7)	m (in, ft)
	2) Distance, parallel to the centerline of the wake, from the trailing edge of the wing root chord to the quarter chord of the horizontal tail mean aerodynamic chord (Section 4.9)	m (in, ft)
x_o	Distance from the nose of body to the point where the potential flow ceases	m (in, ft)
x_1	1) Distance from the nose of body to the point of maximum negative rate of change of body cross-sectional area with body length (Section 4.3)	m (in, ft)
	2) Distance from the wing leading edge to the centroid of the forward Δx segment of the body planform area (Section 4.8)	m (in, ft)
x_1'	Distance from the wing trailing edge to the centroid of the aft Δx segment of the body planform area	m (in, ft)
$\bar{x}_1$	Length of the Δx segment of the body planform area adjacent to and forward of the wing leading edge	m (in, ft)
x_{ac}	Distance from the lifting-surface apex to the aerodynamic center of the surface	m (in, ft)
$(x_{ac}/c_{r_e})_{f(w)}$	Contribution to the aerodynamic center due to the lift carryover of the wing onto the fuselage, as a fraction of the root chord of the exposed wing panels	
$(x_{ac}/c_{r_e})_{w(f)}$	Aerodynamic center of the wing with the wing in the presence of the fuselage, as a fraction of and about the leading edge of the root chord of the exposed wing panels	

Symbol	Definition	Dimension
x_{cg}	Distance to the center of gravity from the leading edge of the wing mean aerodynamic chord	m (in, ft)
x/c	Section coordinate dimensions	
x_h	Distance, parallel to the X-body axis, from the quarter chord of the horizontal tail mean aerodynamic chord to the leading edge of the wing mean aerodynamic chord	m (in, ft)
x_m	Distance from the nose of body to the chosen moment center (leading edge of the mean aerodynamic chord in this case)	m (in, ft)
x_n	Distance from the lifting surface apex to the desired reference center (leading edge of the mean aerodynamic chord in this case)	m (in, ft)
x_p	Distance from center of gravity to the propeller, positive forward	m (in, ft)
x_p'	Distance from quarter chord of the mean aerodynamic chord of the immersed portion of the wing to the propeller, positive forward	m (in, ft)
x_w	Distance from the aerodynamic center of the mean aerodynamic chord of the immersed portion of the wing to the center of gravity	m (in, ft)
$y_{\bar{c}}$	Lateral distance from the root chord to the mean aerodynamic chord	m (in, ft)
z/c	Section coordinate dimensions	
z_h	Distance, parallel to the Z-body axis, from the X-body axis to the quarter chord of the horizontal tail mean aerodynamic chord, positive down	m (in, ft)

Symbol	Definition	Dimension
z_{h}'	Vertical distance from the root-chord plane of the wing to the quarter chord point of the horizontal tail mean aerodynamic chord	m (in, ft)
z_{h}''	Vertical distance from the centerline of the wake to the quarter chord of the horizontal tail mean aerodynamic chord	m (in, ft)
$z_{h_{eff}}$	Effective distance, parallel to the Z-body axis, from the quarter chord of the horizontal tail mean aerodynamic chord to the centerline of the propeller slipstream, positive down	m (in, ft)
$z_{h_{T}}$	Distance, parallel to the Z-body axis, from the thrust axis to the quarter chord of the horizontal tail mean aerodynamic chord, positive down	m (in, ft)
z_{s}	Distance, parallel to the Z-body axis, from the X-body axis to the centerline of the propeller slipstream at the longitudinal station of the quarter chord of the mean aerodynamic chord of the immersed portion of the wing, positive down	m (in, ft)
z_{T}	Distance, parallel to the Z-body axis, from the X-body axis to the thrust axis, positive down	m (in, ft)
z_{w}	Distance, parallel to the Z-body axis, from the X-body axis to the quarter chord of the mean aerodynamic chord of the immersed portion of the wing, positive down	m (in, ft)
α	Angle of attack relative to X-body axis	deg, rad
α^{*}	Limit of linearity of $c_{\ell_{\alpha}}$	deg

Symbol	Definition	Dimension
α_B	Angle of attack of actual body, identical to airplane angle of attack, α, using X-body axis as reference	deg
$\alpha_{B_{eff}}$	Effective angle of attack of an equivalent circular body, $\alpha_B + \alpha_{o_B}$	deg
$\alpha_{C_{L_{max}}}$	Angle of attack of a surface at its $C_{L_{max}}$	deg
$(\alpha_{C_{L_{max}}})_{h(hf)}$	Angle of attack for maximum lift of the horizontal tail in the presence of the fuselage	deg
$(\alpha_{C_{L_{max}}})_{w}$	Angle of attack for maximum lift of the wing relative to the zero-lift line of wing	deg
$(\alpha_{C_{L_{max}}})_{wf}$	Angle of attack for maximum lift of wing-fuselage combination relative to the zero-lift line of wing	deg
$\alpha_{c_{\ell_{max}}}$	Angle of attack at $c_{\ell_{max}}$	deg
α_h	Local angle of attack of the horizontal tail with the stabilizer setting equal to zero	deg
α_o	Angle of attack for zero lift	deg
α_{o_B}	Zero-lift angle of an equivalent circular body relative to the reference X-body axis	deg
α_{o_w}	Angle of attack of wing for zero lift relative to chord line	deg
α_p	Angle of attack of the propeller plane, includes the effect of the wing upwash	deg
$\bar{\alpha}_s$	Average value of angle of attack in the nonlinear lift range to stall	deg

Symbol	Definition	Dimension
α_T	Angle of attack of the thrust axis	deg
α_w	Angle of attack of wing relative to its chord line, $\alpha + i_w$	deg
α_w^*	Limit of linearity of the wing lift curve relative to chord line	deg
$\alpha_{w_{abs}}$	Wing angle of attack relative to the wing zero-lift line, $\alpha - \alpha_{o_w} + i_w$	deg
$(\alpha_\delta)_{C_L}$	$(\partial C_L/\partial\delta)/(\partial C_L/\partial\alpha)$	
$(\alpha_\delta)_{c_\ell}$	$(\partial c_\ell/\partial\delta)/(\partial c_\ell/\partial\alpha)$	
β	$\sqrt{1 - M^2}$	
β'	Propeller blade angle at 0.75 R_p	deg
Γ	Dihedral angle	deg
γ	Angle between the wing chord plane and the line connecting the trailing edge of the wing root chord and the quarter chord of the horizontal tail mean aerodynamic chord	deg
$(\Delta C_D)_{\text{cooling system}}$	Increment of drag coefficient due to cooling system	
ΔC_{D_i}	Increment of drag due to power effects on induced drag	
ΔC_{D_o}	Increment of zero-lift drag due to power	
$(\Delta C_{D_o})_h$	Contribution of the horizontal tail to ΔC_{D_o}	

Symbol	Definition	Dimension
$(\Delta C_{D_o})_{h(f)}$	Increment of zero-lift drag of the horizontal tail due to fuselage interference	
$(\Delta \bar{C}_{D_o})_n$	Contribution of nacelles (including nacelle-wing interference effects) to ΔC_{D_o}	
$(\Delta C_{D_o})_{n(w)}$	Increment of the zero-lift drag of one nacelle due to wing interference	
$(\Delta C_{D_o})_{t(f)}$	Increment of the zero-lift tail drag (horizontal-or vertical tail) due to fuselage interference	
$(\Delta C_{D_o})_{v(f)}$	Increment of the zero-lift drag coefficient of the vertical tail due to fuselage interference	
$(\Delta C_{D_o})_{v(h)}$	Increment of the zero-lift drag coefficient of the vertical tail due to the horizontal tail interference when the vertical tail intersects the horizontal tail	
$(\Delta C_{D_o})_w$	Contribution of the wing to ΔC_{D_o}	
$(\Delta C_D)_T$	Component of the total thrust parallel to the velocity vector, positive thrust is equal to a negative drag contribution	
ΔC_L	Increment of lift	
$(\Delta C_L)_{h(fv)}$	Increment of lift coefficient of the horizontal tail due to the effect of fuselage vortices	
$(\Delta C_L)_{i_h}$	Increment of lift coefficient due to stabilizer deflection	
$(\Delta C_{L_h})_{\Delta \bar{q}_h}$	Increment of horizontal tail contribution to the lift coefficient resulting from the power-induced change in dynamic pressure at the tail	

Symbol	Definition	Dimension
$(\Delta C_{L_h})_{(\Delta\varepsilon_h)_{power}}$	Increment of horizontal tail contribution to the lift coefficient resulting from the power-induced change in downwash at the tail	
$\Delta C_{L_{max}}$	1) Mach number correction of the incompressible maximum lift coefficient (Section 4.2) 2) Increment of maximum lift coefficient due to power (Section 5.1)	
$(\Delta C_{L_{max}})_{\delta_{tab}}$	Increment of maximum lift coefficient due to the tab	
$(\Delta C_L)_{power}$	Difference between predicted power-on lift and predicted propeller-off lift of the complete airplane	
$(\Delta C_L)'_{power}$	Increment of the tail-off lift due to power at the propeller-off maximum lift angle of attack	
$(\Delta C_L)_{\Delta\bar{q}_w}$	Increment of lift coefficient due to the power-induced change in dynamic pressure over the portion of the wing immersed in the propeller slipstreams	
$(\Delta C_L)_T$	Increment of lift coefficient due to the lift component propeller thrust vector	
$(\Delta C_{L_\alpha})_{w_s}$	Correction to reduce $(C_{L_\alpha})_{wfn}$ to an average slope in the nonlinear lift range to stall	deg^{-1}, rad^{-1}
$(\Delta C_L)_{\varepsilon_p}$	Increment of lift coefficient due to the change in angle of attack, resulting from propeller downwash, ε_p, of the portions of the wing immersed in the propeller slipstreams	
$(\Delta C_m)_{B_p}$	Increment of pitching moment coefficient due to propeller effects on body (fuselage or nacelle)	
$(\Delta C_m)_h$	Increment of tail contribution to the pitching moment coefficient due to the propeller induced increments of dynamic pressure and downwash at the tail	

Symbol	Definition	Dimension
$(\Delta C_m)_{N_p}$	Increment of pitching moment due to the propeller normal force	
$(\Delta C_m)_{n_p}$	Increment of pitching moment due to the propeller effects on the nacelles	
$(\Delta C_{m_o})_f$	Correction to $(C_{m_o})_f$ for the non-midwing configuration	
$(\Delta C_{m_o})_{\Delta\bar{q}_w}$	Increment of zero-lift pitching moment coefficient due to the increase in dynamic pressure induced by the propeller slipstreams on the immersed portions of the wing	
$\Delta C_{m_o}/\theta$	Change in wing zero-lift pitching moment coefficient due to a unit change in linear wing twist	deg^{-1}
$(\Delta C_m)_{power}$	Difference between predicted power-on pitching moment coefficient and predicted propeller-off pitching moment coefficient of the complete airplane	
$(\Delta C_m)_T$	Increment of pitching moment coefficient due to the thrust of the propellers	
$(\Delta C_m)_{w_L}$	Increment of pitching moment coefficient due to the net change in wing lift resulting from propeller-slipstream-induced dynamic pressure and angle-of-attack changes on the wing	
$(\Delta C_m)_{\Delta\bar{q}_h}$	Increment of tail contribution to the pitching moment coefficient due to the propeller induced increment of dynamic pressure at the tail	
$(\Delta C_m)_{\Delta\bar{q}_w}$	Increment of pitching moment coefficient due to the increase in dynamic pressure induced by the propeller slipstreams on the immersed portions of the wing	
$(\Delta C_m)_{(\Delta\varepsilon_h)_{power}}$	Increment of tail contribution to the pitching moment coefficient due to the propeller induced increment at downwash of the tail	

LIST OF SYMBOLS (continued)

Symbol	Definition	Dimension
$(\Delta C_m)_{\varepsilon_p}$	Change in the pitching moment coefficient of the wing due to the propeller slipstream induced change in angle of attack	
$\Delta c_{\ell_{max}}$	Correction of $c_{\ell_{max}}$ for Reynolds number	
$(\Delta c_{\ell_{max}})_{base}$	Section maximum lift increment for the 25-percent-chord tab (flap) at a reference tab-deflection angle of 60 degrees	
$(\Delta c_{\ell_{max}})_{tab}$	Section maximum lift increment due to the tab	
$\Delta\bar{q}_h/\bar{q}_\infty$	Increment of power-induced dynamic pressure acting on the horizontal tail as a ratio of the free-stream dynamic pressure	
$(\Delta\bar{q}/\bar{q}_\infty)_h$	Dynamic pressure loss at the horizontal tail as a ratio of the free-stream dynamic pressure	
$(\Delta\bar{q}/\bar{q}_\infty)_o$	Dynamic pressure loss at the wake centerline as a ratio of the free stream dynamic pressure	
$\Delta\bar{q}_w/\bar{q}_\infty$	Increment of power-induced dynamic pressure acting on the wing immersed in the propeller slipstream as a ratio of the free stream dynamic pressure	
$(\Delta S_w)_n$	Wing area overlapped by one nacelle	m^2 (in^2, ft^2)
ΔS_x	Change in the cross-section area of the body across the Δx segment of the body segment considered	m^2 (in^2, ft^2)
Δx	Incremental length of the body	m (in, ft)
Δy	Section leading edge sharpness parameter, percent of chord	
Δz_{wake}	Half-width of the wake at a distance x from trailing edge of the wing root chord	m (in, ft)

LIST OF SYMBOLS (continued)

Symbol	Definition	Dimension
$\Delta\alpha_{C_{L_{max}}}$	Angle of attack correction at $C_{L_{max}}$ for flow separation	deg
$\Delta\alpha_{S_i}$	Change in angle of attack of the portion of the wing immersed in the propeller slipstream due to the propeller	deg
$\Delta\alpha_o/\theta$	Shift in α_o per degree of wing twist	
$(\Delta\epsilon_h)_{power}$	Increment of downwash at the horizontal tail due to power	deg
δ	Deflection	deg
$\partial\beta/\partial\alpha$	Variation of upwash and downwash with angle of attack at the Δx segment of the body forward of the wing leading edge and aft of the wing trailing edge	
$\partial\bar{\beta}/\partial\alpha$	Variation of upwash with angle of attack of the Δx segment of the body forward of and adjacent to the wing leading edge	
$\partial\bar{\epsilon}_h/\partial\alpha$	Average downwash gradient at and across the horizontal tail	
$\partial\epsilon_p/\partial\alpha$	Downwash gradient behind the propeller	
$-(\partial\epsilon_u/\partial\alpha)$	Upwash gradient at the propeller	
$\partial\epsilon_{vc}/\partial\alpha$	Rate of change of downwash, in the plane of symmetry at the height of the vortex core, with the absolute angle of attack	
$\partial\epsilon_w/\partial\alpha$	Rate of change of downwash, behind the wing, with angle of attack	
$\partial\epsilon_\infty/\partial\alpha$	Downwash gradient at infinity	
ε	Twist at spanwise station η	deg

LIST OF SYMBOLS (continued)

Symbol	Definition	Dimension
$\bar{\varepsilon}$	Effective propeller downwash angle average over entire wing	deg
ε_h	Downwash in the plane of symmetry at the vortex sheet	deg
$\bar{\varepsilon}_h$	Average downwash across the horizontal tail	deg
ε_p	Downwash angle behind the propeller	deg
$-\varepsilon_u$	Upwash angle at the propeller	deg
η	1) Drag proportionality factor (Section 4.3) 2) Non-dimensional span-wise station, y/(b/2) (Section 4.2)	
η_i	Distance from centerline of tail to the inboard tab edge as a ratio of the tail semispan	
η_o	Distance from centerline of tail to the outboard edge of the tab as a ratio of the tail semispan	
θ	Twist of the wing tip with respect to the root chord (negative for washout)	deg
Λ	Sweep angle	deg
Λ_β	Corrected sweep angle, $\tan^{-1}[\tan(\Lambda_{c/4})/\beta]$	deg
λ	Taper ratio, c_t/c_r	
ϕ_{te}	Section trailing-edge angle	deg

Subscripts

B	Body
c/2	Half-chord line
c/4	Quarter-chord line

Subscripts	Definition
cg	Center of gravity
cooling system	Engine cooling system (cowl flaps and engine inlets)
e	Exposed panels
f	1) Fuselage 2) Flap (Section 4.13)
fn	Fuselage-nacelle combination
h	Horizontal tail
i	Immersed in propeller slipstream
$i_h = 0$	Stabilizer not deflected
ℓe	Leading edge
low speed	Low subsonic Mach number
ℓs	Lifting surface
M	High subsonic Mach number
max	Maximum
n	Nacelle(s)
prop off	Propeller(s) removed
power on	Propeller(s) installed and power on
r	Root
s	Nonlinear lift range to stall
t	Tip
tab	Tab
v	Vertical tail
w	Wing
wf	Wing-fuselage combination

LIST OF SYMBOLS (continued)

Subscripts	Definition
wfn	Wing-fuselage-nacelle combination
$\delta_{tab} = 0$	Tab deflection is zero

BLANK PAGE

CHAPTER 1

INTRODUCTION

The Advanced Technology Light Twin (ATLIT) airplane was developed by the University of Kansas Flight Research Laboratory as part of a general aviation research program sponsored by the National Aeronautics and Space Administration, Langley Research Center. Background information on this program together with the history of the ATLIT development and performance predictions are given in Reference 1. The broad objective of this research program was to apply existing jet-transport wing technology to general aviation airplanes for the purpose of improving safety, efficiency and utility.

The ATLIT project was managed by the University of Kansas and, in addition, involved the Robertson Aircraft Company for detailed design; the Piper Aircraft Company for modification, fabrication and initial flight testing; and Wichita State University for wind tunnel tests in support of the spoiler lateral-control-system development.

The Piper PA-34-200 Seneca I was selected for modification as a typical example of current twin-engine general aviation aircraft which are virtually all limited in single-engine climb performance at gross weight. As pointed out in Reference 1, the conceptual study which led to the ATLIT design showed a potential for the much needed improvement in single-engine climb performance without increasing installed power or reducing gross-weight. Improved single-engine climb performance became the major goal of the ATLIT project.

The preliminary flight test results (Reference 1) indicated that the ATLIT failed to achieve the predicted improvements in climb and

cruise performance. They were not better than those of the basic Seneca at the same gross-weight and with the same installed power. A full-scale wind tunnel investigation of the ATLIT airplane was undertaken to evaluate the various advanced aerodynamic concepts and to determine the cause for the lack of performance improvement. The results of this wind tunnel investigation are presented in Reference 2.

In this report the first phase will be described of a project performed by the Flight Research Laboratory of the University of Kansas sponsored by Grant NSG 1574 from NASA, Langley Research Center. The objectives of this project are to

1. correlate theoretical predictions of longitudinal aerodynamic characteristics with full-scale wind tunnel data;
2. correlate theoretical predictions of lateral directional aerodynamic characteristics with full-scale wind tunnel data;
3. correlate the results of point 1 and point 2 with flight test data.

In this report only work toward the first objective will be discussed. References 3 and 4 will be used as guidelines for the theoretical predictions. Use will also be made of References 5 and 6, and the results will be compared with those obtained with References 3 and 4 and the experimental data (Reference 2). Also the results mentioned in Reference 7 will be discussed.

CHAPTER 2

THE ATLIT AIRPLANE

The airplane used in the analysis is the full-scale ATLIT (Advanced Technology Light Twin) which is an extensively modified Piper PA-34-200 Seneca I general aviation low-wing monoplane with an all-movable horizontal stabilizer. Pertinent physical characteristics are listed in Table 2.1 and a three-view drawing is presented in Figure 2.1.

The advanced technology improvements implemented on the ATLIT were

1. replacement of the basic untapered, aspect ratio 7.25 Seneca wing having a 65_2415 airfoil and an area of 19.4 m^2 (208.7 ft^2) with a newly designed tapered (taper ratio 0.5), high aspect ratio (aspect ratio 10.32) wing having a 17-percent thick GA(W)-1 airfoil and an area of 14.4 m^2 (155.0 ft^2);
2. installation of full-span 30-percent chord Fowler flaps instead of the partial span 20-percent chord plain flaps used on the Seneca;
3. use of a spoiler lateral control system instead of conventional ailerons.

The planform changes were made to lower the induced drag, while the GA(W)-1 airfoil was chosen for its high lift-to-drag ratio and for its high maximum lift coefficient. Also supercritical propellers, designed for increased propulsive efficiency, were used. These, however, were not installed during the wind tunnel investigation.

Special thrust-torque balances were installed on the propeller shafts to measure the propeller characteristics. The balances made it necessary to extend the nacelles with 8 inches.

As already mentioned in Chapter 1, the climb and top speed performance of the ATLIT fell short of predictions. This was the reason that part of the full-scale wind tunnel investigation was devoted to drag evaluation of the airplane "as built." A drag clean-up investigation was initiated and several factors were established which adversely affected the lift and drag of the airplane. These factors are discussed in detail in Reference 2. The result of the drag clean-up program was a "fully clean" configuration of the ATLIT airplane. Comparisons between experimental and theoretical results will be based on the ATLIT "fully clean."

Table 2.1: Specifications of the ATLIT airplane

Wing:	
Area, m^2 (ft^2)	14.40 (155.0)
Span, m (ft)	12.19 (40.0)
Aspect ratio	10.32
Thickness ratio	0.17
Dihedral, deg	7
Taper ratio	0.5
Incidence angle at root, deg	0.5
Incidence angle at tip, deg	-2.5
Leading edge and trailing edge sweep, deg	3.67
Mean aerodynamic chord, m (ft)	1.225 (4.018)
Root chord, m (in)	1.575 (62.0)
Tip chord, m (in)	0.787 (31.0)
Airfoil	GA(W)-1
Flap:	
Type	Fowler
Area (total), m^2 (ft^2)	3.56 (38.3)
Span/side, m (ft)	5.15 (16.91)
Chord, perc. of wing chord	30
Inboard wing station, m (in)	0.711 (28.0)
Outboard wing station, m (in)	5.867 (231.0)
Leading edge retracted, perc. of wing chord	70
Maximum deflection, deg	40
Maximum travel, m (in)	0.343 (13.50)
Root chord, m (in)	0.445 (17.50)
Tip chord, m (in)	0.244 (9.62)

Table 2.1: Continued

Spoiler:	
Type	Differential-Slat-Upper Surface
Area (total), m^2 (ft^2)	0.488 (5.25)
Span/side, m (in)	3.226 (127.0)
Inboard wing station, m (in)	2.565 (101.0)
Outboard wing station, m (in)	5.791 (228.0)
Hinge, perc. of wing chord	70
Maximum deflection, deg	60
Root chord, m (in)	0.177 (6.975)
Tip chord, m (in)	0.124 (4.880)
Tail:	
Stabilator:	
Area (including tab), m^2 (ft^2)	3.60 (38.7)
Span, m (ft)	4.13 (13.56)
Chord (constant), m (in)	0.871 (34.29)
Aspect ratio	4.75
Sweep angle, deg	0
Dihedral, deg	0
Hinge line, perc. of chord	26.6
Airfoil	NACA 0010
Vertical:	
Area (including tab), m^2 (ft^2)	1.85 (19.9)
Span, m (ft)	1.52 (5.00)
Aspect ratio	1.19
Taper ratio	0.42
Root chord, m (in)	1.708 (67.23)
Tip chord, m (in)	0.723 (28.45)

Table 2.1: Continued

Mean aerodynamic chord, m (in)	1.282 (50.47)
Leading edge sweep angle, deg	39.92
Airfoil	NACA 0009
Stabilator tab:	
Area, m^2 (ft^2)	0.539 (5.8)
Span, m (in)	3.023 (119.0)
Chord (constant), m (in)	0.178 (7.0)
Tab hinge line to stabilator hinge line, m (in)	0.462 (18.17)
Rudder:	
Area (including tab), m^2 (ft^2)	0.706 (7.6)
Span, m (in)	1.525 (60.02)
Chord (constant), m (in)	0.449 (17.69)
Rudder trim tab:	
Area, m^2 (ft^2)	0.158 (1.7)
Span, m (in)	0.895 (35.25)
Chord (constant), m (in)	0.175 (6.9)
Powerplant:	
Number of engines	2
Manufacturer	Lycoming
Model	IO-360-CIE6
Takeoff rpm	2700
Takeoff power, hp	200
Propeller:	
Manufacturer	Hartzell
Model	HC-C2YK-ICEF/FO 7666A
Number of blades	2
Diameter, m (in)	1.930 (76.0)

Table 2.1: Concluded

Weights and Loading:	
Gross weight, N (lb)	17,792 (4,000)
Empty weight, N (lb)	11,018 (2,477)
Useful load, N (lb)	6,774 (1,523)
Wing loading (at gross weight), N/m^2 (lb/ft^2)	1,236 (25.8)

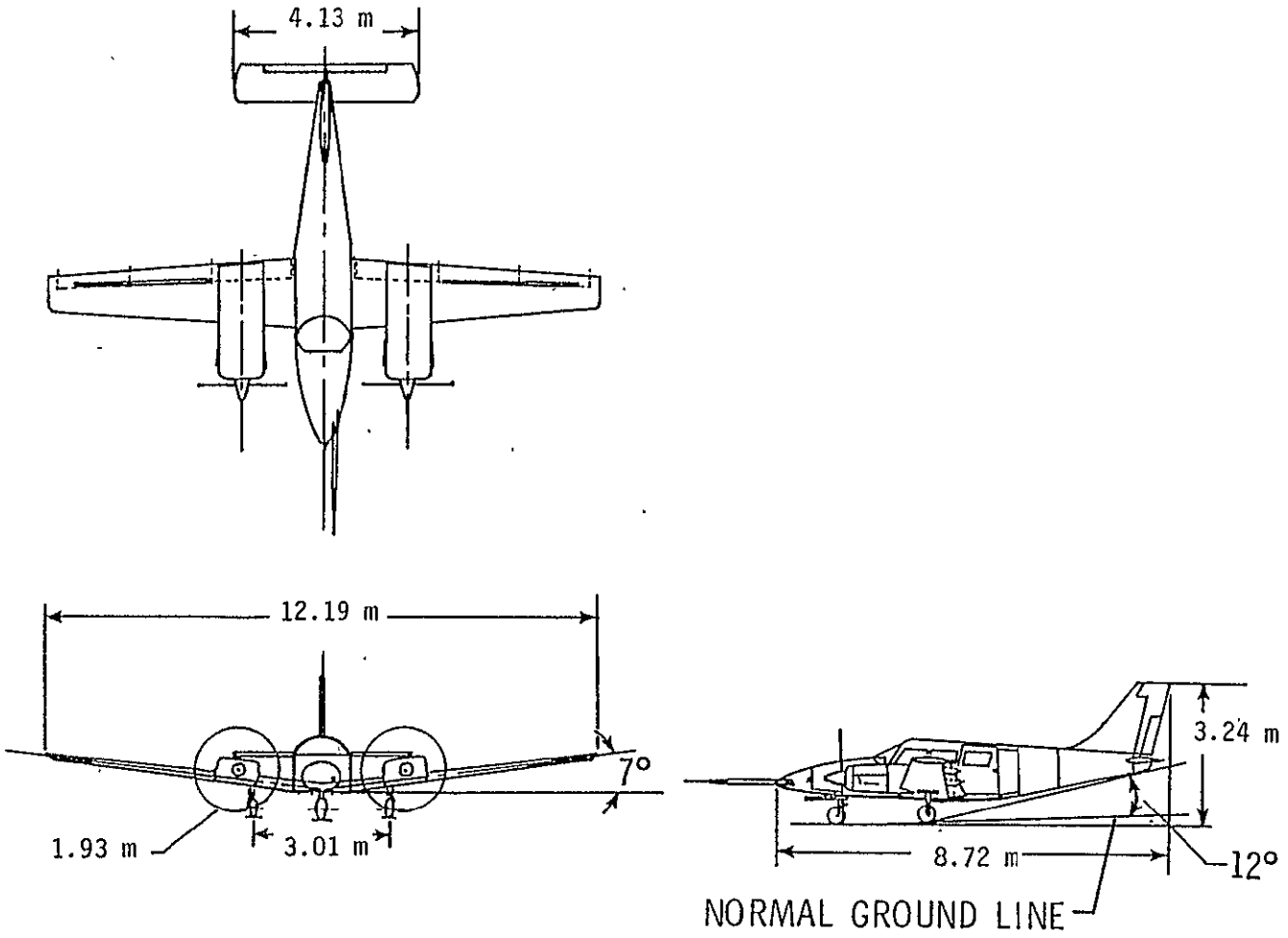

Figure 2.1: Three-view drawing of the ATLIT airplane (Reference 1)

2.1 Geometric Parameters of Wing and Tail

Depending on which characteristic has to be determined, the total area or the exposed area of the wing and the tail are considered. The total planform is considered to extend through the nacelle and the fuselage, while the exposed planform terminates at the fuselage. Pertinent dimensions for the wing, the horizontal tail and the vertical tail are shown in Figures 2.1.1, 2.1.2 and 2.1.3, respectively. Table 2.1.1 lists the geometric parameters of the wing and the tail pertinent in the analysis.

Table 2.1.1: Pertinent wing and tail geometric parameters used in the analysis

Symbol	Description	Wing		Horizontal Tail		Vertical Tail
		Total	Exposed	Total	Exposed	Exposed
S	Area, m^2 (ft^2)	14.40 (155.0)	12.53 (134.8)	3.60 (38.7)	3.25 (34.9)	1.75 (18.8)
b	Span, m (ft)	12.19 (40.0)	10.96 (36.0)	4.13 (13.56)	3.73 (12.23)	1.52 (5.0)
A	Aspect ratio, b^2/S	10.32	9.61	4.75	4.28	1.33
c_t	Tip chord, m (in)	0.787 (31.00)	0.787 (31.00)	0.871 (34.29)	0.871 (34.29)	0.723 (28.45)
c_r	Root chord, m (in)	1.575 (62.00)	1.495 (58.87)	0.871 (34.29)	0.871 (34.29)	1.575 (62.0)
λ	Taper ratio, c_t/c_r	0.50	0.527	1	1	0.459
$\bar{c}$	* Mean aerodynamic chord, m (in)	1.225 (48.22)	1.178 (46.38)	0.871 (34.29)	0.871 (34.29)	1.201 (47.30)
$y_{\bar{c}}$	** Lateral position of mean aerodynamic chord, m (in)	2.709 (106.67)	2.46 (96.85)	1.033 (40.68)	0.932 (36.69)	0.334 (13.15)
Γ	Dihedral angle, deg.	7	7	0	0	-
Λ_{le}	Leading-edge sweep, deg.	3.67	3.67	0	0	40.0
$\Lambda_{c/4}$	Sweep of c/4 line, deg.	1.835	1.835	0	0	34.5
$\Lambda_{c/2}$	Sweep of c/2 line, deg.	0	0	0	0	29.0

* $\bar{c} = \frac{2}{3} c_r \left(\frac{1 + \lambda + \lambda^2}{1 + \lambda} \right)$

** $y_{\bar{c}} = \frac{1}{3} \left(\frac{1 + 2\lambda}{1 + \lambda} \right) \frac{b}{2}$

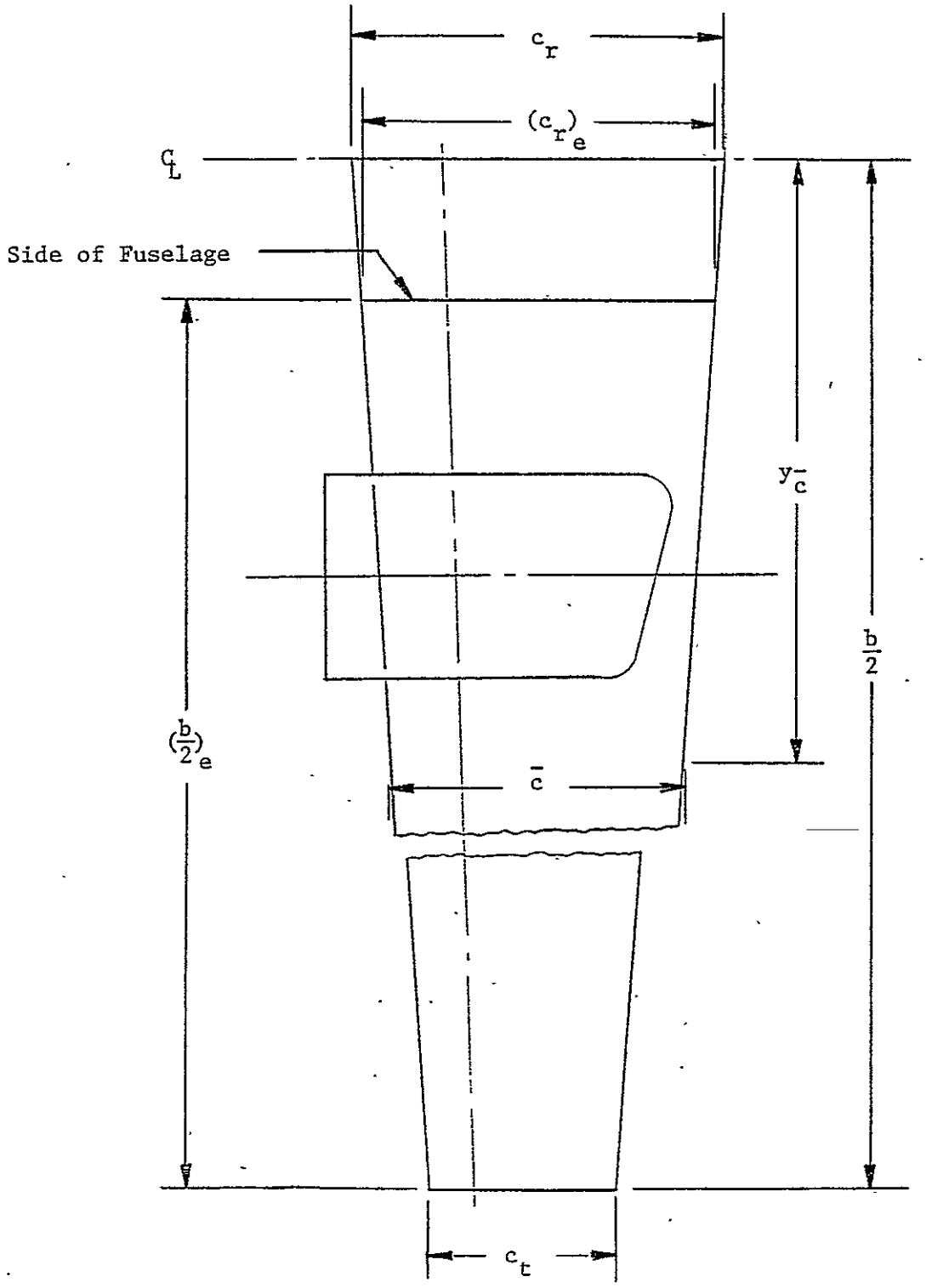

Figure 2.1.1: Definition sketch of wing dimensions

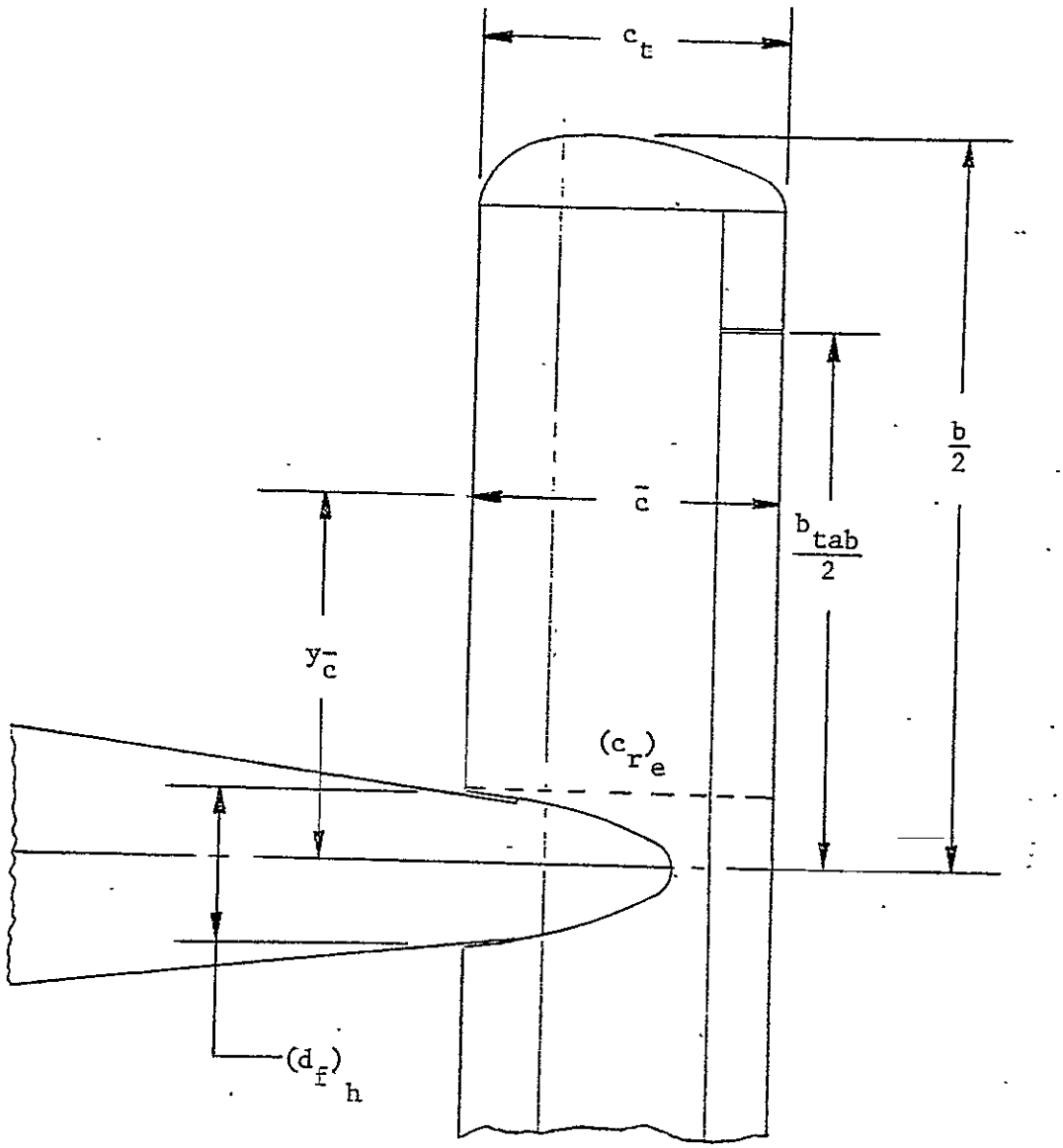

Figure 2.1.2: Definition sketch of horizontal tail dimensions

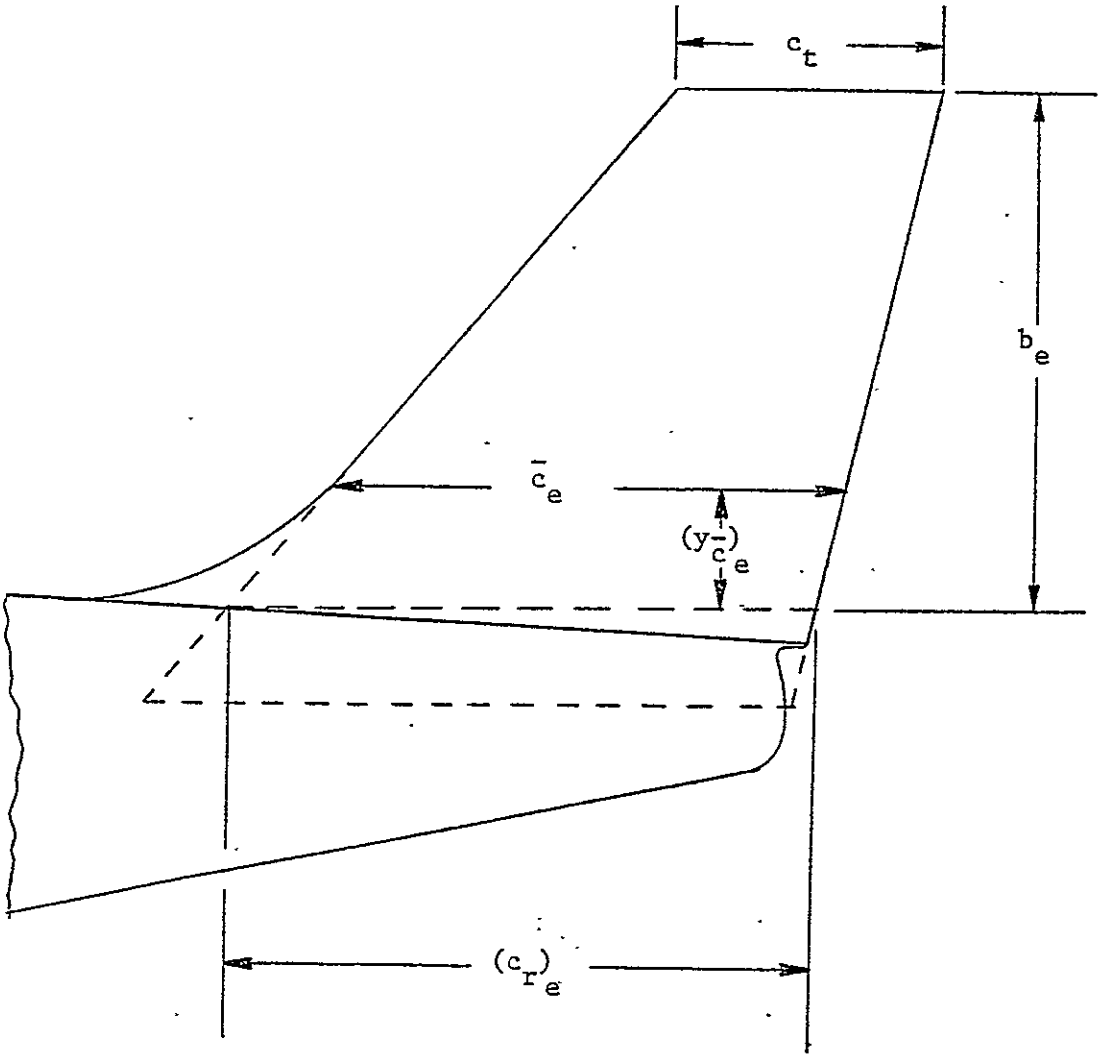

Figure 2.1.3: Definition sketch of exposed vertical tail dimensions

CHAPTER 3

LISTING OF IMPORTANT RESULTS

In this chapter the calculated longitudinal characteristics of the ATLIT airplane will be compared with full-scale wind tunnel data of Reference 2. The results are only discussed briefly, a more detailed discussion of the results and how to improve the results can be found in Chapters 4 through 6.

3.1 Lift Characteristics of the ATLIT Airplane

The lift of the airplane without horizontal tail is discussed in Section 4.1 to 4.4. The calculated lift curve of the ATLIT without horizontal tail is shown in Figure 3.1.1 and compared with wind tunnel results. In this figure results obtained with Reference 5 are also shown. These references both represent lifting surface prediction methods. Reference 5 is based on the thin wing theory, while Reference 6 is based on the thick wing theory. The calculated lift curve shows fair agreement with the experimental results, except for the discrepancy in the zero-lift angle of attack.

The lift of the complete airplane is discussed in Section 4.10 and the calculated lift curve is shown in Figure 3.1.2. The predicted lift curve shows fair agreement with the wind tunnel data. No results were obtained with the computer program of Reference 6.

The power-on lift of the airplane is determined in Section 5.1. The predicted lift curve is drawn for $T_c' = 0.0915$ and 0.1970 in Figure 3.1,3 and 3.1.4, respectively. The calculated lift curves show poor agreement with the experimental results. This is caused, however, by

the difference between the predicted and experimental propeller-off lift curve. When the predicted increment in lift due to power, $(\Delta C_{L_{power}})_{pred}$, is added to the experimental lift curve (propellers off, cowl flaps and engine inlets open) good agreement is obtained with the wind tunnel data.

3.2 Pitching Moment Characteristics of the ATLIT Airplane

The pitching moment of the airplane without horizontal tail is described in Section 4.5 through 4.8. In Figure 3.2.1 the predicted horizontal-tail-off pitching moment is compared with experimental results of Reference 2 and with results obtained with Reference 5 and Reference 6. The calculated results show good agreement with the wind tunnel data.

The pitching moment of the complete airplane is discussed in Section 4.11. The calculated results are plotted in Figures 3.2.2 and 3.2.3 and they show good agreement with experimental data.

In Section 5.2 the power-on pitching moment is described and the results are shown in Figures 3.2.4 through 3.2.7 for two power settings. The calculated characteristics show fair agreement with the wind tunnel data. The predictions have been performed for a Reynolds number of 2.3 million. No power-on wind tunnel data, however, were available for the ATLIT in the "fully clean" configuration at a Reynolds number of 2.3 million. Data were available for a Reynolds number of 3.5 million. In the case of the ATLIT, this increase in Reynolds number resulted in an increase in pitching moment $(\Delta C_m)_{N_{Re}} \simeq 0.03$, in the linear lift region. The predicted pitching moment, including the Reynolds number correction,

is also shown in Figures 3.2.4 through 3.2.7. When the predicted movement in pitching moment due to power, $(\Delta C_{m_{power}})_{pred}$, is added to the experimental pitching moment curve (propellers off, cowl flaps and engine inlets open) good agreement is obtained with the wind-tunnel data.

3.3 Drag Characteristics of the ATLIT Airplane

The drag of the airplane is discussed in Section 4.12, while the power-on drag is described in Section 5.3. In both cases the calculated drag polar shows good agreement with the wind tunnel data, as shown in Figures 3.3.1 through 3.3.4.

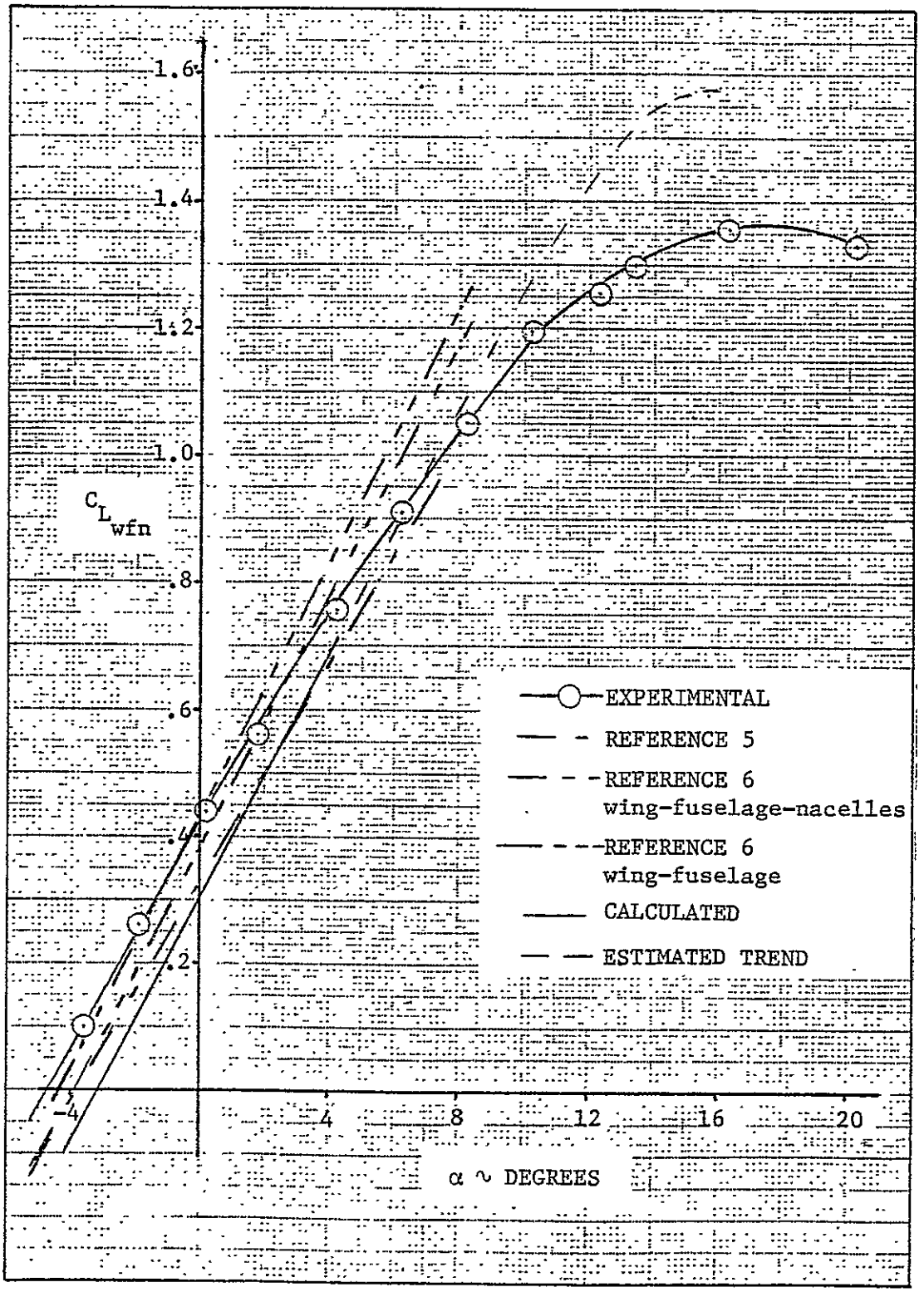

Figure 3.1.1: Comparison of lift predictions with wind tunnel data (N_{Re}= 2.3x10^6, horizontal tail and propellers removed)

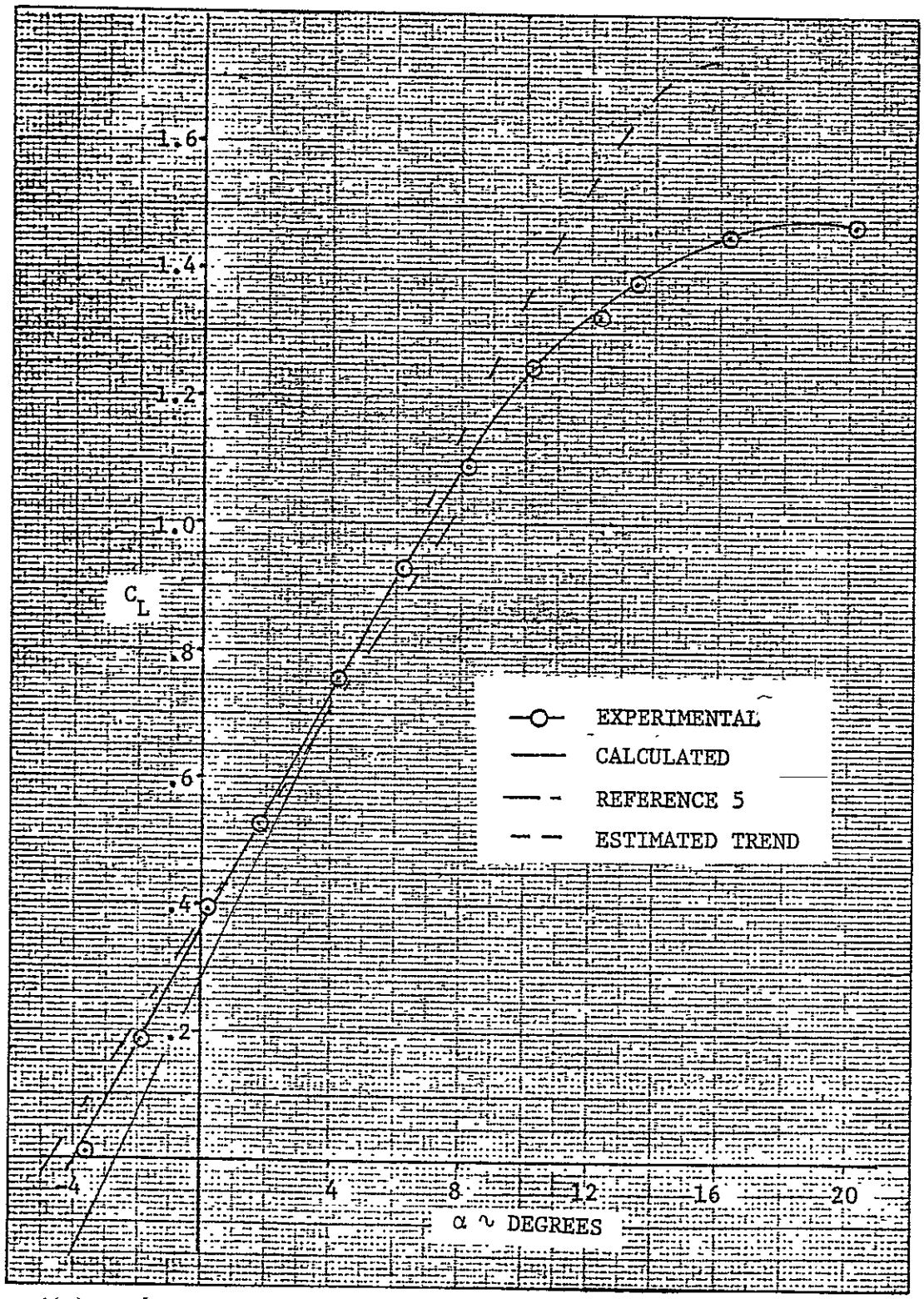

Figure 3.1.2: Comparison of predicted airplane lift curve with wind tunnel data (propellers removed, N_{Re} = 2.3 million)

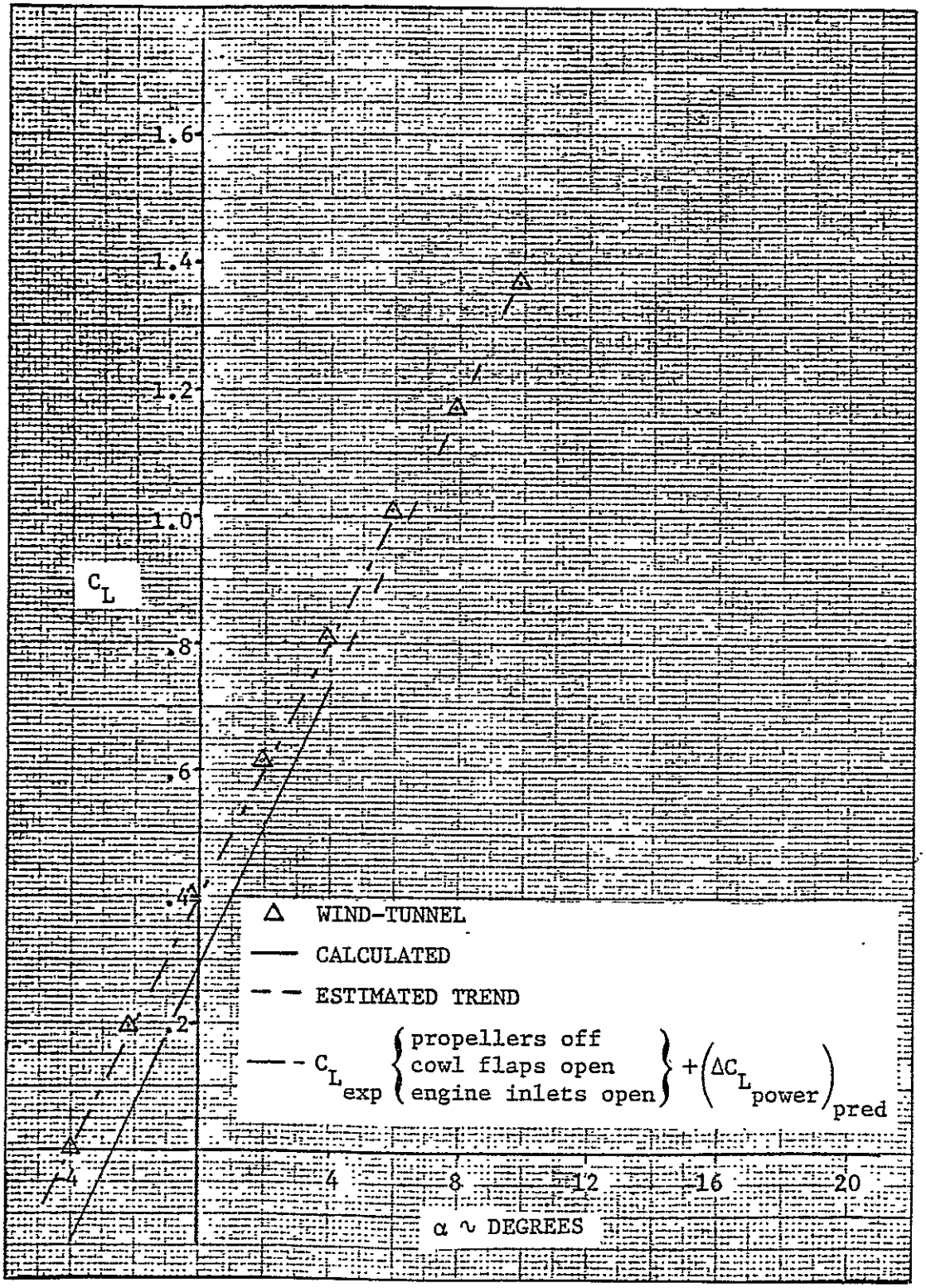

Figure 3.1.3: Comparison of predicted lift curve with full-scale wind tunnel data (T_c' = 0.0915, no stabilizer deflection)

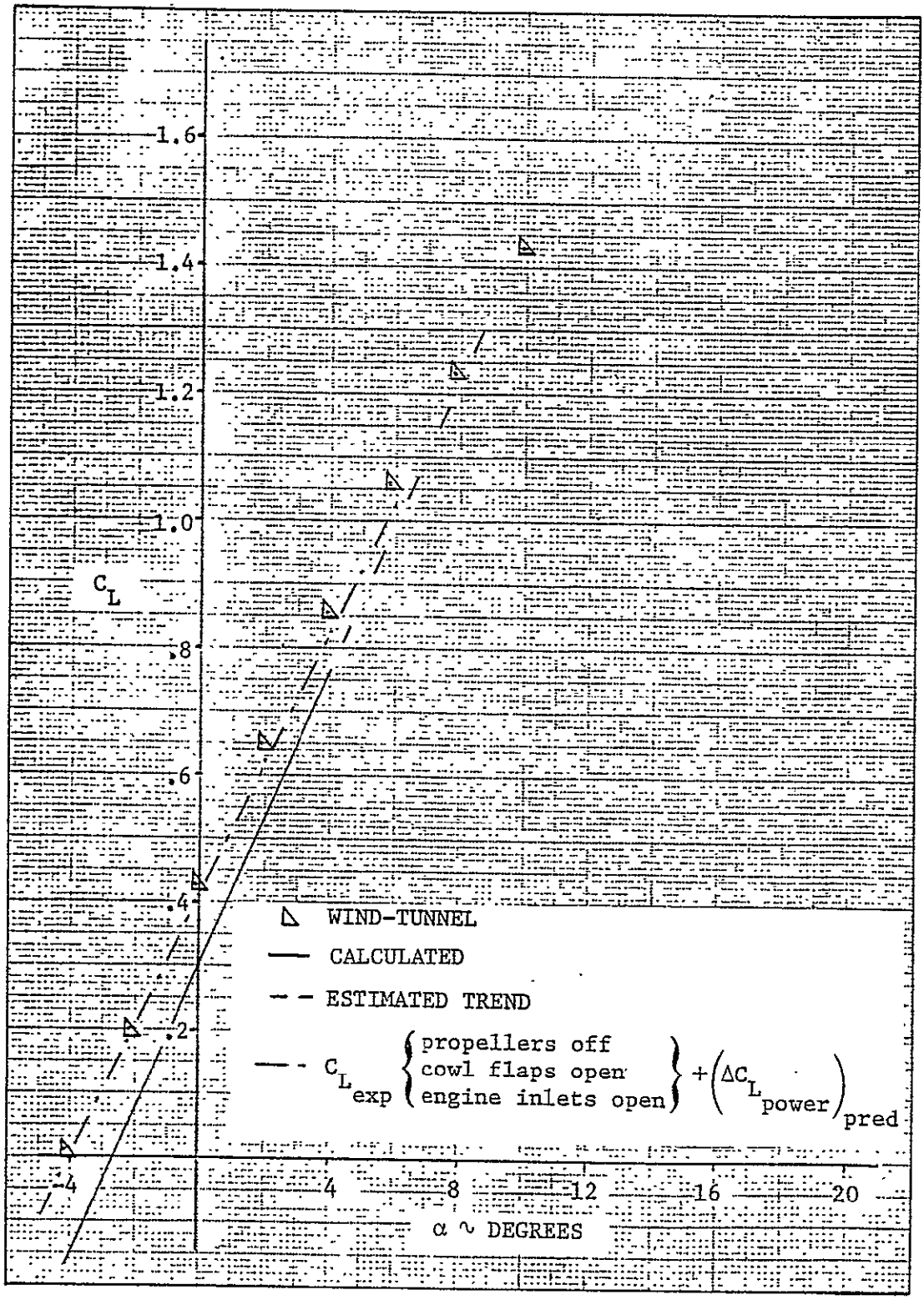

Figure 3.1.4: Comparison of predicted lift curve with full-scale wind tunnel data (T_c' = 0.1970, no stabilizer deflection)

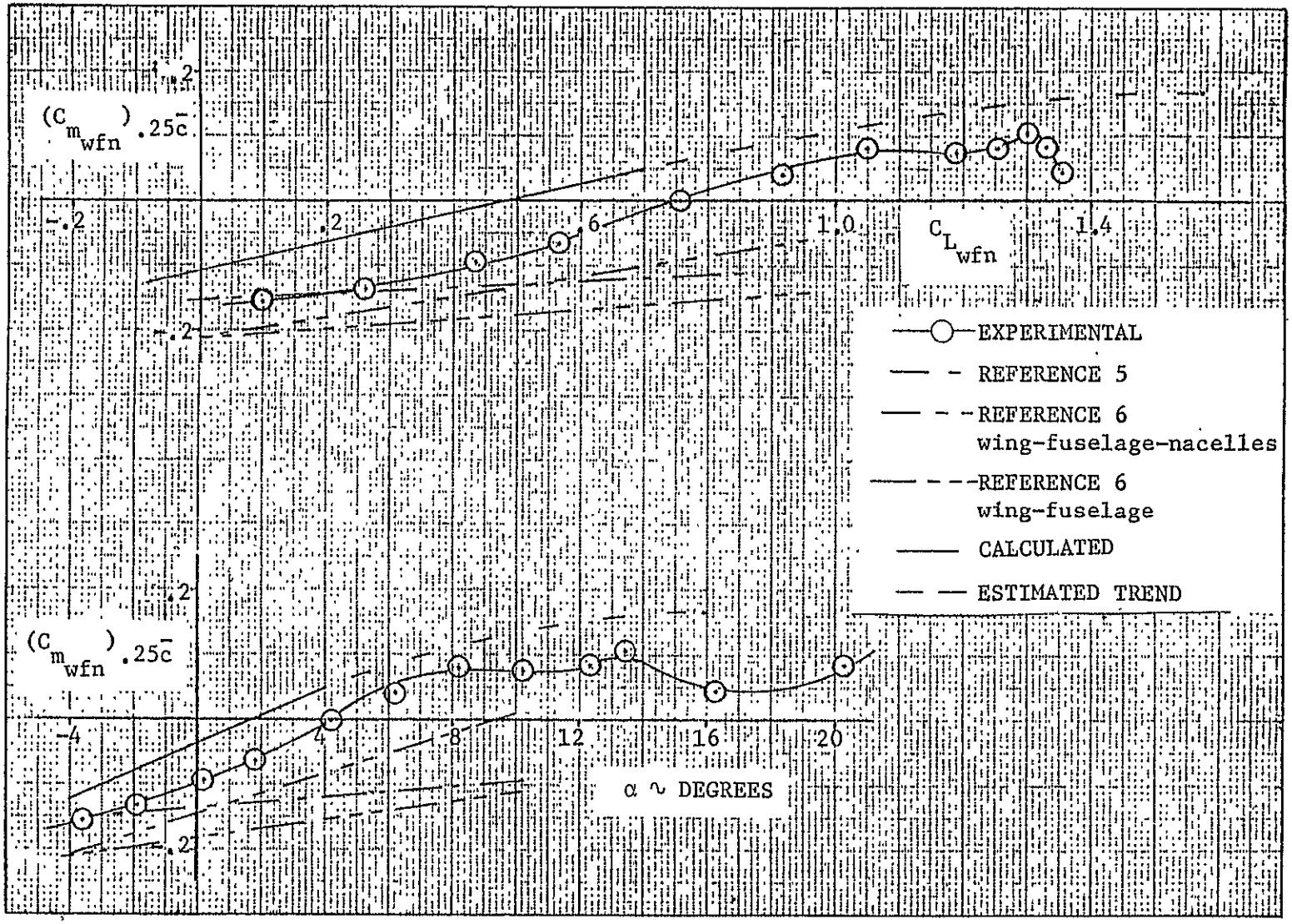

Figure 3.2.1: Comparison of predicted pitching moments with wind tunnel data (horizontal tail off, propellers removed, N_{Re} = 2.3 million)

See note on Page 109

Figure 3.2.2: Comparison of predicted airplane pitching moment with full-scale wind tunnel data (propellers removed, stabilizer not deflected, N_{Re} = 2.3 million)

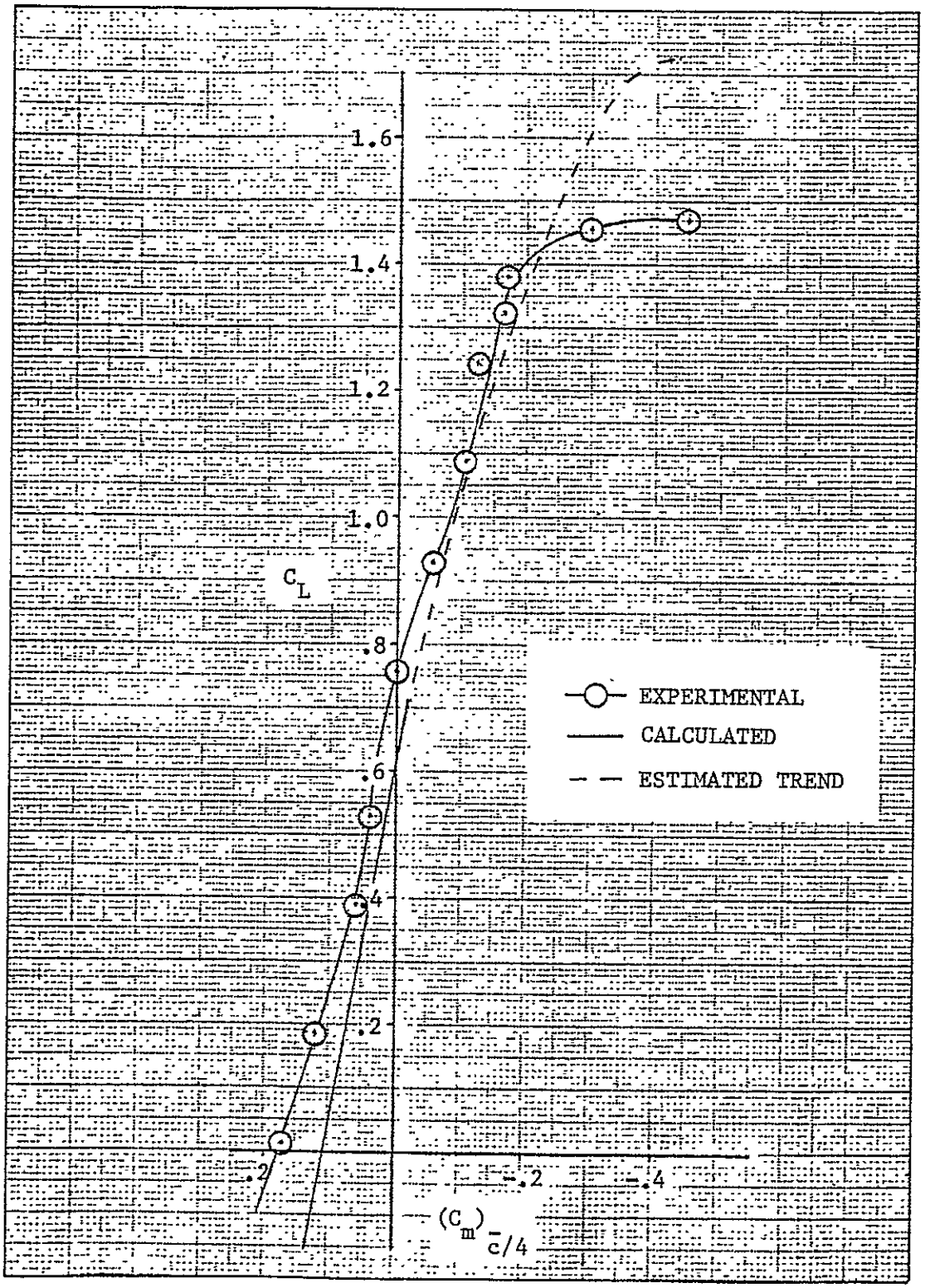

Figure 3.2.3: Comparison of predicted airplane pitching moment with full-scale wind tunnel data (propellers removed, stabilizer not deflected, N_{Re} = 2.3 million)

Figure 3.2.4: Comparison of predicted pitching moments with full-scale wind-tunnel data ($T_c' = 0.0915$, no stabilizer deflection)

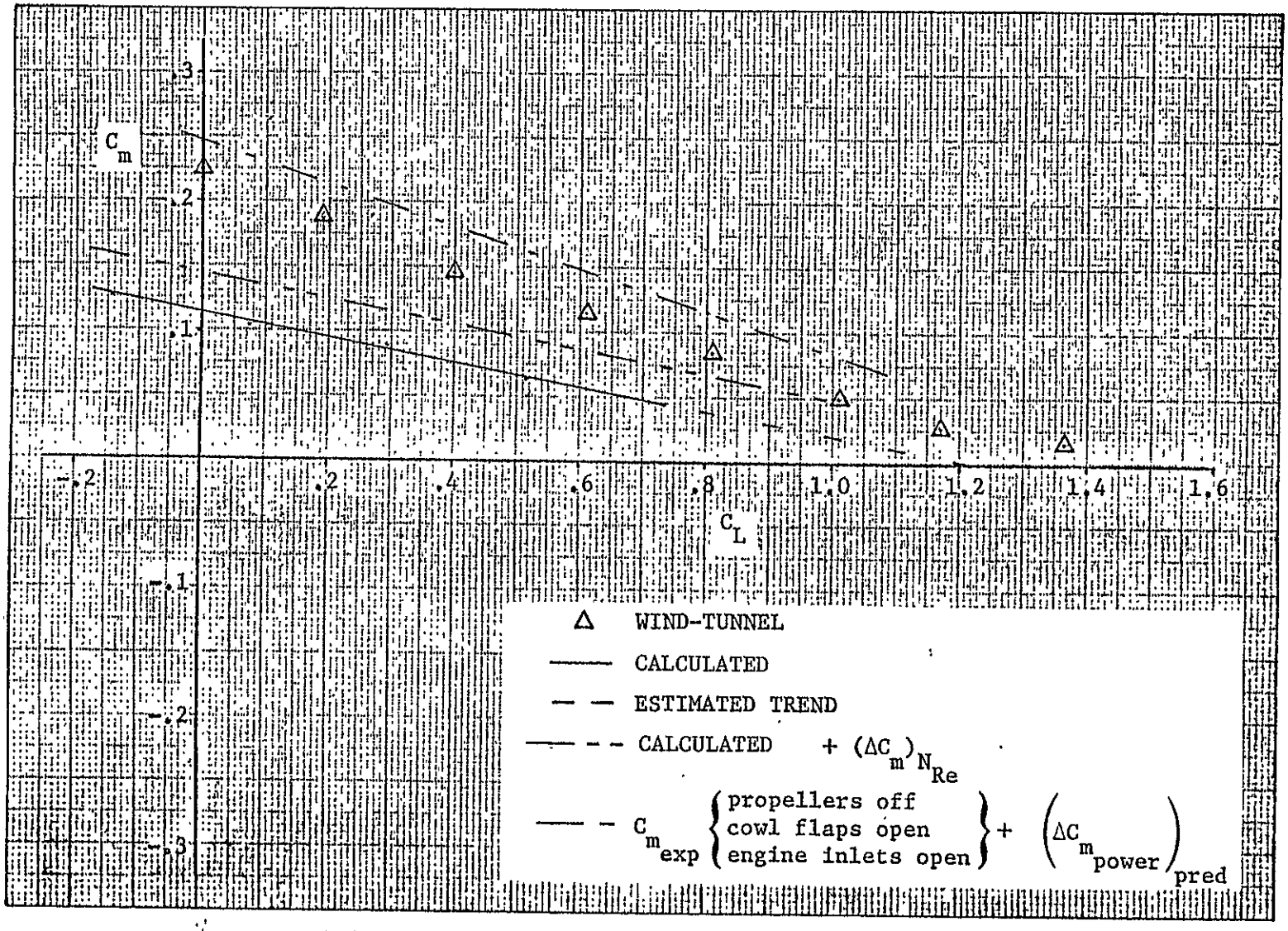

Figure 3.2.5: Comparison of predicted pitching moments with wind tunnel results ($T_c' = 0.0915$, no stabilizer deflection)

Figure 3.2.6: Comparison of calculated pitching moment with full-scale wind tunnel results (T_c' = 0.1970, no stabilizer deflection)

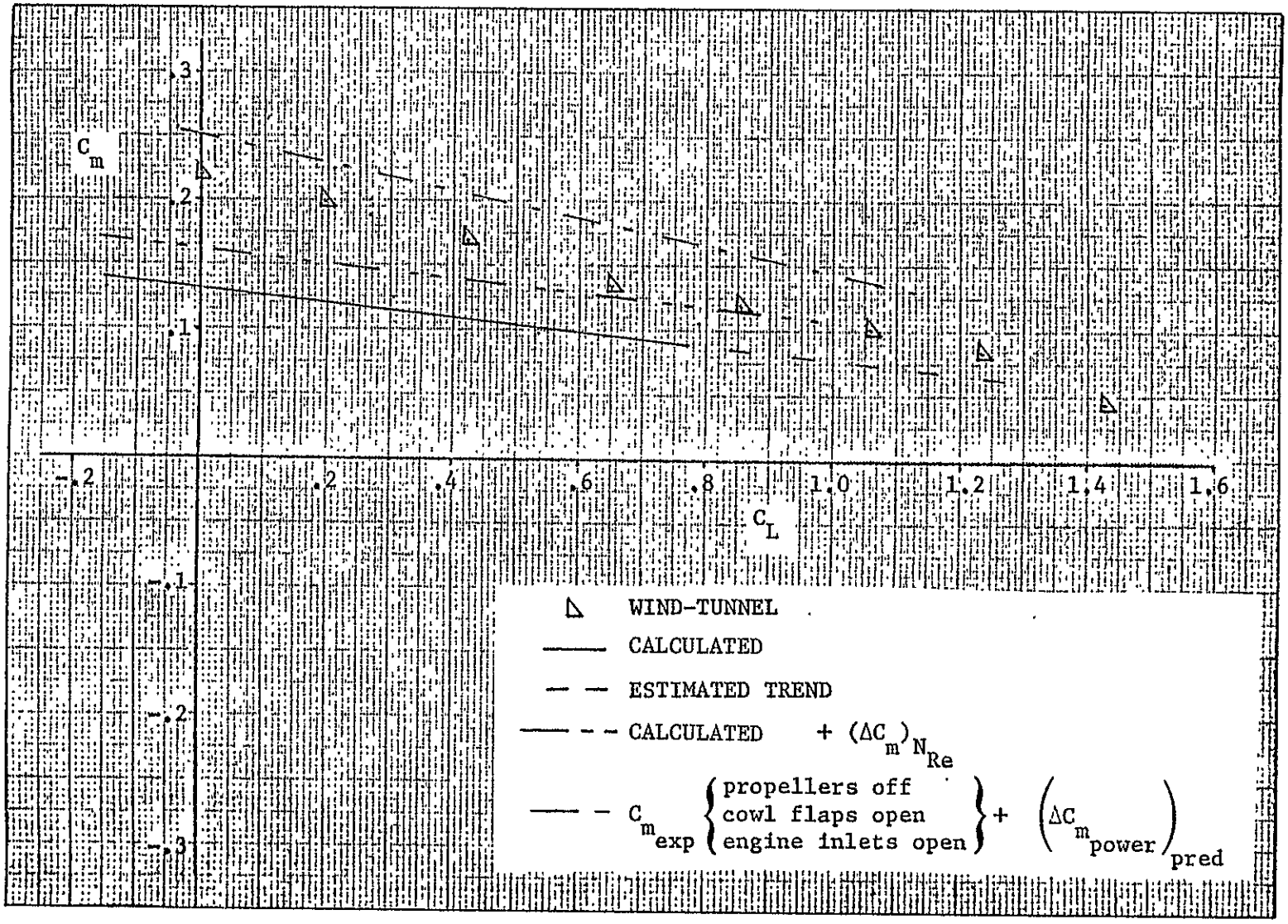

Figure 3.2.7: Comparison of predicted pitching moments with experimental results ($T_c' = 0.1970$, no stabilizer deflection)

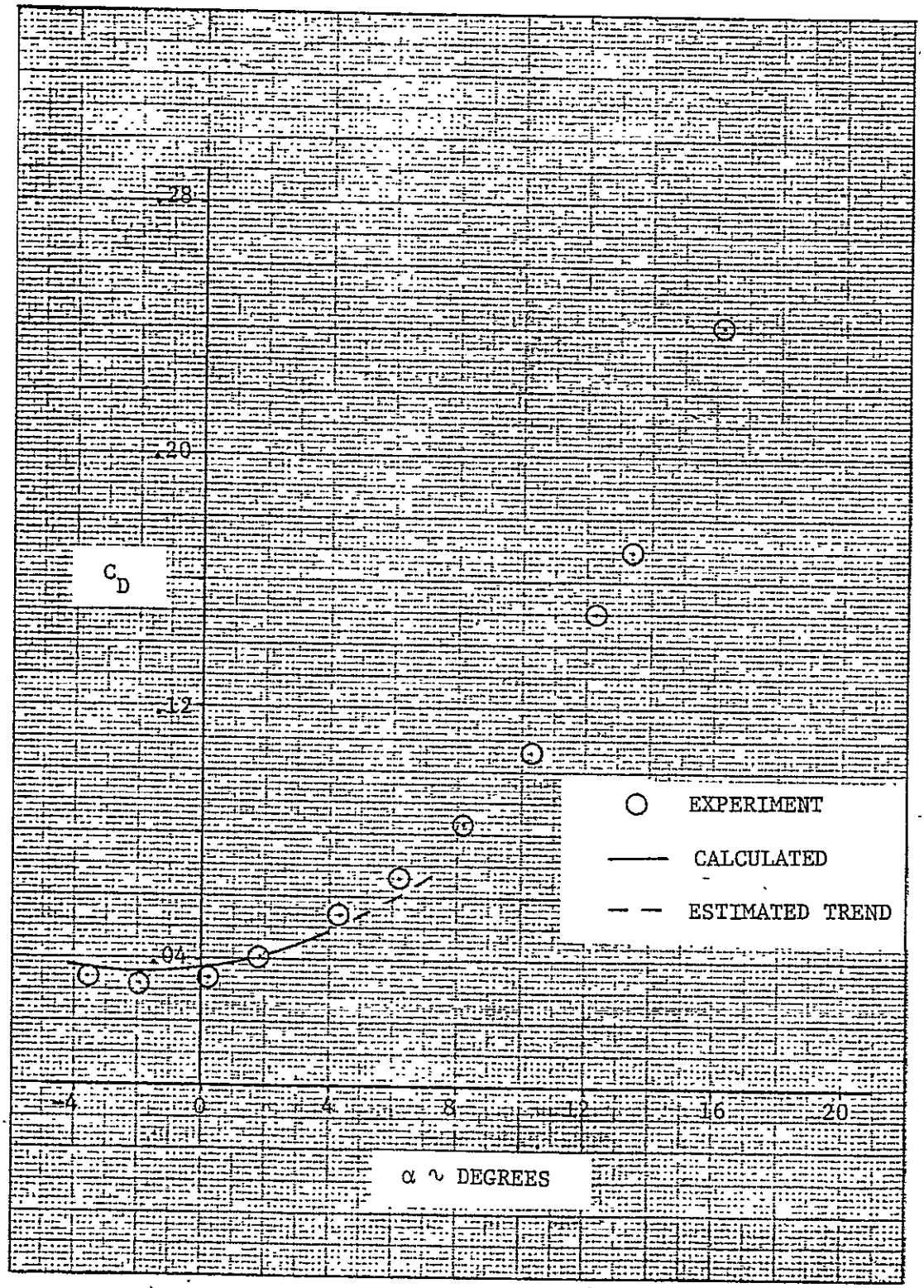

Figure 3.3.1: Comparison of predicted airplane drag with full-scale wind tunnel data (propellers removed, no engine cooling drag, N_{Re} = 2.3 million)

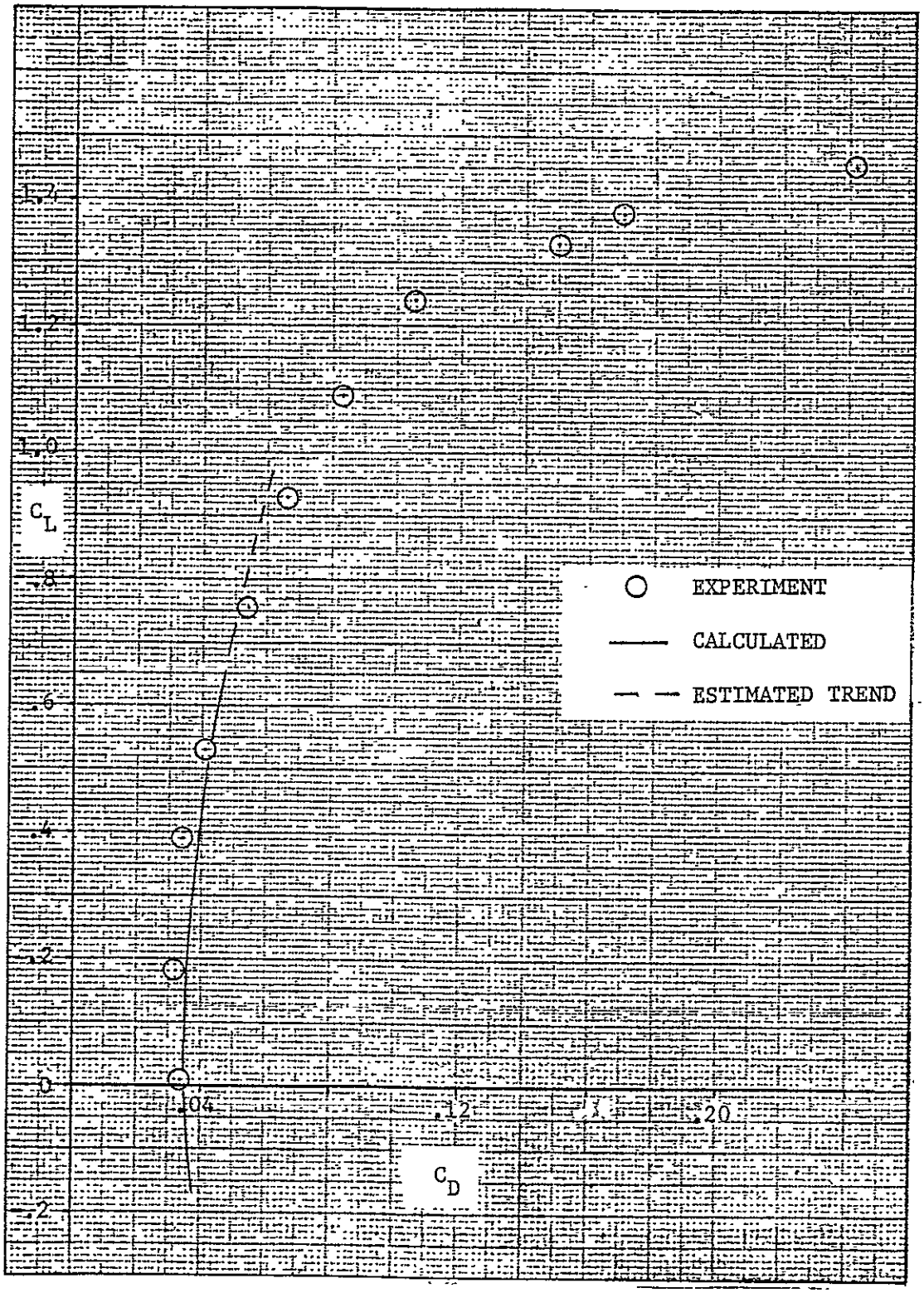

Figure 3.3.2: Comparison of predicted airplane drag with full-scale wind tunnel data (propellers removed, no engine cooling drag, N_{Re} = 2.3 million)

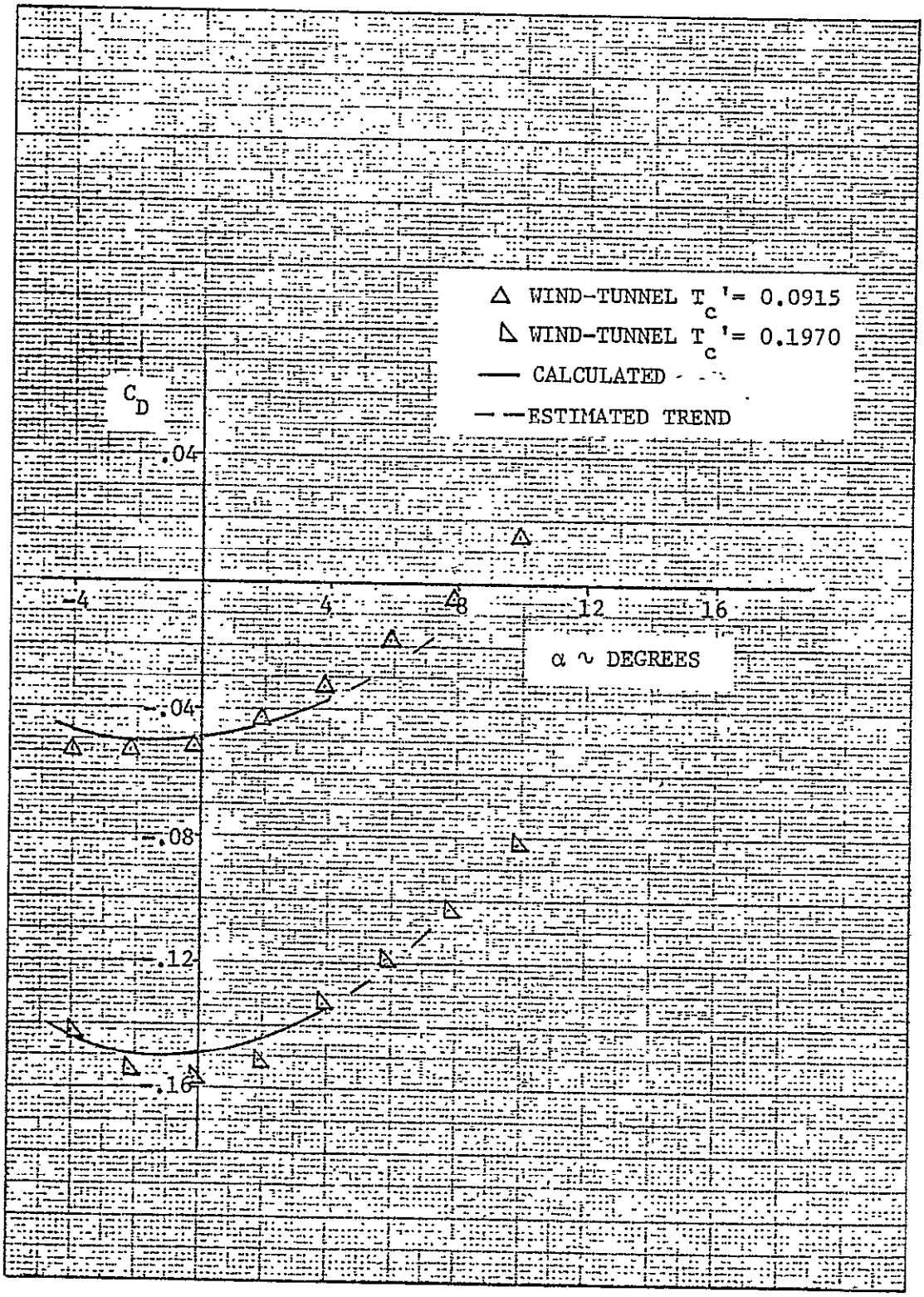

Figure 3.3.3: Comparison of calculated and wind-tunnel-determined drag at different power conditions

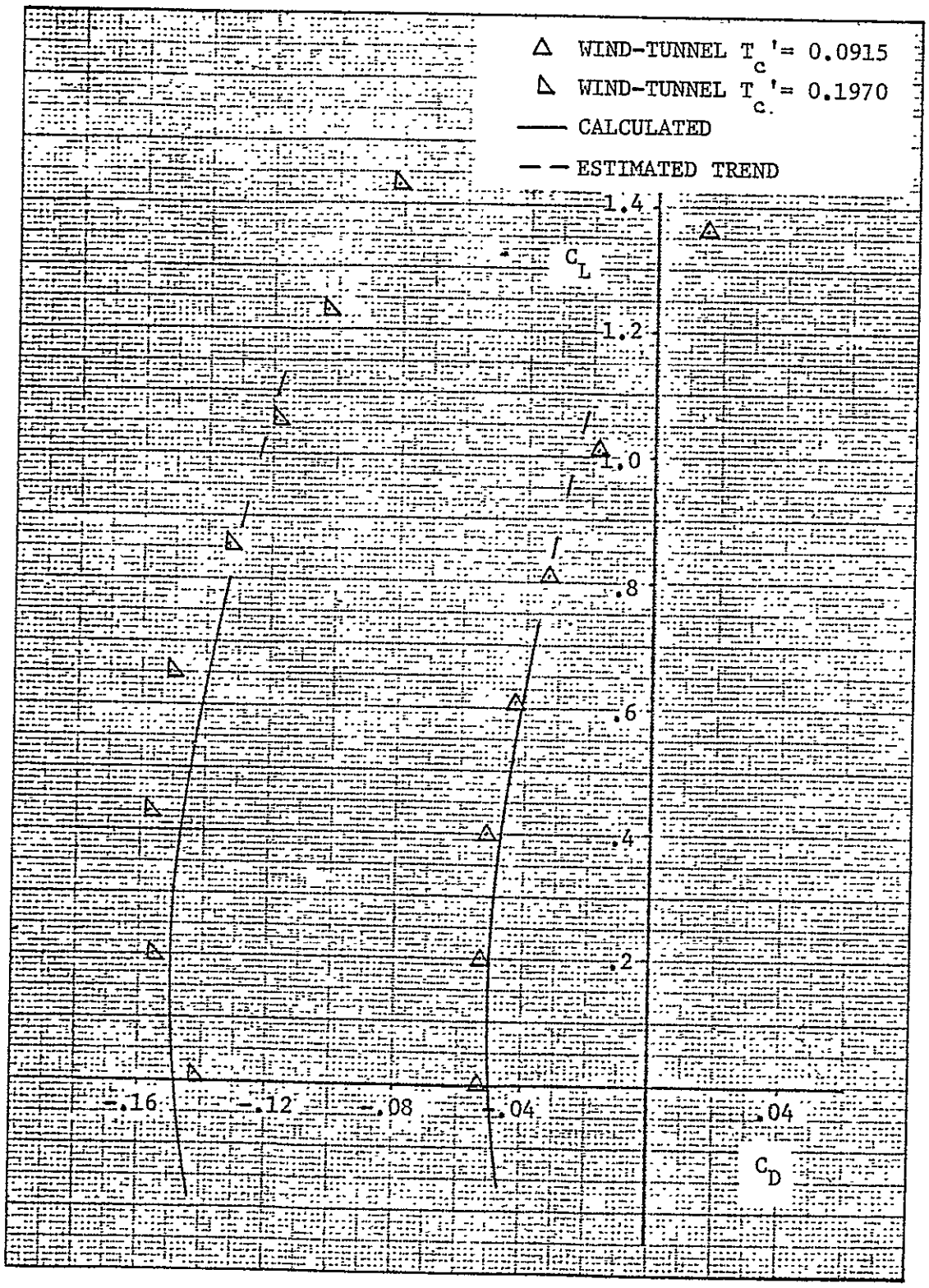

Figure 3.3.4: Comparison of predicted drag with full-scale wind tunnel data at different power conditions

CHAPTER 4

PREDICTION OF PROPELLER-OFF AERODYNAMIC CHARACTERISTICS

In this chapter the propeller-off aerodynamic characteristics will be discussed. Mainly, the method of Reference 3 will be used. However, Reference 3 does not discuss the influence of wing twist on the lift, pitching moment and drag of the airplane. References 4 and 8 will be used to incorporate this effect.

4.1 Wing and Horizontal Tail Airfoil Section Characteristics

A great deal of theoretical and experimental work has been done toward the development of airfoil sections. The theoretical airfoil design, however, is hampered by the viscous effects in the form of the boundary layer between the airfoil surface and the free stream. This boundary layer affects the section drag and maximum lift coefficient and also the slope of the lift curve, the angle of attack for zero lift and the section pitching-moment coefficient. Since the boundary layer is influenced by the surface roughness, the curvature of the surface, the pressure gradient, heat transfer between the surface and the boundary layer and viscous interaction with the free stream, it is apparent that no simple theoretical considerations can accurately predict all the airfoil characteristics. For these reasons, experimental data are always preferable to theoretical calculations.

Table 4.1.1 summarizes experimental data for the NACA four- and five-digit airfoils and for the NACA 6-series airfoils. The data, from Reference 3, are for smooth-leading-edge conditions and 9×10^6 Reynolds number. Information is presented on the following airfoil

characteristics:

1. angle of attack for zero-lift, α_o
2. lift curve slope, c_{ℓ_α}
3. angle of attack at which the lift curve deviates from linear variation, α^*
4. maximum lift coefficient, $c_{\ell_{max}}$
5. angle of attack for maximum lift, $\alpha_{c_{\ell_{max}}}$
6. zero-lift pitching moment coefficient, c_{m_o}
7. position of the aerodynamic center as a ratio of the chord length, a.c.

From the first five quantities the approximate lift-curve shape can be synthesized. Experimental data for a large number of additional airfoils are available in the literature (see Reference 4).

In this section a theoretical approach will not be considered. Section characteristics will be based on experimental data with the maximum lift coefficient corrected to the Reynolds number being considered. The effect of Reynolds number on the maximum lift coefficient can be accounted for by using Figure 4.1.1, which uses the leading-edge sharpness parameter, Δy, as the correlating parameter. The leading-edge sharpness parameter is defined in Figure 4.1.2. From this figure, the leading-edge sharpness parameter can be obtained as a function of the airfoil type and the thickness ratio. Another important parameter is the airfoil trailing-edge angle, ϕ_{te}, which can be obtained from Figure 4.1.3.

In the case of the ATLIT airplane, Reference 9 has been used to obtain the section airfoil characteristics of the wing. Figure 4.1.4

shows the section lift coefficient and the section pitching moment coefficient of the GA(W)-1 airfoil as being used in this study. The section airfoil characteristics of the horizontal tail are determined from Table 4.1.1. The leading-edge sharpness parameter and the trailing-edge angle of the horizontal tail (NACA 0010) airfoil can be obtained from Figures 4.1.2 and 4.1.3, respectively. For the GA(W)-1 airfoil, however, these parameters have to be obtained from the section shape of the airfoil (Figure 4.1.5). Table 4.1.2 summarizes the airfoil section characteristics of the wing and horizontal-tail.

Table 4.1.1: Experimental low-speed airfoil section aerodynamic characteristics (Reference 3)

(a) 4- and 5-digit airfoils, $N_{Re} = 9 \times 10^6$, smooth leading edge

Airfoil	α_o, deg	c_{m_o}	c_{l_α}, per deg	a.c.	$\alpha_{c_{l_{max}}}$, deg	$c_{l_{max}}$	α^*, deg
0006	0	0	0.108	0.250	9.0	0.92	9.0
0009	0	0	.109	.250	13.4	1.32	11.4
1408	.8	-.023	.109	.250	14.0	1.35	10.0
1410	-1.0	-.020	.108	.247	14.3	1.50	11.0
1412	-1.1	-.025	.108	.252	15.2	1.58	12.0
2412	-2.0	-.047	.105	.247	16.8	1.68	9.5
2415	-2.0	-.049	.106	.246	16.4	1.63	10.0
2418	-2.3	-.050	.103	.241	14.0	1.47	10.0
2421	-1.8	-.040	.103	.241	16.0	1.47	8.0
2424	-1.8	-.040	.098	.231	16.0	1.29	8.4
4412	-3.8	-.093	.105	.247	14.0	1.67	7.5
4415	-4.3	-.093	.105	.245	15.0	1.64	8.0
4418	-3.8	-.088	.105	.242	14.0	1.53	7.2
4421	-3.8	-.085	.103	.238	16.0	1.47	6.0
4424	-3.8	-.082	.100	.239	16.0	1.38	4.8
23012	-1.4	-.014	.107	.247	18.0	1.79	12.0
23015	-1.0	-.007	.107	.243	18.0	1.72	10.0
23018	-1.2	-.005	.104	.243	16.0	1.60	11.8
23021	-1.2	0	.103	.238	15.0	1.50	10.3
23024	-.8	0	.097	.231	15.0	1.40	9.7

(b) 6-series airfoils, $N_{Re} = 9 \times 10^6$, smooth leading edge

Airfoil	α_o, deg	c_{m_o}	c_{l_α} per deg	a.c.	$\alpha_{c_{l_{max}}}$, deg	$c_{l_{max}}$	α^*, deg
63-006	0	0.005	0.112	0.258	10.0	0.87	7.7
63-009	0	0	.111	.258	11.0	1.15	10.7
63-206	-1.9	-.037	.112	.254	10.5	1.06	6.0
63-209	-1.4	-.032	.110	.262	12.0	1.40	10.8
63-210	-1.2	-.035	.113	.261	14.5	1.56	9.6
63_1-012	0	0	.116	.265	14.0	1.45	12.8
63_1-212	-2.0	-.035	.114	.263	14.5	1.63	11.4
63_1-412	-2.8	-.075	.117	.271	15.0	1.77	9.6
63_2-015	0	0	.117	.271	14.5	1.47	11.0
63_2-215	-1.0	-.030	.116	.267	15.0	1.60	8.8
63_2-415	-2.8	-.069	.118	.262	15.0	1.68	10.0
63_2-615	-3.6	-.108	.117	.266	15.0	1.67	8.6
63_3-018	0	0	.118	.271	15.5	1.54	11.2
63_3-218	-1.4	-.033	.118	.271	14.5	1.85	8.0
63_3-418	-2.7	-.064	.118	.272	16.0	1.57	7.0
63_3-618	-3.8	-.097	.118	.267	16.0	1.59	4.2
63_4-021	0	0	.118	.273	17.0	1.38	9.0
63_4-221	-1.5	-.035	.118	.269	15.0	1.44	9.2
63_4-421	-2.8	-.062	.120	.275	16.0	1.48	6.7
63,4-420	-2.2	-.059	.109	.265	14.0	1.42	7.6
63,4-420 a = .3	-2.4	-.037	.111	.265	16.0	1.35	6.0
63(420)-422	-3.2	-.065	.112	.271	14.0	1.36	6.0
63(420)-517	-3.0	-.084	.108	.264	15.0	1.60	8.0
64-006	0	0	.109	.256	9.0	.8	7.2
64-009	0	0	.110	.262	11.0	1.17	10.0
64-108	0	-.015	.110	.255	10.0	1.10	10.0
64-110	-1.0	-.020	.110	.261	13.0	1.40	10.0
64-206	-1.0	-.040	.110	.253	12.0	1.03	8.0
64-208	-1.2	-.039	.113	.257	10.5	1.23	8.8
64-209	-1.5	-.040	.107	.261	13.0	1.40	8.9
64-210	-1.6	-.040	.110	.258	14.0	1.45	10.8
64_1-012	0	0	.111	.262	14.5	1.45	11.0
64_1-112	-.8	-.017	.113	.267	14.0	1.50	12.2
64_1-212	-1.3	-.027	.113	.262	15.0	1.55	11.0
$64_1$412	-2.6	-.065	.112	.267	15.0	1.67	8.0

Table 4.1.1: Concluded

Airfoil	α_0, deg	c_{m_o}	c_{l_α} per deg	a.c.	$\alpha_{c_{l_{max}}}$, deg	$c_{l_{max}}$	α^*, deg
64_2-015	0	0	0.112	0.267	15.0	1.48	13.0
64_2-215	-1.6	-.030	.112	.265	15.0	1.57	10.0
64_2-415	-2.8	-.070	.115	.264	15.0	1.65	8.0
64_3-018	0	.004	.111	.266	17.0	1.50	12.0
64_3-218	-1.3	-.027	.115	.271	16.0	1.53	10.0
64_3-418	-2.9	-.065	.116	.273	14.0	1.57	8.0
64_3-618	-3.8	-.095	.116	.273	16.0	1.58	5.6
64_4-021	0	.005	.110	.274	14.0	1.30	10.3
64_4-221	-1.2	-.029	.117	.271	13.0	1.32	6.8
64_4-421	-2.8	-.068	.120	.276	13.0	1.42	6.4
65-006	0	0	.105	.258	12.0	.92	7.6
65-009	0	0	.107	.264	11.0	1.08	9.8
65-206	-1.6	-.031	.105	.257	12.0	1.03	6.0
65-209	-1.2	-.031	.106	.259	12.0	1.30	10.0
65-210	-1.6	-.034	.108	.262	13.0	1.40	9.6
65-410	-2.5	-.067	.112	.262	14.0	1.52	8.0
65_1-012	0	0	.110	.261	14.0	1.36	10.0
65_1-212	-1.0	-.032	.108	.261	14.0	1.47	9.4
65_1-212 a = .6	-1.4	-.033	.108	.269	14.0	1.50	9.6
65_1-412	-3.0	-.070	.111	.265	15.5	1.66	10.5
65_2-015	0	0	.111	.257	15.0	1.42	11.2
65_2-215	-1.2	-.032	.112	.269	15.5	1.53	10.0
65_2-415	-2.6	-.060	.111	.268	16.0	1.61	8.7
65_2-415 a = .5	-2.6	-.051	.111	.264	20.0	1.60	7.0
65(215)-114	-.7	-.019	.112	.265	15.0	1.44	10.5
65(216)-415 a = .5	-3.0	-.057	.106	.267	18.0	1.60	6.0
65,3-018	0	0	.100	.262	17.0	1.44	10.0
65-418 a = .8	-3.0	-.081	.112	.266	20.0	1.58	4.4
65-618	-4.0	-.100	.110	.273	20.0	1.60	4.9
65_3-018	0	0	.100	.267	16.0	1.37	10.0
65_3-218	-1.2	-.030	.100	.263	18.0	1.48	8.8
65_3-418	-2.4	-.059	.110	.265	18.0	1.54	4.9
65_3-418 a = .5	-2.8	-.055	.115	.267	18.0	1.50	6.0
65_3-618	-4.0	-.102	.113	.276	18.0	1.64	5.2
65_3-618 a = .5	-4.2	-.078	.104	.265	20.0	1.51	5.3
65_4-021	0	0	.112	.267	18.5	1.40	7.4
65_4-221	-1.3	-.029	.115	.274	20.5	1.46	6.0
65_4-421	-2.8	-.066	.116	.272	22.0	1.56	5.0
65_4-421 a = .5	-2.8	-.052	.116	.272	20.0	1.43	5.6
65(421)-420	-2.4	-.061	.116	.276	20.0	1.52	4.7
66-006	0	0	.100	.252	9.0	.80	6.5
66-009	0	0	.103	.259	10.0	1.05	10.0
66-206	-1.6	-.038	.108	.257	10.5	1.00	7.0
66-209	-1.0	-.034	.107	.257	11.0	1.17	9.0
66-210	-1.3	-.035	.110	.261	11.0	1.27	10.0
66_1-012	0	0	.106	.258	14.0	1.25	11.2
66_1-212	-1.2	-.032	.102	.259	15.0	1.46	11.6
66_2-015	0	.005	.105	.265	15.5	1.35	12.0
66_2-215	-1.3	-.031	.106	.260	16.0	1.50	11.4
66_2-415	-2.6	-.069	.106	.260	17.0	1.60	10.0
66(215)-016	0	0	.105	.260	14.0	1.33	10.0
66(215)-216	-2.0	-.044	.114	.262	16.0	1.55	8.8
66(215)-216 a = .6	-1.2	-.030	.100	.257	16.0	1.46	7.0
66(215)-416	-2.6	-.068	.100	.265	18.0	1.60	4.0
63A010	0	.005	.105	.254	13.0	1.20	10.0
63A210	-1.5	-.040	.103	.257	14.0	1.43	10.0
64A010	0	0	.110	.253	12.0	1.23	10.0
64A210	-1.5	-.040	.105	.251	3.0	1.44	10.0
64A410	-3.0	-.080	.100	.254	15.0	1.61	10.0
64_1A212	-2.0	-.040	.100	.252	14.0	1.54	11.0
64_2A215	-2.0	-.040	.095	.252	15.0	1.50	12.0

Table 4.1.2: Airplane wing and horizontal tail airfoil section characteristics

Symbol	Description	Reference	Wing	Reference	Horizontal Tail
-	Airfoil section	Table 2.1	GA(W)-1	Table 2.1	NACA 0010
t/c	Thickness ratio	Table 2.1	0.17	Table 2.1	0.10
Δy	Leading-edge-sharpness parameter	Figure 4.1.5	4.9	Figure 4.1.2	2.6
ϕ_{te}	Trailing-edge-angle, deg	Figure 4.1.5	14.5	Figure 4.1.3	13.0
α_o	Zero-lift α relative to chord line, deg	Figure 4.1.4	-3.7	Table 4.1.1	0
c_{ℓ_α}	Lift-curve slope, per deg per rad	Figure 4.1.4 -	0.115 6.589	Table 4.1.1 -	0.109 6.245
α^*	Limit of linearity of c_{ℓ_α}, relative to chord line, deg	Figure 4.1.4	3.6	Table 4.1.4	12.2
$\alpha_{c_{\ell_{max}}}$	α at $c_{\ell_{max}}$ (relative to chord line), deg	Figure 4.1.4	16.0	Table 4.1.1	14.9
$(N_{R_e})_{base}$	Reynolds number of airfoil wind-tunnel data	Figure 4.1.4	2.1×10^6	Table 4.1.1	9×10^6
$(c_{\ell_{max}})_{base}$	Maximum lift coefficient	Figure 4.1.4	1.59	Table 4.1.1	1.45
$\Delta c_{\ell_{max}}$	Correction of maximum c_ℓ to $N_{R_e} = 2.3 \times 10^6$	Figure 4.1.1	0	Figure 4.1.1	-0.10
$c_{\ell_{max}}$	Maximum lift coefficient at wind-tunnel test condition = $(c_{\ell_{max}})_{base} + \Delta c_{\ell_{max}}$	-	1.59	-	1.35
c_{m_o}	Zero-lift pitching-moment coefficient	Figure 4.1.4	-0.095	Table 4.1.1	0
a.c.	Location of aerodynamic center			Table 4.1.1	0.250

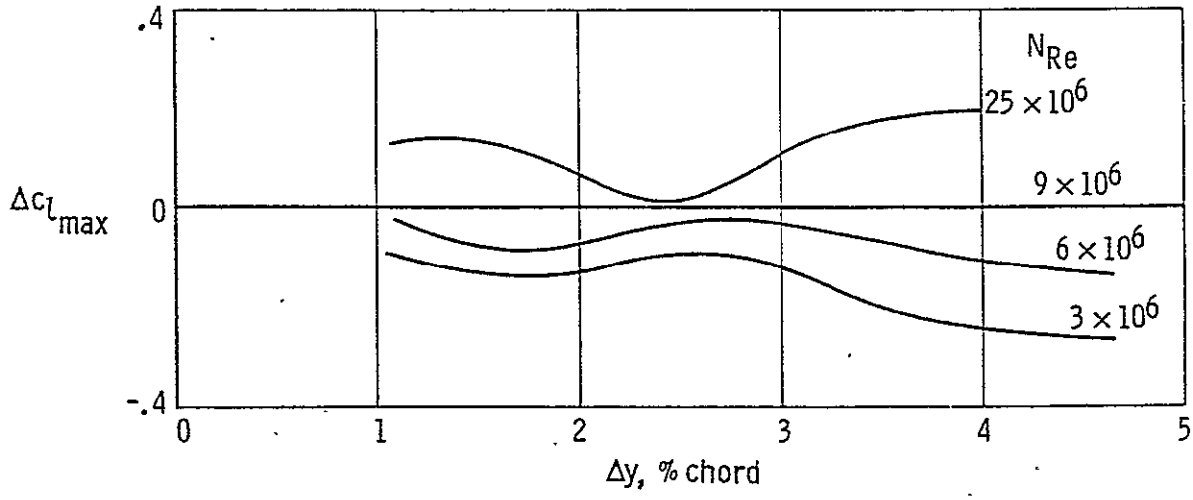

Figure 4.1.1: Effect of Reynolds number on section maximum lift coefficient (Reference 3)

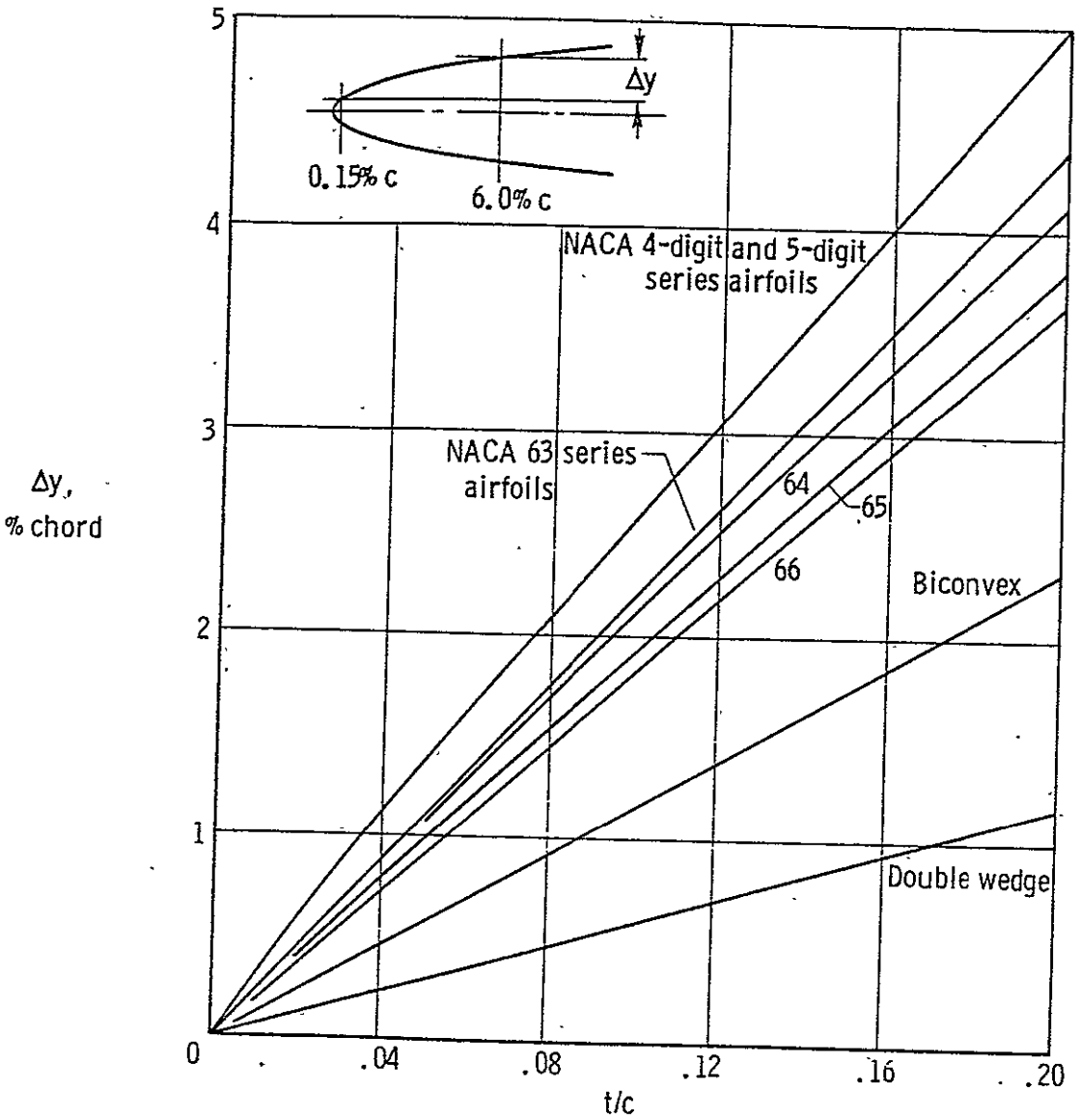

Figure 4.1.2: Variation of leading-edge sharpness parameter with airfoil thickness ratio (Reference 3)

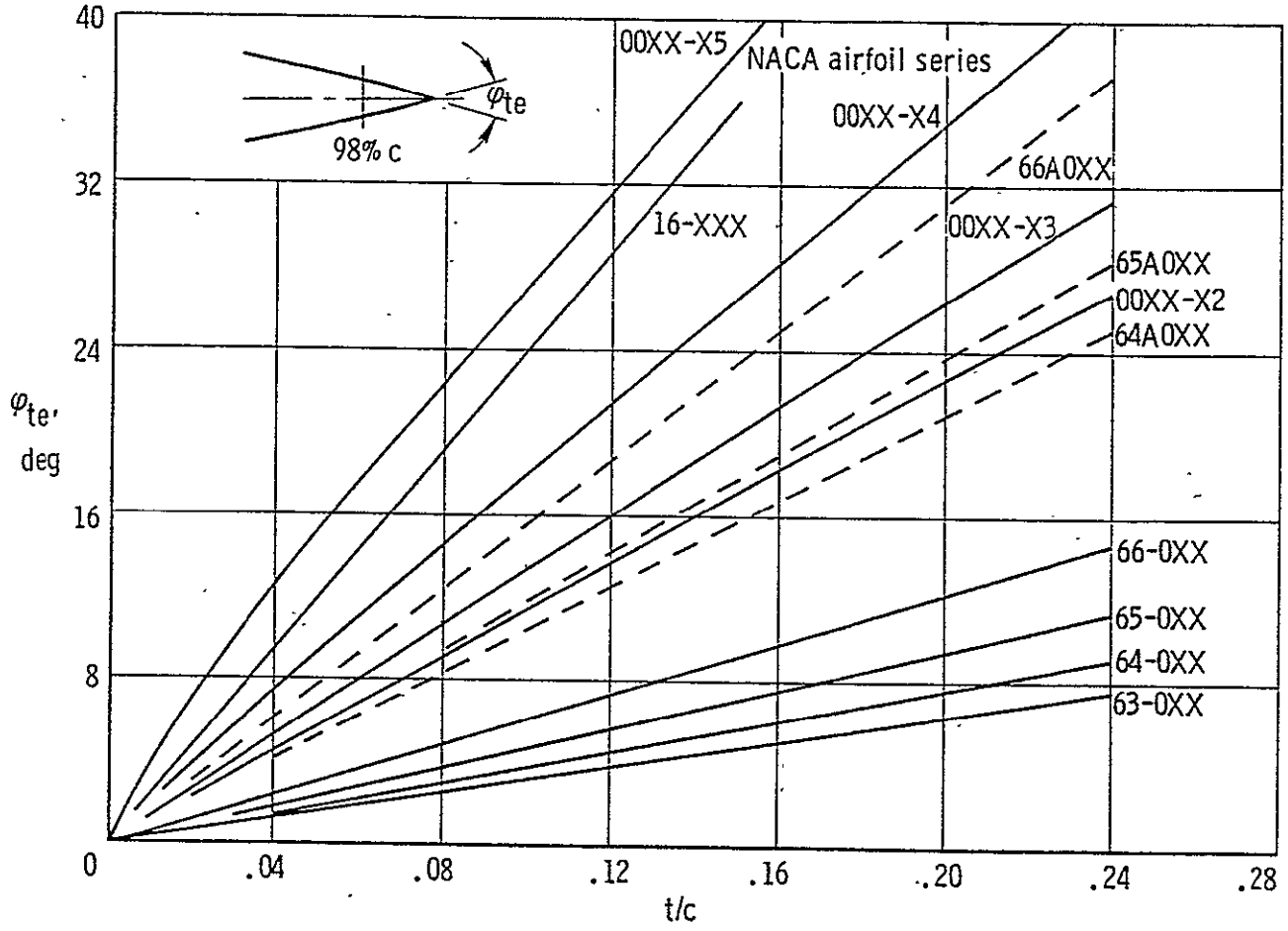

Figure 4.1.3: Variation of trailing-edge angle with airfoil thickness ratio (Reference 3)

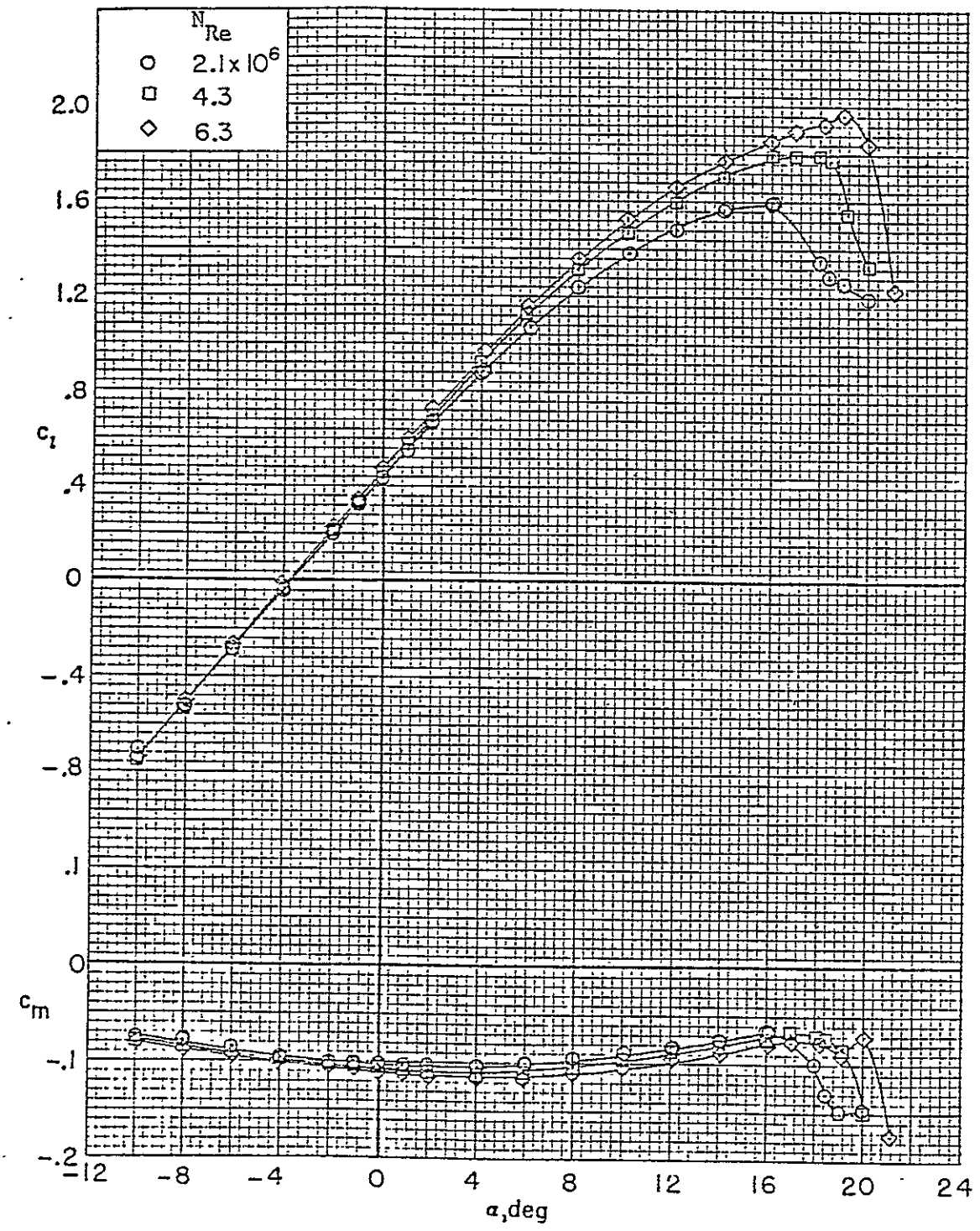

Figure 4.1.4: Aerodynamic characteristics of GA(W)-1 airfoil section. M=0.15 and number 80 roughness at 0.08c (Reference 9)

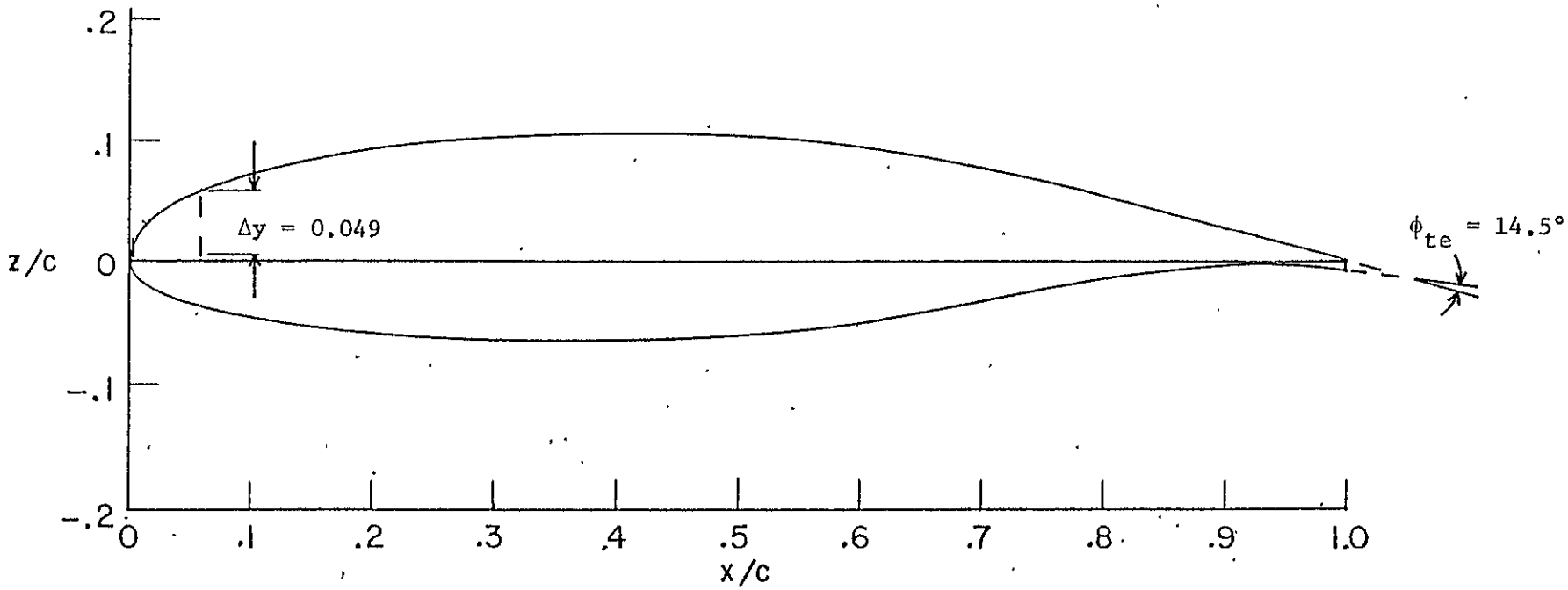

Figure 4.1.5: Section shape for NASA GA(W)-1 airfoil (Reference 9)

4.2 Lift Characteristics of the Wing and Horizontal Tail

The approximate wing lift-curve can be estimated when the following characteristics are known:

1. lift curve slope, C_{L_α}
2. angle of attack for zero-lift, α_o
3. limit of linearity of the lift curve slope, α^*
4. maximum lift coefficient, $C_{L_{max}}$
5. angle of attack for maximum lift, $\alpha_{C_{L_{max}}}$

In the following subsections methods are presented for calculating these characteristics.

4.2.1 Lift Curve Slope

The lift curve slope of a tapered straight wing, in the subsonic region to M = 0.6, can be determined by the modified lifting line theory method of Polhamus. The lift curve slope is calculated as a function of the aspect ratio, A, the midchord sweep angle, $\Lambda_{c/2}$, Mach number, M, and the section lift curve slope, c_{ℓ_α}, by the following expression:

$$(C_{L_\alpha})_{Pol} = \frac{2\pi A}{2 + \sqrt{\frac{A^2}{k^2}(\beta^2 + \tan^2\Lambda_{c/2}) + 4}} \qquad (4.2.1.1)$$

where

$$\beta = \sqrt{1 - M^2} \quad \text{and} \quad k = c_{\ell_\alpha}/2\pi.$$

As compared to results from the lifting surface theory, Equation (4.2.1.1) overestimates the value of C_{L_α} by the value K_{Pol}, or:

$$C_{L_\alpha} = \left(1 - \frac{K_{Pol}}{100}\right) (C_{L_\alpha})_{Pol} \qquad (4.2.1.2)$$

where

K_{Pol} follows from Figure 4.2.1.1.

4.2.2 Angle of Attack for Zero-Lift

According to Reference 4, the zero-lift angle of attack of a wing may be calculated as follows:

$$\alpha_{o_w} = \alpha_o + \frac{\Delta\alpha_o}{\theta}\,\theta \qquad (4.2.2.1)$$

where

α_o can be assumed to be the section zero-lift angle at low Mach number, obtained from Section 4.1.

$\Delta\alpha_o/\theta$ represents the shift in the wing angle of attack for zero lift per degree of wing twist, obtained from Figure 4.2.2.1.

θ is the twist of the wing tip with respect to the root section (negative for washout).

A Mach number correction is presented in Figure 4.2.2.2. This chart gives the ratio of the zero-lift angle of attack at any subsonic Mach number to the corresponding value at M = 0.3.

The upper limit of linearity of the wing lift curve slope is considered to be:

$$\alpha_w^* = \alpha^* + \frac{\Delta\alpha_o}{\theta}\,\theta \qquad (4.2.2.2)$$

where

α^* indicates the limit of linearity of the section airfoil lift curve slope, obtained from Section 4.1.

4.2.3 Maximum Lift of the Wing

The maximum lift coefficient and angle of attack for maximum lift of wings at subsonic conditions may be determined by the empirical method of Reference 4. For high-aspect-ratio (general aviation airplanes are concerned with high-aspect-ratio wings), untwisted, constant section wings:

$$C_{L_{max}} = \frac{C_{L_{max}}}{c_{\ell_{max}}} c_{\ell_{max}} + \Delta C_{L_{max}} \qquad (4.2.3.1)$$

$$\alpha_{C_{L_{max}}} = \frac{C_{L_{max}}}{C_{L_\alpha}} + \alpha_{o_w} + \Delta\alpha_{C_{L_{max}}} \qquad (4.2.3.2)$$

The first term on the right side of Equation (4.2.3.1) is the maximum lift coefficient at M = 0.2 and the second term is the lift increment due to Mach effect.

$C_{L_{max}}/c_{\ell_{max}}$ is obtained from Figure 4.2.3.1.

$c_{\ell_{max}}$ is the section maximum lift coefficient at low Mach number obtained from Section 4.1.

$\Delta C_{L_{max}}$ is the Mach number correction obtained from Figure 4.2.3.2.

C_{L_α} is the wing lift curve slope obtained from Equation (4.2.1.2).

α_{o_w} is the wing zero-lift angle obtained, for the appropriate Mach number, from Equation (4.2.2.1).

$\Delta\alpha_{C_{L_{max}}}$ is obtained from Figure 4.2.3.3. The leading-edge sharpness parameter, Δy, must be used in reading values from the charts. The value of Δy is expressed in percent chord and is obtained from Section 4.1.

For twisted wings the calculations are more involved. The method used in this report is identical to the one described in Reference 8. The lift may be divided into additional and basic lift:

$$c_\ell = c_{\ell_a} + c_{\ell_b} \tag{4.2.3.3}$$

The additional lift coefficient can be written as follows:

$$c_{\ell_a} = \frac{C_L}{c/c_g} \left(C_1 \frac{c}{c_g} + C_2 \frac{4}{\pi} \sqrt{1-\eta^2} + C_3 f \right) \tag{4.2.3.4}$$

and the basic lift coefficient is:

$$c_{\ell_b} = c_{\ell_a}(C_L=1)\ \theta\ c_{\ell_\alpha}\ C_4 \left(\frac{\varepsilon}{\theta} + \frac{\Delta\alpha_o}{\theta} \right) \cos\Lambda_\beta \tag{4.2.3.5}$$

where

c/c_g is the ratio of the chord length at $\eta = y/(b/2)$ to the mean geometric chord:

$$c_g = \frac{c_r + c_t}{2} = c_r \frac{1+\lambda}{2} \tag{4.2.3.6}$$

C_1 through C_4 follow from Figure 4.2.3.4.

f is the lift distribution function and can be obtained from Figure 4.2.3.5.

ε/θ is the ratio of the wing twist at η to the wing twist of the tip, with respect to the root section.

$$\Lambda_\beta = \tan^{-1}\left(\frac{\tan \Lambda_{c/4}}{\beta}\right) \qquad (4.2.3.7)$$

The maximum lift coefficient of the wing, $C_{L_{max}}$, may be estimated from the assumption that this coefficient is reached when the local section lift coefficient, c_ℓ, at any position along the span is equal to the local $c_{\ell_{max}}$ for the corresponding section. This value may be found by the process indicated in Figure 4.2.3.6. Spanwise variations of the local $c_{\ell_{max}}$ and of the additional lift coefficient, c_{ℓ_a}, for $C_L = 1$ (Equation [4.2.3.4]) and c_{ℓ_b} (Equation [4.2.3.5]), distributions are plotted. The spanwise variation of $(c_{\ell_{max}} - c_{\ell_b})$ is plotted, and the minimum value of the ratio of $(c_{\ell_{max}} - c_{\ell_b})$ to c_{ℓ_a} at $C_L = 1$ is then found. This ratio is considered to be the maximum lift coefficient of the wing.

The angle of attack for maximum lift can be estimated with Equation (4.2.3.2).

4.2.4 Lift of the Wing and Horizontal Tail for the ATLIT Airplane

Pertinent aspects of the calculation of the wing and horizontal tail of the ATLIT airplane at wind tunnel Mach conditions are summarized in Table 4.2.4.1.

During this study it appeared that the ATLIT wing had parabolic twist instead of the common linear twist. This led to a change in the value of $\Delta\alpha_o/\theta$. In Appendix A the calculations to obtain $\Delta\alpha_o/\theta$ for the case of parabolic twist are shown. The calculations which lead to maximum lift coefficient, $C_{L_{max}}$, of the wing are presented in Appendix B.

The results from Table 4.2.4.1 are applied to the lift curves shown in Figure 4.2.4.1. In this figure, results obtained with References 5 and 6 are also shown. The results obtained with Reference 5 are in good agreement with those obtained with Reference 6. However, the lift curve slope of the former is slightly less steep than the lift curve slope of the latter. This difference is caused by the thickness effect and discussed in more detail in Appendix C. The difference in the angle of attack for zero-lift between the results of References 5 and 6 and the results from Table 4.2.4.1 is understandable. The former are lifting surface prediction methods, while the latter is based on the lifting line theory.

Table 4.2.4.1: Lift chacacteristics of wing and horizontal tail for the ATLIT airplane

Symbol	Description	Reference	Wing		Reference	Horizontal Tail	
			Total	Exposed		Total	Exposed
M	Mach number	-	0.081	0.081	-	0.081	0.081
β^2	$1 - M^2$	-	0.993	0.993	-	0.993	0.993
A	Aspect ratio	Table 2.1.1	10.32	9.61	Table 2.1.1	4.75	4.28
θ	Twist angle at the tip with respect to root section, deg	Table 2.1	-3.0	-3.0	Table 2.1	0	0
$\Lambda_{c/2}$	Sweep at half chord, deg	Table 2.1.1	0	0	Table 2.1.1	0	0
Λ_{le}	Leading edge sweep, deg	Table 2.1.1	3.67	3.67	Table 2.1.1	0	0
Δy	Leading-edge-sharpness parameter	Table 4.1.2	4.9	4.9	Table 4.1.2	2.6	2.6
c_{l_α}	Section airfoil lift curve slope, rad^{-1}	Table 4.1.2	6.589	6.589	Table 4.1.2	6.245	6.245
k	$c_{l_\alpha}/2\pi$	-	1.049	1.049	-	0.994	0.994
$(C_{L_\alpha})_{Pol}$	Wing lift curve slope according to Polhamus, rad^{-1}	Eq. (4.2.1.1)	5.401	5.322	Eq. (4.2.1.1)	4.165	3.993
K_{Pol}	Correction factor	Figure 4.2.1.1	5.75	5.95	Figure 4.2.1.1	6.90	6.85
C_{L_α}	Wing lift curve slope, rad^{-1} deg^{-1}	Eq. (4.2.1.2) -	5.090 0.0888	5.005 0.0874	Eq. (4.2.1.2) -	3.878 0.0677	3.719 0.0649
$c_{l_{max}}$	Section airfoil maximum lift coefficient	Table 4.1.2	1.59	1.59	Table 4.1.2	1.35	1.35
$(C_{L_{max}}/c_{l_{max}})$	Maximum lift coefficient factor at M=0.2				Figure 4.2.3.1	0.9	0.9
$\Delta C_{L_{max}}$	Mach number correction to M=0.081				Figure 4.2.3.2	0	0
$C_{L_{max}}$	Maximum lift coefficient at M=0.081	Appendix B	1.494	1.494	Eq. (4.2.3.1)	1.215	1.215
α_o	Section zero-lift angle of	Table 4.1.2	-3.7	-3.7	Table 4.1.2	0	0
$\Delta\alpha_o/\theta$	Shift in zero-lift angle of attack per unit twist	Appendix A	-0.27	-0.27	Figure 4.2.2.1	0	0
α_{o_w}	Wing zero-lift angle of attack, deg	Eq. (4.2.2.1)	-2.89	-2.89	Eq. (4.2.2.1)	0	0
α^*	Limit of linearity of section lift curve, deg	Table 4.1.2	3.6	3.6	Table 4.1.2	12.2	12.2
α_w^*	Limit of linearity of wing lift curve, deg	Eq. (4.2.2.2)	4.41	4.41	Eq. (4.2.2.2)	12.2	12.2
$(C_{L_{max}}/C_{L_\alpha})$	Maximum α for extended linearity conditions, deg	-	16.82	17.09	-	17.95	18.72
$\Delta\alpha_{C_{L_{max}}}$	Correction for flow separation, deg	Figure 4.2.3.3	2.5	2.5	Figure 4.2.3.3	0.8	0.8
$\alpha_{C_{L_{max}}}$	Angle of attack at $C_{L_{max}}$ at M=0.081, relative to chord, deg	Eq. (4.2.3.2)	16.43	16.70	Eq. (4.2.3.2)	18.75	19.52

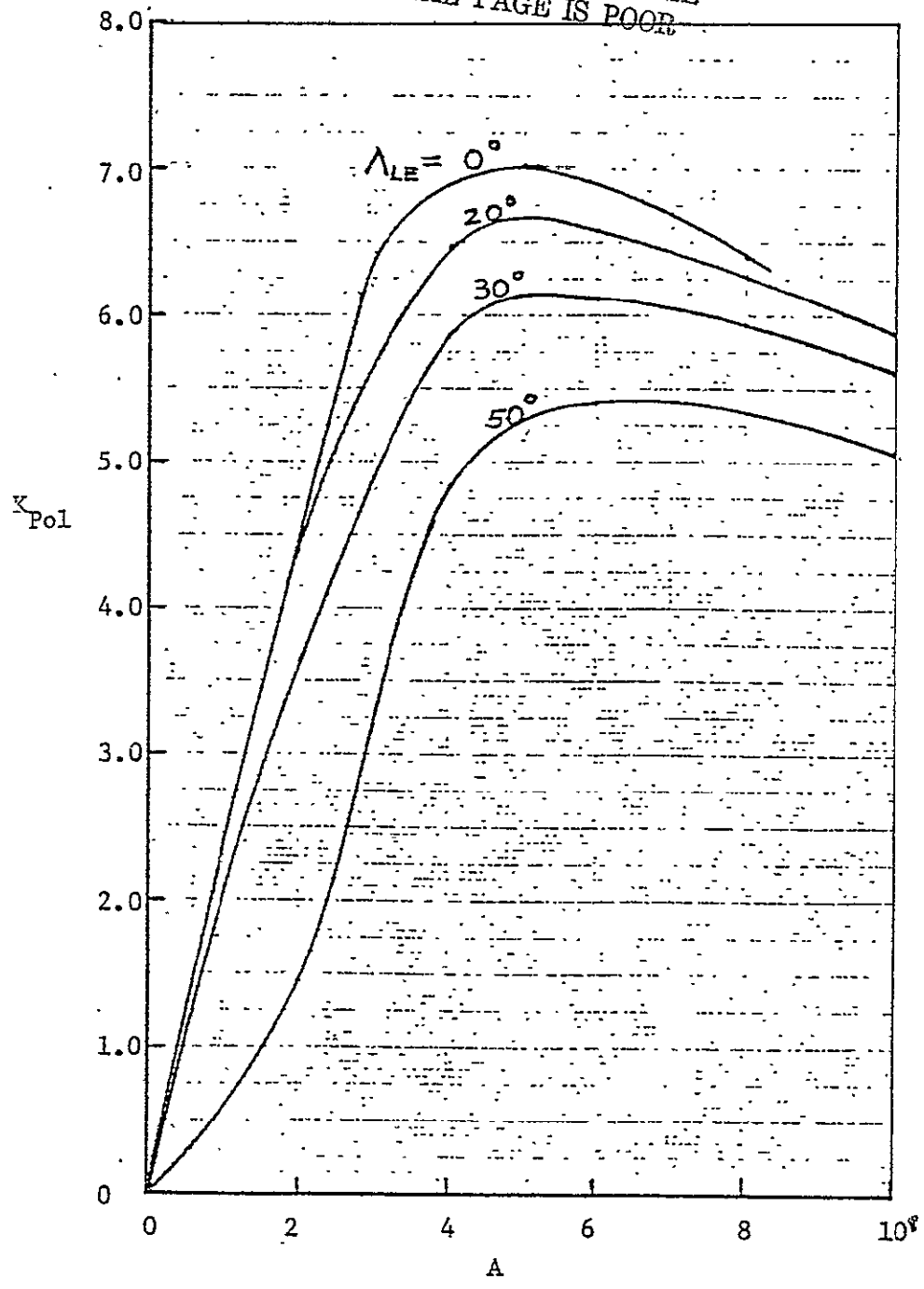

Figure 4.2.1.1: Error in Polhamus formula when compared with lifting surface method (Reference 10)

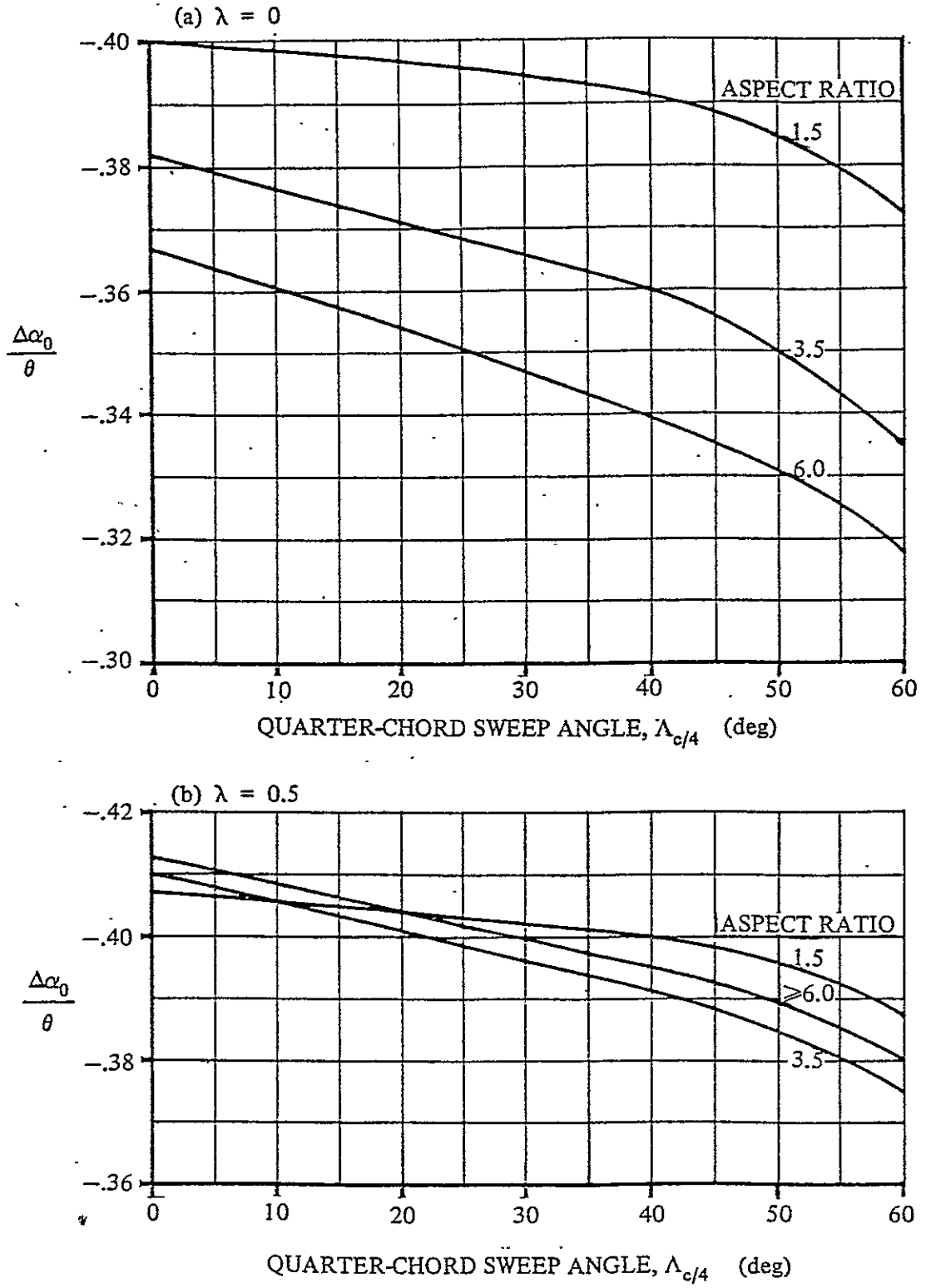

Figure 4.2.2.1: Effect of linear twist on angle of attack for zero-lift (Reference 4)

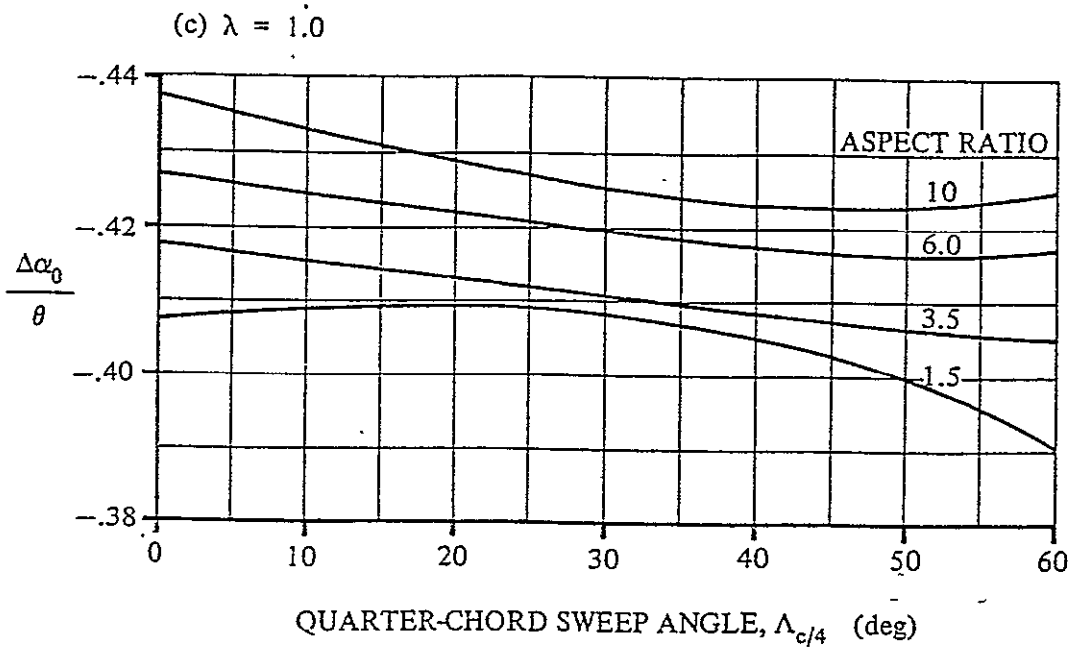

Figure 4.2.2.1: Concluded

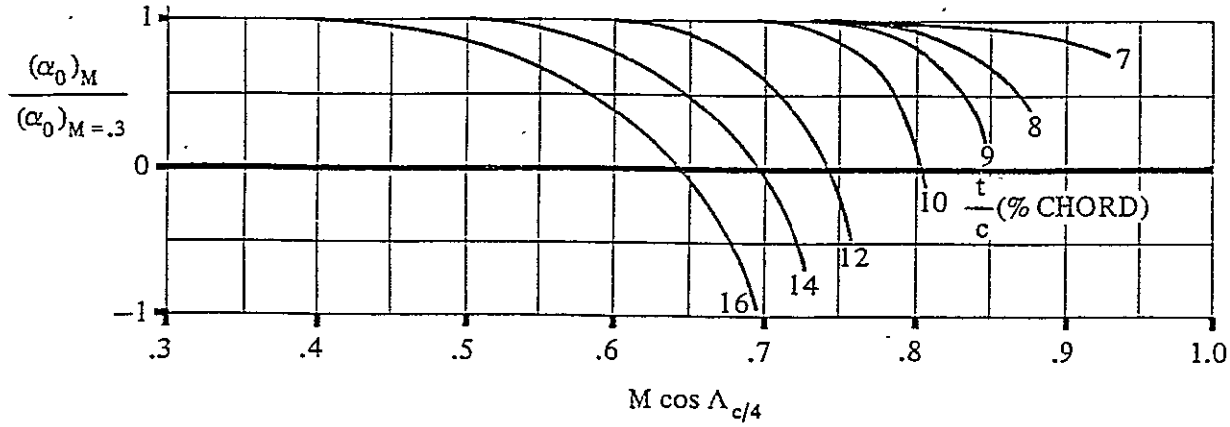

Figure 4.2.2.2: Mach number correction for zero-lift angle of attack for cambered airfoils (Reference 4)

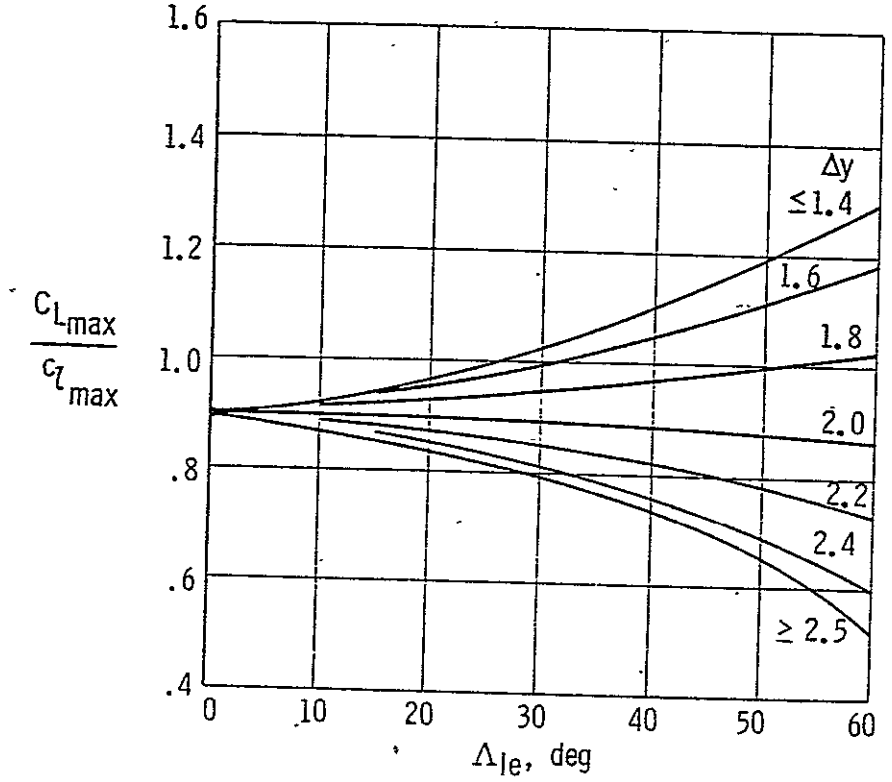

Figure 4.2.3.1: Subsonic maximum lift of high-aspect-ratio, untwisted constant airfoil section wings at M=0.2 (Reference 3)

C-2

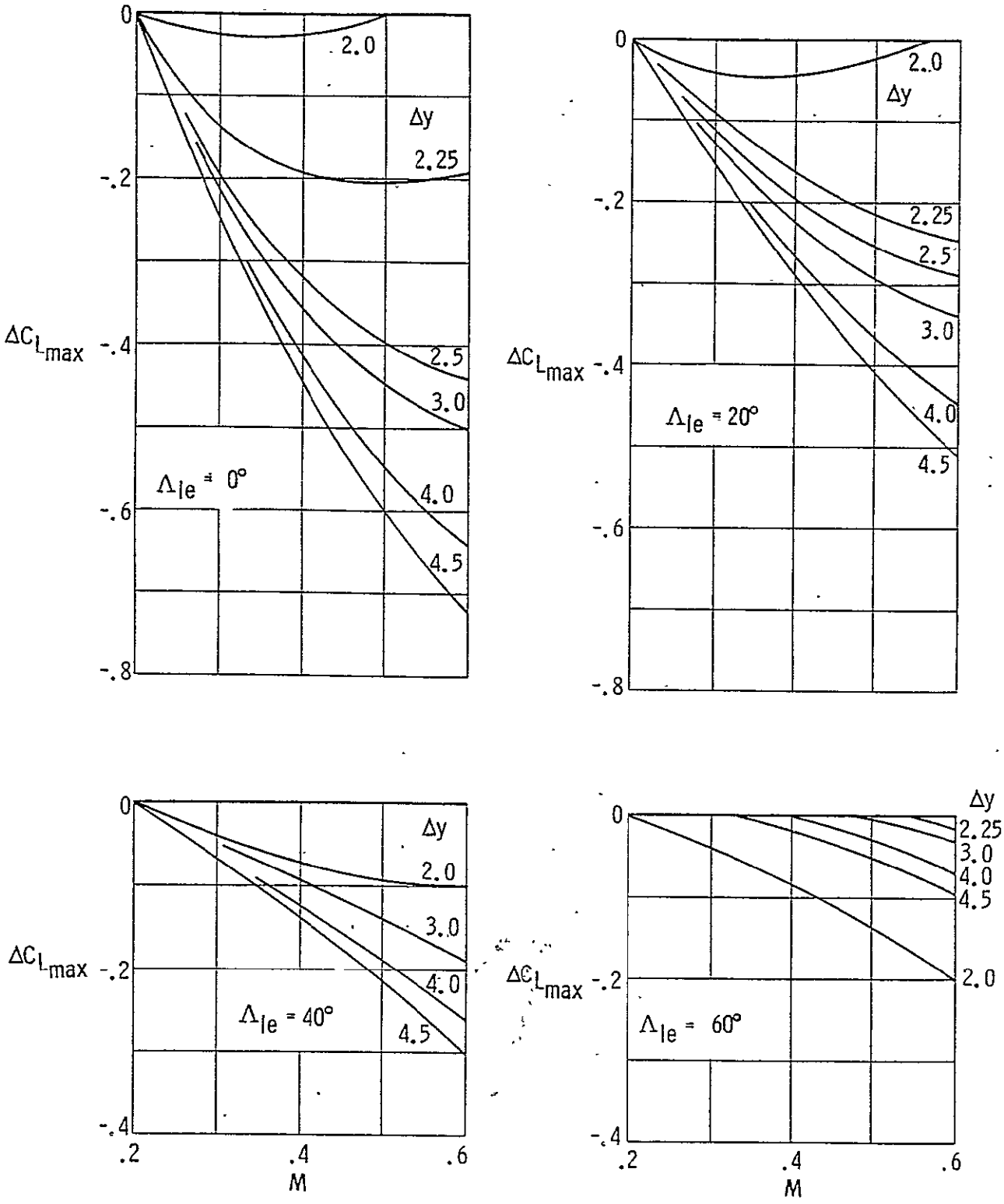

Figure 4.2.3.2: Mach number correction for subsonic maximum lift of high-aspect-ratio, untwisted, constant airfoil section wings (Reference 3)

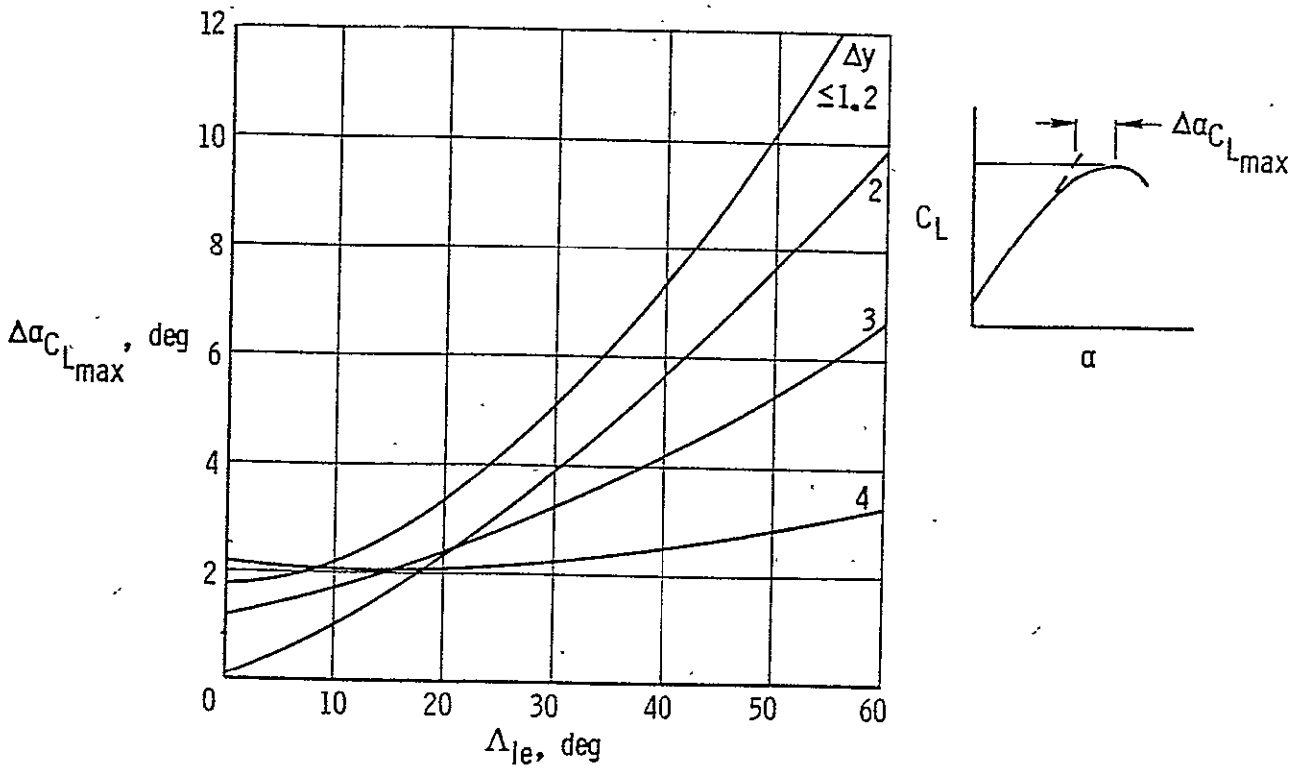

Figure 4.2.3.3: Angle of attack increment for subsonic maximum lift of high-aspect-ratio, untwisted, constant airfoil section wings at M=0.2 - 0.6 (Reference 3)

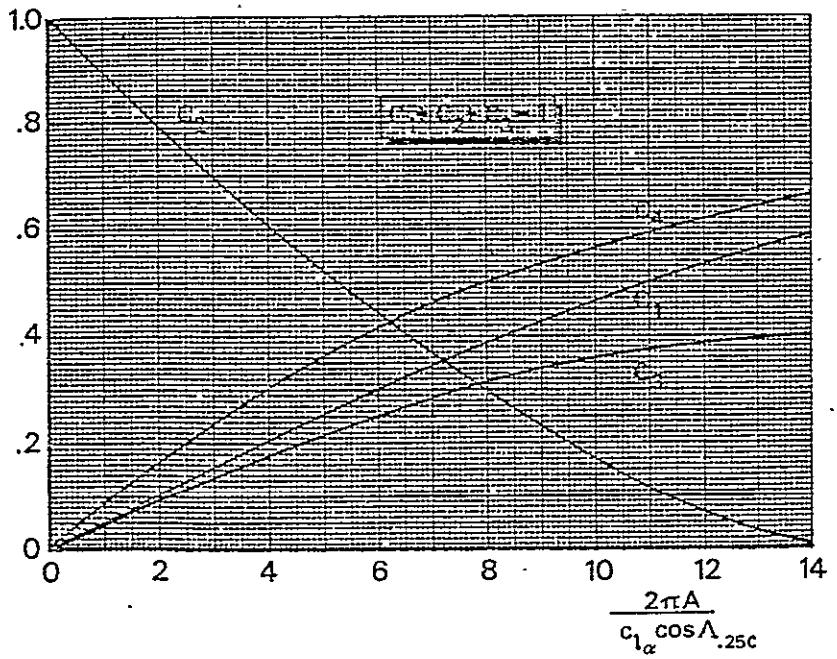

Figure 4.2.3.4: Coefficients for additional and basic lift distribution (Reference 8)

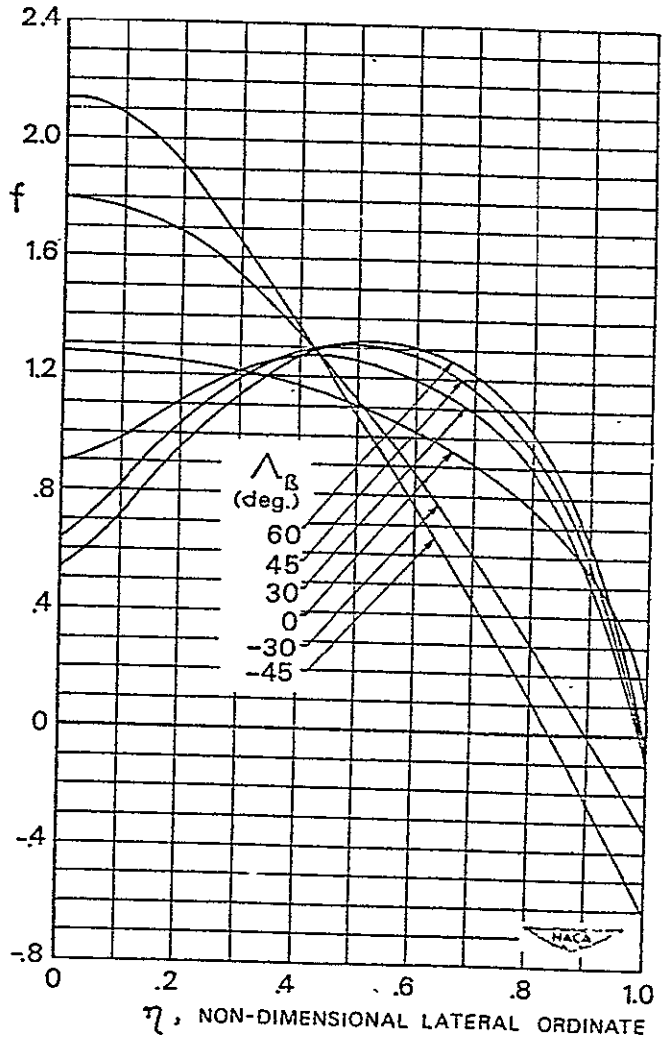

Figure 4.2.3.5: Lift distribution function (Reference 8)

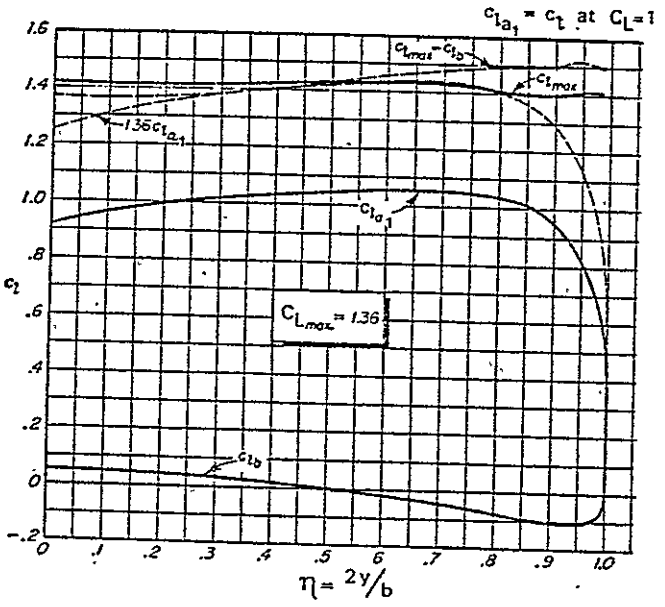

Figure 4.2.3.6: Example of lift distribution (Reference 8)

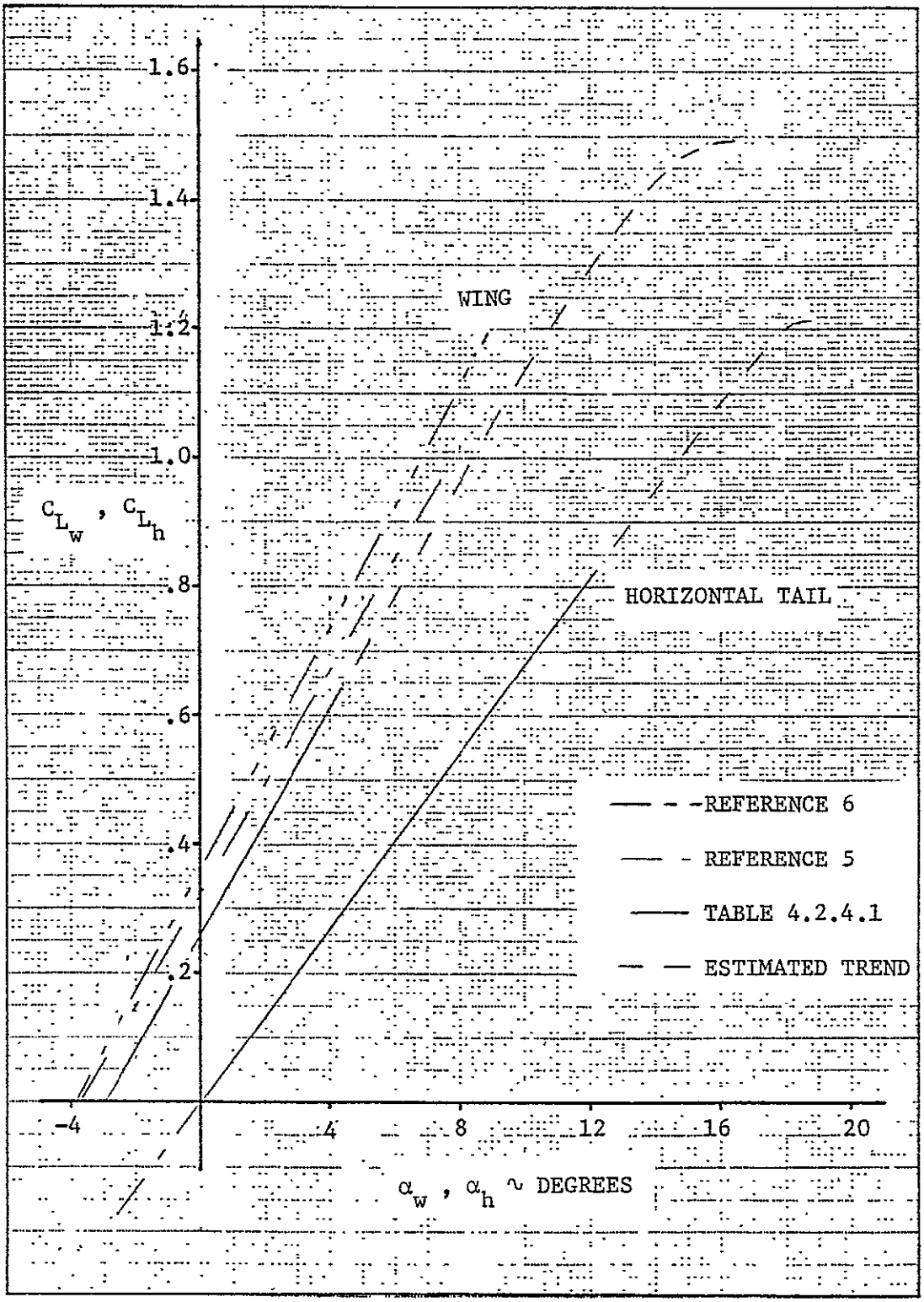

Figure 4.2.4.1: Lift curve of wing and horizontal tail at $N_{Re} = 2.3 \times 10^6$ for the ATLIT airplane (total surfaces).

4.3 Lift Due to Fuselage and Nacelles

The method used in Reference 3 to predict the lift due to the fuselage and the nacelles is also used in this study. This method is also discussed in Reference 4. It is based on the assumption that the flow is potential over the forward part of the body and has no viscous contribution in this region. At the position x_o the potential flow over the forward portion of the body changes into a viscous flow for the remainder of the body.

The expression for the lift coefficient of a body of revolution, based on the wing area, S_w, is:

$$C_{L_B} = \frac{2(k_2-k_1)\alpha_{B_{eff}} S_o}{57.3\, S_w} + \frac{2\alpha^2_{B_{eff}} \eta c_{d_c}}{(57.3)^2 S_w} \int_{x_o}^{\ell_B} r\,dx \qquad (4.3.1)$$

where the first part on the right hand side of Equation (4.3.1) represents the potential flow contribution and the second part represents the viscous crossflow contribution and where

(k_2-k_1) is the apparent mass factor obtained from Figure 4.3.1 as a function of body fineness ratio, d_{max}/ℓ_B.

S_o is the body cross-sectional area at x_o. In this study the maximum cross-sectional area of the equivalent circular body will be used, which results in slightly optimistic contributions of bodies (see Reference 3).

x_o is the body station where the flow ceases to be potential. This is a function of x_1, the body station where the rate of change of the cross-sectional area with x reaches its maximum negative value. x_o and x_1 are correlated in Figure 4.3.2.

$\alpha_{B_{eff}}$ is the effective angle of attack of the equivalent circular body in degrees, or:

$$\alpha_{B_{eff}} = \alpha_B + \alpha_{o_B} \tag{4.3.2}$$

α_B is the angle of attack of the actual body, identical to the airplane angle of attack, α, using X-body axis as a reference.

α_{o_B} is the zero-lift angle of the equivalent circular body relative to the reference X-body axis.

c_{d_c} is the steady-state cross-flow drag coefficient of a circular cylinder of infinite length, obtained from Figure 4.3.3.

η is the ratio of the drag of a finite cylinder to the drag of an infinite cylinder, obtained from Figure 4.3.4.

ℓ_B is the body length.

$\int_{x_o}^{\ell_B} r\,dx$ represents half of the projected area of the equivalent circular body from x_o to the end of the body. Using the Simpson integration method:

$$\int_{x_o}^{\ell_B} r\,dx = \sum_{x_o}^{\ell_B} r\,\Delta x \tag{4.3.3}$$

r is the body radius at any longitudinal station.

dx, Δx is the increment length of the body.

In many cases it will be possible to determine the location of x_1 by inspection. For cases that are doubtful, the area distribution should be plotted and examined to determine the location where dS_x/dx first reaches its maximum negative value.

Because the equation for lift of bodies is based on bodies of revolution, it is necessary to replace the actual body by an approximate equivalent body of revolution to serve as a mathematical model for analysis.

For the ATLIT Figure 4.3.5(a) shows the estimated equivalent circular fuselage in relation to the actual fuselage. The equivalent fuselage has a zero-lift angle of 2.5 degrees below the reference X-body axis. The nacelle does not lend itself to such a simple estimate of equivalence because of its wide rectangular shape and irregular profile. However, in Figure 4.3.5(b) an approximation for equivalence is shown. The axis of the equivalent nacelle is parallel to the X-body axis.

In Figure 4.3.5(b) the actual nacelle is shown. Not included is the extension of 8 inches due to installation of the thrust/torque balance. This factor has not been taken into account in the calculations. However, the effect of the extension on the lift of the nacelle will be negligible.

Table 4.3.1 summarizes the calculations for the lift contributions of the fuselage and the nacelles. The lift coefficient of the fuselage based on the wing, S_w, is:

$$C_{L_f} = 0.002574(\alpha_B - 2.5) + 0.0000402(\alpha_B - 2.5)^2 \qquad (4.3.4)$$

and the total lift coefficient of the nacelles based on the reference wing area is:

$$C_{L_n} = 0.002031\ \alpha_B + 0.0000201\ \alpha_B^2 \qquad (4.3.5)$$

where

α_B is the angle of attack, in degrees, of the actual body and identical to the airplane angle of attack.

Table 4.3.1: Fuselage and nacelle lift contribution

Symbol	Description	Reference	Fuselage	Nacelle
M	Mach number	-	0.081	0.081
S_w	Reference wing area, m^2 (ft^2)	Table 2.1.1	14.40 (155.0)	14.40 (155.0)
d_{max}	Maximum diameter of equivalent circular body, m (in)	Figure 4.3.5	1.238 (48.75)	0.889 (35.0)
$S_{o_{max}}$	Maximum cross sectional area of equivalent circular body, m^2 (ft^2)	-	1.204 (12.96)	0.621 (6.68)
x_1	Location of $S_{o_{max}}$ from nose of body, m, (in)	Figure 4.3.5	3.97 (156.3)	0.76 (30.0)
ℓ_B	Body length, m (in)	Figure 4.3.5	8.35 (328.8)	2.43 (95.6)
ℓ_B/d_{max}	Fineness ratio	-	6.745	2.731
(k_2-k_1)	Reduced mass factor	Figure 4.3.1	0.882	0.675
η	Ratio of drag coefficient of finite to infinite length cylinder	Figure 4.3.4	0.650	0.575
x_1/ℓ_B	Location from nose of $S_{o_{max}}$	-	0.475	0.314
x_o/ℓ_B	Location from nose where potential flow ceases	Figure 4.3.2	0.627	0.541
x_o	$(x_o/\ell_B)\ell_B$, m (in)	-	5.24 (206.2)	1.31 (51.7)
$\int_{x_o}^{\ell_B} r\,dx$	Half projected area of equivalent circular body from x_o to ℓ_B, m^2 (ft^2)	Figure 4.3.5	1.22 (13.1)	0.34 (3.7)
α_{o_B}	Zero-lift angle of equivalent circular body, deg	Figure 4.3.5	-2.5	0
$\alpha_{B_{eff}}$	Angle of attack of equivalent circular body, deg	Eq. (4.3.2)	α_B-2.5	α_B
M_c	$M \sin \alpha_{B_{eff}}$	-	$0.081 \sin(\alpha_B-2.5)$	$0.081 \sin \alpha_B$
c_{d_c}	Crossflow drag coefficient of infinite length cylinder	Figure 4.3.3	1.2	1.2

Summary: Fuselage $C_{L_f} = 0.002574\ (\alpha_B-2.5) + 0.0000402\ (\alpha_B-2.5)^2$

Nacelles (2) $C_{L_n} = 0.002031\ \alpha_B + 0.0000201\ \alpha_B^2$

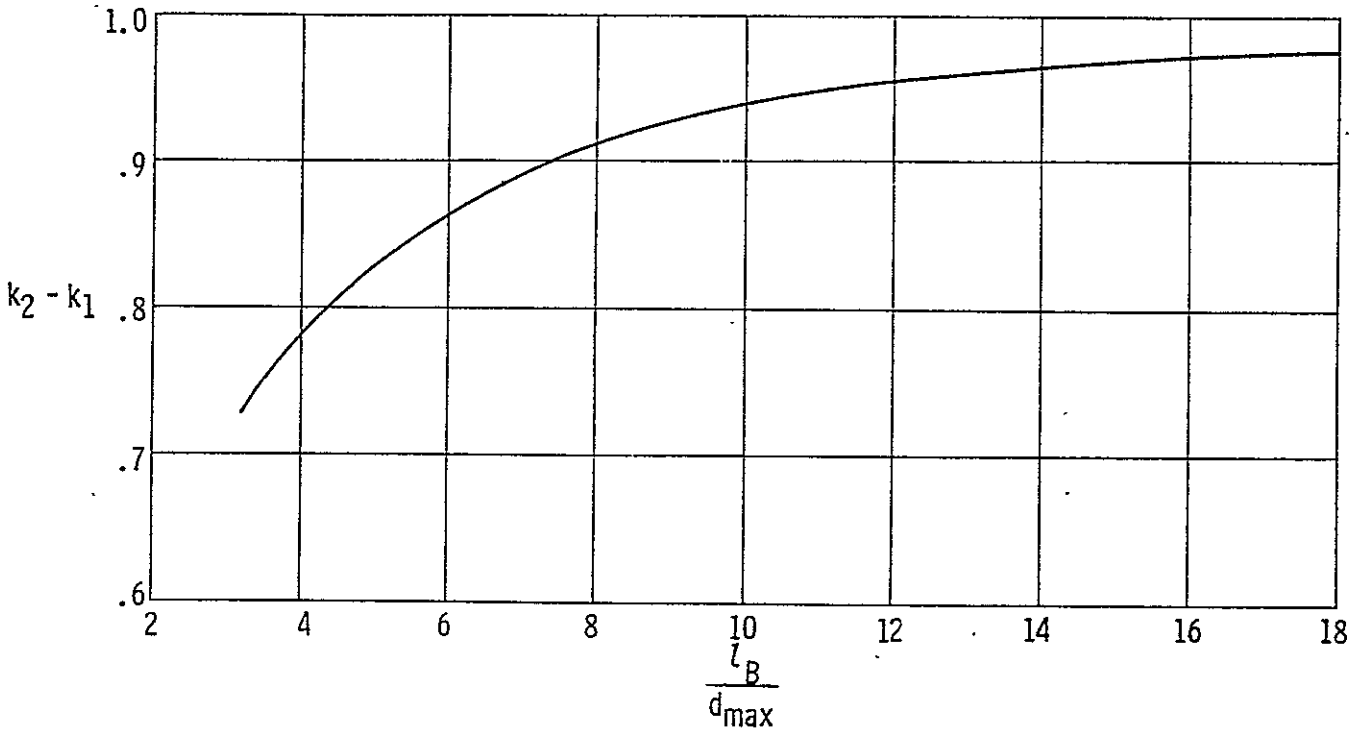

Figure 4.3.1: Apparent mass factor (Reference 3)

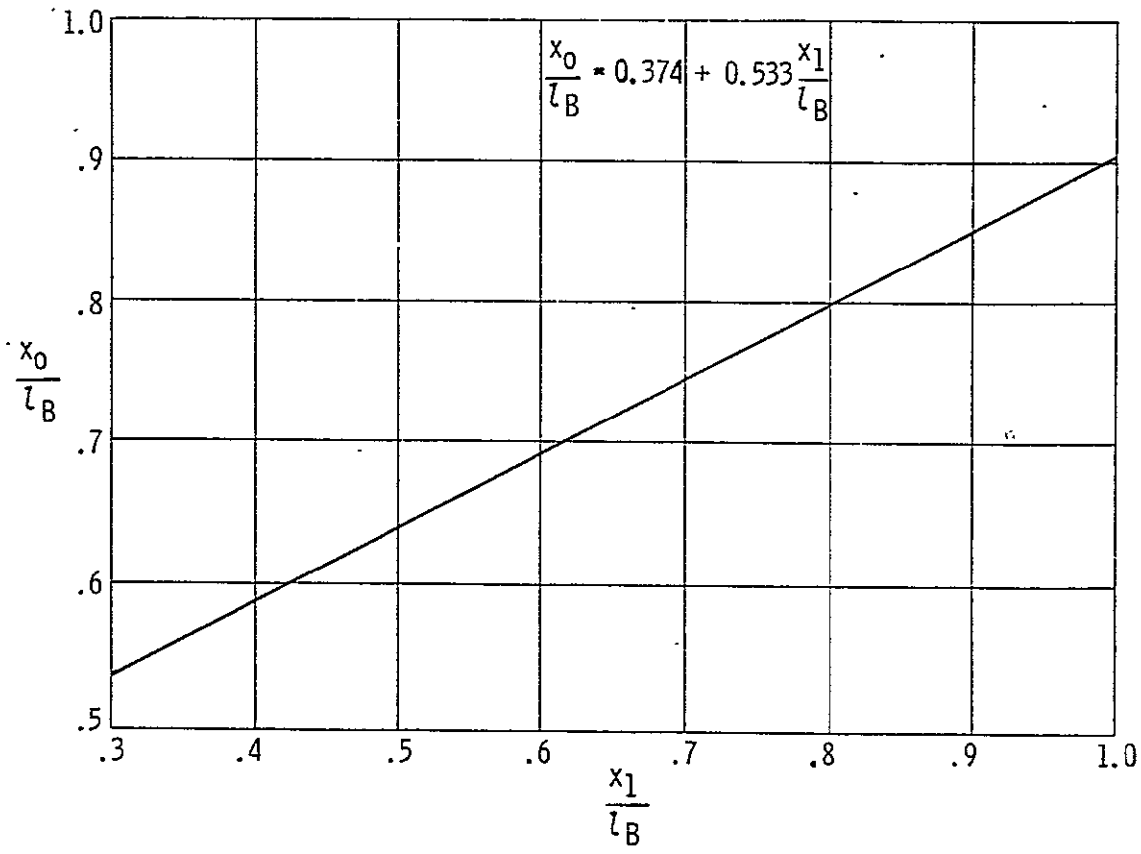

Figure 4.3.2: Position of change of potential flow to viscous flow (Reference 3)

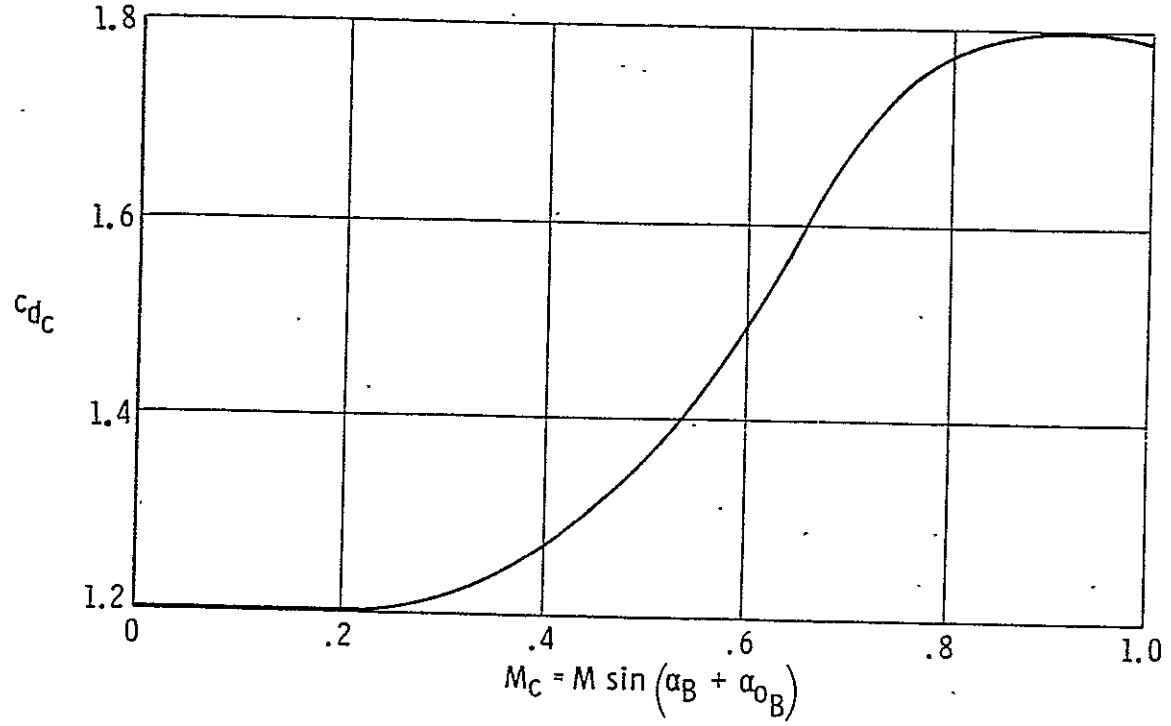

Figure 4.3.3: Steady state drag coefficient for infinite cylinder (Reference 3)

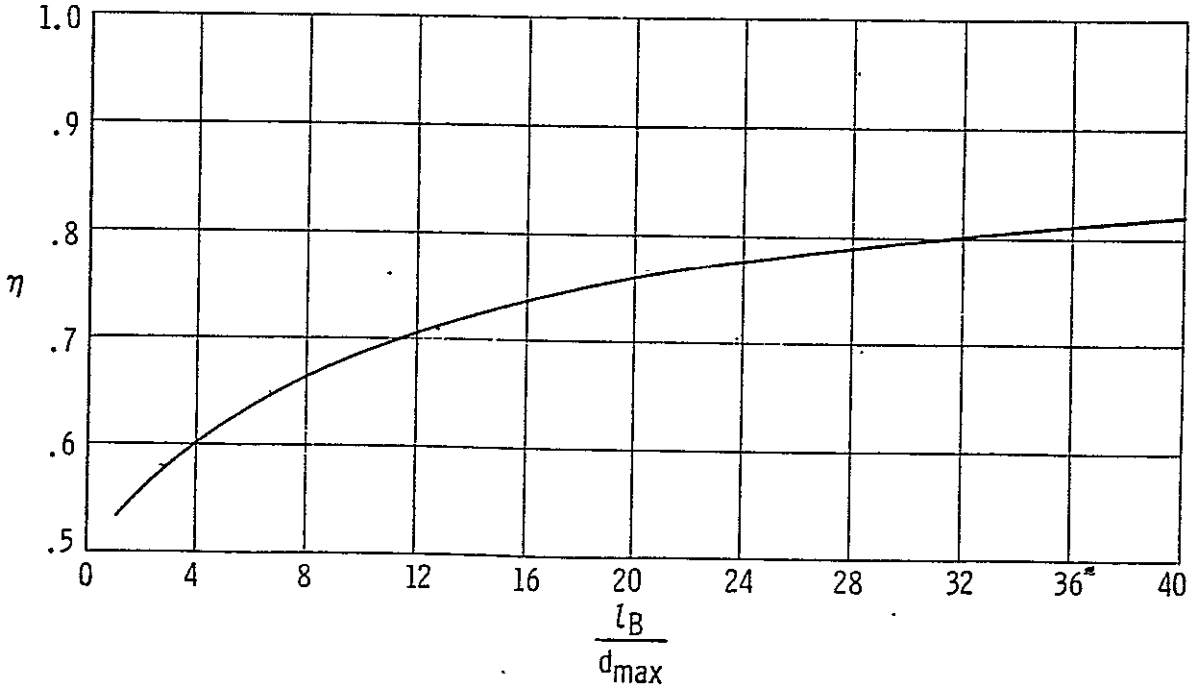

Figure 4.3.4: Ratio of drag coefficient of a cylinder of finite length to that of a cylinder of infinite length (Reference 3)

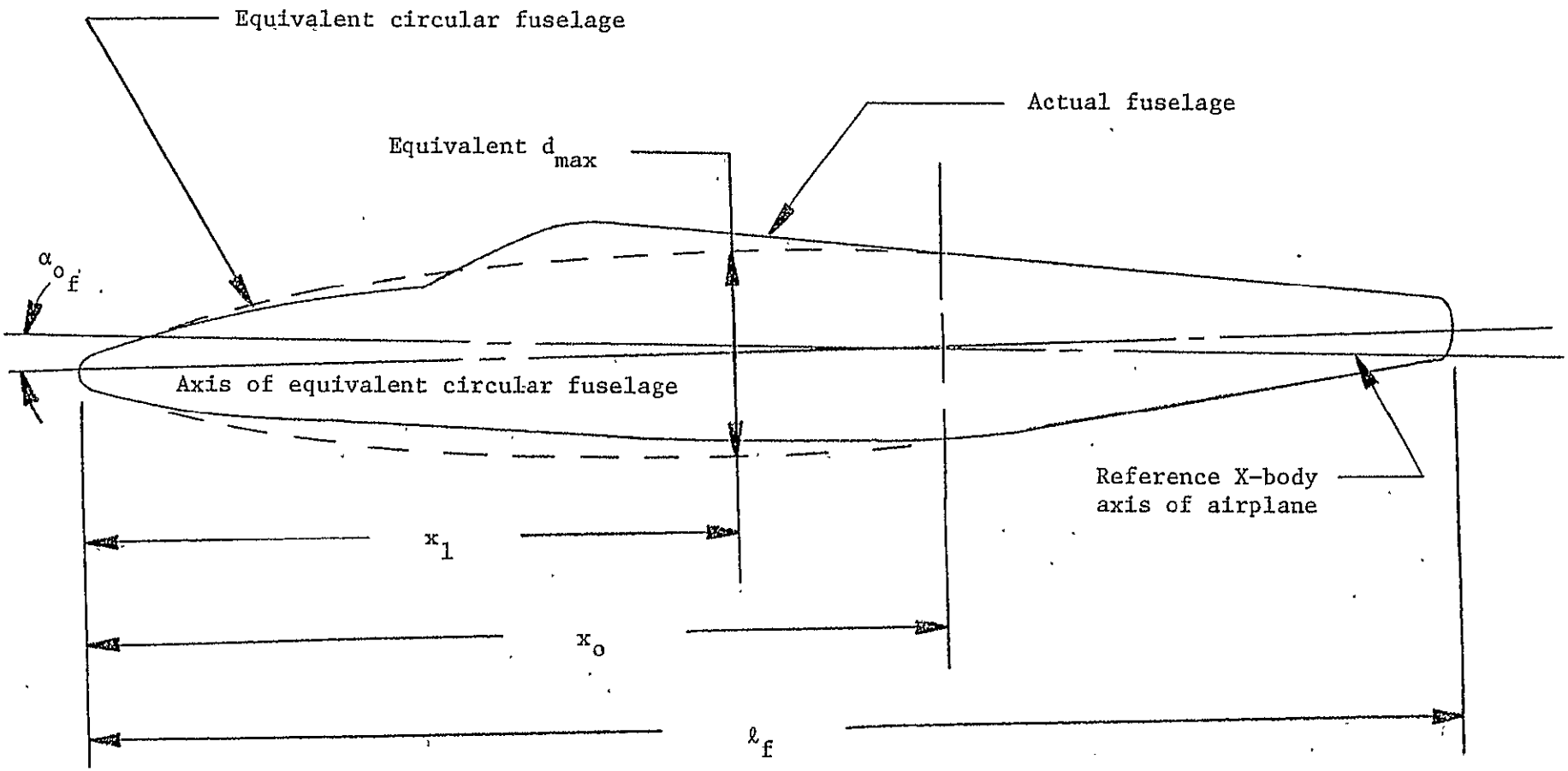

Figure 4.3.5: Pertinent dimensions of approximated equivalent circular fuselage and nacelle

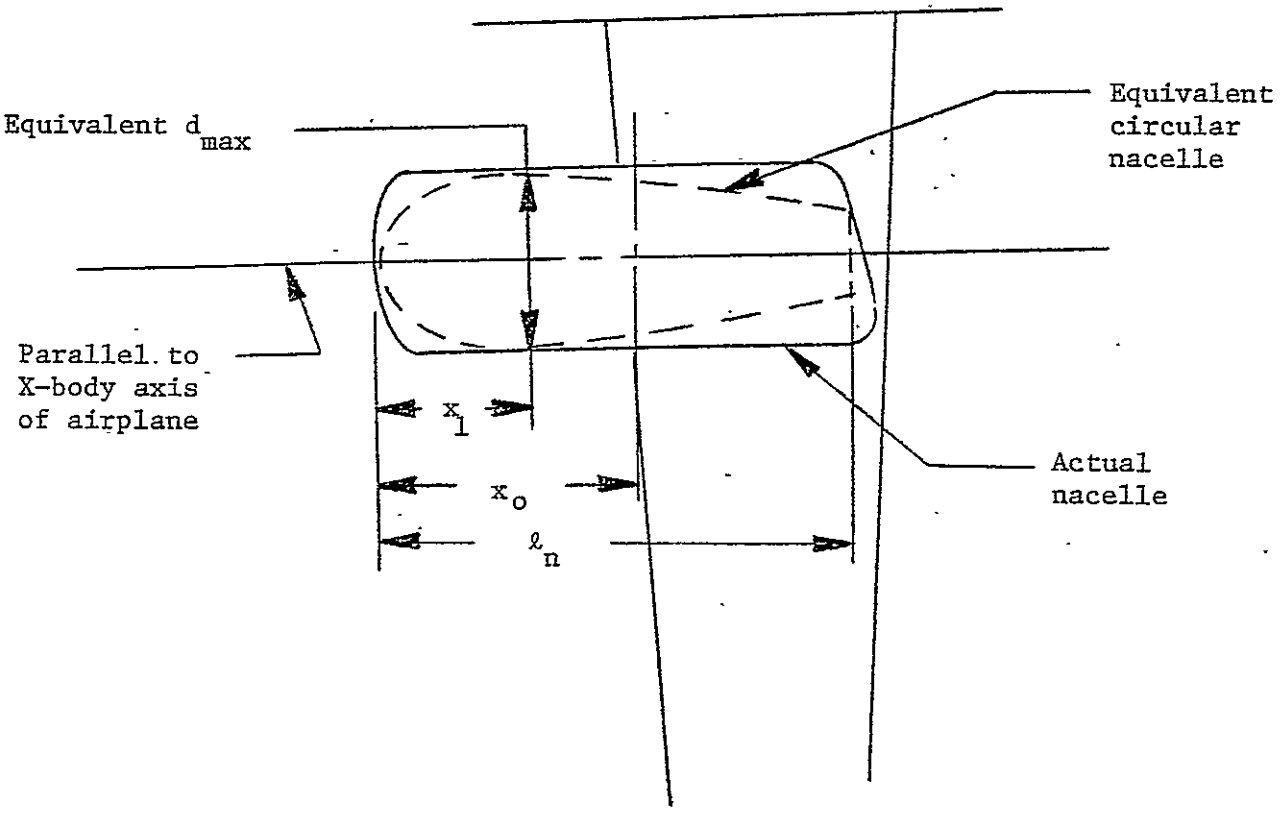

Figure 4.3.5: Concluded

4.4 Lift Due to Combined Wing-Fuselage-Nacelle

The addition of a body to a wing results in mutual interference effects. Lift of the wing-body combination is influenced by the body upwash effect on wing lift and the lift carry-over of wing panel loading onto the body. Net wing upwash and downwash effects on the body influence body pitching moment primarily. Symmetrical body vortices which result from flow separation just behind or above the area of minimum pressure along the side of the body near the nose are normally negligible for most airplane types of wing-body configurations.

4.4.1 Wing-Fuselage-Nacelle Lift in the Linear Lift Range

The lift of the wing-fuselage-nacelle combination accounting for the mutual interference effects of wing and fuselage may be estimated from:

$$C_{L_{wfn}} = C_{L_f} + C_{L_n} + [K_{w(f)} + K_{f(w)}](C_{L_\alpha})_{w_e} \alpha_{w_{abs}} \frac{S_{w_e}}{S_w} \qquad (4.4.1.1)$$

where

C_{L_f} is the fuselage lift obtained from Section 4.3

C_{L_n} is the lift from the nacelles from Section 4.3

$K_{w(f)}$ is the ratio of the lift on the wing in the presence of the body to the lift on an isolated wing, obtained from Figure 4.4.1.1

$K_{f(w)}$ is the ratio of wing lift carry-over onto the body to wing lift alone, obtained from Figure 4.4.1.1

$(C_{L_\alpha})_{w_e}$ is the lift-curve slope of the exposed wing panels, obtained from Section 4.2

$\alpha_{w_{abs}}$ is the absolute angle of attack of the wing:

$$\alpha_{w_{abs}} = \alpha + i_w - \alpha_{o_w} \qquad (4.4.1.2)$$

i_w is the incidence angle of the wing root with respect to the X-body axis

α_{o_w} is the zero-lift angle of attack of the wing, obtained from Section 4.2

S_{w_e} is the exposed wing area; see Section 2.1.

Because of the lack of suitable data, the interference effects of the nacelles are not accounted for.

The use of the interference factors, $K_{w(f)}$ and $K_{f(w)}$, is restricted to wings which do not have sweptback trailing edges or sweptforward leading edges. The factors were obtained for wings mounted as midwings on bodies of revolution but have been used for other configurations.

4.4.2 Maximum Lift of Wing-Fuselage-Nacelle Combination

The addition of a body of revolution to a wing at high angles of attack increases the wing-induced angle of attack at all spanwise stations. The increase is greatest at the root and falls off in an exponential manner with increasing distance from the body. This effective increase in angle of attack tends to make the wing in the presence of the body stall at a lower geometric angle of attack than that corresponding to the wing alone. However, this tendency to stall at a lower angle of attack may be modified by changes in the wing stall pattern. The changes are the result of nonlinear spanwise variation of body-induced flow and also of the partial coverage of the wing by the body. The

relative magnitudes of these latter two effects are largely dependent on specific wing planform shape.

In absence of theoretical methods which predict the effect of the addition of a body to a wing on the maximum lift coefficient and corresponding angle of attack, Reference 4 presents empirical relations to predict this effect. The following expressions are defined:

$$(C_{L_{max}})_{wf} = \left[\frac{(C_{L_{max}})_{wf}}{(C_{L_{max}})_{w}}\right] (C_{L_{max}})_{w} \qquad (4.4.2.1)$$

and:

$$(\alpha_{C_{L_{max}}})_{wf} = \left[\frac{(\alpha_{C_{L_{max}}})_{wf}}{(\alpha_{C_{L_{max}}})_{w}}\right] (\alpha_{C_{L_{max}}})_{w} \qquad (4.4.2.2)$$

where

$(C_{L_{max}})_{wf}/(C_{L_{max}})_{w}$ is an empirical correction factor, obtained from Figure 4.4.2.2.

$(\alpha_{C_{L_{max}}})_{wf}/(\alpha_{C_{L_{max}}})_{w}$ can be obtained from Figure 4.4.2.3. Both factors are presented as a function of the ratio of the fuselage diameter to the wing span, d/b, and the factor c_2, which follows from Figure 4.4.2.1.

4.4.3 Wing-Fuselage-Nacelle Lift for the ATLIT

For the ATLIT the lift of the wing in the presence of the body and the carry-over of the wing lift onto the body, $C_{L_{w(f)+f(w)}}$, is calculated in Table 4.4.3.1. The net lift of the wing-fuselage-nacelle combination in the linear lift range is:

$$C_{L_{wfn}} = C_{L_f} + C_{L_n} + C_{L_{w(f)+f(w)}} \qquad (4.4.3.1)$$

or:

$$C_{L_{wfn}} = 0.002574(\alpha-2.5) + 0.0000402(\alpha-2.5)^2 + 0.002031\alpha + 0.0000201\,\alpha^2 + 0.0920(\alpha+3.4) \qquad (4.4.3.2)$$

Pertinent aspects of the calculations for $(C_{L_{max}})_{wf}$ and $(\alpha_{C_{L_{max}}})_{wf}$ are listed in Table 4.4.3.2.

The net lift of the wing-fuselage-nacelle combination for the ATLIT airplane is summarized in Table 4.4.3.3, while in Figure 4.4.3.1 the results are plotted and compared with full-scale wind tunnel data from Reference 2. The "fully clean" configuration of the ATLIT airplane has not been tested with the horizontal tail removed. However, in Appendix D a procedure is shown with which the lift curve of the "fully clean" ATLIT, without horizontal tail, can be determined.

Figure 4.4.3.1 also shows results obtained with References 5 and 6, respectively.

The results obtained with Reference 5 do not include the lift due to the nacelles. However, the data obtained with Reference 6 show that the lift contribution of the nacelles is substantial. Addition of the lift due to nacelles to the results of Reference 5 will result in a lift curve for the wing-fuselage-nacelle combination which shows good agreement with the experimental results in the linear lift region.

The results from Table 4.4.3.3 show poor agreement with the full-scale wind tunnel data. The angle of attack for zero-lift is 1.5 degrees off. Part of the discrepancy is caused by the wing lift prediction as is shown in Figure 4.2.4.1. An additional factor is the omission of wing-nacelle interference effects.

The results obtained with Reference 6 show, in the linear lift region, good agreement with the experimental data. However, the predicted lift curve slope is too steep. This is caused by the thickness effect as is explained in Appendix C.

Table 4.4.3.1: Wing lift in linear range including mutual wing-fuselage interference

Symbol	Description	Reference	Magnitude
d	Fuselage width at wing, m (ft)	Figure 2.1.1	1.23 (4.0)
b	Wing span, m (ft)	Table 2.1.1	12.19 (40.0)
S_w	Wing area, m^2 (ft^2)	Table 2.1.1	14.40 (155.0)
S_{w_e}	Exposed wing area, m^2 (ft^2)	Table 2.1.1	12.53 (134.8)
α_{o_w}	Zero-lift angle of attack relative to wing chord, deg	Table 4.3.4.1	-2.9
i_w	Wing incidence at wing root relative to X-body axis, deg	Table 2.1	0.5
$\alpha_{w_{abs}}$	Wing angle of attack relative to zero lift, deg	Eq. (4.4.1.2)	$\alpha + 3.4$
$(C_{L_\alpha})_{w_e}$	Lift-curve slope of exposed wing panels, deg^{-1}	Table 4.3.4.1	0.0874
d/b	Fuselage width to wing span ratio	-	0.1
$K_{w(f)}$	Ratio of lift on wing in presence of fuselage to wing alone	Figure 4.4.1.1	1.08
$K_{f(w)}$	Ratio of wing lift carry-over on fuselage to wing alone	Figure 4.4.1.1	0.13

Summary: $C_{L_{w(f)+f(w)}} = \left[K_{w(f)} + K_{f(w)}\right] (C_{L_\alpha})_{w_e} \alpha_{w_{abs}} \frac{S_{w_e}}{S_w}$

$= 0.0920(\alpha+3.4)$

Table 4.4.3.2: Maximum lift of wing including mutual wing-fuselage interference

Symbol	Description	Reference	Magnitude
λ	Wing taper ratio	Table 2.1.1	0.5
c_2	Taper ratio correction factor	Figure 4.4.2.1	1.07
Λ_{le}	Leading edge sweep of wing, deg	Table 2.1.1	3.67
A	Wing aspect ratio	Table 2.1.1	10.32
$(c_2+1)A \tan \Lambda_{le}$	-	-	1.37
d/b	-	Table 4.4.3.1	0.10
$\left[\frac{(C_{L_{max}})_{wf}}{(C_{L_{max}})_{w}}\right]$	Ratio of $C_{L_{max}}$ of wing-fuselage to wing alone	Figure 4.4.2.2	1.0
$\left[\frac{(\alpha_{C_{L_{max}}})_{wf}}{(\alpha_{C_{L_{max}}})_{w}}\right]$	Ratio of stall angle of wing fuselage to wing alone	Figure 4.4.2.3	1.0
$(C_{L_{max}})_{w}$	Maximum lift coefficient of wing alone	Table 4.2.4.1	1.494
$(\alpha_{C_{L_{max}}})_{w}$	Stall angle of wing alone relataive to zero-lift, deg	Table 4.2.4.1	16.4 + 2.9
$(C_{L_{max}})_{wfn}$	Maximum lift coefficient of wing-fuselage-nacelle combination	Eq. (4.4.2.1)	1.494
$(\alpha_{C_{L_{max}}})_{wfn}$	Stall angle of wing-fuselage-nacelle combination relative to zero lift, deg	Eq. (4.4.2.2)	19.3

Table 4.4.3.3: Summary of wing-fuselage-nacelle lift of the ATLIT airplane

α, deg	$\alpha_{w_{abs}}$, deg Eq. (4.4.1.2)	C_{L_f} Eq. (4.3.4)	C_{L_n} Eq. (4.3.5)	$C_{L_{w(f)+f(w)}}$ Table (4.4.3.1)	$C_{L_{wfn}}$ Eq. (4.4.3.1)
-4	-0.6	-0.01673 + 0.00170	-0.00812 + 0.00032	-0.05520	-0.07803
-2	1.4	-0.01158 + 0.00081	-0.00406 + 0.00008	0.12880	0.11405
0	3.4	-0.00644 + 0.00025	0	0.31280	0.30661
2	5.4	-0.00129 + 0.00001	0.00406 + 0.00008	0.49680	0.49966
4	7.4	0.00386 + 0.00009	0.00812 + 0.00032	0.68080	0.69319
15.9	*19.3	0.03449 + 0.00722	0.03229 + 0.00508	*1.49400	1.57308

* from Table 4.4.3.2

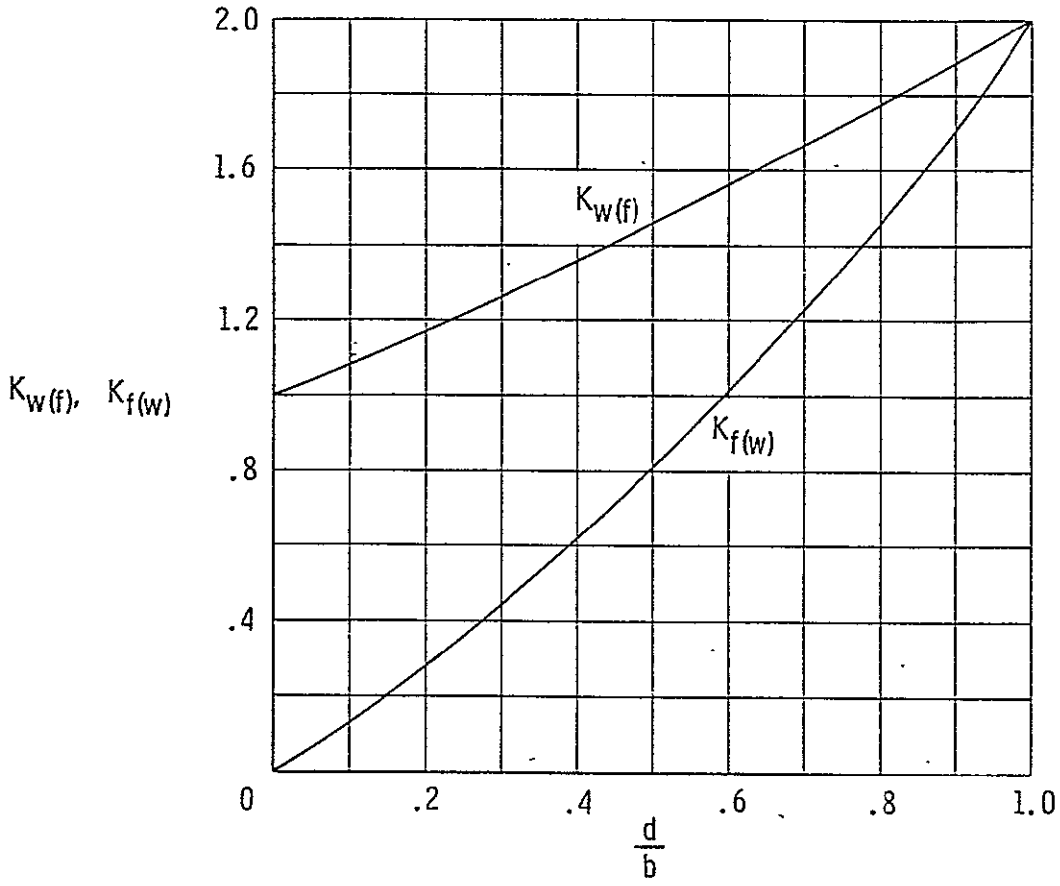

Figure 4.4.1.1: Lift ratios $K_{w(f)}$ and $K_{f(w)}$ based on slender-body theory (Reference 3)

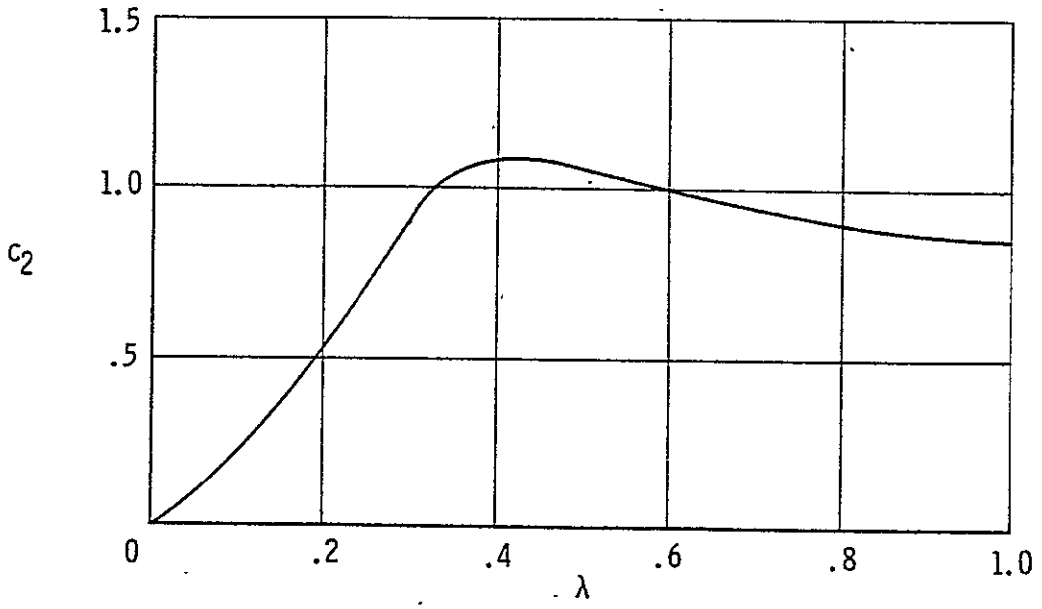

Figure 4.4.2.1: Taper ratio correction factor (Reference 3)

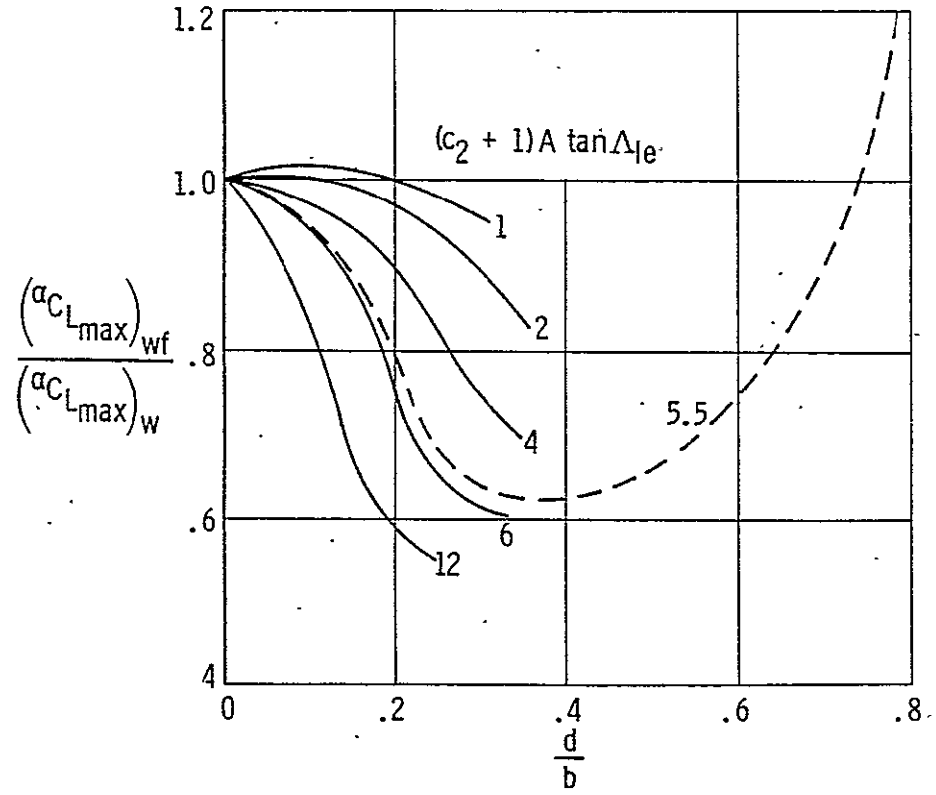

Figure 4.4.2.2: Wing-body maximum lift below M=0.6 (Reference 3)

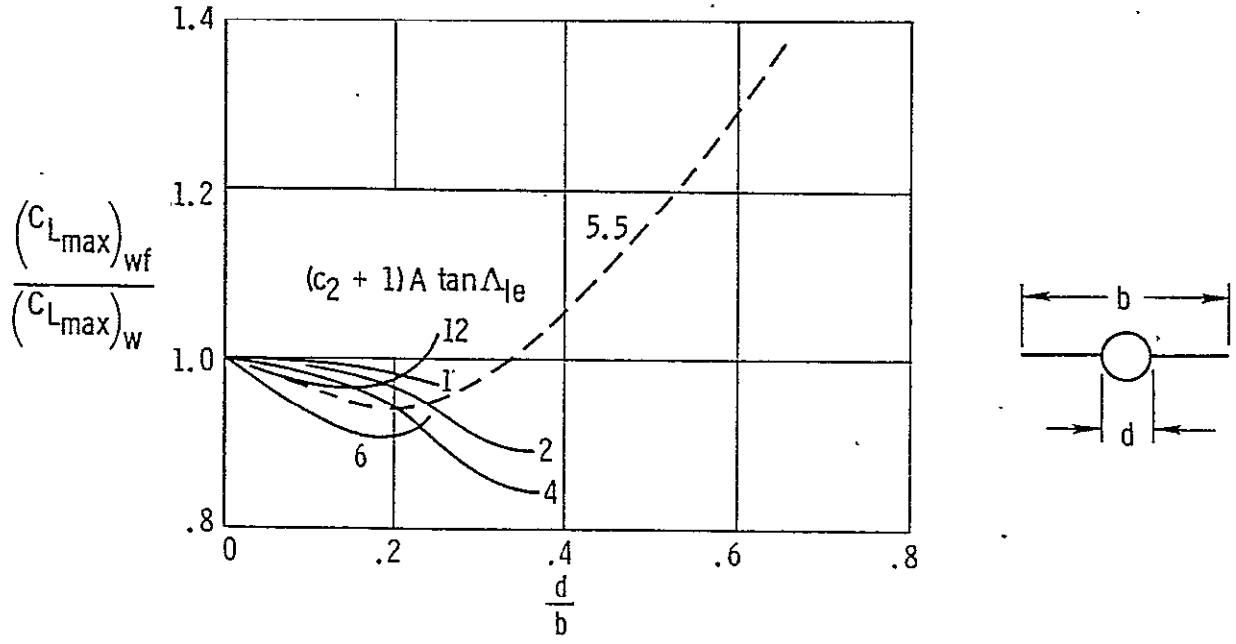

Figure 4.4.2.3: Wing-body angle of attack for maximum lift below M=0.6 (Reference 3)

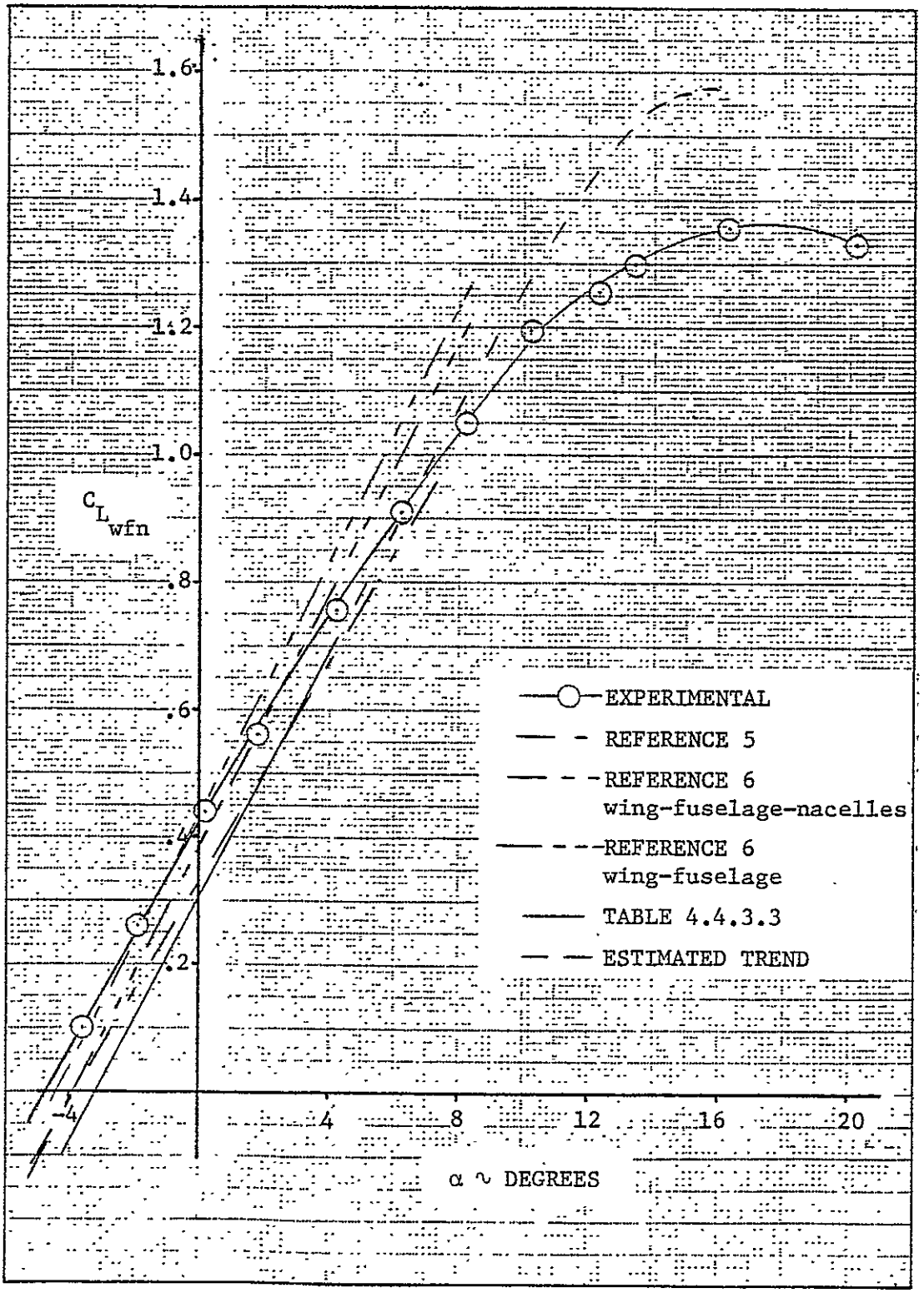

Figure 4.4.3.1: Comparison of lift predictions with wind tunnel data (N_{Re}= 2.3x10^6, horizontal tail and propellers removed)

4.5 Wing Zero-Lift Pitching-Moment and Aerodynamic Center of Wing and Horizontal Tail

Subsonic zero-lift pitching moment coefficients for constant section airfoil lifting surfaces can be predicted with the following expression:

$$C_{m_o} = c_{m_o} \frac{A \cos^2 \Lambda_{c/4}}{A + 2\cos\Lambda_{c/4}} + \left(\frac{\Delta C_{m_o}}{\theta}\right)\theta \qquad (4.5.1)$$

where

c_{m_o} is the section zero-lift pitching moment obtained from Section 4.1

$\Delta C_{m_o}/\theta$ is the change in wing zero-lift pitching moment coefficient due to a unit change in linear wing twist. This parameter is obtained from Figure 4.5.1.

θ is the twist of the wing tip with respect to the root section, in degrees (negative for washout)

The aerodynamic center, the point about which the lifting surface pitching-moment coefficient is invariant with lift, may be determined relative to a desired reference center on and as ratio of the mean aerodynamic chord of the lifting surface by using Figure 4.5.2 and the expression:

$$-\frac{d C_m}{d C_L} = -\left(\frac{x_n}{c_r} - \frac{x_{ac}}{c_r}\right)\frac{c_r}{\bar{c}} \qquad (4.5.2)$$

where

$-d C_m/d C_L$ is the static margin, the distance from the reference center on the mean aerodynamic chord of the lifting surface to the aerodynamic center of the surface as a ratio of the mean aerodynamic chord

x_n/c_r is the chordwise distance from the wing apex to the point about which the pitching moment is desired, measured in root chords, positive aft or:

$$\frac{x_n}{c_r} = \frac{y_{\bar{c}} \tan \Lambda_{le}}{c_r} \tag{4.5.3}$$

when the leading edge of the mean aerodynamic chord is the moment center.

x_{ac}/c_r is the chordwise distance from the wing apex to the aerodynamic center, measured in root chords, positive aft, obtained from Figure 4.5.2.

Tabels 4.5.1 and 4.5.2 summarize the calculations made to determine the zero-lift pitching moment of the wing and the horizontal tail of the ATLIT and the location of the aerodynamic centers of the surfaces relative to the leading edges of the mean aerodynamic chords of the surfaces.

Table 4.5.1: Zero-lift pitching moment coefficient of wing and horizontal tail

Symbol	Description	Reference	Wing		Horizontal Tail	
			Total	Exposed	Total	Exposed
A	Aspect ratio	Table 2.1.1	10.32	9.61	4.75	4.28
θ	Twist angle at wing tip, deg	Table 2.1	-3.0	-3.0	0	0
$\Lambda_{c/4}$	Sweep of quarter chord line, deg	Table 2.1.1	1.835	1.835	0	0
λ	Taper ratio	Table 2.1.1	0.50	0.527	1	1
$\Delta C_{m_o}/\theta$	Shift in C_{m_o} per degree of wing twist	Figure 4.5.1	-0.0004	-0.0004	0	0
c_{m_o}	Section airfoil zero-lift pitching moment coefficient	Table 4.1.2	-0.095	-.095	0	0
C_{m_o}	Zero-lift pitching moment coefficient	Eq. (4.5.1)	-0.0783	-0.0774	0	0

Table 4.5.2: Aerodynamic center of wing and horizontal tail of the ATLIT

Symbol	Description	Reference	Wing		Horizontal Tail	
			Total	Exposed	Total	Exposed
M	Mach number	-	0.081	0.081	0.081	0.081
β	$\sqrt{1 - M^2}$	-	0.9967	0.9967	0.9967	0.9967
c_r	Root chord of surface, m (in)	Table 2.1.1	1.575 (62.00)	1.495 (58.87)	0.871 (34.29)	0.871 (34.29)
$\bar{c}$	Mean aerodynamic chord, m (in)	Table 2.1.1	1.225 (48.22)	1.178 (46.38)	0.871 (34.29)	0.871 (34.29)
$y_{\bar{c}}$	Lateral position of $\bar{c}$ from root chord, m (in)	Table 2.1.1	2.709 (106.67)	2.460 (96.85)	1.033 (40.68)	1.033 (40.68)
Λ_{le}	Sweep of leading edge, deg	Table 2.1.1	3.67	3.67	0	0
A tan Λ_{le}	-	-	0.6619	0.6164	0	0
tan Λ_{le}/β	-	-	0.0644	0.0644	0	0
x_{ac}/c_r	Distance from apex of surface to a.c as ratio of c_r	Figure 4.5.2	0.294	0.297	0.250	0.250
x_n/c_r	Distance from apex of surface to leading edge of m.a.c. as ratio of c_r	Eq. (4.5.3)	0.110	0.106	0	0
a.c.	Aerodynamic center relative to leading edge of mean aerodynamic chord as ratio of $\bar{c}$	Eq. (4.5.2)	0.236	0.243	0.250	0.250

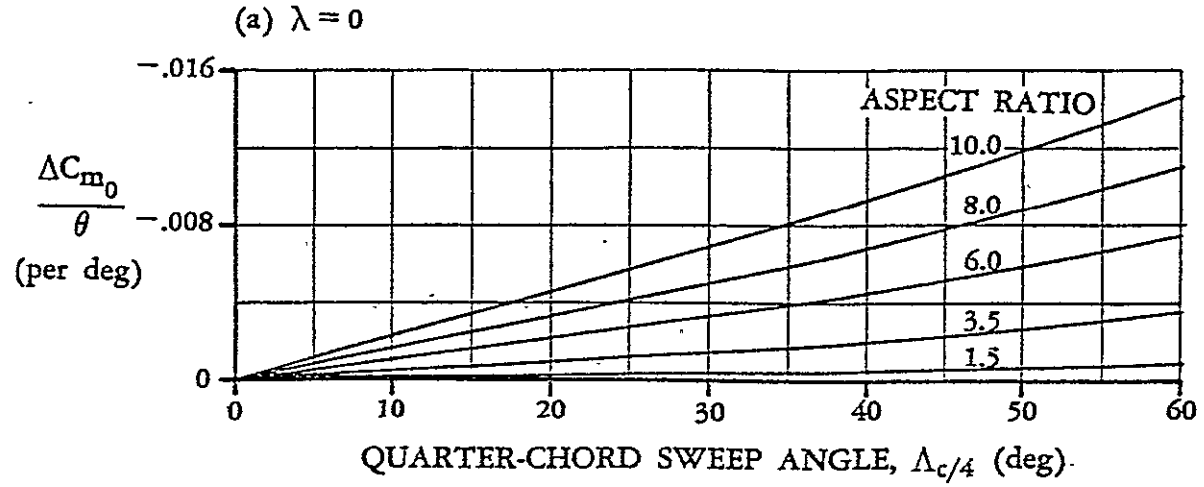

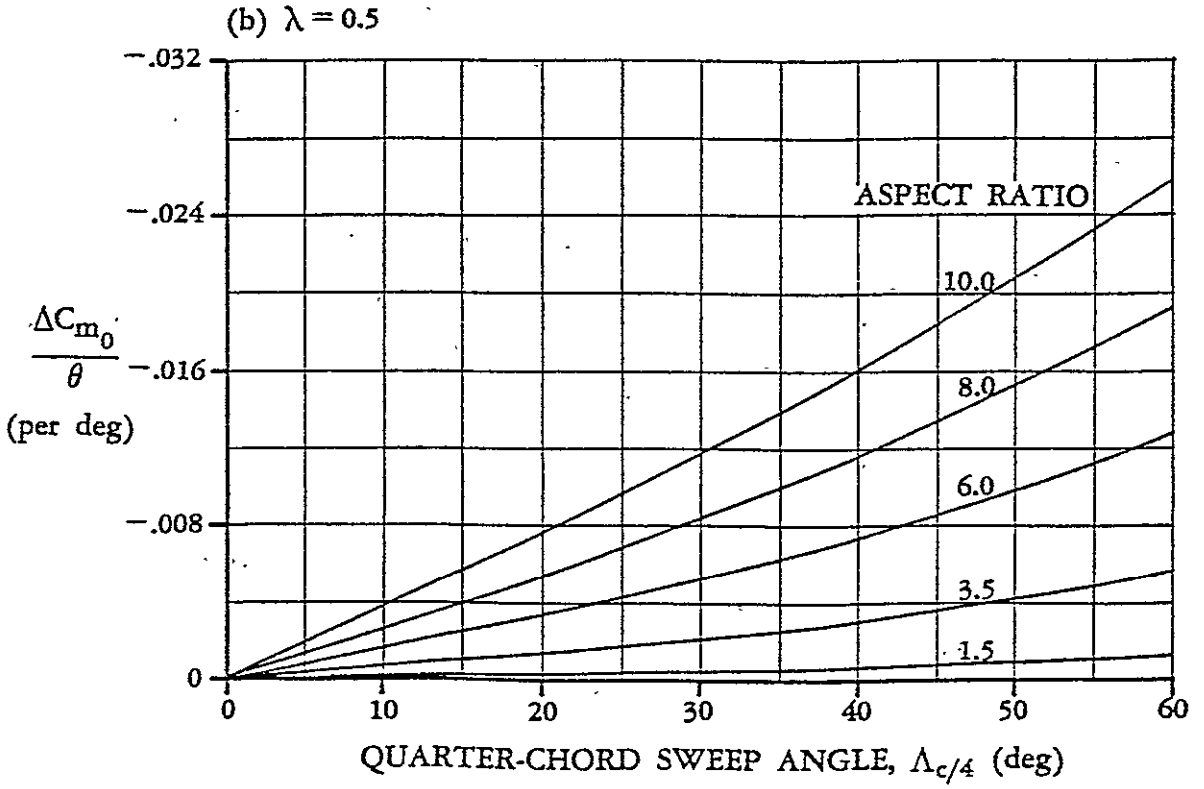

Figure 4.5.1: Effect of linear twist on the zero-lift pitching moment of the lifting surface (Reference 4)

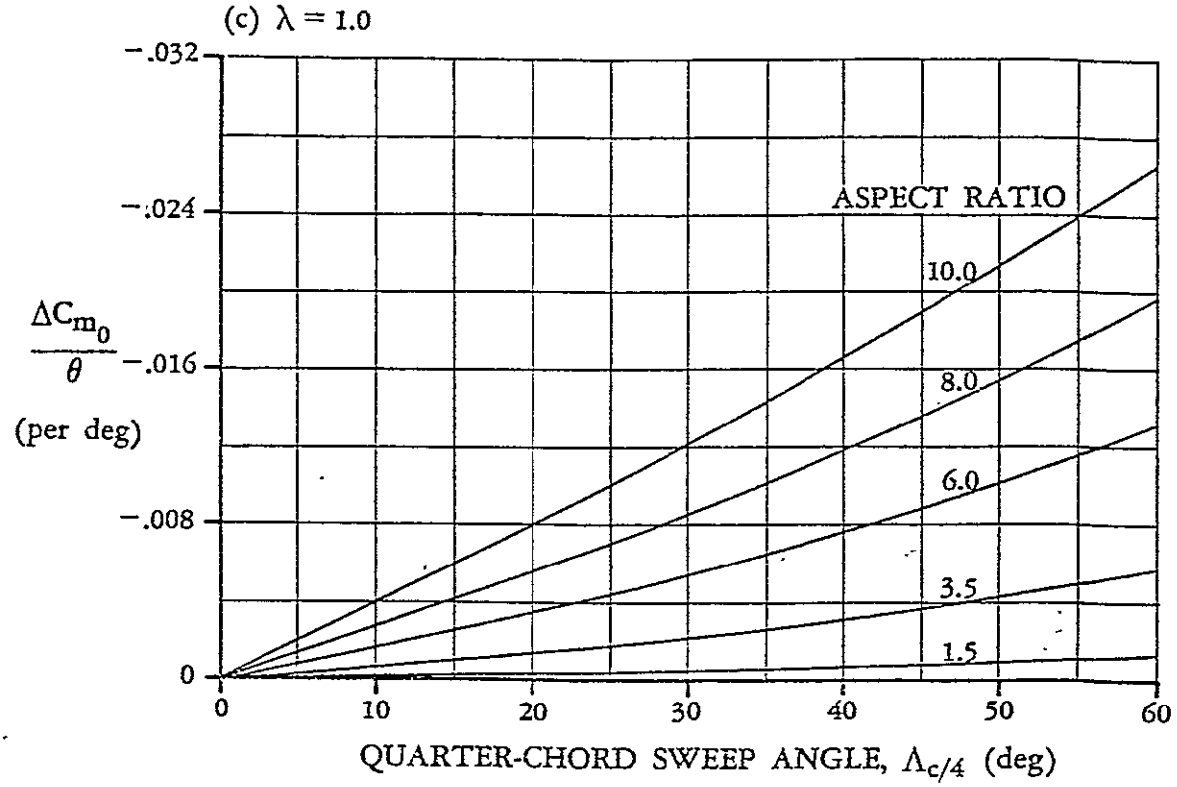

Figure 4.5.1: Concluded

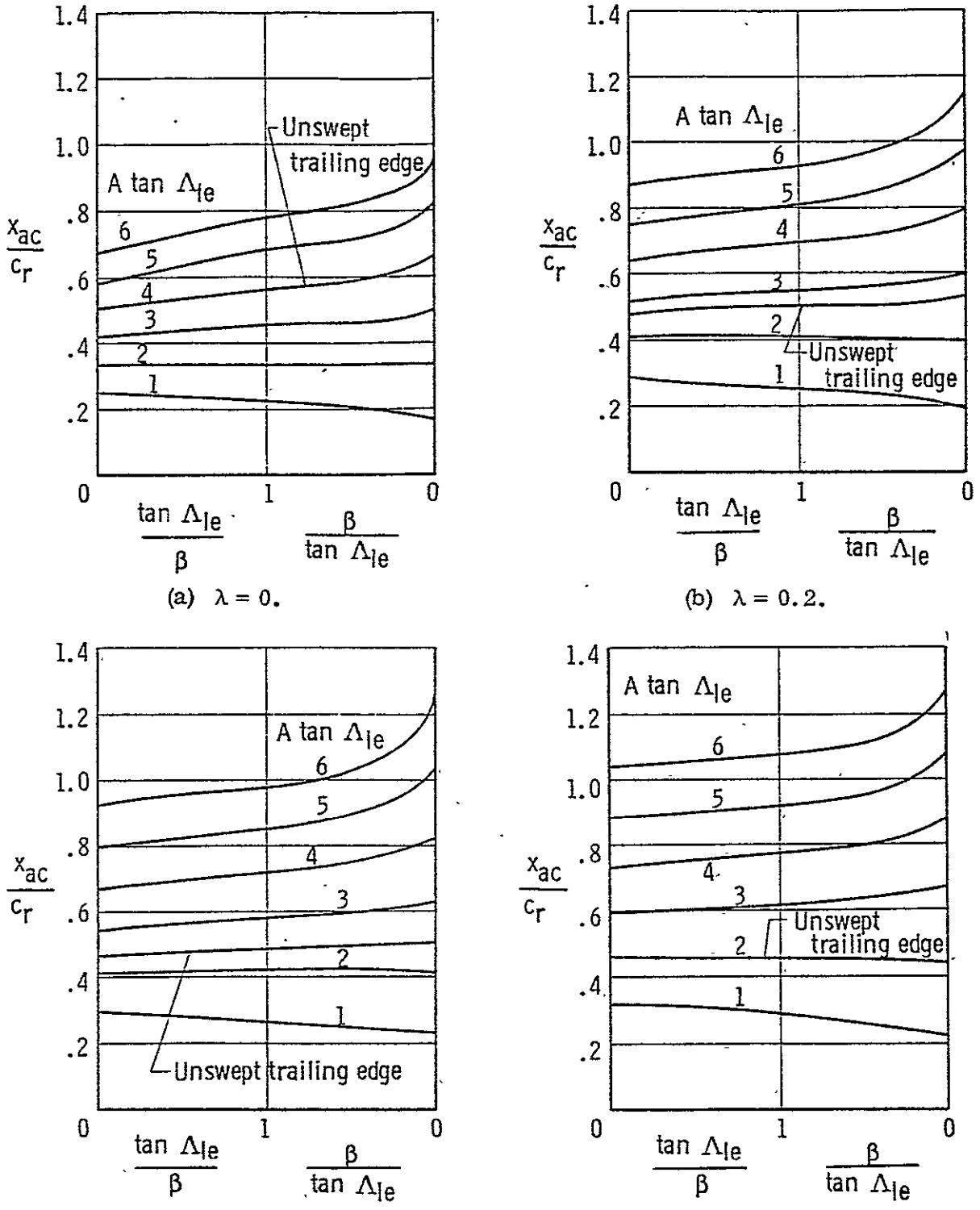

(a) $\lambda = 0.$

(b) $\lambda = 0.2.$

(c) $\lambda = 0.25.$

(d) $\lambda = 0.33.$

Figure 4.5.2: Wing aerodynamic center position for subsonic conditions (Reference 3)

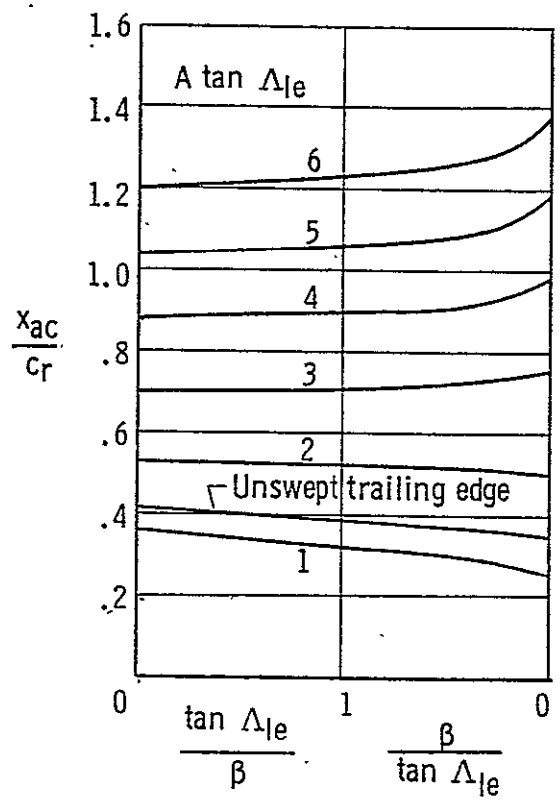

(e) $\lambda = 0.5$.

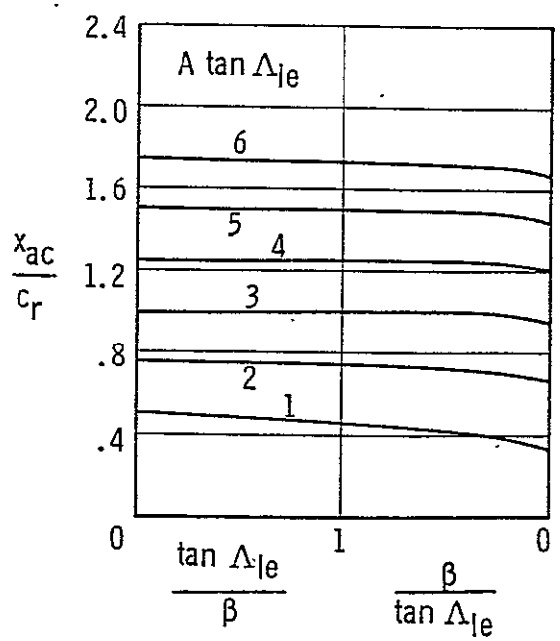

(f) $\lambda = 1$.

Figure 4.5.2: Concluded

BLANK PAGE

4.6 Wing-Fuselage Pitching Moment at Zero-Lift

The addition of a fuselage to a wing results in a fuselage contribution, $(C_{m_o})_f$, to the pitching moment at zero lift. This contribution may be estimated from Figure 4.6.1, which is based on streamline bodies of circular or near circular cross section for midwing conditions. For high- or low-wing configurations a positive or negative increment, $(\Delta C_{m_o})_f$, of 0.004 has to be added, respectively, to the value obtained from Figure 4.6.1. In the absence of suitable data, the effects of the nacelles on C_{m_o} are considered to be negligible.

The effect of Mach number on the wing-fuselage zero-lift pitching moment is presented in Figure 4.6.2. When using this chart, no correction should be made to the section c_{m_o} value and the wing pitching moment, $(C_{m_o})_w$, at zero-lift. The wing-fuselage-nacelle pitching-moment coefficient is:

$$(C_{m_o})_{wfn} = \left[(C_{m_o})_w + (C_{m_o})_f + (\Delta C_{m_o})_f\right] \frac{(C_{m_o})_M}{(C_{m_o})_{M=0}} \qquad (4.6.1)$$

where

$(C_{m_o})_w$ is the wing zero-lift pitching moment coefficient uncorrected for Mach number effects, obtained from Section 4.5.

$(C_{m_o})_f$ is the fuselage zero-lift pitching moment, obtained from Figure 4.6.1.

$(\Delta C_{m_o})_f$ is the correction for high- or low-wing configurations.

$(C_{m_o})_M/(C_{m_o})_{M=0}$ is the Mach number correction factor obtained from Figure 4.6.2.

In Table 4.6.1 the calculations are summarized which lead to the wing-fuselage-nacelle pitching moment coefficient at zero-lift of the ATLIT airplane. The final result is:

$$(C_{m_o})_{wfn} = -0.1072 \qquad (4.6.2)$$

Table 4.6.1: Wing-fuselage-nacelle pitching moment coefficient at zero-lift of the ATLIT airplane

Symbol	Description	Reference	Magnitude
w	Width of fuselage at the wing, m (ft)	Figure 2.1.1	1.219 (4.0)
S_f	Planform area of fuselage, m^2 (ft^2)	Figure 4.6.3	7.72 (83.1)
$\bar{S}_f$	Planform area of fuselage forward of $\bar{c}/4$ of wing, m^2 (ft^2)	Figure 4.6.3	3.17 (34.1)
ℓ_f	Length of fuselage, m (ft)	Figure 4.6.3	8.352 (27.40)
$\bar{\ell}_f$	Distance from nose of fuselage to $\bar{c}/4$ of wing, m (ft)	Figure 4.6.3	3.127 (10.26)
S_w	Reference wing area, m^2 (ft^2)	Table 2.1.1	14.4 (155.0)
$\bar{c}_w$	Wing mean aerodynamic chord	Table 2.1.1	1.225 (4.018)
$(i_w)_o$	Incidence of zero-lift line of wing = $i_w - \alpha_{o_w}$, rad	Table 4.4.3.1	0.0593
w^2/S_f	-	-	0.193
$\bar{S}_f\bar{\ell}_f/S_f\ell_f$	-	-	0.154
$\dfrac{(C_{m_o})_f S_w \bar{c}}{(i_w)_o S_f \ell_f}$	-	Figure 4.6.1	-0.115
$(C_{m_o})_f$	C_{m_o} of fuselage	-	-0.0249
$(\Delta C_{m_o})_f$	Correction for low-wing configuration of airplane	-	-0.004
$(C_{m_o})_w$	Zero-lift pitching moment coefficient of wing	Table 4.5.1	-0.0783
$(C_{m_o})_{wfn}$	Zero-lift pitching moment of wing-fuselage-nacelle combination	Eq. (4.6.1)	-0.1072

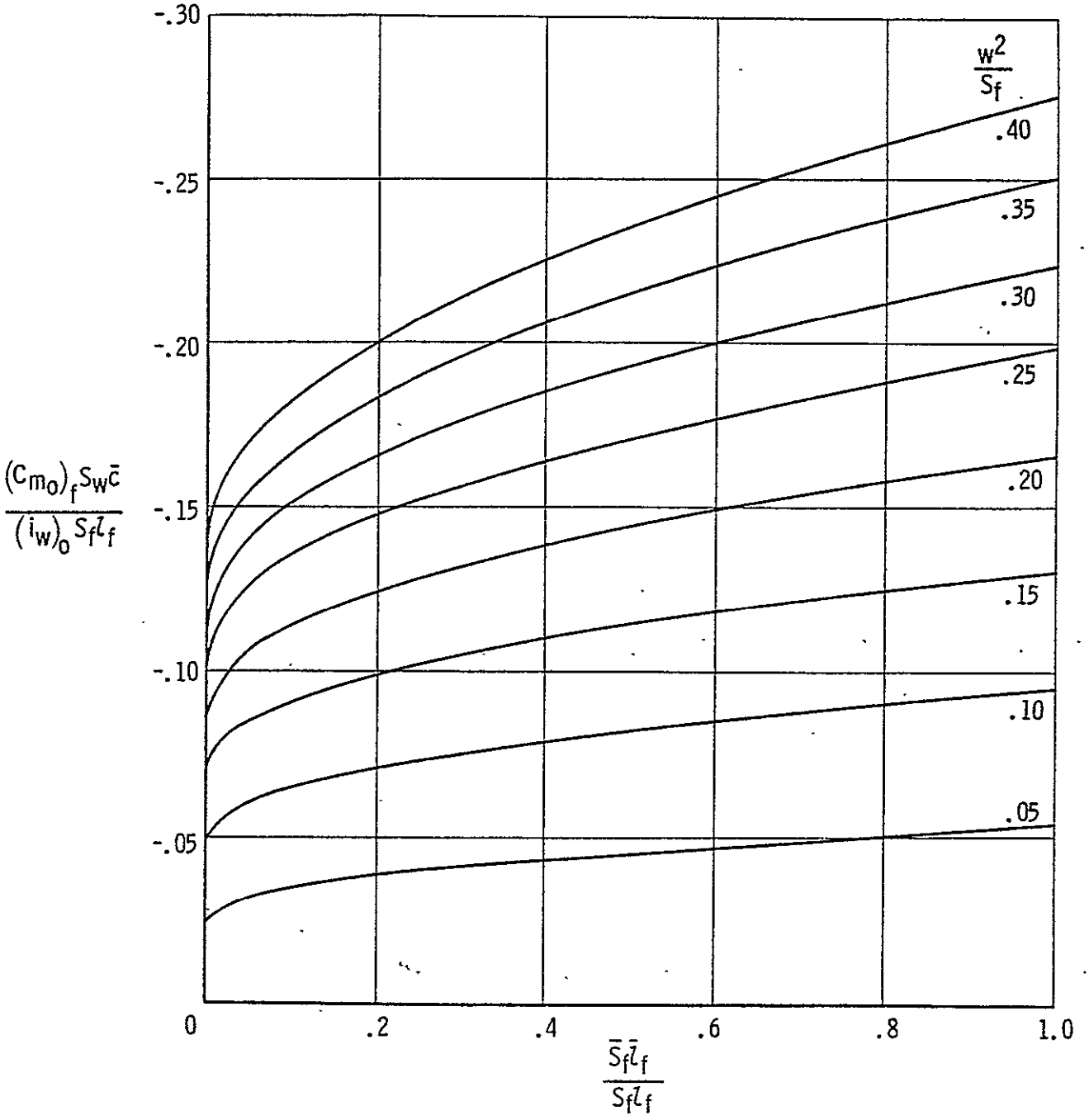

Figure 4.6.1: Effect of fuselage on C_{m_o}. Midwing configuration (Reference 3)

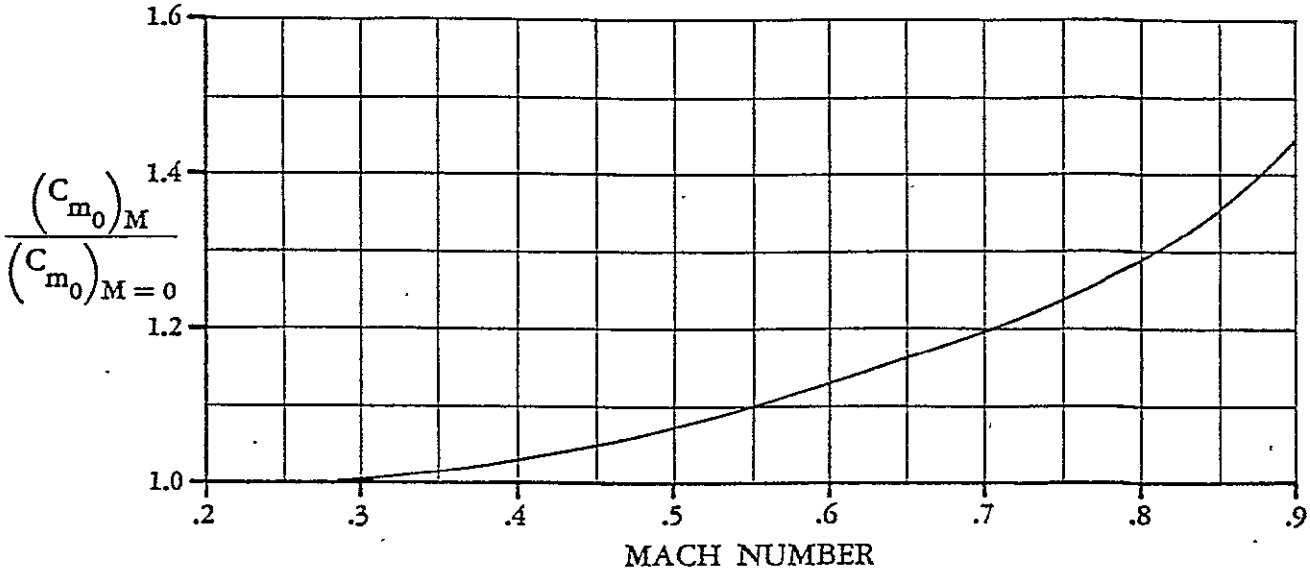

Figure 4.6.2: Mach effect on zero-lift pitching moment coefficient (Reference 4)

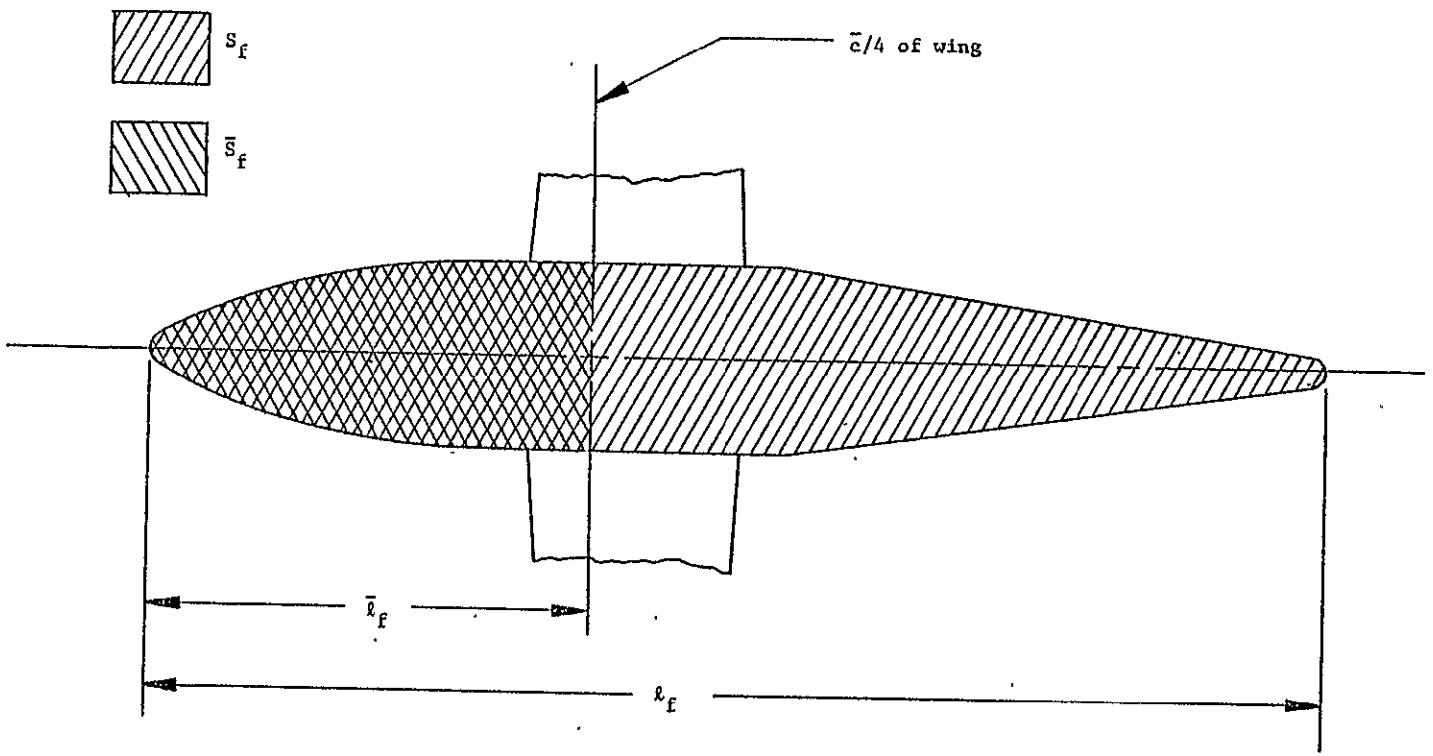

Figure 4.6.3: Top view of the ATLIT airplane

4.7 Fuselage and Nacelle Pitching Moments

The slope of the pitching moment curve of the fuselage and the nacelles at subsonic Mach numbers may be determined from the following expression:

$$(C_{m_\alpha})_B = \frac{2(k_2-k_1)}{57.3\, S_w \bar{c}_w} \int_0^{x_o} (x_m-x)\,dS_x + \frac{4\eta\, c_{d_c}\, \alpha}{(57.3)^2 S_w \bar{c}_w} \int_{x_o}^{\ell_B} r(x_m-x)\,dx \qquad (4.7.1)$$

where

$(C_{m_\alpha})_B$ is the slope of the body pitching moment curve, based on the reference wing area, about a moment center at a longitudinal distance, x_m, from the nose of the body.

Above expression is based on potential-flow lift effects on the forebody and on viscous-flow lift effects on the afterbody, which are discussed in more detail in Section 4.3.

Table 4.7.1 summarizes the calculation of the slope of the pitching moment curve of the fuselage and the nacelles of the ATLIT airplane about the leading edge of the total wing mean aerodynamic chord. Table 4.7.2 shows the tabular integration procedure used to obtain the values of the integrals, $\int_0^{x_o} (x_m-x)\,dS_x$ and $\int_{x_o}^{\ell_B} r(x_m-x)\,dx$, for the fuselage. The same procedure is used for the nacelles as is shown in Table 4.7.3.

The slope of the pitching-moment curve of the fuselage and the nacelles of the ATLIT about the leading edge of the total wing mean aerodynamic chord is:

$$(C_{m_\alpha})_{fn} = 0.00533 - 0.000252\alpha \qquad (4.7.2)$$

where

α is the angle of attack with respect to the X-body axis in degrees.

Not included in the calculation of the pitching moment curve slope of the nacelles is the extension of the nacelles by 8 inches due to installation of the thrust/torque balances. However, the effect of the extension on the pitching moment of the nacelles is negligible.

Table 4.7.1: Fuselage and nacelle pitching moments of the ATLIT airplane

Symbol	Description	Reference	Fuselage	Nacelle
M	Mach number	-	0.081	0.081
S_w	Reference wing area, m^2 (ft^2)	Table 2.1.1	14.4 (155.0)	14.4 (155.0)
S_x	Equivalent body cross-section, m^2 (ft^2)	Figure 4.3.5	Variable	Variable
ℓ_B	Body length, m (in)	Table 4.3.1	8.351 (328.8)	2.428 (95.6)
x_o	Location from body nose where potential flow ceases, m (in)	Table 4.3.1	5.237 (206.2)	1.313 (51.7)
x_m	Distance from body nose to leading edge of wing mean aerodynamic chord, m (in)	Figure 4.6.3	2.819 (111.0)	1.334 (52.5)
x	Distance from body nose to centroid of Δ quantity, m (in)	Figure 4.3.5	Variable	Variable
r	Effective body radius of Δx segment, m (in)	Figure 4.3.5	Variable	Variable
$\bar{c}_w$	Wing mean aerodynamic chord, m (ft)	Table 2.1.1	1.225 (4.018)	1.225 (4.018)
k_2-k_1	Reduced mass factor	Table 4.3.1	0.882	0.675
η	Ratio of drag coefficient of finite to infinite length cylinder	Table 4.3.1	0.650	0.575
c_{d_c}	Cross flow drag coefficient of infinite length cylinder	Table 4.3.1	1.2	1.2
$\int_o^{x_o} (x_m-x)dS_x$	$\sum_o^{x_o} (x_m-x)\Delta S_x$, m^3 (ft^3)	Table 4.7.2/3	2.10 (74.2)	0.62 (22.0)
$\int_{x_o}^{\ell_B} r(x_m-x)dx$	$\sum_{x_o}^{\ell_B} r(x_m-x)\Delta x$, m^3 (ft^3)	Table 4.7.2/3	-4.38 (-154.7)	-0.17 (-6.0)
$(C_{m_\alpha})_f$	Slope of fuselage pitching moment curve, deg^{-1}	Eq. (4.7.1)	0.00367-0.000236α	-
$(C_{m_\alpha})_n$	Slope of nacelle (one) pitching moment curve, deg^{-1}	Eq. (4.7.1)	—	0.00083-0.0000081α
Summary: $(C_{m_\alpha})_{fn} = 0.00533 - 0.000252\alpha$				

Table 4.7.2: Tabular integration of fuselage pitching moment parameters

Distance from nose to S_x, in	x, in	w, in	S_x, in^2	ΔS_x, in^2	$(x_m-x)\Delta S_x$ in^3
0		0	0		
	10.9			209	20921
16.3		16.3	209		
	26.5			334	28223
32.5		26.3	543		
	41.0			354	24780
49.4		33.8	897		
	56.6			285	15504
63.8		38.8	1182		
	71.6			197	7762
79.4		41.9	1379		
	87.5			169	3972
95.6		44.4	1548		
	103.5			136	1020
111.3		46.3	1684		
	119.1			88	-713
126.9		47.5	1772		
	134.7			98	-2323
142.5		48.8	1870		
	150.0			0	0
157.5		48.8	1870		
	165.7			0	0
173.8		48.8	1870		
	181.6			-124	8754
189.4		47.5	1746		
	197.8			-239	20745
206.2		43.8	1507		
					128645

$$\int_{o}^{x_o} (x_m-x)\, dS_x = \sum_{o}^{x_o} (x_m-x)\, \Delta S_x = 128645\ in^3 = 74.2\ ft^3$$

Table 4.7.2: Concluded

Distance from nose, in.	Δx, in.	r, in.	x, in.	$r(x_m-x)\Delta x$, in^3
206.2				
	16.3	21.6	214.4	-34603
222.5				
	16.3	19.7	230.7	-38434
238.8				
	14.9	17.5	246.3	-35280
253.7				
	16.3	15.6	261.9	-38376
270.0				
	15.6	13.8	277.8	-35914
285.6				
	15.6	11.6	293.4	-33005
301.2				
	16.3	9.7	309.4	-31363
317.5				
	11.2	7.8	323.1	-18533
328.7				
				-267308

$$\int_{x_o}^{\ell_f} r(x_m-x)dx = \sum_{x_o}^{\ell_f} r(x_m-x)\Delta x = -267308 \text{ in}^3 = -154.7 \text{ ft}^3$$

Table 4.7.3: Tabular integration of nacelle pitching moment parameters

Distance from nose to ΔS_x, in	x, in	w, in	S_x, in^2	ΔS_x, in^2	$(x_m-x)\Delta S_x$, in^3
0		0	0		
	5.8			491	22930
8.8		25.0	491		
	14.5			406	15428
17.5		33.8	897		
	21.9			65	1989
26.3		35.0	962		
	30.7			-33	-719
35.0		34.4	929		
	39.4			-99	-1297
43.8		32.5	830		
	47.8			-61	-287
51.7		31.3	769		
					38044

$$\int_{o}^{x_o} (x_m-x)\, dS_x = \sum_{o}^{x_o} (x_m-x)\,\Delta S_x = 38044\ in^3 = 22.0\ ft^3$$

Distance from nose, in.	Δx, in	r, in	x, in	$r(x_m-x)\Delta x$, in^3
51.7				
	10.0	15.0	56.7	-634
61.7				
	10.0	13.4	66.7	-1900
71.7				
	10.0	11.9	76.7	-2880
81.7				
	10.0	10.9	86.7	-3456
91.7				
	10.0	9.1	93.7	-1469
95.6				
				-10339

$$\int_{x_o}^{\ell_n} r(x_m-x)dx = \sum_{x_o}^{\ell_n} r(x_m-x)\Delta x = -10339\ in^3 = -6.0\ ft^3$$

4.8 Wing-Fuselage-Nacelle Pitching Moments

The wing-fuselage-nacelle pitching moment characteristics are considered in terms of pitching moment slopes, aerodynamic center and pitching moment coefficient. A first-order approximation of the pitching moment coefficient beyond the limit of linearity of the lift curve slope up to the stall is also considered. The prediction method described in this section is similar to the one in Reference 3.

4.8.1 Factors Contributing to Wing-Fuselage-Nacelle Pitching Moments

a) Zero-lift pitching moments: The zero-lift pitching moments of the wing, fuselage, nacelles and wing-fuselage interference were accounted for in Section 4.6. For the ATLIT:

$$(C_{m_o})_{wfn} = -0.1072 \qquad (4.6.2)$$

b) Fuselage and nacelle pitching moments: The fuselage and nacelle pitching moments due to potential- and viscous-flow lift effects were calculated in Section 4.7. For the ATLIT, with the moment center about the leading edge of the total wing mean aerodynamic (geometric) chord:

$$(C_{m_\alpha})_{fn} = 0.00533 - 0.000252\alpha \text{ per degree} \qquad (4.7.2)$$

c) Wing pitching moment due to effective wing lift: This coefficient includes the effects of body upwash on the wing and wing lift carry-over onto the fuselage. The following expression calculates the pitching moment slope about the leading edge of the total wing mean aerodynamic (geometric) chord:

$$(C_{m_\alpha})_{w(f)+f(w)} = -\left[\left(\frac{x_{ac}}{c_{r_e}}\right)_{w(f)} K_{w(f)} + \left(\frac{x_{ac}}{c_{r_e}}\right)_{f(w)} K_{f(w)} - \frac{(y_{\bar{c}} - d/2)}{c_{r_e}} \tan\Lambda_{le}\right]\left(\frac{c_{r_e}}{\bar{c}_w}\right)\left(\frac{S_{w_e}}{S_w}\right)(C_{L_\alpha})_{w_e} \qquad (4.8.1.1)$$

where

$(x_{ac}/c_{r_e})_{w(f)}$ is the aerodynamic center of the wing in the presence of the fuselage as a fraction of and about the leading edge of the root chord of the exposed wing panels, obtained from Figure 4.5.2.

$K_{w(f)}$ is the ratio of the lift on the wing in the presence of the body to the lift on the isolated wing, obtained from Figure 4.4.1.1.

$K_{f(w)}$ is the ratio of wing lift carry-over onto the body to wing lift alone, obtained from Figure 4.4.1.1.

$(x_{ac}/c_{r_e})_{f(w)}$ is the contribution to the aerodynamic center due to the lift carry-over of the wing on the fuselage. For general aviation airplanes ($A_w \sqrt{1-M^2} \geq 4$, $d/b < 0.5$) this contribution is:

$$\left(\frac{x_{ac}}{c_{r_e}}\right)_{f(w)} = \frac{1}{4} + \frac{b-d}{2c_{r_e}} \tan\Lambda_{c/4} \left[-\frac{k}{1-k} + \frac{\frac{b}{2}\sqrt{1-2k}\,\ell n\left(\frac{1-k}{k}+\frac{1}{k}\sqrt{1-2k}\right) - \frac{b}{2}(1-k) + \frac{\pi b}{4}k}{\frac{b}{2}\frac{k(1-k)}{\sqrt{1-2k}}\ell n\left(\frac{1-k}{k}+\frac{1}{k}\sqrt{1-2k}\right) + \frac{b}{2}\frac{(1-k)^2}{k} - \frac{\pi b}{4}(1-k)} \right] \qquad (4.8.1.2)$$

The wing pitching moment slope about the leading edge of the mean aerodynamic chord due to the effective wing lift in presence of the body for the ATLIT airplane is summarized in Table 4.8.1.1:

$$(C_{m_\alpha})_{w(f)+f(w)} = -0.02464 \text{ per degree} \qquad (4.8.1.3)$$

d) Wing pitching moment due to wing drag: The wing pitching moment due to wing drag can be predicted as follows:

$$(C_{m_\alpha})_{w(D)} = -C_{L_{wfn}} \left[\frac{(C_{L_\alpha})_w}{(C_{L_\alpha})_{wfn}}\right] \left[\frac{2(C_{L_\alpha})_w}{\pi A_w e}\right] \frac{z_w}{\bar{c}_w} \qquad (4.8.1.4)$$

where

z_w is the vertical distance from the X-body axis to the quarter chord of the mean aerodynamic chord of the wing, positive down.

e is the wing efficiency factor for induced drag.

For the ATLIT the distance, z_w, is negligible. In that case the wing pitching moment slope due to wing drag is zero:

$$(C_{m_\alpha})_{w(D)} = 0 \qquad (4.8.1.5)$$

e) Fuselage and nacelle "free moments": The fuselage and nacelle "free moments" due to induced flow from the wing can be estimated with the Multhopp method. It is indicated that, in considering wing lift carry-over onto the body, there remains a free moment of the body due to wing upwash ahead of the wing and downwash behind the wing or:

$$(C_{m_\alpha})_{B(\varepsilon)} = \frac{1}{36.5\ S_w \bar{c}_w} \sum_{o}^{\ell_B} w_B^2\, \Delta x \frac{\partial \beta}{\partial \alpha} \qquad (4.8.1.6)$$

where

w_B is the mean width of the body planform segment Δx

$\partial\beta/\partial\alpha$ is the variation of the local flow with the angle of attack, α. Curves of $\partial\beta/\partial\alpha$ are shown in Figure 4.8.1.1 as a function of the Δx segment position ahead of the wing leading edge, x_1/c_w, where c_w is the exposed root chord of the wing for the fuselage, and the chord at the centerline of the nacelle for the nacelle. For Δx segments immediately ahead of the wing leading edge, $\partial\beta/\partial\alpha$ rises so abruptly that integrated values, $\partial\bar{\beta}/\partial\alpha$, are given based on the length, $\bar{x}_1$, of the segment adjacent to the wing leading edge. For segments aft of the trailing edge of the wing, $\partial\beta/\partial\alpha$ is assumed to vary linearly, or:

$$\frac{\partial \beta}{\partial \alpha} = \frac{x_1'}{\ell_h} \left(1 - \frac{\partial \varepsilon_w}{\partial \alpha}\right) \qquad (4.8.1.7)$$

where

$\partial\varepsilon_w/\partial\alpha$ can be obtained from Section 4.9 and is considered to be similar to $(\partial\bar{\varepsilon}_h/\partial\alpha)_M$

ℓ_h is the distance from the wing trailing edge to the centroid of the last aft Δx segment

x_1' is the distance from the wing trailing edge to the centroid of the Δx segment.

Fuselage and nacelle "free moments" for the ATLIT are summarized in Table 4.8.1.2 or:

$$(C_{m_\alpha})_{f(\varepsilon)+n(\varepsilon)} = (C_{m_\alpha})_{f(\varepsilon)} + (C_{m_\alpha})_{n(\varepsilon)}$$

$$= 0.00966 + 0.00737 \qquad (4.8.1.8)$$

$$= 0.01703 \quad \text{per degree}$$

4.8.2 Static Margin of Wing-Fuselage-Nacelle Combination

The pitching-moment characteristics in terms of static margin, the distance from the center of gravity to the aerodynamic center, are obtained from the following expression:

$$-\left(\frac{d\,C_{m.}}{d\,C_L}\right)_{cg} = -\frac{x_{cg}}{\bar{c}_w} - \frac{\Sigma(C_{m_\alpha})_{le}}{\Sigma\,C_{L_\alpha}} \qquad (4.8.2.1)$$

where

$x_{cg}/\bar{c}_w$ is the distance from the leading edge of the total wing mean aerodynamic chord to the center of gravity as a ratio of the mean aerodynamic chord.

$(\Sigma C_{m_\alpha})_{le}$ is the pitching moment slope about the leading edge of the mean aerodynamic chord

ΣC_{L_α} is the lift curve slope of the wing-fuselage-nacelle combination, which can be obtained from Section 4.4.

For the wing-fuselage-nacelle configuration:

$$-\left(\frac{d\,C_m}{d\,C_L}\right)_{cg} = -\frac{x_{cg}}{\bar{c}} - \frac{\left[(C_{m_\alpha})_{fn} + (C_{m_\alpha})_{w(f)+f(w)} + (C_{m_\alpha})_{w(D)} + (C_{m_\alpha})_{f(\varepsilon)+n(\varepsilon)}\right]_{le}}{(C_{L_\alpha})_{wfn}} \qquad (4.8.2.2)$$

where

$(C_{m_\alpha})_{fn}$ is the pitching moment slope of the fuselage and nacelle obtained from Section 4.7

$(C_{m_\alpha})_{w(f)+f(w)}$ is the wing pitching moment slope due to effective wing lift, obtained from Equation (4.8.1.1)

$(C_{m_\alpha})_{w(D)}$ is the pitching moment slope due to wing drag, obtained from Equation (4.8.1.4)

$(C_{m_\alpha})_{f(\varepsilon)+n(\varepsilon)}$ is pitching moment due to the fuselage and nacelle "free moments"

$(C_{L_\alpha})_{wfn}$ is the lift curve slope of the wing-fuselage-nacelle combination, obtained from Section 4.4

To express the static margin as a function of the lift coefficient of the wing-fuselage-nacelle configuration, replace α in Equation (4.8.2.2) by:

$$\alpha = \frac{C_{L_{wfn}}}{(C_{L_\alpha})_{wfn}} + (\alpha_o)_{wfn} \qquad (4.8.2.3)$$

where

$(\alpha_o)_{wfn}$ represents the angle of attack at zero-lift of the wing-fuselage-nacelle combination, which can be obtained from Section 4.4.

For the ATLIT airplane:

$$-\left(\frac{d\,C_m}{d\,C_L}\right)_{0.25\bar{c}} = -0.25 - \frac{(0.00533 - 0.000252\alpha) - 0.02464 + 0. + 0.01703}{0.0964}$$

$$= -0.2263 + 0.00261\alpha \qquad (4.8.2.4)$$

Substitution of the following expression:

$$\alpha = \frac{C_{L_{wfn}}}{0.0964} - 3.2 \qquad (4.8.2.5)$$

into Equation (4.8.2.4) results in:

$$-\left(\frac{d\,C_m}{d\,C_L}\right)_{0.25\bar{c}} = -0.2347 + 0.02707\,C_{L_{wfn}} \qquad (4.8.2.6)$$

4.8.3 Pitching Moment Coefficient of Wing-Fuselage-Nacelle Combination

Linear lift range: The pitching moment coefficient of the airplane without horizontal tail in the linear lift range can be determined as follows:

$$(C_{m_{wfn}})_{0.25\bar{c}} = -\int -\left(\frac{d C_m}{d C_L}\right)_{0.25\bar{c}} d C_{L_{wfn}} + (C_{m_o})_{wfn} \qquad (4.8.3.1)$$

where

$-(d C_m/d C_L)_{0.25\bar{c}}$ follows from Equation (4.8.2.5) and $(C_{m_o})_{wfn}$ from Equation (4.6.2).

For the ATLIT airplane the pitching moment of the airplane without horizontal tail about quarter chord of the mean aerodynamic chord is given by:

$$(C_{m_{wfn}})_{0.25\bar{c}} = 0.2347\ C_{L_{wfn}} - 0.01354\ C_{L_{wfn}}^{2} - 0.1072 \qquad (4.8.3.2)$$

Non-linear lift range: In Reference 3 a method is given which estimates the pitching moment coefficient in the lift region between the upper limit of linearity of the lift curve slope and stall.

The average pitching moment slope in the non-linear lift region can be obtained as follows:

a) Calculate the average value of the lift curve slope of the wing in the non-linear range approaching stall by:

$$(C_{L_\alpha})_{w_s} = \frac{1}{2}\left[(C_{L_\alpha})_w + \frac{(C_{L_{max}})_w - (C_{L_\alpha})_w\{\alpha_w^* - (\alpha_o)_w\}}{(\alpha_{C_{L_{max}}})_w - \alpha_w^*}\right] \qquad (4.8.3.3)$$

For the ATLIT, the wing lift data can be obtained from Section 4.2. The average wing lift slope is:

$$(C_{L_\alpha})_{w_s} = 0.0796 \text{ per degree} \qquad (4.8.3.4)$$

b) Calculate the difference in linear and non-linear lift curve slopes from:

$$(\Delta C_{L_\alpha})_{w_s} = (C_{L_\alpha})_w - (C_{L_\alpha})_{w_s} \tag{4.8.3.5}$$

For the ATLIT airplane:

$$\begin{aligned}(\Delta C_{L_\alpha})_{w_s} &= 0.0888 - 0.0796 \\ &= 0.0092 \text{ per degree}\end{aligned} \tag{4.8.3.6}$$

c) Calculate the average slope of the wing pitching moment coefficient about the leading edge of the wing mean aerodynamic chord in the non-linear lift range to stall by:

$$(C_{m_\alpha})_{w_s} = - (ac)_{w_s} (C_{L_\alpha})_{w_s} \tag{4.8.3.7}$$

where

$(ac)_{w_s}$ is the average value of the aerodynamic center in the non-linear range of the wing lift curve slope to stall expressed as a fraction of the wing mean aerodynamic chord, assumed to be 0.375.

For the ATLIT:

$$\begin{aligned}(C_{m_\alpha})_{w_s} &= -0.375\ (0.0796) \\ &= - 0.0299 \text{ per degree}\end{aligned} \tag{4.8.3.8}$$

d) Calculate the average value of the angle of attack in the non-linear lift range from:

$$\bar{\alpha}_s = \frac{1}{2} (\alpha^* + \alpha_{C_{L_{max}}}) \tag{4.8.3.9}$$

For the ATLIT the average value of α in the non-linear range can be determined from Figure 4.4.3.1:

$$\begin{aligned}\bar{\alpha}_s &= \frac{1}{2} (4 + 15.9) \\ &\simeq 10 \text{ degrees}\end{aligned} \tag{4.8.3.10}$$

e) Calculate the pitching moment slope in the non-linear lift range as follows:

$$-\left(\frac{d C_m}{d C_L}\right)_{cg_s} = -\frac{x_{cg}}{\bar{c}} - \frac{(C_{m_\alpha})_{fn} + (C_{m_\alpha})_{w_s} + (C_{m_\alpha})_{f(\varepsilon)+n(\varepsilon)}}{(C_{L_\alpha})_{wfn} - (\Delta C_{L_\alpha})_{w_s}} \qquad (4.8.3.11)$$

where

$(C_{m_\alpha})_{fn}$ follows from Section 4.7

$(C_{m_\alpha})_{w_s}$ follows from Equation (4.8.3.7)

$(C_{m_\alpha})_{f(\varepsilon)+n(\varepsilon)}$ is obtained from Equation (4.8.1.8).

For the ATLIT airplane the pitching moment slope is the non-linear lift range is:

$$-\left(\frac{d C_m}{d C_L}\right)_{0.25\bar{c}_s} = -0.25 - \frac{(0.00533 - 0.000252\bar{\alpha}_s) - 0.0299 + 0.01703}{0.0964 - 0.0092} = -0.1346 \qquad (4.8.3.12)$$

4.8.4 Pitching Moment Characteristics of the ATLIT

The pitching moment characteristics of the ATLIT airplane, including the non-linear region, are summarized in Table 4.8.4.1, while in Figure 4.8.4.1 the results are shown and compared with the full-scale wind tunnel data. These results are obtained from Appendix D, because no wind tunnel data were obtained with the ATLIT in the "fully clean" configuration and horizontal tail removed. Figure 4.8.4.1 also shows results obtained with References 5 and 6.

The pitching moment curve obtained with Reference 5 shows poor agreement with the experimental results. The results obtained with Reference 5 do not include the pitching moment due to the nacelles. However, the data obtained with Reference 6 show that the contribution of the nacelles is substantial.

The results obtained with Reference 6 show good agreement with the experimental data. This is also true for the results from Table 4.8.4.1. Both methods predict the pitching moment slope fairly well.

In Section 4.13 the stabilizer effectiveness in lift and pitch, $C_{L_{i_h}}$ and $C_{m_{i_h}}$, respectively, is discussed. For the ATLIT the stabilizer effectiveness in pitch is $C_{m_{i_h}} \approx -0.08$ per degree of stabilizer deflection. This means that the discrepancy between the predicted pitching moment curve (from Table 4.8.4.1) and the experimental curve is identical to a stabilizer deflection, i_h, of approximately one degree.

Note:

At the time of finishing this report it appeared that the pitching moment coefficient, obtained with Reference 6, is defined as:

$$C_m = \frac{\text{Pitching Moment}}{\bar{q}_\infty S_w b_w/2} \qquad (4.8.4.1)$$

while the normal definition is:

$$C_m = \frac{\text{Pitching Moment}}{\bar{q}_\infty S_w \bar{c}_w} \qquad (4.8.4.2)$$

The pitching moment coefficients obtained with Reference 6 and shown in Figure 4.8.4.1 have to be corrected in the following manner:

$$C_m = C_{m_{Ref.6}} \frac{b_w/2}{\bar{c}_w} = 4.98\ C_{m_{Ref.6}} \qquad (4.8.4.3)$$

This correction will result in poor agreement of the results obtained with Reference 6 with the wind tunnel data of Reference 2.

Table 4.8.1.1: Wing pitching moment due to wing lift including mutual wing-fuselage interference

Symbol	Description	Reference	Magnitude
$\bar{c}_w$	Total wing mean aerodynamic chord, m (in)	Table 2.1.1	1.225 (43.22)
c_{r_e}	Root chord of exposed wing panels, m (in)	Table 2.1.1	1.495 (58.87)
S_w	Reference wing area, m^2 (ft^2)	Table 2.1.1	14.40 (155.0)
S_{w_e}	Exposed panel wing area, m^2 (ft^2)	Table 2.1.1	12.53 (134.8)
$(C_{L_\alpha})_{w_e}$	Lift curve slope of exposed wing panels, deg^{-1}	Table 4.2.4.1	0.0874
$K_{w(f)}$	Ratio of lift of wing in presence of fuselage to wing alone	Table 4.4.3.1	1.08
$K_{f(w)}$	Ratio of wing lift carry-over onto fuselage to wing alone	Table 4.4.3.1	0.13
$(x_{ac}/c_{r_e})_{w(f)}$	Aerodynamic center of wing in presence of fuselage, as fraction of and about leading edge of c_{r_e}	Figure 4.5.2	0.297
d	Fuselage width at wing, m (in)	Table 4.6.1	1.219 (48.0)
b	Wing span, m (in)	Table 2.1.1	12.19 (480.0)
k	d/b	-	0.10
$\Lambda_{c/4}$	Sweep of wing quarter chord line, deg	Table 2.1.1	1.835
$(x_{ac}/c_{r_e})_{f(w)}$	Contribution to the aerodynamic center due to lift carry-over of wing onto fuselage, as fraction of c_{r_e}	Eq. (4.8.1.2)	0.268
$\bar{y_c}$	Lateral distance from root chord to total wing mean aerodynamic chord, m (in)	Table 2.1.1	2.709 (106.67)
Λ_{le}	Leading edge sweep angle of wing, deg	Table 2.1.1	3.67
$(C_{m_\alpha})_{w(f)+f(w)}$	Pitching moment slope, about leading edge of wing mean aerodynamic chord, due to effective wing lift, deg^{-1}	Eq. (4.8.1.1)	-0.02464

Table 4.8.1.2: "Free moments" of fuselage and nacelle

Symbol	Description	Reference	Magnitude
w_B	Mean width of body planform segment Δx, m (in)	Figure 4.8.1.2	Variable
x_1	Distance from wing leading edge to centroid of forward Δx segments, m (in)	Figure 4.8.1.2	Variable
x_1'	Distance from wing trailing edge to centroid of aft Δx segments, m (in)	Figure 4.8.1.2	Variable
c_{r_e}	Root chord of exposed wing panels, m (in)	Table 2.1.1	1.495 (58.87)
c_n	Chord of wing at centerline of nacelle, m (in)	Figure 4.8.1.2	1.331 (52.4)
ℓ_h	Distance from wing trailing edge to centroid of last aft Δx segment, m (in)	Figure 4.8.1.2	3.581 (141.0)
$\partial\varepsilon_w/\partial\alpha$	Rate of change of downwash behind wing	Table 3.9.3.2	= 0.4
$\partial\beta/\partial\alpha$	•For Δx segments forward of wing leading edge: the variation of upwash at segment with angle of attack	Figure 4.8.1.1	Variable
	•For Δx segments aft of wing trailing edge: the variation of downwash at segment with angle of attack	Eq. (4.8.1.7)	Variable
S_w	Reference wing area, m^2 (ft^2)	Table 2.1.1	14.4 (155.0)
$\bar{c}_w$	Reference mean aerodynamic chord, m (ft)	Table 2.1.1	1.225 (4.018)
$(C_{L_\alpha})_w$	Lift curve slope of wing, deg^{-1}	Table 4.2.4.1	0.0888

Table 4.8.1.2: Concluded

Segment	Δx, in Figure 4.8.1.2	w_f, in Figure 4.8.1.2	$w_f^2 \Delta x$, ft^3	x_1, in Figure 4.8.1.2	x_1', in Figure 4.8.1.2	$\frac{x_1}{c_{r_e}}$	$\frac{x_1'}{\ell_h}$	$\frac{\partial \beta^*}{\partial \alpha}$ Figure 4.8.1.1	$\frac{\partial \beta}{\partial \alpha}$ Eq. (4.8.1.7)	$w_f^2 \Delta x \frac{\partial \beta}{\partial \alpha}$ ft^3
1	20.5	16.9	3.388	88.8	-	1.508	-	1.223	-	4.144
2	20.5	33.8	13.554	70.0	-	1.189	-	1.261	-	17.092
3	20.5	43.8	22.759	51.3	-	0.871	-	1.346	-	30.634
4	20.5	49.4	28.952	30.8	-	0.523	-	1.500	-	43.428
5	20.5	51.3	31.221	20.5**	-	0.348	-	3.301	-	103.061
6	31.75	49.4	44.840	-	15.9	-	0.113	-	0.068	3.049
7	31.75	40.6	30.287	-	47.3	-	0.335	-	0.201	6.088
8	31.75	31.3	18.001	-	78.5	-	0.557	-	0.334	6.012
9	31.75	22.5	9.303	-	109.8	-	0.779	-	0.467	4.344
10	31.75	12.5	2.872	-	141.0	-	1.0	-	0.600	1.723
										219.586

Summary: $(C_{m_\alpha})_{f(\varepsilon)} = \frac{1}{36.5\, S_w \bar{c}_w} \sum_{o}^{\ell_f} w_f^2 \Delta x \frac{\partial \beta}{\partial \alpha} = \frac{219.586}{36.5\, S_w \bar{c}_w} = 0.00966$

Segment	Δx, in Figure 4.8.1.2	w_n, in Figure 4.8.1.2	$w_n^2 \Delta x$, ft^3	x_1, in Figure 4.8.1.2	x_1', in	$\frac{x_1}{c_n}$	$\frac{x_1'}{\ell_n}$	$\frac{\partial \beta^*}{\partial \alpha}$ Figure 4.8.1.1	$\frac{\partial \beta}{\partial \alpha}$ Eq. (4.8.1.7)	$w_n^2 \Delta x \frac{\partial \beta}{\partial \alpha}$ ft^3
1	10	32.0	5.926	44	-	0.840	-	1.321	-	7.828
2	10	38.75	8.690	35	-	0.668	-	1.381	-	12.001
3	10	38.75	8.690	25	-	0.477	-	1.481	-	12.870
4	10	38.75	8.690	15	-	0.286	-	1.635	-	14.280
5	10	38.75	8.690	10**	-	0.190	-	4.245	-	36.889
										83.868

Summary: $(C_{m_\alpha})_{n(\varepsilon)} = 2 \frac{1}{36.5\, S_w \bar{c}_w} \sum_{o}^{\ell_n} w_n^2 \Delta x \frac{\partial \beta}{\partial \alpha} = 2 \frac{83.868}{36.5\, S_w \bar{c}_w} = 0.00737$

* Including $(C_{L_\alpha})_w$ correction: $\frac{\partial \beta}{\partial \alpha} = \left(\frac{\partial \beta}{\partial \alpha}\right)_{(C_{L_\alpha})_w = 0.0785} \cdot \frac{(C_{L_\alpha})_w}{0.0785}$

** For segment 5: $x_1 = \bar{x}_1$

Table 4.8.4.1: Pitching moments of the ATLIT airplane with horizontal tail removed

α, deg.	$C_{L_{wfn}}$ Table 4.4.3.3	$C_{L_{wfn}}^2$	$(C_{m_{wfn}})_{0.25\bar{c}}$ Eq. (4.8.3.2)
-4	-0.07803	0.00609	-0.12560
-2	0.11405	0.01301	-0.08061
0	0.30661	0.09401	-0.03651
2	0.49966	0.24966	0.00669
4	0.69319	0.48051	0.04899
15.9	1.57308	-	*0.16742

* With Equation (4.8.3.12)

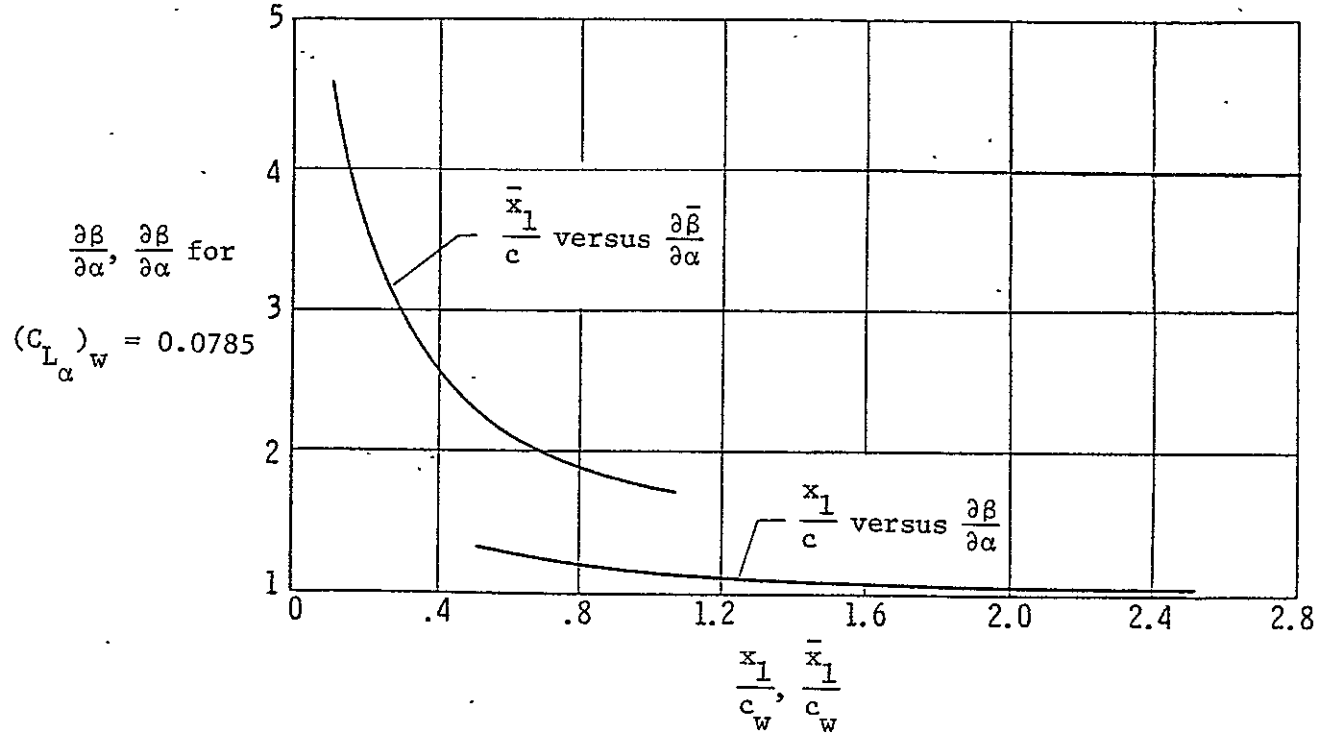

Figure 4.8.1.1: Variation of the wing upwash derivative with position along the body (Reference 3)

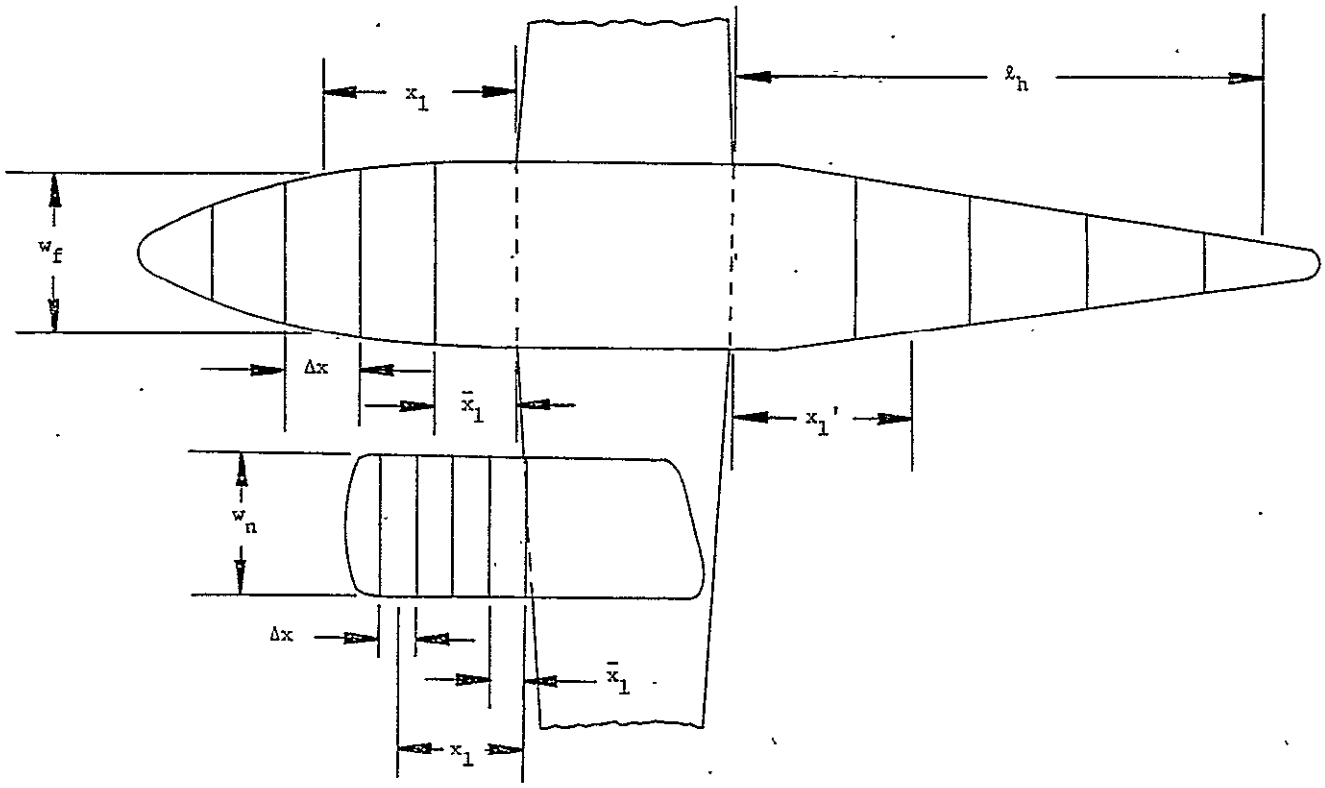

Figure 4.8.1.2: Pertinent dimensions used to determine the "free moments" of fuselage and nacelle

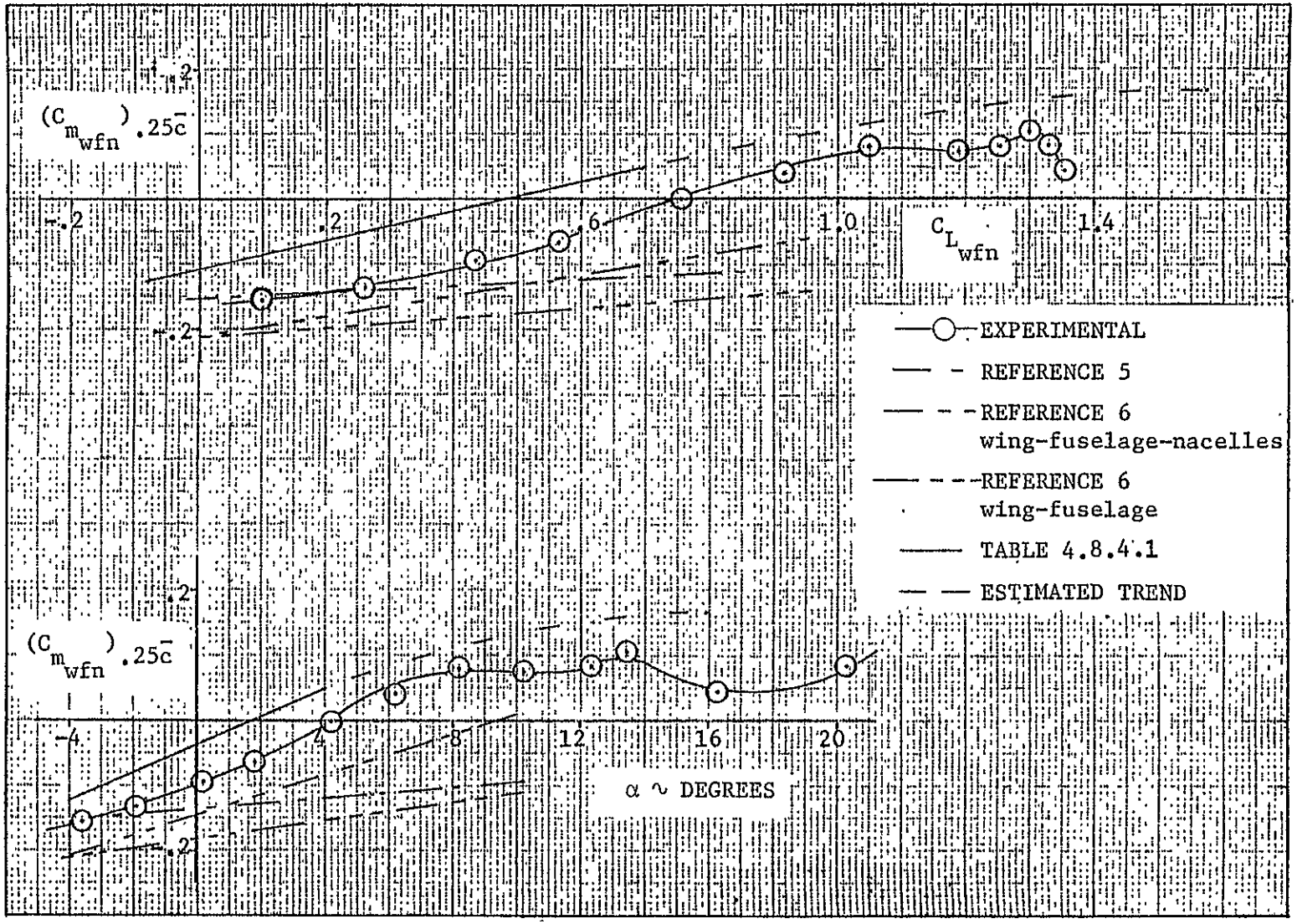

Figure 4.8.4.1: Comparison of predicted pitching moments with wind tunnel data (horizontal tail off, propellers removed, N_{Re} = 2.3 million)

See note on Page 109

4.9 Downwash and Dynamic Pressure at the Horizontal Tail

The method presented for predicting the subsonic downwash and dynamic pressure in the region of the tail plane was developed for the linear lift region for swept- and unswept-wing airplanes. This method, however, provides a reasonable approximation for the downwash and dynamic pressure in the nonlinear lift range below stall.

4.9.1 Downwash at the Horizontal Tail

The method discussed is also in References 3 and 4. The method is applicable to configurations in which the span of the wing is at least 1.5 times as large as that of the horizontal tail ($b_w/b_h \geq 1.5$). The basic approach is as follows:

1) Determine the downwash in the plane of symmetry at the height of the vortex cores and at the longitudinal station of the quarter chord point of the horizontal tail mean aerodynamic chord.

2) Correct this value for the horizontal tail height above or below the trailing vortices.

3) Evaluate the effect of horizontal tail span by relating the average downwash at the tail to the downwash determined in Step 2.

The downwash gradient, $\partial\varepsilon/\partial\alpha$, at the trailing edge of the wing is unity. The value at a distance infinitely for downstream is given by:

$$\frac{\partial\varepsilon_\infty}{\partial\alpha} = \frac{360}{\pi^2 A_w} (C_{L_\alpha})_w \qquad (4.9.1.1)$$

where

$(C_{L_\alpha})_w$ is the wing lift curve slope per degree. If these two values are known, the downwash gradient for any intermediate longitudinal

position can be found by means of the lifting line theory.

For straight wings that have tip stall or thin swept wings that shed the leading edge vortices inboard of the wing tips, the effective wing aspect ratio is considerably less than the geometric aspect ratio. An effective aspect ratio is presented for these wings.

Because of the spanwise variation of downwash, the effective downwash acting on the horizontal tail is different from that at the plane of symmetry. A correction for tail-span effect is presented and it is based on the assumption that the vortices are essentially rolled up at the longitudinal tail station.

The subsonic downwash is obtained from the following precedure (see also Figure 4.9.1.1):

1) Determine the effective wing aspect ratio, $A_{w_{eff}}$, and the effective wing span, $b_{w_{eff}}$, from Figure 4.9.1.2 as a function of the wing angle of attack parameter:

$$\frac{\alpha_w - \alpha_{o_w}}{(\alpha_{C_{L_{max}}})_w - \alpha_{o_w}}$$

2) Determine the downwash gradient, $(\partial\epsilon_{vc}/\partial\alpha)_{low\ speed}$ in the plane of symmetry at the height of the vortex core from Figure 4.9.1.3. This figure is entered with $2\ell_2/b_w$ and $A_{w_{eff}}$, where ℓ_2 is the distance measured parallel to the wing root chord between the aft end of the wing root and the quarter chord point of the mean aerodynamic chord of the horizontal tail.

3) Determine the vertical position, a, of the quarter chord point of the mean aerodynamic chord of the horizontal tail relative to the vortex core. This distance depends upon the type of wing flow separation as determined from Figure 4.9.1.4. For trailing edge separation:

$$a = z_h' - \ell_{eff}\left(\frac{\alpha_w \pi}{180} - \frac{0.41\ C_{L_w}}{\pi\ A_w}\right) - \frac{b_{w_{eff}}}{2} \tan \Gamma \qquad (4.9.1.2)$$

For leading edge separation:

$$a = z_h' - (\ell_2 + \ell_3)\left(\frac{\alpha_w \pi}{180} - \frac{0.41\ C_{L_w}}{\pi\ A_{w_{eff}}}\right) \qquad (4.9.1.3)$$

where

ℓ_{eff} is the distance measured parallel to the wing root, between the effective wing tip quarter point and the quarter chord point of the horizontal tail mean aerodynamic chord.

Γ is the dihedral angle of the wing

z_h' is the height of the horizontal tail mean aerodynamic chord quarter chord point above or below the plane of the wing root chord, measured in the plane of symmetry and normal to the extended wint root chord, positive for the tail above the plane of the wing root chord.

ℓ_3 is the distance measured parallel to the plane of symmetry, between the leading edge of the wing mean aerodynamic chord to the trailing edge of the wing root chord.

ℓ_2 is defined in Step 2.

4) Calculate the span of the vortices at the longitudinal location of the quarter chord point of the horizontal tail mean aerodynamic chord by:

$$b_{vor} = b_{w_{eff}} - (b_{w_{eff}} - b_{ru})\sqrt{\frac{2\ell_{eff}}{b_w \ell_{ru}}} \qquad (4.9.1.4)$$

where

b_{ru}, the span of the completely rolled up vortices, is obtained from:

$$b_{ru} = [0.78 + 0.10\ (\lambda_w - 0.4) + 0.003\ (\Lambda_{c/4})_w]\ b_{w_{eff}} \qquad (4.9.1.5)$$

where

$(\Lambda_{c/4})_w$ is the quarter chord sweep angle of the wing in degrees

and:

$$\ell_{ru} = \frac{0.56\ A_w}{C_{L_w}} \qquad (4.9.1.6)$$

5) Determine the average downwash gradient acting on the tail by:

$$\left(\frac{\partial \bar{\varepsilon}_h}{\partial \alpha}\right)_{\text{low speed}} = \left[\frac{\partial \bar{\varepsilon}_h / \partial \alpha}{\partial \varepsilon_{vc} / \partial \alpha}\right]_{\text{low speed}} \left(\frac{\partial \varepsilon_{vc}}{\partial \alpha}\right)_{\text{low speed}} \qquad (4.9.1.7)$$

where the [ ] quantity is obtained from Figure 4.9.1.5 by using the parameters calculated in the above steps.

6) For high subsonic Mach number the downwash gradient is given by:

$$\left(\frac{\partial \bar{\varepsilon}_h}{\partial \alpha}\right)_M = \left(\frac{\partial \bar{\varepsilon}_h}{\partial \alpha}\right)_{\text{low speed}} \frac{(C_{L_\alpha})_{w_M}}{(C_{L_\alpha})_{w_{\text{low speed}}}} \qquad (4.9.1.8)$$

7) Determine the average downwash acting on the horizontal tail by integrating the average downwash gradient from Step 5 or 6 as follows:

$$\bar{\varepsilon}_h = \int_0^\alpha \frac{\partial \bar{\varepsilon}_h}{\partial \alpha}\, d\alpha \qquad (4.9.1.9)$$

4.9.2 Dynamic-Pressure Ratio at the Horizontal Tail

In the linear angle of attack range, the ratio of the dynamic pressure in the plane of symmetry at some distance x aft of the wing root chord trailing edge to the free stream dynamic pressure, $\bar{q}_h/\bar{q}_\infty$, is obtained from the procedure outlined in the following steps (see also Figure 4.9.2.1).

1) Calculate the half width of the wing wake by:

$$\Delta z_{wake} = 0.68\ \bar{c}_w \sqrt{C_{D_f}\left(\frac{x}{\bar{c}_w} + 0.15\right)} \qquad (4.9.2.1)$$

where C_{D_f} is the wing zero-lift drag coefficient.

2) Calculate the downwash in the plane of symmetry at the vortex sheet (assumed to be the same location as the wake centerline) by:

$$\varepsilon_h = \frac{180}{\pi} \frac{1.62\ C_{L_w}}{\pi A_w} \text{ (degrees)} \qquad (4.9.2.2)$$

3) Determine the vertical distance, z_h'', from the vortex sheet to the point of interest (usually the quarter chord point of the mean aerodynamic chord of the horizontal tail) by:

$$z_h'' = x \tan (\gamma + \varepsilon_h - \alpha_w) \qquad (4.9.2.3)$$

where γ is defined in Figure 4.9.2.1.

4) Determine the dynamic pressure loss in the wake center by:

$$\left(\frac{\Delta \bar{q}}{\bar{q}_\infty}\right)_o = \frac{2.42\ C_{D_f}^{0.5}}{\frac{x}{\bar{c}_w} + 0.30} \qquad (4.9.2.4)$$

5) Determine the dynamic pressure loss ratio for points not on the wake center line by:

$$\left(\frac{\Delta \bar{q}}{\bar{q}_\infty}\right)_h = \left(\frac{\Delta \bar{q}}{\bar{q}_\infty}\right)_o \cos^2\left(\frac{\pi}{2} \frac{\dot{z}_h''}{\Delta z_{wake}}\right) \qquad (4.9.2.5)$$

where $\left(\frac{\pi}{2} \frac{\dot{z}_h''}{\Delta z_{wake}}\right)$ is expressed in radians. When $\dot{z}_h''/\Delta \dot{z}_{wake}$ is greater than one, the dynamic-pressure ratio loss is zero.

6) Determine the dynamic-pressure ratio in the plane of symmetry at an arbitrary distance x (usually the quarter chord point of the mean aerodynamic chord of the horizontal tail) aft of the wing root chord trailing edge by:

$$\frac{\bar{q}_h}{\bar{q}_\infty} = 1 - \left(\frac{\Delta\bar{q}}{\bar{q}_\infty}\right)_h \qquad (4.9.2.6)$$

4.9.3 Downwash and Dynamic-Pressure Ratio at the Horizontal Tail of the ATLIT Airplane

Tables 4.9.3.1 and 4.9.3.2 show the calculations to obtain the downwash angle at the horizontal tail as function of the angle of attack while the result is shown in Figure 4.9.3.1.

In Figure 4.9.3.1 also the downwash angle at the tail obtained from the experimental wind tunnel data is shown. Appendix E demonstrates in what manner these results were obtained from the wind tunnel data of Reference 2. The slope of the predicted curve shows fair agreement with the slope fo the experimental downwash curve. However, in the linear lift range the predicted value of $\bar{\varepsilon}_h$ is approximately 1.5 degrees too small.

A summary of the calculations which lead to the dynamic pressure ratio at the horizontal tail is listed in Table 4.9.3.3 and 4.9.3.4. The results indicate that the horizontal tail, except at high angles of attack, stays out of the wake. Therefore, the dynamic pressure ratio at the horizontal tail will be assumed to be constant and equal to one. The result of the calculations is shown in Figure 4.9.3.2.

In Section 4.13 the effect of deflection of the stabilizer on the lift and pitching moment of the ATLIT is predicted. From the results of that section it seems that the assumption:

$$\bar{q}_h/\bar{q}_\infty = 1.0$$

is too optimistic. In Reference 8 the following values are listed: $\bar{q}_h/\bar{q}_\infty$ may be assumed equal to 0.85 for a fuselage mounted stabilizer and 0.95 for a fin mounted stabilizer, except in the case of a T-tail (with $\bar{q}_h/\bar{q}_\infty \simeq 1$). For the ATLIT airplane this would mean that the dynamic pressure ratio, $\bar{q}_h/\bar{q}_\infty$, is equal to 0.85 instead of equal to 1 (one).

Table 4.9.3.1: Pertinent parameters for computing average downwash at the horizontal tail of the ATLIT airplane.

Symbol	Description	Reference	Magnitude
$(\alpha_o)_w$	Wing zero-lift angle relative to chord, deg.	Table 4.2.4.1	-2.9
$(\alpha_{C_{L_{max}}})_w$	Wing angle of attack at $C_{L_{max}}$, relative to wing chord, deg.	Table 4.2.4.1	16.4
$(\Lambda_{c/4})_w$	Wing sweep angle along c/4 line, deg.	Table 2.1.1	1.835
Δy	Wing leading edge sharpness parameter, perc. of chord	Table 4.1.2	4.9
λ_w	Wing taper ratio	Table 2.1.1	0.5
A_w	Wing aspect ratio	Table 2.1.1	10.32
b_w	Wing span, m(ft)	Table 2.1.1	12.19(40.0)
Γ	Wing dihedral, deg.	Table 2.1.1	7.0
z_h	Perpendicular distance from wing-root chord plane to $\bar{c}/4$ of horizontal tail, m(ft)	Figure 4.9.1.1	0.832(2.73)
ℓ_2	Tail length in wing-root chord plane from wing-root, trailing edge to $\bar{c}/4$ of horizontal tail, m(ft)	Figure 4.9.1.1	3.716(12.19)
ℓ_3	Distance from leading edge of wing, mean aerodynamic to trailing edge of wing root chord, m(ft)	Figure 4.9.1.1	1.414(4.64)
$A_{w_{eff}}/A_w$	Ratio of effective to geometric wing aspect ratio	Figure 4.9.1.2	1.0
$b_{w_{eff}}/b_w$	Ratio of effective to geometric wing span	Figure 4.9.1.2	1.0
ℓ_{eff}	Tail length in root chord plane from vortex tip of c/4 of $b_{w_{eff}}$ to $\bar{c}/4$ of horizontal tail, m(ft)	Figure 4.9.1.1	4.700(15.42)
$(C_{L_\alpha})_w$	Lift curve slope of wing, $(deg)^{-1}$	Table 4.2.4.1	0.0888
$\partial\varepsilon_\infty/\partial\alpha$	Downwash gradient at infinity	Eq.(4.9.1.1)	0.314
$2\ell_2/b_w$	—	—	0.6095
$(\partial\varepsilon_{vc}/\partial\alpha)_{low\ speed}$	Downwash gradient in plane of symmetry at height of vortex core	Figure 4.9.1.3	0.395
b_{ru}	Span of complete rolled up wing tip vortices, m(ft)	Eq.(4.9.1.5)	7.714(31.82)
ℓ_{ru}	Distance required for complete rollup of wing tip vortices in chord plane, semispans	Eq.(4.9.1.6)	$5.7792/C_{L_w}$
b_{vor}	Span of vortices at longitudinal station of $\bar{c}/4$ of horizontal tail, m(ft)	Eq.(4.9.1.4)	Variable
a	Vertical distance from horizontal tail root chord to vortex core if trailing edge separation, m(ft)	Eq.(4.9.1.2)	Variable
$\left[\frac{\partial\bar{\varepsilon}_h/\partial\alpha}{\partial\varepsilon_{vc}/\partial\alpha}\right]_{low\ speed}$	Ratio of average downwash acting on horizontal tail to downwash at vortex core height	Figure 4.9.1.5	Variable
$(\partial\bar{\varepsilon}_h/\partial\alpha)_{low\ speed}$	Downwash gradient at horizontal tail at low speed	Eq.(4.9.1.7)	Variable
$(\partial\bar{\varepsilon}_h/\partial\alpha)_M$	Downwash gradient at Mach number	Eq.(4.9.1.8)	Variable
$\bar{\varepsilon}_h$	Downwash at horizontal tail, deg.	Eq.(4.9.1.9)	Variable

Table 4.9.3.2: Calculation of downwash at the horizontal tail of the ATLIT

α, deg	α_w, relative to chord		$(\alpha_w)_{abs}$	C_{L_w}	a, ft	ℓ_{ru}
	deg	rad	deg	Figure 4.2.4.1	Eq.(4.9.1.2)	Eq.(4.9.1.6)
①	②a	②b	③	④	⑤	⑥
-4	-3.5	-0.0611	-0.6	-0.0533	1.206	-108.43
-2	-1.5	-0.0262	1.4	0.1243	0.702	46.49
0	0.5	0.0087	3.4	0.3019	0.199	19.14
2	2.5	0.0436	5.4	0.4795	-0.305	12.05
4	4.5	0.0785	7.4	0.6571	-0.808	8.80
15.9	16.4	0.2862	19.3	1.494	-3.848	3.87

b_{vor}	$2a/b_{vor}$	b_h/b_{vor}	$\frac{\partial\bar{\varepsilon}_h/\partial\alpha}{\partial\varepsilon_{vc}/\partial\alpha}$	$(\partial\bar{\varepsilon}_h/\partial\alpha)_{low\ speed}$	$\bar{\varepsilon}_h$ = ③ · ⑪, deg
Eq.(4.9.1.4)			Figure 4.9.1.5	Eq.(4.9.1.7)	
⑦	⑧	⑨	⑩	⑪	⑫
-	-	-	-	-	-
38.95	0.036	0.348	1.019	0.403	0.564
38.36	0.010	0.353	1.025	0.405	1.377
37.93	-0.016	0.358	1.027	0.406	2.192
37.58	-0.043	0.361	1.023	0.404	2.990
36.35	-0.212	0.373	0.950	0.375	7.238

Table 4.9.3.3: Dynamic-pressure ratio at the horizontal tail of the ATLIT

Symbol	Description	Reference	Magnitude
α_w	Wing angle of attack relative to root chord = $\alpha + i_w$, deg.	Table 4.4.3.1	$\alpha + 0.5$
γ	Angle between wing chord plane and line connecting trailing edge of wing root chord and $\bar{c}/4$ of horizontal tail, deg.	Figure 4.9.2.1	12.9
$\bar{c}_w$	Wing mean aerodynamic chord, m(ft)	Table 2.1.1	1.225(4.018)
A_w	Wing aspect ratio	Table 2.1.1	10.32
x	Distance from trailing edge of wing root chord to $\bar{c}/4$ of horizontal tail measured along centerline wake, m(ft)	Figure 4.9.2.1	3.65(11.98)
C_{D_f}	Wing zero-lift drag coefficient of total wing per procedure of Section 4.12	—	0.0111
ε_h	Downwash in plane of symmetry at vortex sheet, deg.	Eq.(4.9.2.2)	2.863 C_{L_w}
z_h''	Vertical distance from vortex sheet to $\bar{c}/4$ of horizontal tail, m(ft)	Eq.(4.9.2.3)	Variable
Δz_{wake}	Half width of wake, m(ft)	Eq.(4.9.2.1)	0.155(0.5094)
$(\Delta\bar{q}/\bar{q}_\infty)_0$	Dynamic pressure loss in the wake centerline	Eq.(4.9.2.4)	0.0777
$(\Delta\bar{q}/\bar{q}_\infty)_h$	Dynamic pressure loss at the horizontal tail	Eq.(4.9.2.5)	Variable
$\bar{q}_h/\bar{q}_\infty$	Dynamic pressure ratio at the horizontal tail	Eq.(4.9.2.6)	Variable

α, deg	α_w, deg	C_{L_w} Figure 4.2.4.1	ε_h, deg Eq.(4.9.2.2)	z_h'', ft Eq.(4.9.2.3	$z_h''/\Delta z_{wake}$	$(\Delta\bar{q}/\bar{q}_\infty)_h$ Eq.(4.9.2.5)	$\bar{q}_h/\bar{q}_\infty$ Eq.(4.9.2.6)
-4	-3.5	-0.0533	-0.1526	3.49	6.85	0.	1.
-2	-1.5	0.1243	0.3559	3.04	5.97	0.	1.
0	0.5	0.3019	0.8643	2.83	5.56	0.	1.
2	2.5	0.4795	1.3728	2.49	4.89	0.	1.
4	4.5	0.6571	1.8813	2.17	4.26	0.	1.
14	14.5	1.465	4.194	0.54	1.07	0.	1.
15	15.5	1.490	4.266	0.35	0.68	0.018	0.982
15.9	16.4	1.494	4.277	0.17	0.33	0.059	0.941

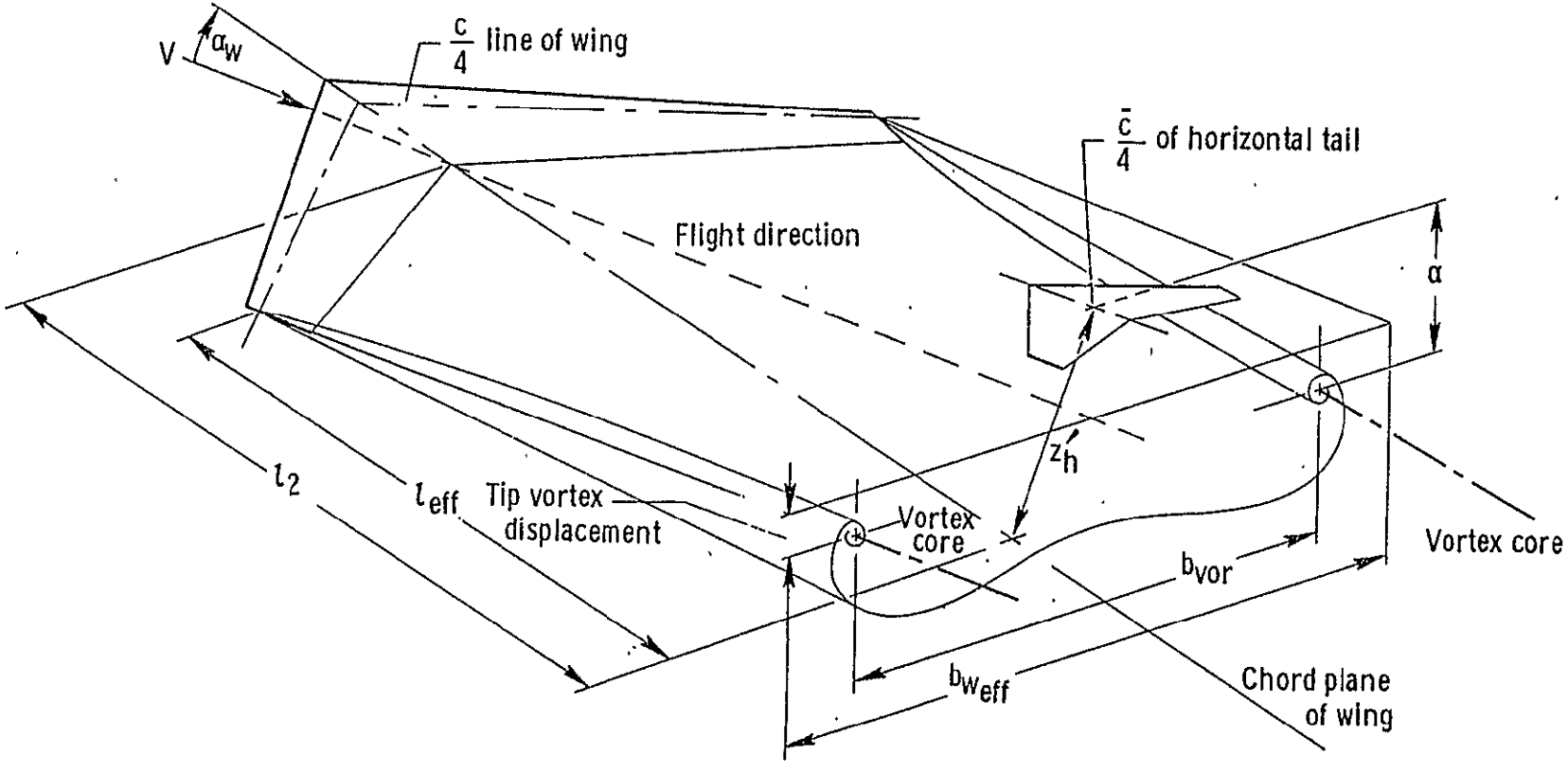

Figure 4.9.1.1: Wing vortex system

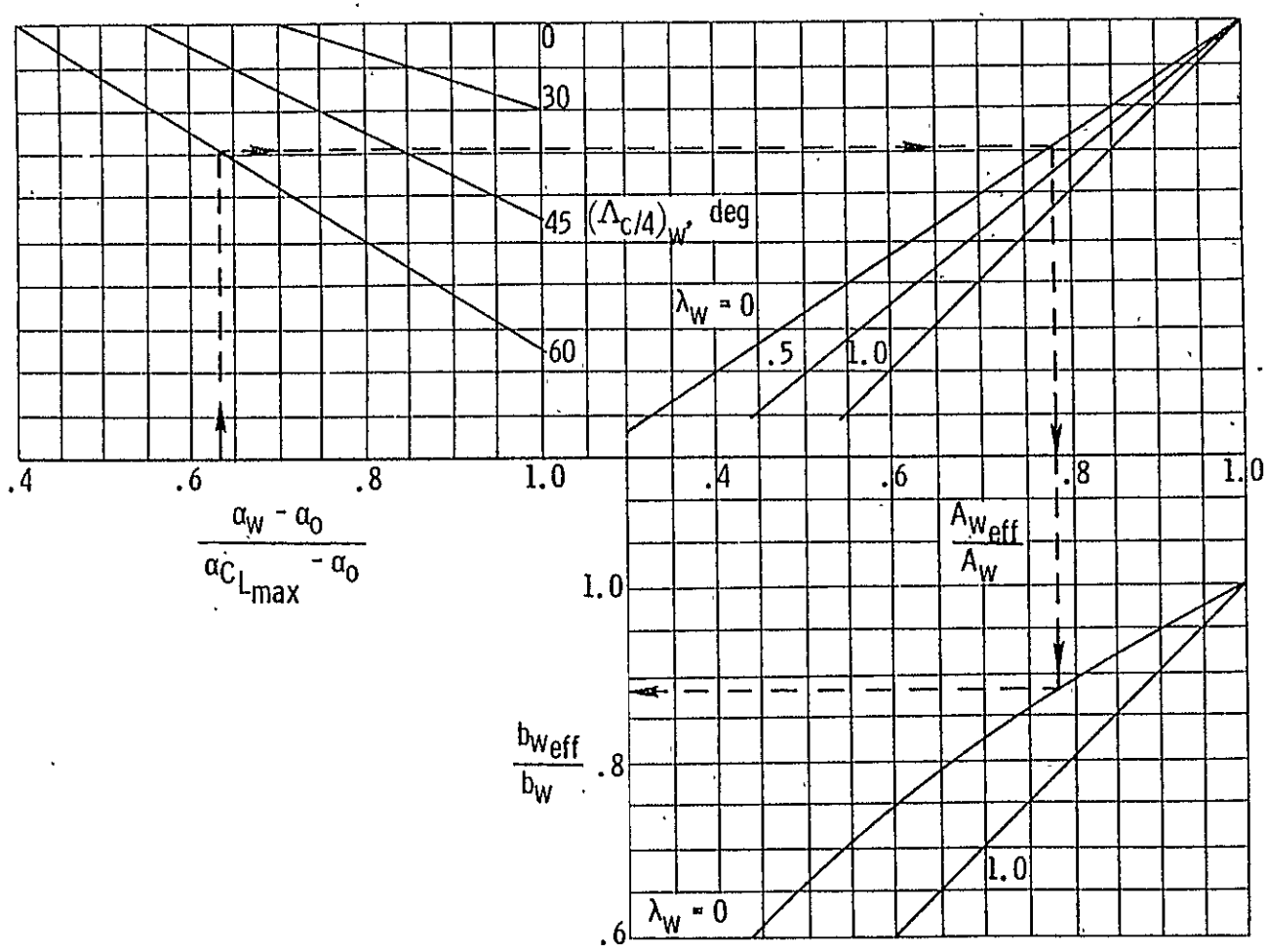

Figure 4.9.1.2: Effective wing aspect ratio and span for low speeds (Reference 3)

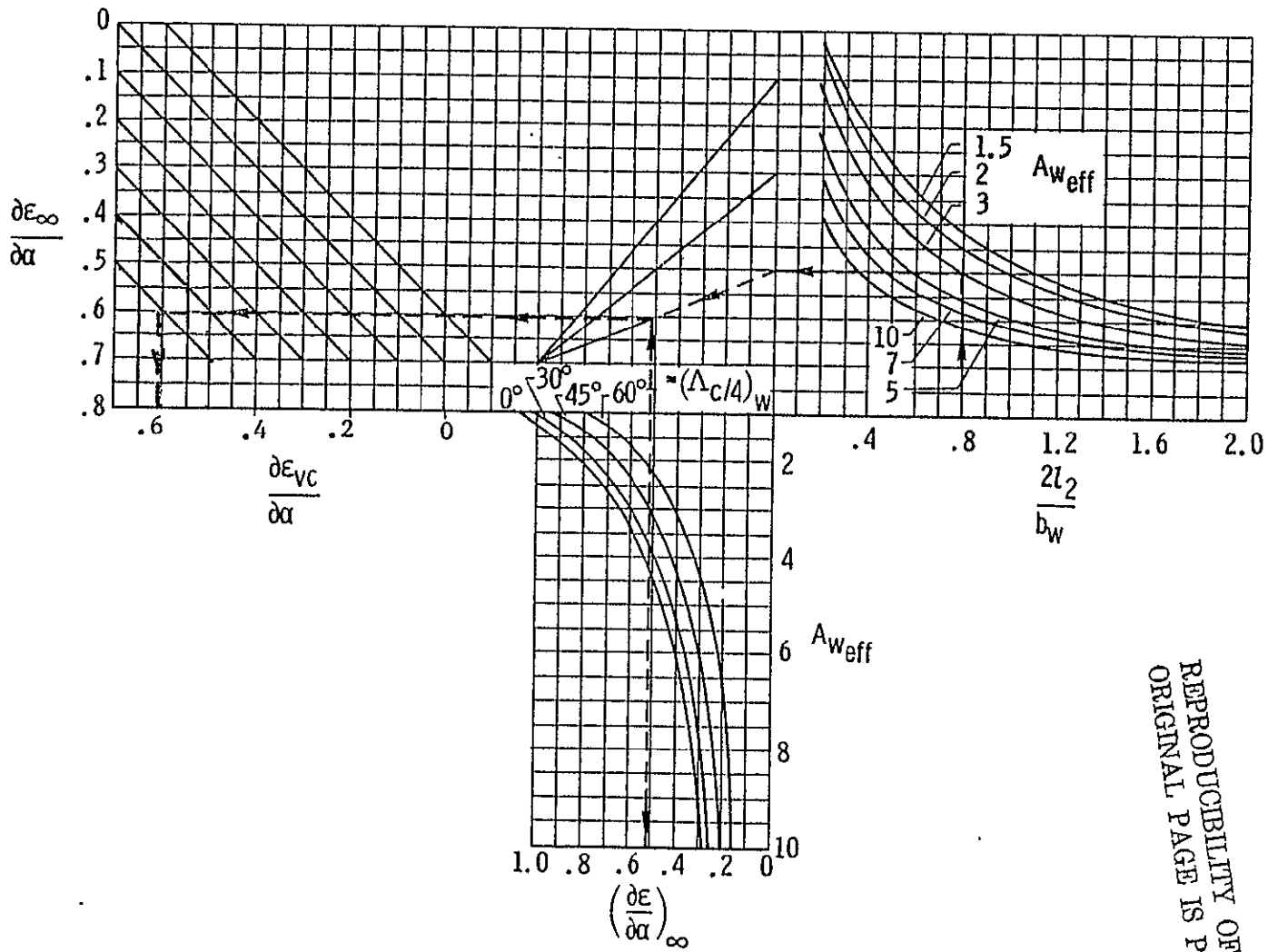

Figure 4.9.1.3: Downwash at plane of symmetry and height of vortex core for low speeds (Reference 3)

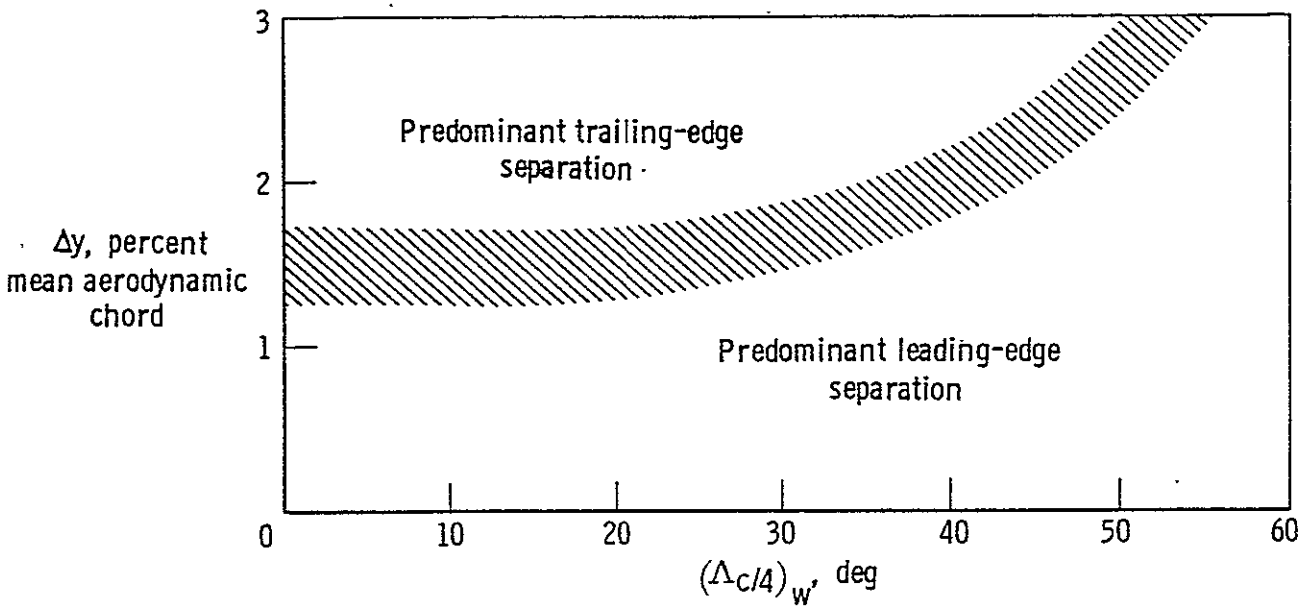

Figure 4.9.1.4: Type of flow separation as a function of airfoil and wing sweep (Reference 3)

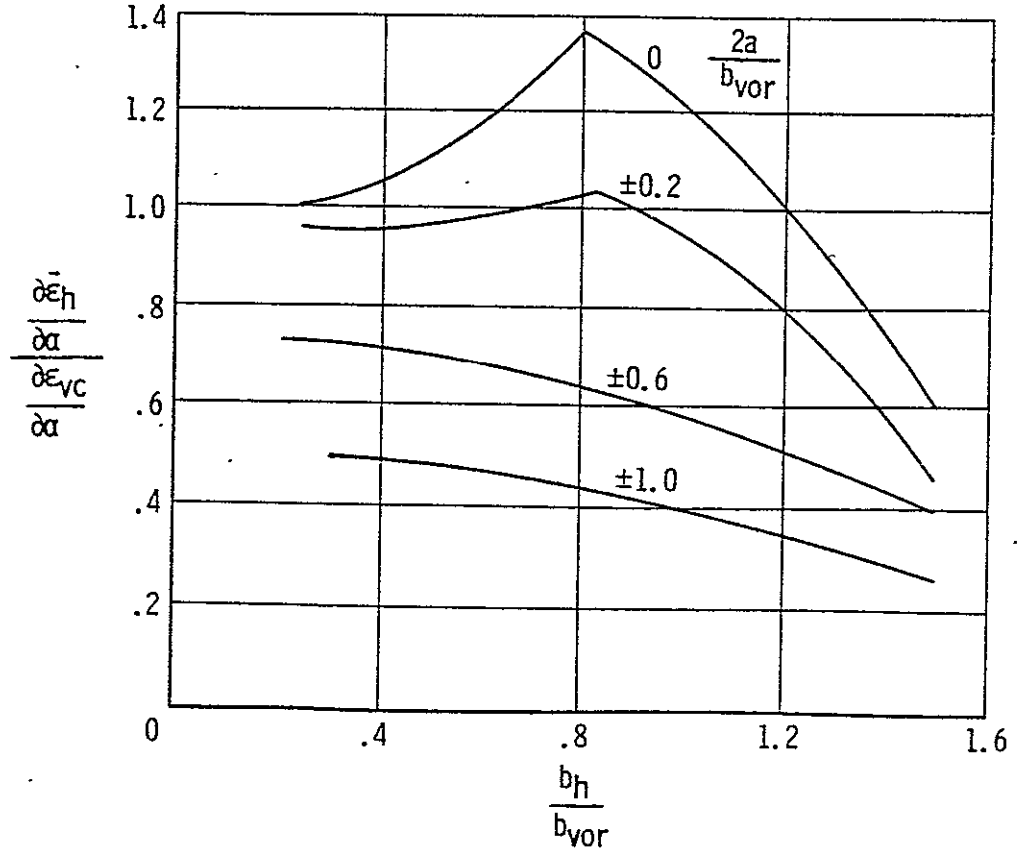

Figure 4.9.1.5: Average downwash acting on aft lifting surface for low speeds (Reference 3)

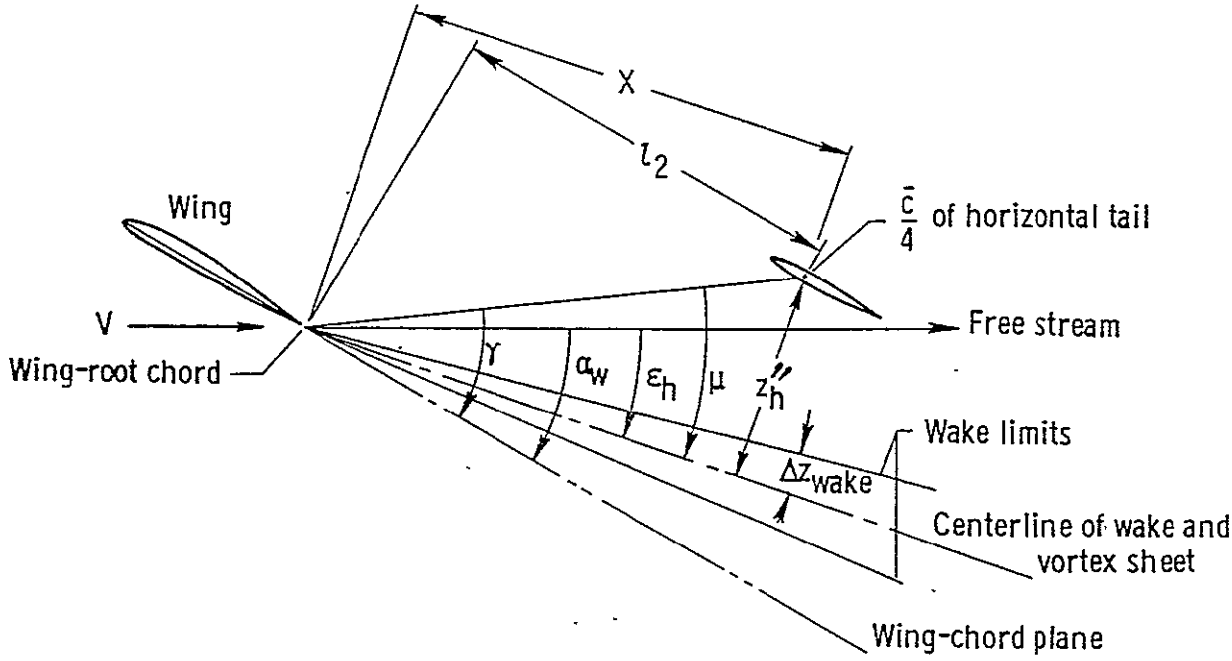

Figure 4.9.2.1: Relative positions of horizontal tail, wing wake, and wing-chord plane

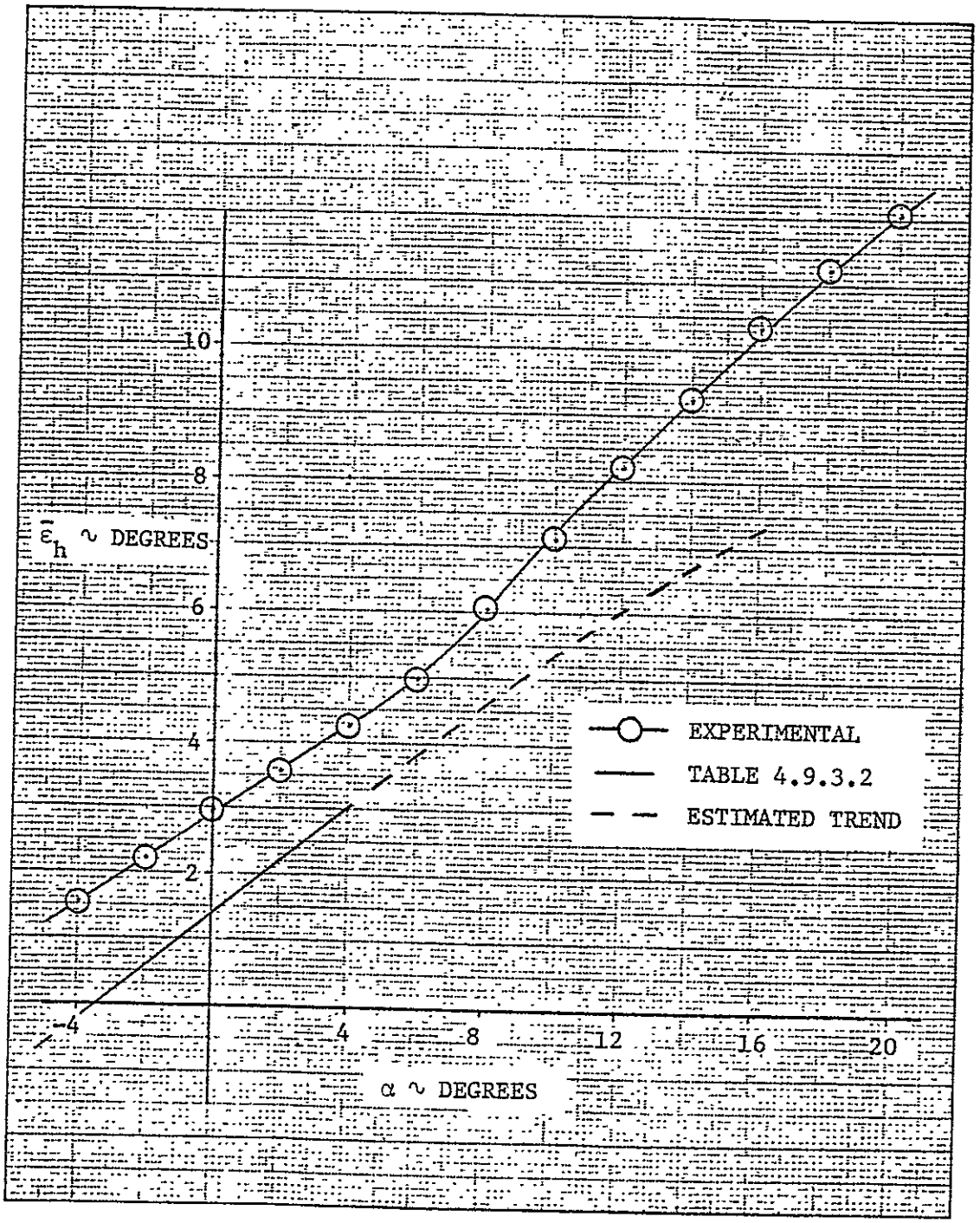

Figure 4.9.3.1: Comparison of predicted downwash at horizontal tail with full-scale wind tunnel data (propellers removed, N_{Re} = 2.3 million) .

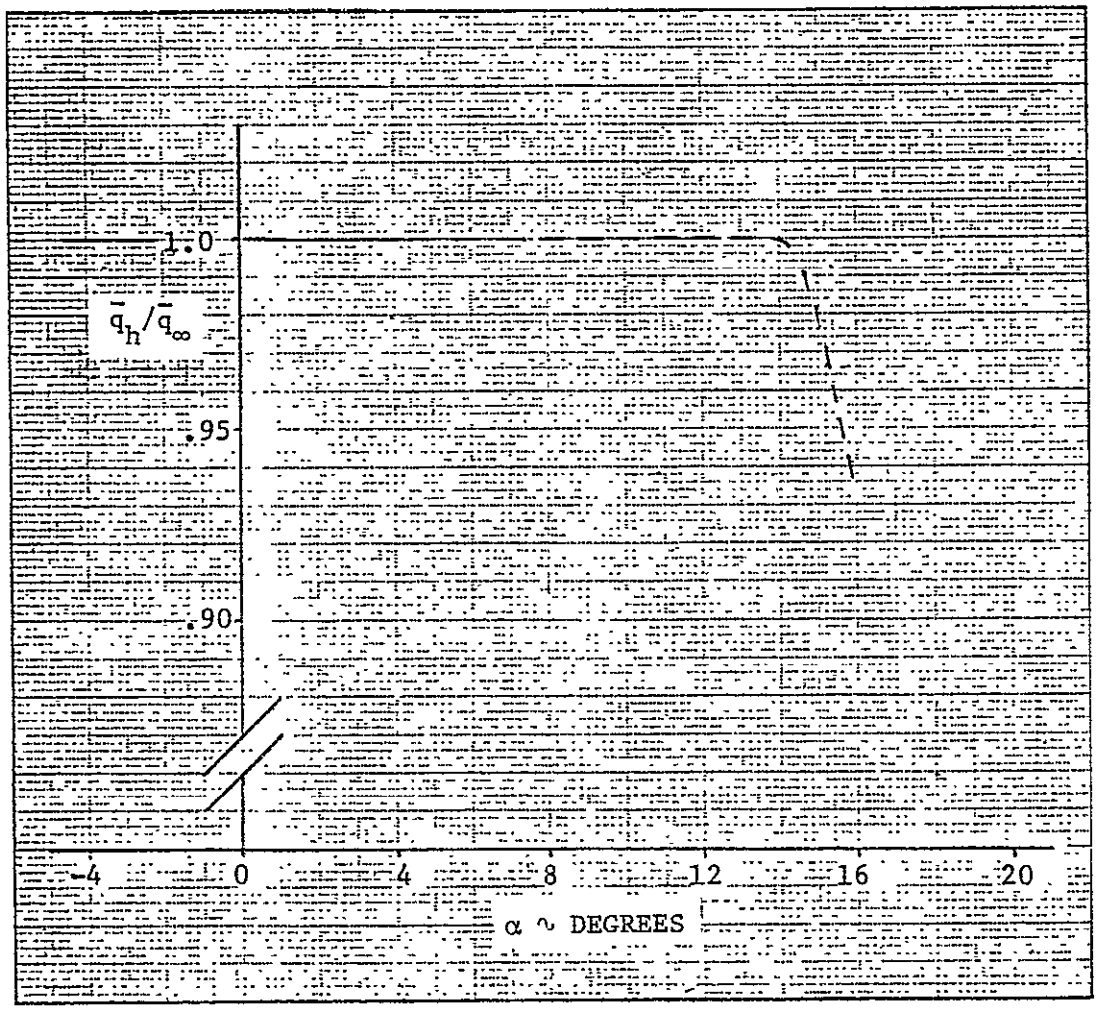

Figure 4.9.3.2: Prediction of dynamic-pressure ratio at horizontal tail (propellers removed)

4.10 Lift of the Complete Airplane

In this section the lift of the complete airplane will be discussed. Lift due to flap-and-elevator-deflection will not be included. The method discussed is similar to the method used in Reference 3.

4.10.1 Lift in the Linear Lift Range

The net lift of the complete airplane in the linear lift range may be written as follows:

$$C_L = C_{L_{wfn}} + C_{L_{h(hf)}} + (\Delta C_L)_{h(fv)} \qquad (4.10.1.1)$$

where

$C_{L_{wfn}}$ is the tail-off lift coefficient considered in Section 4.4.

$C_{L_{h(hf)}}$ is the lift contribution of the horizontal tail including tail-fuselage interactions, wing downwash and dynamic-pressure effects.

$(\Delta C_L)_{h(fv)}$ is the effect of fuselage vortices on the lift coefficient of the horizontal tail.

The lift contribution of the horizontal tail in the presence of the fuselage due to angle of attack at the tail can be estimated as follows:

$$C_{L_{h(hf)}} = (C_{L_\alpha})_{h_e} [K_{h(f)} + K_{f(h)}] \alpha_h \frac{S_{h_e}}{S_w} \frac{\bar{q}_h}{\bar{q}_\infty} \qquad (4.10.1.2)$$

where

$(C_{L_\alpha})_{h_e}$ is the lift curve slope of the exposed panels of the tail.

$K_{h(f)}$ is the ratio of the lift on the horizontal tail in the presence of the body to tail alone, obtained from Figure 4.4.1.1.

$K_{f(h)}$ is the ratio of the tail-lift carryover onto the body to tail alone, obtained from Figure 4.4.1.1

α_h is the angle of attack of the horizontal tail:

$$\alpha_h = \alpha - \bar{\varepsilon}_h + i_h \qquad (4.10.1.3)$$

where

$\bar{\varepsilon}_h$ is the average downwash acting on the horizontal tail, obtained from Section 4.9.

i_h is the incidence angle of the horizontal tail.

S_{h_e} is the exposed area of the horizontal tail.

$(\bar{q}_h/\bar{q}_\infty)$ represents the dynamic-pressure ratio at the horizontal tail, obtained from Section 4.9.

According to Reference 3, the effect of body vortices on the lift of the horizontal tail can be considered negligible when the horizontal tail span is greater than three times the body diameter at the tail ($b_h > 3(d_f)_h$). This ratio is exceeded by almost all general aviation aircraft.

4.10.2 Maximum Lift of the Complete Airplane

The maximum lift coefficient of the horizontal tail in the presence of the fuselage, $(C_{L_{max}})_{h(hf)}$, and the corresponding angle of attack, $(\alpha_{C_{L_{max}}})_{h(hf)}$, are determined by the methods used in Section 4.4 to obtain the maximum lift characteristics of the wing in presence of the fuselage. The method uses an empirical taper ratio correction

factor, c_2, which can be obtained from Figure 4.4.2.1 and may be used up to M = 0.6:

$$(C_{L_{max}})_{h(hf)} = \left[\frac{(C_{L_{max}})_{h(hf)}}{(C_{L_{max}})_h} \right] (C_{L_{max}})_h \left(\frac{S_h}{S_w}\right) \quad (4.10.2.1)$$

$$(\alpha_{C_{L_{max}}})_{h(hf)} = \left[\frac{(\alpha_{C_{L_{max}}})_{h(hf)}}{(\alpha_{C_{L_{max}}})_h} \right] (\alpha_{C_{L_{max}}})_h \quad (4.10.2.2)$$

where

$(C_{L_{max}})_h$ is the maximum lift coefficient of the horizontal tail based on the horizontal tail area, obtained from Section 4.2.

$(\alpha_{C_{L_{max}}})_h$ is the horizontal tail stall angle relative to the chord, obtained from Section 4.2.

$(C_{L_{max}})_{h(hf)}/(C_{L_{max}})_h$ and $(\alpha_{C_{L_{max}}})_{h(hf)}/(\alpha_{C_{L_{max}}})_h$ are empirical correction factors obtained from Figure 4.4.2.3 and 4.4.2.2, respectively, as a function of $(c_2 + 1)A_h \tan(\Lambda_{\ell e})_h$ and $(d_f)_h/b_h$.

4.10.3 Lift Characteristics of the ATLIT Airplane

In Table 4.10.3.1 the summary calculations for the tail-lift in the linear lift range are presented. A summary of the calculations of the maximum tail-lift is listed in Table 4.10.3.2, while in Table 4.10.3.3 the total lift predictions of the ATLIT are shown. The resulting lift curve is shown in Figure 4.10.3.1 and compared with the experimental results of Reference 2. In this figure also, lift curve obtained with Reference 5 is shown.

In the linear lift range the slope of the hand-calculated lift curve shows good agreement with the slope of the experimental lift-curve.

The angle of attack at zero-lift prediction, however, is more than one degree off.

The lift curve obtained with Reference 5 shows fair agreement with the full-scale wind tunnel data, while no results were obtained with the computer program of Reference 6.

In Figure 4.10.3.2 the effect of the engine cooling system on the lift coefficient is shown. In this report no attempt will be made to predict this effect because of uncertainties in the determination.

Table 4.10.3.1: Lift of horizontal tail in linear lift range in presence of fuselage

Symbol	Description	Reference	Magnitude
α_h^*	Limit of linearity of horizontal tail lift curve, relative to tail chord, deg.	Table 4.2.4.1	12.2
$(d_f)_h$	Fuselage width at horizontal tail, m(ft)	Figure 2.1.2	0.405 (1.33)
b_h	Horizontal tail span, m(ft)	Table 2.1.1	4.133 (13.56)
$(d_f)_h/b_h$	—	—	0.098
$K_{h(f)}$	Ratio of lift on tail in presence of fuselage to tail alone	Figure 4.4.1.1	1.082
$K_{f(h)}$	Ratio of tail-lift carryover on fuselage to tail alone	Figure 4.4.1.1	0.130
$(C_{L_\alpha})_{h_e}$	Lift-curve slope of exposed horizontal tail panels, deg^{-1}	Table 4.2.4.1	0.0649
S_{h_e}	Area of exposed horizontal tail panels, $m^2(ft^2)$	Table 2.1.1	3.24 (34.9)
S_w	Reference wing area, $m^2(ft^2)$	Table 2.1.1	14.40 (155.0)
i_h	Horizontal tail incidence angle, deg.	—	0
$\bar{q}_h/\bar{q}_\infty$	Dynamic-pressure ratio at the horizontal tail	Figure 4.10.3.2	1.0
Summary: $C_{L_{h(hf)}} = 0.0177\ (\alpha - \bar{\epsilon}_h)$ based on S_w and up to $\alpha_h^* = 12.2$ degrees			

Table 4.10.3.2: Maximum lift characteristics of horizontal tail in presence of the fuselage

Symbol	Description	Reference	Magnitude
$(\Lambda_{le})_h$	Horizontal tail leading-edge sweep angle, deg.	Table 2.1.1	0.
A_h	Horizontal tail aspect ratio	Table 2.1.1	4.75
λ_h	Horizontal tail taper ratio	Table 2.1.1	1
$(d_f)_h/b_h$	Ratio of body width to tail span at tail	Table 4.10.1	0.098
$(C_{L_{max}})_h$	Horizontal tail maximum lift coefficient, based on S_h	Table 4.2.4.1	1.215
$(\alpha_{C_{L_{max}}})_h$	Horizontal tail stall angle, deg.	Table 4.2.4.1	18.75
c_2	Taper ratio correction factor	Figure 4.4.2.1	0.0852
$(c_2+1)A_h\tan(\Lambda_{le})_h$	—	—	0
$\left[\frac{(C_{L_{max}})_{h(hf)}}{(C_{L_{max}})_h}\right]$	—	Figure 4.4.2.3	1.0
$\left[\frac{(\alpha_{C_{L_{max}}})_{h(hf)}}{(\alpha_{C_{L_{max}}})_h}\right]$	—	Figure 4.4.2.2	1.030
S_h	Horizontal tail area, $m^2(ft^2)$	Table 2.1.1	3.60 (38.7)
S_w	Reference wing area, $m^2(ft^2)$	Table 2.1.1	14.40 (155.0)
$(C_{L_{max}})_{h(hf)}$	Maximum lift coefficient of the horizontal tail in the presence of the fuselage based on S_w	Eq. (4.10.2.1)	0.303
$(\alpha_{C_{L_{max}}})_{h(hf)}$	Angle of attack for zero horizontal tail lift, with respect to chord of horizontal tail, deg.	Eq. (4.10.2.2)	19.3

Table 4.10.3.3: Lift of the ATLIT airplane (no flap and stabilizer deflection)

α, deg.	$\bar{\varepsilon}_h$, deg. Table 4.9.3.2	α_h, deg. Eq. (4.10.1.3)	$C_{L_{h(hf)}}$ Table 4.10.3.1	$C_{L_{wfn}}$ Table 4.4.3.3	C_L Eq. (4.10.1.1)
-4	-0.26	-3.74	-0.0662	-0.0780	-0.1442
-2	0.56	-2.56	-0.0453	0.1141	0.0688
0	1.38	-1.38	-0.0244	0.3066	0.2822
2	2.19	-0.19	-0.0034	0.4997	0.4963
4	2.99	1.01	0.0179	0.6932	0.7111
15.9	7.24	8.66	0.1533	1.5731	1.7264

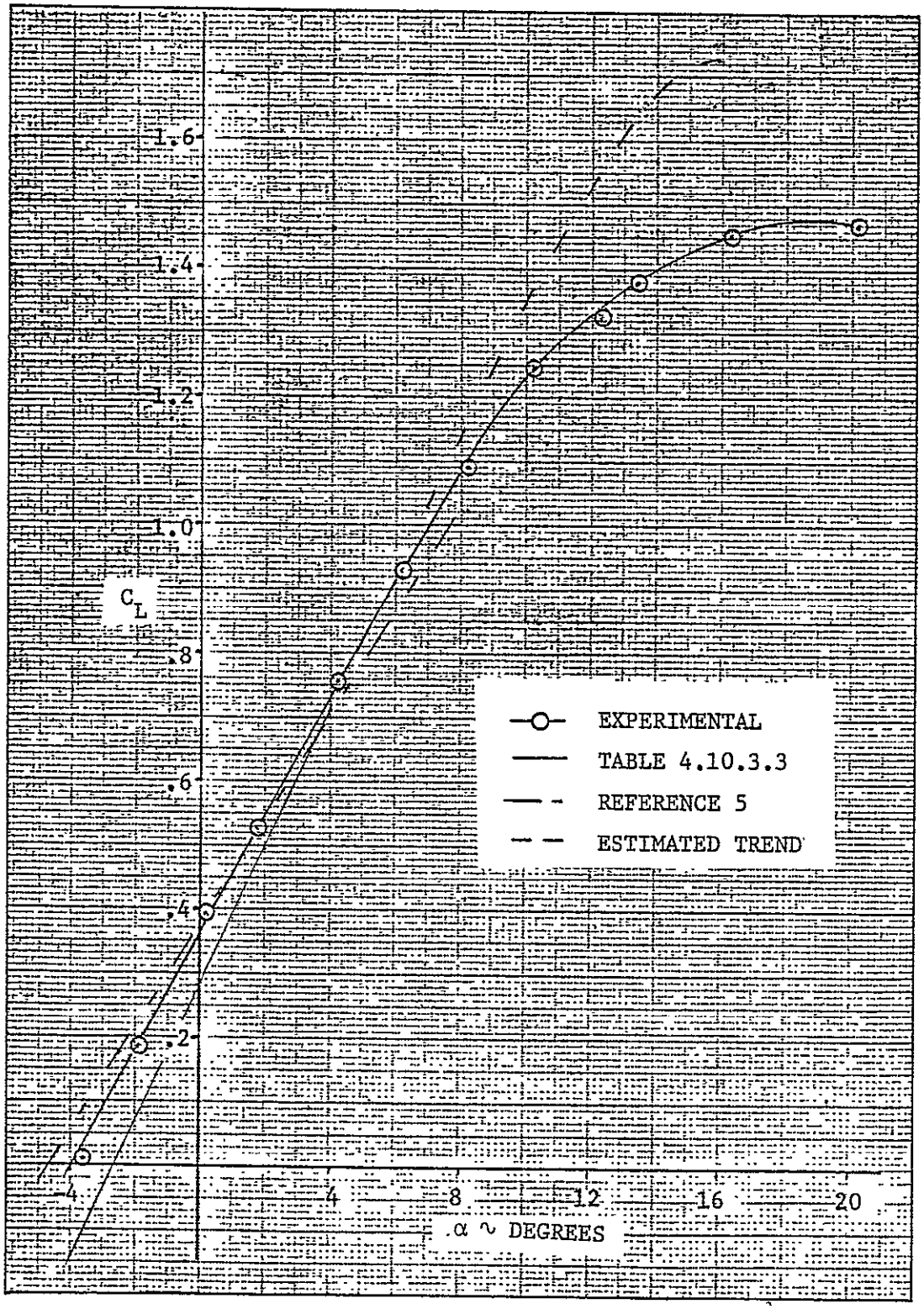

Figure 4.10.3.1: Comparison of predicted airplane lift curve with wind tunnel data (propellers removed, N_{Re} = 2.3 million)

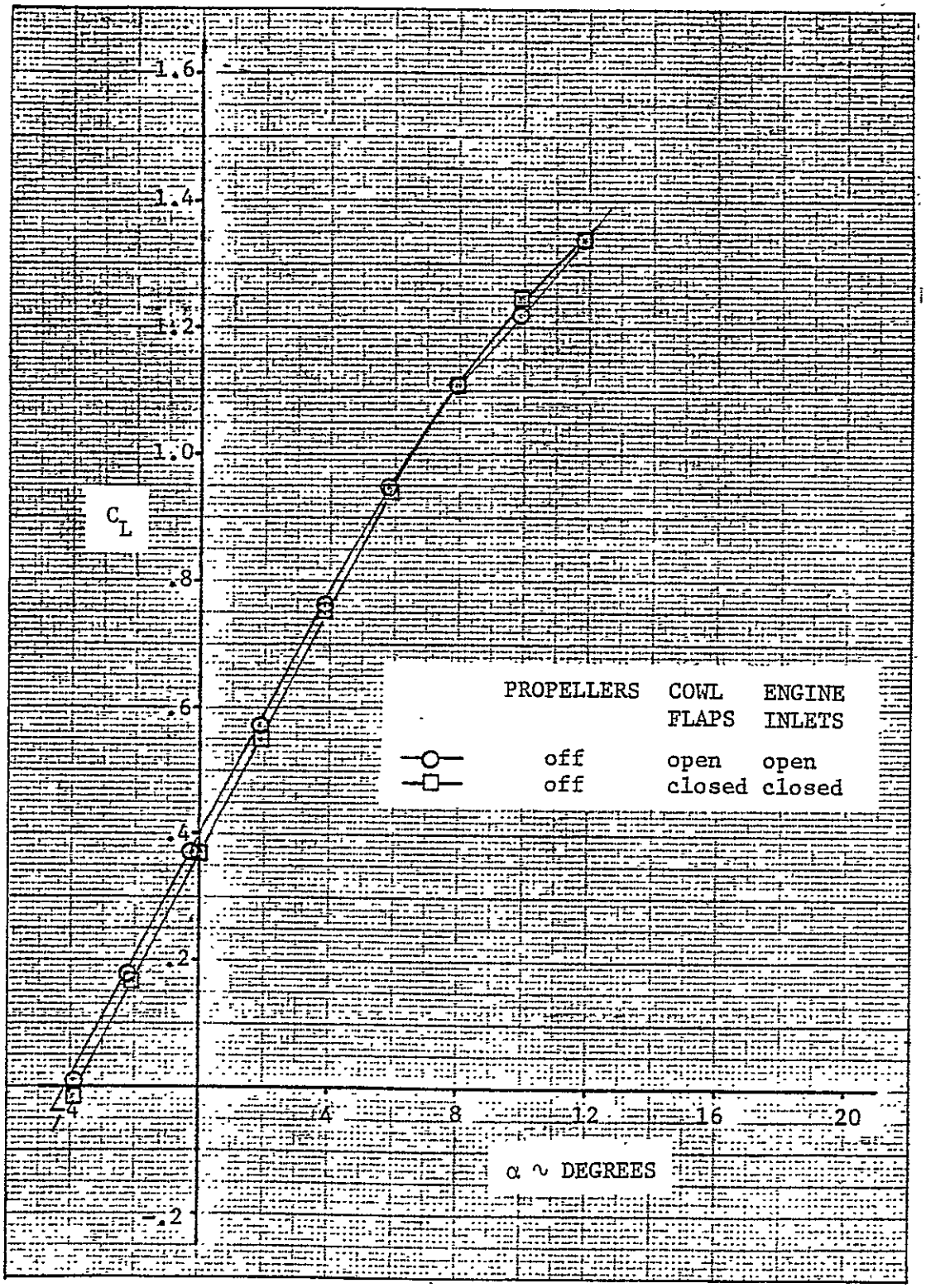

Figure 4.10.3.2: Effect of engine cooling on airplane lift coefficient (N_{Re} = 3.5 million)

4.11 Pitching Moment of the Complete Airplane

The pitching moment of the complete airplane may be estimated as follows:

$$C_m = C_{m_{wfn}} + C_{m_{h(hf)}} \tag{4.11.1}$$

where

$C_{m_{wfn}}$ is the tail-off pitching moment coefficient considered in Section 4.8.

$C_{m_{h(hf)}}$ is the contribution of the horizontal tail, including tail-fuselage interference effects, to the pitching moment coefficient of the airplane. The pitching moment due to the horizontal tail is determined from:

$$C_{m_{h(hf)}} = \left(\frac{x_{cg}}{\bar{c}_w} - \frac{x_h}{\bar{c}_w}\right) C_{L_{h(hf)}} \tag{4.11.2}$$

where

x_{cg} is the distance, parallel to the X-body axis, from the leading edge of the wing mean aerodynamic chord to the airplane center of gravity (positive aft)

x_h is the distance, parallel to the X-body axis, from the leading edge of the wing mean aerodynamic chord to the quarter chord of the horizontal tail mean aerodynamic chord (positive aft)

$C_{L_{h(hf)}}$ is the lift of the horizontal tail in the presence of the fuselage, obtained from Section 4.10

Summary calculations for the pitching moment of the ATLIT airplane relative to the quarter chord of the wing mean aerodynamic chord are presented in Tables 4.11.1 and 4.11.2. The resulting pitching moment curves are shown in Figure 4.11.2 and 4.11.3 as function of the angle of attack and the total lift coefficient, respectively.

The results from Table 4.11.2 show good agreement with the experimental results of Reference 2.

In Figures 4.11.4 and 4.11.5 the pitching moment contribution due to the engine cooling system is shown. These curves are obtained from Reference 2, and they demonstrate that the contribution of the cooling system to the pitching moment is not negligible. An analytical treatment of lift (pitching moment) due to the cooling system is beyond the scope of this report because of uncertainties in the determination.

Table 4.11.1: Pitching moment contribution of the horizontal tail (stabilizer not deflected)

Symbol	Description	Reference	Magnitude
$x_{cg}/\bar{c}_w$	Airplane center of gravity location from leading edge of wing mean aerodynamic chord	-	0.25
x_h	Distance from wing mean aerodynamic chord leading edge to $\bar{c}/4$ of horizontal tail, m (ft)	Figure 4.11.1	5.127 (16.82)
$\bar{c}_w$	Wing mean aerodynamic (geometric) chord, m (ft)	Table 2.1.1	1.225 (4.018)
$x_h/\bar{c}_w$	-	-	4.186
$C_{L_{h(hf)}}$	Lift coefficient of horizontal tail on basis of S_w	Table 4.10.3.1	Variable
$C_{m_{h(hf)}}$	Pitching moment coefficient of total airplane	Eq.(4.11.2)	$-3.936\ C_{L_{h(hf)}}$

Table 4.11.2: Pitching moment of complete airplane

α, deg	C_L Table 4.10.3.3	$C_{L_{h(hf)}}$ Table 4.10.3.1	$C_{m_{h(hf)}}$ Eq.(4.11.2)	$C_{m_{wfn}}$ Table 4.8.4.1	C_m Eq.(4.11.1)
-4	-0.1442	-0.0662	0.2606	-0.1256	0.1350
-2	0.0688	-0.0453	0.1783	-0.0806	0.0977
0	0.2822	-0.0244	0.0960	-0.0365	0.0595
2	0.4963	-0.0034	0.0134	0.0067	0.0201
4	0.7111	0.0179	-0.0705	0.0490	-0.0215
15.9	1.7264	0.1533	-0.6034	0.1674	-0.4360

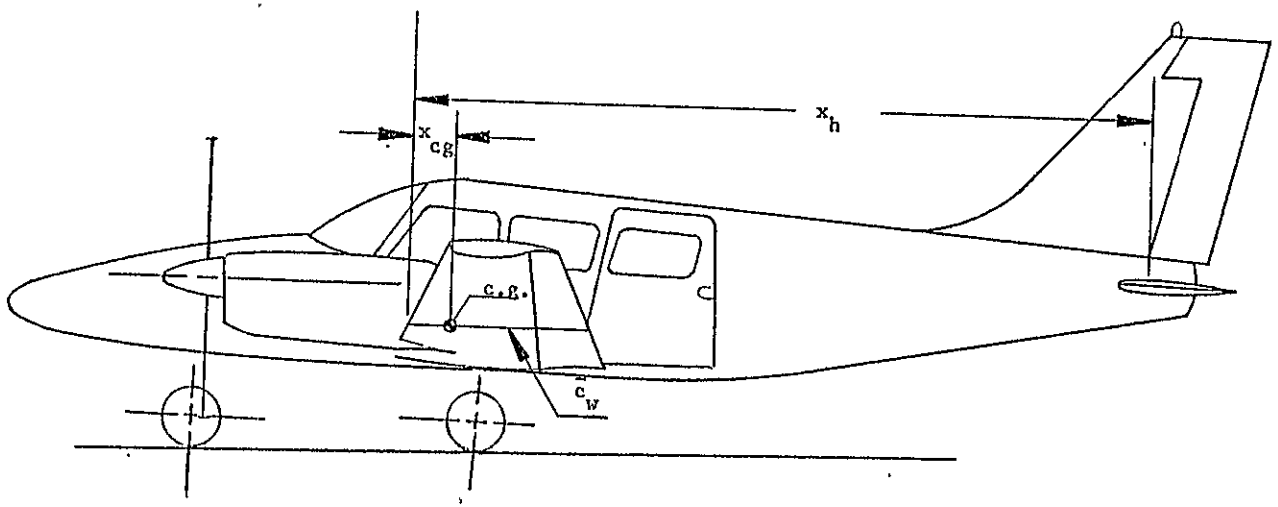

Figure 4.11.1: Side view drawing of the ATLIT airplane

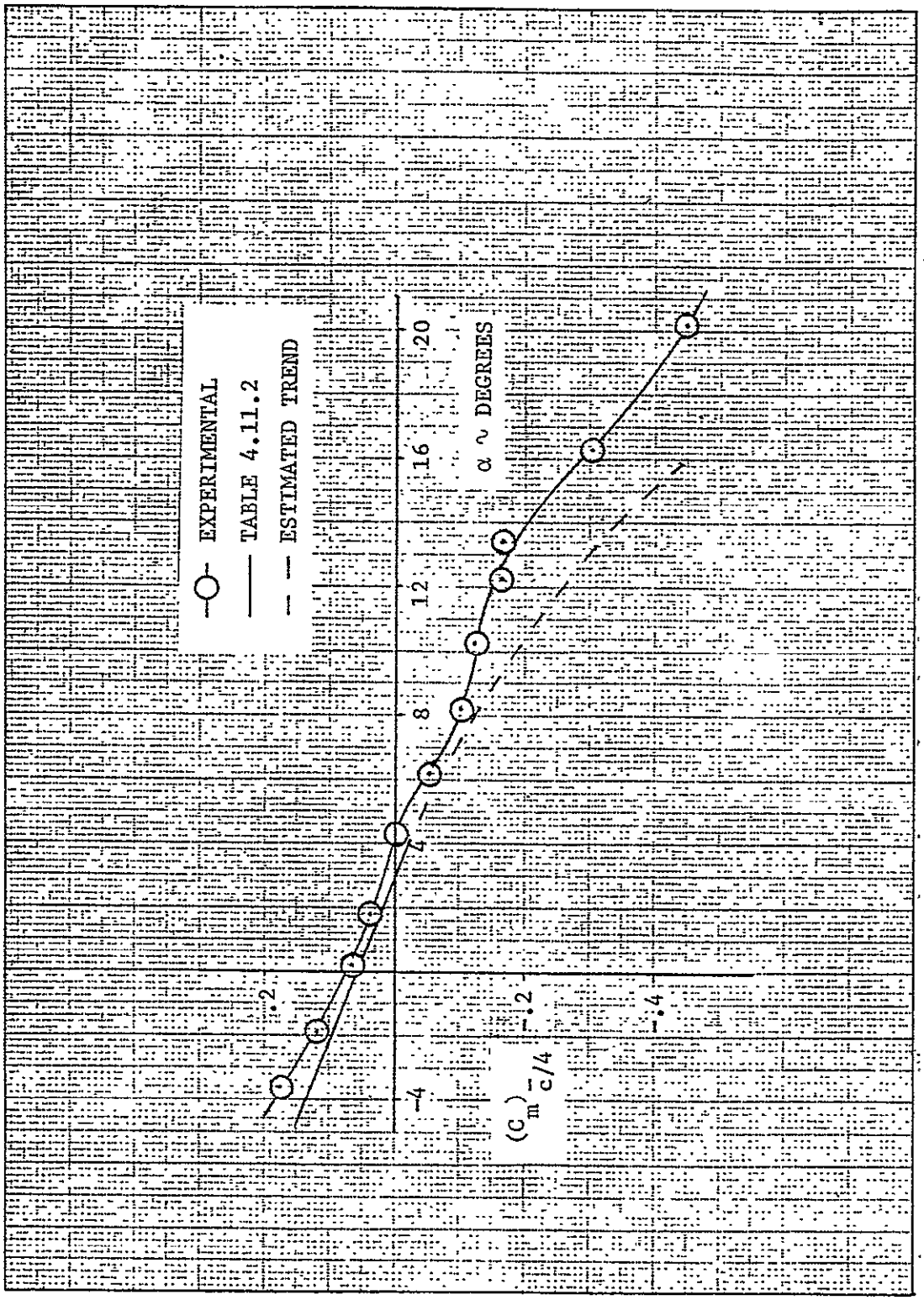

Figure 4.11.2: Comparison of predicted airplane pitching moment with full-scale wind tunnel data (propellers removed, stabilizer not deflected, N_{Re} = 2.3 million)

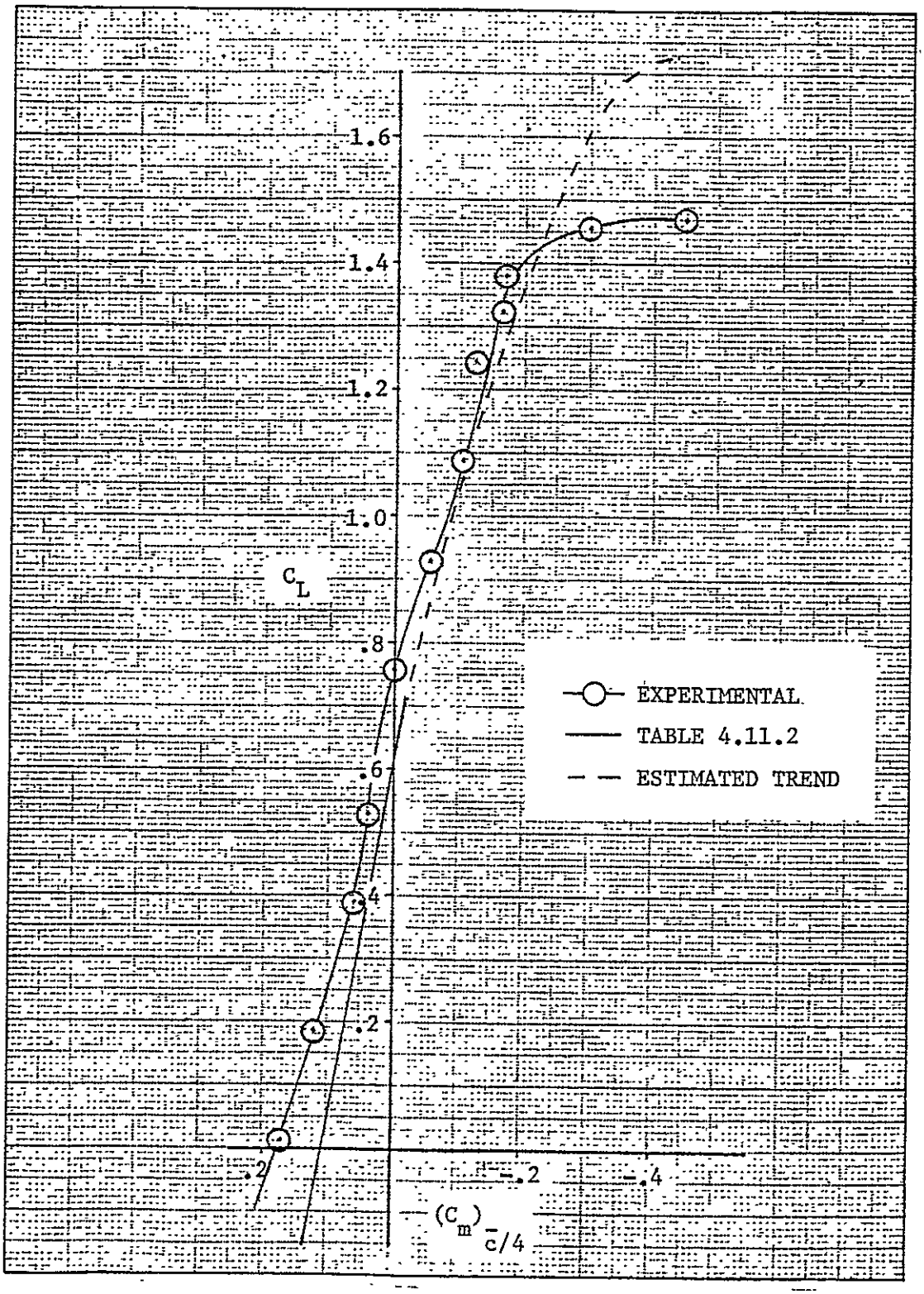

Figure 4.11.3: Comparison of predicted airplane pitching moment with full-scale wind tunnel data (propellers removed, stabilizer not deflected, N_{Re} = 2.3 million)

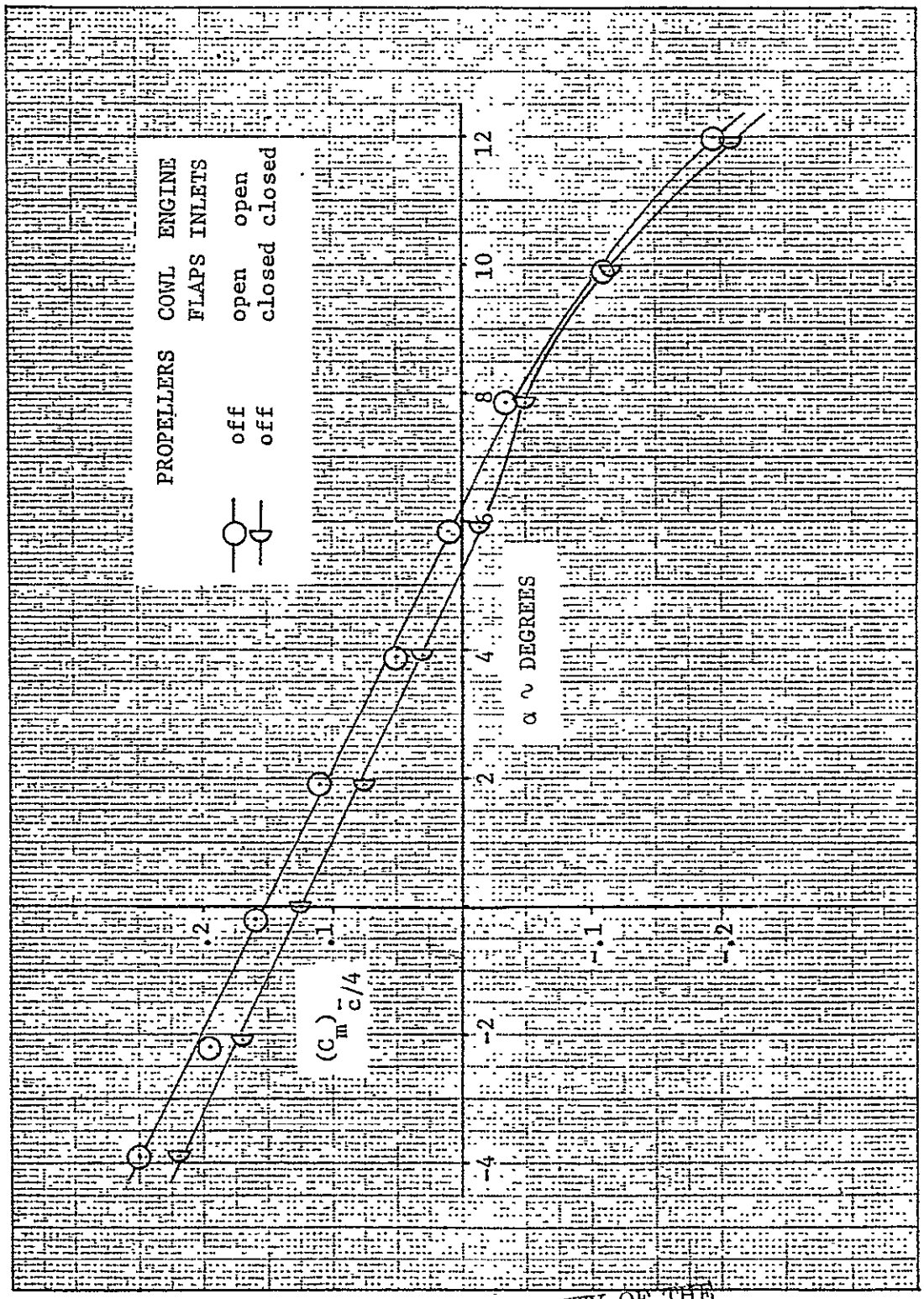

Figure 4.11.4: Effect of engine cooling system on airplane pitching moment (N_{Re} = 3.5 million)

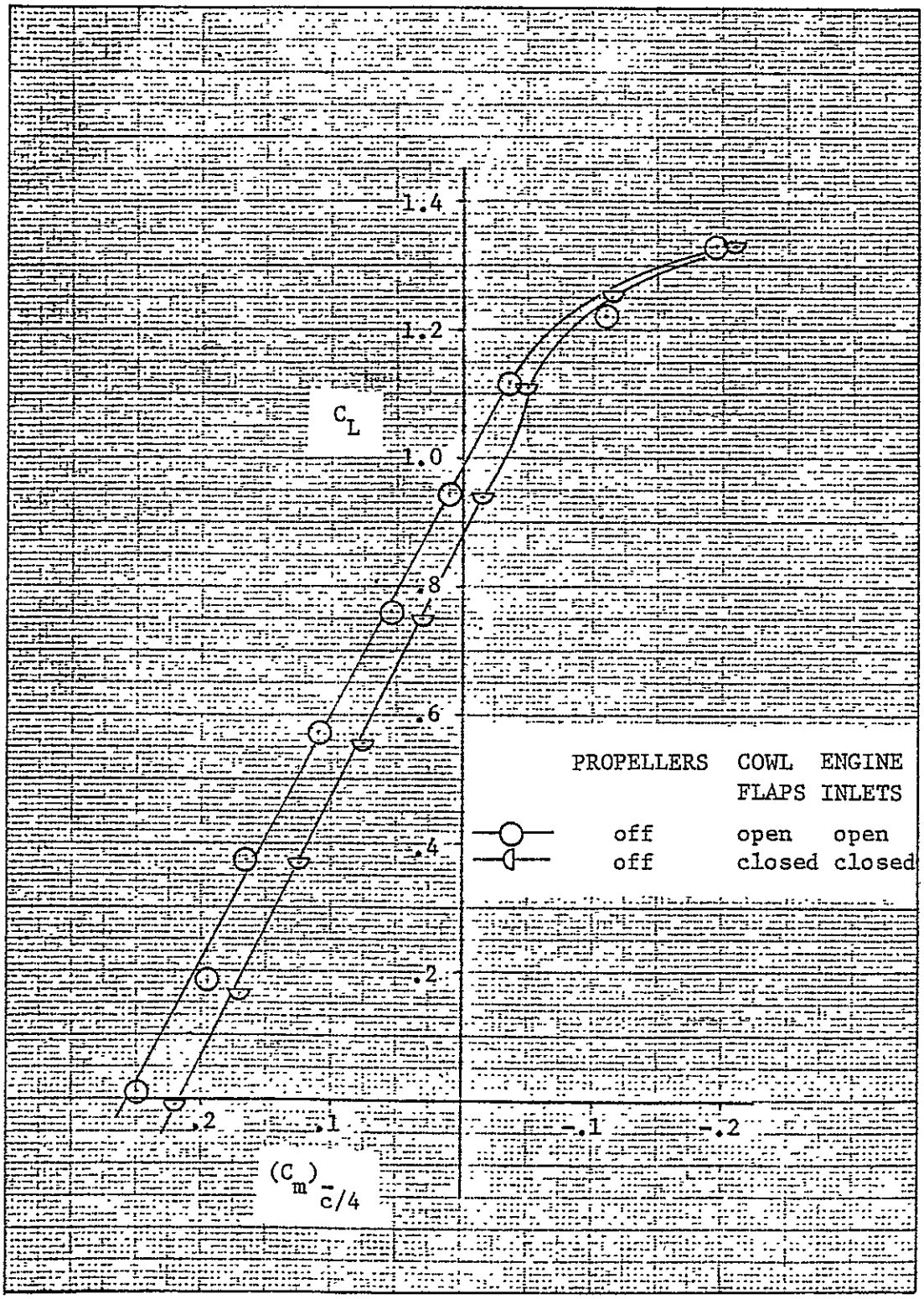

Figure 4.11.5: Effect of engine cooling on airplane pitching moments (N_{Re} = 3.5 million)

4.12 Drag of the Complete Airplane

The drag of an airplane can be split up into the following components:

(1) Zero-lift drag of the wing, horizontal tail and vertical tail

(2) Zero-lift drag of the fuselage and nacelles

(3) Zero-lift interference drag of the wing-fuselage, tail-fuselage, vertical tail-horizontal tail and wing-nacelle

(4) Lift induced drag of the wing and horizontal tail

(5) Lift induced drag of the fuselage and nacelles

(6) Lift induced wing-fuselage and wing-nacelle interference drag

(7) Cooling drag due to nacelle inlets and cooling flaps.

4.12.1 Zero-Lift Drag of Wing, Horizontal Tail and Vertical Tail

The zero-lift drag of a lifting surface is composed of skin-friction drag and pressure drag. The pressure drag is caused by the boundary layer which prevents complete pressure recovery at the trailing edge of the lifting surface. The skin friction drag is a function of the roughness of the surface of the lifting surface and the type of boundary layer flow. In the case of general aviation aircraft the boundary layer may be considered to be turbulent.

The following expression is used in Reference 3 to predict the zero-lift drag of a lifting surface based on the reference wing area, S_w:

$$(C_{D_o})_{\ell s} = 2\, C_f \left[1 + 2\left(\frac{t}{c}\right) + 120\left(\frac{t}{c}\right)^4\right] \frac{S_{\ell s_e}}{S_w} \qquad (4.12.1.1)$$

where

C_f is the skin-friction coefficient of a flat plate, obtained from Figure 4.12.1.1 as a function of Reynolds number, N_{Re}, and the parameter ℓ/k

ℓ is the reference length of the lifting surface, in this case the mean aerodynamic chord of the exposed area of the lifting surface

k is the surface roughness height, estimated from Table 4.12.1.1 on the basis of surface finish

t/c is the thickness ratio of the lifting surface

$S_{\ell s_e}$ represents the exposed area of the lifting surface

The summary calculations of the zero-lift drag of wing, horizontal tail and vertical tail are listed in Table 4.12.1.2, and the final results based on the wing area are:

$$\begin{aligned} &\text{wing } (C_{D_o})_w && = 0.00970 \\ &\text{horizontal tail } (C_{D_o})_h && = 0.00221 \\ &\text{vertical tail } (C_{D_o})_v && = 0.00111 \end{aligned} \qquad (4.12.1.2)$$

4.12.2 Zero-Lift Drag of Fuselage and Nacelles

The zero-lift drag of an isolated body is composed of skin-friction drag, pressure drag and base drag. Equation (4.12.2.1), which estimates the zero-lift drag of an isolated body, is only valid for axixymmetric bodies of revolution. Therefore the fuselage and nacelles have to be treated as equivalent bodies of revolution having an axially distributed circumferential area similar to that of the actual body. For subsonic conditions ($M \leq 0.6$) and on the basis of the reference wing area, S_w, the zero-lift drag coefficient of an isolated body is:

C-3

$$(C_{D_o})_B = C_{D_f} + C_{D_b}$$

$$(C_{D_o})_B = C_f \left[1 + \frac{60}{(\ell_B/d_B)^3} + \frac{\ell_B/d_B}{400} \right] \frac{S_{wet}}{S_w} + C_{D_b} \qquad (4.12.2.1)$$

where

C_f is the skin friction coefficient of a flat plate, obtained from Figure 4.12.1.1 as a function of Reynolds number, N_{Re}, based on the actual body length, ℓ_B, and the parameter ℓ_B/k

ℓ_B is the actual body length

k is the surface roughness height, obtained from Table 4.12.1.1

d_B is the diameter of a circle having the same circumference as the circumference of the maximum frontal area

S_{wet} is the net wetted surface area of the body and can be estimated from Figure 4.12.2.1 as a function of the body fineness ratio, ℓ_B/d_B, and the parameter, d_b/d_B

d_b is the diameter of the equivalent circular circumference of the base area of the body

S_B is the maximum frontal area of an axisymmetric body having a diameter, d_B, or:

$$S_B = \frac{\pi}{4} d_B^2 \qquad (4.12.2.2)$$

C_{D_b} is the base drag coefficient which can be written as follows (based on S_w):

$$C_{D_b} = 0.029 \left(\frac{d_b}{d_B} \right)^3 \sqrt{C_{D_f} \frac{S_B}{S_w}} \qquad (4.12.2.3)$$

In Table 4.12.2.1 the calculations to obtain the zero-lift drag of the fuselage and nacelles are summarized. The net wetted area of the fuselage and nacelles are summarized and the results based on the refer-

ence wing area, S_w, are:

$$\text{fuselage } (C_{D_o})_f = 0.00616$$
$$\text{nacelle } (C_{D_o})_n = 0.00614 \tag{4.12.2.4}$$

4.12.3 Zero-Lift Interference Drag of Wing-Fuselage, Tail-Fuselage, Vertical Tail-Horizontal Tail and Wing-Nacelle

The correlation factor, R_{wf}, will be used to predict the wing-fuselage zero-lift drag coefficient. The zero-lift drag of the fuselage in the presence of the wing relative to the reference wing area, may be written as follows:

$$(C_{D_o})_{f(w)} = (C_{D_f})_f R_{wf} + C_{D_b} \tag{4.12.3.1}$$

where

$(C_{D_f})_f$ is the skin friction and pressure drag coefficient of the fuselage obtained from Section 4.12.2

R_{wf} is the ratio of the wing-fuselage to the fuselage alone zero-lift drag with the base drag omitted obtained from Figure 4.12.3.1

The net zero-lift wing-fuselage coefficient based on the reference wing area is:

$$(\overline{C_{D_o}})_{wf} = (C_{D_o})_w + (C_{D_o})_{f(w)} \tag{4.12.3.2}$$

where

$(C_{D_o})_w$ is the zero-lift wing drag obtained from Section 4.12.1

For the ATLIT airplane the calculations are summarized in Table 4.12.3.1, and the result is:

$$(\overline{C_{D_o}})_{wf} = 0.01632 \tag{4.12.3.3}$$

On the basis of the reference wing area, S_w, the increment of tail drag due to fuselage drag is approximately:

$$(\Delta C_{D_o})_{t(f)} = n_1 \left[0.8 \left(\frac{t}{c}\right)^3 - 0.0005 \right] \frac{c_{r_e}^2}{S_w} \qquad (4.12.3.4)$$

where

n_1 is the number of junctures of the tail surface with the fuselage

c_{r_e} is the root chord of the exposed panels

t/c is the thickness ratio of the root chord of the exposed surface

When the vertical tail intersects with the horizontal tail instead of the fuselage, the interference drag on the basis of the reference wing area, S_w, is:

$$(\Delta C_{D_o})_{v(h)} = \frac{n_2}{2} \left[17 \left(\frac{t}{c}\right)^4_{int} - 0.05 \left(\frac{t}{c}\right)^2_{int} \right] \frac{c_{int}^2}{S_w} \qquad (4.12.3.5)$$

where

n_2 is the number of corners at the intersection (normally $n_2 = 4$)

$(t/c)_{int}$ is the average thickness ratio of the intersecting surfaces at the intersection

c_{int} is the chord at the intersection

For the ATLIT, the horizontal and vertical tail intersect with the fuselage. In Table 4.12.3.2 the calculations are summarized and the net zero-lift fuselage-horizontal tail drag based on the reference wing area is:

$$(\overline{C_{D_o}})_h = (C_{D_o})_h + (\Delta C_{D_o})_{h(f)}$$

$$(\overline{C_{D_o}})_h = 0.00224 \qquad (4.12.3.6)$$

while the net zero-lift fuselage-vertical tail drag based on the reference wing area is:

$$(\overline{C_{D_o}})_v = (C_{D_o})_v + (\Delta C_{D_o})_{v(f)}$$

$$(\overline{C_{D_o}})_v = 0.00112 \qquad (4.12.3.7)$$

where

$(C_{D_o})_h$ represents the zero-lift drag coefficient of the horizontal tail, obtained from Section 4.12.1

$(C_{D_o})_v$ is the zero-lift drag coefficient of the vertical tail from Section 4.12.1

According to Reference 3 the interference drag of a nacelle faired into the wing may be roughly accounted for by the increment of zero-lift wing drag due to wing area covered by the nacelle, or for one nacelle:

$$(\Delta C_{D_o})_{n(w)} = (C_{D_o})_w \frac{(\Delta S_w)_n}{S_w} \qquad (4.12.3.8)$$

where

$(\Delta S_w)_n$ is the wing area overlapped by one nacelle

The summary calculations of Table 4.12.3.3 show the net zero-lift drag of the two nacelles on the basis of the reference wing area, S_w:

$$(\overline{C_{D_o}})_{n(w)} = 2\left\{(C_{D_o})_n + (\Delta C_{D_o})_{n(w)}\right\}$$
$$(\overline{C_{D_o}})_{n(w)} = 0.01384 \qquad (4.12.3.9)$$

where

$(C_{D_o})_n$ is the zero-lift drag of one nacelle, obtained from Section 4.12.2

4.12.4 Lift Induced Drag of Wing and Horizontal Tail

In Reference 3 the drag of twisted wings due to lift has not been discussed. The method for straight-tapered wings of Reference 4 will be used.

The drag due to lift of a twisted, swept-back straight wing (and horizontal tail) is given by:

$$(C_{D_i})_w = \frac{C_{L_w}^2}{\pi A e} + C_{L_w}\ \theta\ c_{\ell_\alpha}\ v + (\theta\ c_{\ell_\alpha})^2\ w \qquad (4.12.4.1)$$

where

C_{L_w} is the wing lift coefficient obtained from Section 4.2

c_{ℓ_α} is the airfoil section lift-curve slope from Section 4.1

θ is the wing twist (negative for washout)

v is the induced drag factor due to linear twist obtained from Figures 4.12.4.1

w is the zero-lift drag factor due to linear twist obtained from Figures 4.12.4.2

e is the span-efficiency factor determined by:

$$e = \frac{1.1\ (C_{L_\alpha})_w}{R\ (C_{L_\alpha})_w + (1 - R)\ \pi A} \qquad (4.12.4.2)$$

where

$(C_{L_\alpha})_w$ is the wing-lift curve slope in radians, obtained from Section 4.2

R is the leading-edge-suction parameter defined as the ratio of leading-edge suction actually obtained to that theoretically possible. The parameter is presented in Figure 4.12.4.3 as a function of Mach number, wing aspect ratio, wing sweepback and leading-edge-radius Reynolds number, $(N_{Re})_{LER}$, is based on the leading edge radius of the airfoil at the wing mean aerodynamic (geometric) chord:

$$(N_{Re})_{LER} = LER \cdot \frac{\bar{c}_{\ell_s}}{\bar{c}_w} \cdot (N_{Re})_{MAC} \qquad (4.12.4.3)$$

where

LER is the leading-edge radius of the airfoil as a ratio of the chord

In Table 4.12.4.1 the induced drag calculations of the wing and horizontal tail are summarized. The drag of the wing at angle of

attack based on the reference wing area, S_w is:

$$(C_{D_i})_w = \frac{C_{L_w}^2}{29.487} - 0.000210 \cdot C_{L_w} + 0.000264 \qquad (4.12.4.4)$$

while the drag of the horizontal tail based on the horizontal tail area, S_h, is:

$$(C_{D_i})_h = \frac{C_{L_h}^2}{14.6987} \qquad (4.12.4.5)$$

Above expressions are applied in Table 4.12.4.2 to determine the lift drag contributions of the two surfaces as function of angle of attack, α, and based on the reference wing area, S_w.

4.12.5 Lift Induced Drag of Fuselage and Nacelles

According to Reference 3 the drag of a body at angle of attack may be written

$$(C_{D_i})_B = C_{L_B} \alpha_{B_{eff}} \qquad (4.12.5.1)$$

where

C_{L_B} is the lift of the body, obtained from Section 4.3

$\alpha_{B_{eff}}$ is the angle of attack (in radians) of the equivalent circular body, which can be determined as follows:

$$\alpha_{B_{eff}} = \alpha + \alpha_{o_B} \qquad (4.12.5.2)$$

where

α_{o_B} is the zero-lift angle of the equivalent circular body relative to the reference X-body axis of the airplane.

The drag of the fuselage of the ATLIT at angle of attack, based on the reference wing area, S_w, is:

$$(C_{D_i})_f = C_{L_f} \frac{\pi (\alpha - 2.5)}{180} \qquad (4.12.5.3)$$

while the drag of the nacelles at angle of attack is:

$$(C_{D_i})_n = C_{L_n} \frac{\pi\alpha}{180} \qquad (4.12.5.4)$$

where

C_{L_f} and C_{L_n} (total lift of both nacelles) can be obtained from Section 4.3. In Table 4.12.5.1 a summary is listed of the calculations of the drag of the fuselage and nacelles of the ATLIT airplane.

4.12.6 Lift Induced Wing-Fuselage and Wing-Nacelle Interference Drag

In the absence of applicable representative data no attempt is made to account for wing-fuselage and wing-nacelle interference drag at angle of attack.

4.12.7 Cooling Drag

The discussion of nacelle drag in the previous section did not take into account the effect of drag due to the cooling system. An analytical treatment of cooling drag is beyond the scope of this paper because of the complexity and uncertainties in its determination. However, in Reference 2 drag curves are listed of the airplane with inlets and cowl flaps open and closed. From these data the increment of drag due to the cooling system could be determined and the cooling drag is shown in Figure 4.12.7.1.

4.12.8 Drag Characteristics of the ATLIT Airplane

The zero-lift drag of the components plus the interference drag between components is:

$$C_{D_o} = (\overline{C_{D_o}})_{wf} + (\overline{C_{D_o}})_h + (\overline{C_{D_o}})_v + (\overline{C_{D_o}})_{n(w)}$$

$$= 0.01634 + 0.00224 + 0.00112 + 0.01384 \qquad (4.12.8.1)$$

$$= 0.03352$$

The net drag of the ATLIT is summarized in Table 4.12.8.1 and may be written as follows:

$$C_D = C_{D_o} + (C_{D_i})_w + (C_{D_i})_h + (C_{D_i})_f + (C_{D_i})_n \qquad (4.12.8.2)$$

and the result is plotted in Figures 4.12.8.1 and 4.12.8.2. In these figures the experimental drag data are also presented. The predicted drag polar shows good agreement with the experimental results.

Table 4.12.1.1: Surface roughness height (Reference 3)

Type of surface	k, in.
Aerodynamically smooth	0
Polished metal or wood	0.02 to 0.08×10^{-3}
Natural sheet metal	0.16×10^{-3}
Smooth matte paint, carefully applied	0.25×10^{-3}
Standard camouflage paint, average application	0.40×10^{-3}
Camouflage paint, mass production spray	1.20×10^{-3}
Dip galvanized metal surface	6.0×10^{-3}
Natural surface of cast iron	10.0×10^{-3}

Table 4.12.1.2: Zero-lift drag of wing, horizontal and vertical tail of the ATLIT airplane

Symbol	Description	Reference	Wing	Horizontal Tail	Vertical Tail
k_i	Surface roughness height, m (in)	Table 4.12.1.1	0.635×10^{-5} (0.25×10^{-3})	0.635×10^{-5} (0.25×10^{-3})	0.635×10^{-5} (0.25×10^{-3})
ℓ_i	Mean aerodynamic chord of exposed area of surface, m (in)	Table 2.1.1	1.178 (46.38)	0.871 (34.29)	1.201 (47.30)
ℓ_i/k_i	-	-	1.86×10^5	1.37×10^5	1.89×10^5
$\bar{c}_w$	Mean aerodynamic chord of total wing, m(in)	Table 2.1.1	1.225 (48.22)	1.225 (48.22)	1.225 (48.22)
$(N_{Re})_{MAC}$	Reynolds number based on $\bar{c}_w$	-	2.3×10^6	2.3×10^6	2.3×10^6
$(N_{Re})_{\ell_i}$	Reynolds number based on ℓ_i	-	2.21×10^6	1.64×10^6	2.26×10^6
C_{f_i}	Skin friction coefficient of flat plate	Figure 4.12.1.1	3.87×10^{-3}	4.05×10^{-3}	3.86×10^{-3}
$(t/c)_i$	Thickness ratio of surface	Table 4.1.2	0.17	0.10	0.09
S_{i_e}	Exposed area of lifting surface, m^2 (ft^2)	Table 2.1.1	12.53 (134.8)	3.25 (34.9)	1.75 (18.8)
S_w	Reference wing area, m^2 (ft^2)	Table 2.1.1	14.40 (155.0)	14.40 (155.0)	14.40 (155.0)
$(C_{D_o})_i$	Zero-lift drag, of lifting surface on basis of S_w	Eq. (4.12.1.1)	0.00970	0.00221	0.00111

Table 4.12.2.1: Zero-lift drag of fuselage and nacelle

Symbol	Description	Reference	Fuselage	Nacelle
C_{B_i}	Circumference of the maximum frontal area of body m (ft)	Figure 2.1	4.69 (15.4)	3.14 (10.3)
d_{B_i}	Diameter of equivalent perimeter of maximum frontal area = C_{B_i}/π, m (ft)	-	1.49 (4.9)	1.01 (3.3)
S_{B_i}	Frontal area of equivalent perimeter of body, m^2 (ft^2)	Eq. (4.12.2.2)	1.75 (18.86)	0.79 (8.55)
ℓ_i	Length of body, m (ft)	Figure 4.8.1.2	8.35 (27.4)	2.65 (8.7)*
C_{b_i}	Circumference of base area of body	Figure 2.1	≈ 0	≈ 0
d_{b_i}	Diameter of equivalent perimeter of base area = C_{b_i}/π, m (ft)	-	0	0
$(S_{wet})_i$	Wetted surface area, m^2 (ft^2)	Appendix F	23.3 (251.0)	6.08 (65.4)*
k_i	Surface roughness height, m (in)	Table 4.12.1.1	0.635×10^{-5} (0.25×10^{-3})	0.635×10^{-5} (0.25×10^{-3})
$(\ell/k)_i$	Ratio in common units	-	1.32×10^{6}	4.18×10^{5}
$\bar{c}_w$	Mean aerodynamic chord of wing, m (ft)	Table 2.1.1	1.225 (4.018)	1.225 (4.018)
$(N_{Re})_{MAC}$	Reynolds number based on $\bar{c}_w$	-	2.3×10^{6}	2.3×10^{6}
$(N_{Re})_{\ell_i}$	Reynolds number based on ℓ_i	-	1.57×10^{7}	4.98×10^{6}
C_{f_i}	Skin friction coefficient of flat plate	Figure 4.12.1.1	2.8×10^{-3}	3.4×10^{-3}
S_w	Reference wing area, m^2 (ft^2)	Table 2.1.1	14.40 (155.0)	14.40 (155.0)
$(C_{D_o})_i$	Zero-lift drag coefficient of body based on S_w	Eq. (4.12.2.1)	0.00616	0.00614

*Including 8-inch extension of nacelle due to installation of thrust/torque balance.

Table 4.12.3.1: Net zero-lift drag of wing-fuselage combination

Symbol	Description	Reference	Magnitude
$(C_{D_o})_w$	Zero-lift drag of isolated exposed wing panels	Table 4.12.1.2	0.00970
$(C_{D_b})_f$	Base drag of fuselage	Table 4.12.2.1	0
$(C_{D_f})_f$	Zero-lift drag of isolated fuselage with base drag omitted	Table 4.12.2.1	0.00616
M	Mach number	-	0.081
ℓ_f	Length of fuselage, m (ft)	Table 4.12.2.1	8.35 (27.4)
$\bar{c}_w$	Wing mean aerodynamic chord, m (ft)	Table 2.1.1	1.225 (4.018)
$(N_{Re})_{MAC}$	Reynolds number based on $\bar{c}_w$	-	2.3×10^6
$(N_{Re})_{\ell_f}$	Reynolds number based on ℓ_f	-	1.57×10^6
R_{wf}	Wing-body interference correlation factor	Figures 4.12.3.1	1.075
$(\overline{C_{D_o}})_{wf}$	Net zero-lift drag of wing-fuselage combination	Eq. (4.12.3.2)	0.01632

Table 4.12.3.2: Net zero-lift drag of tail surfaces in presence of the fuselage

Symbol	Description	Reference	Horizontal Tail	Vertical Tail
$(C_{D_o})_h$	Zero-lift drag of isolated exposed horizontal tail panels	Table 4.12.1.2	0.00221	-
$(C_{D_o})_v$	Zero-lift drag of isolated exposed vertical tail panels	Table 4.12.1.2	-	0.00111
n_1	Number of junctures of tail with fuselage	Figure 2.1	2	1
t/c	Thickness ratio of tail at juncture	Table 4.1.2	0.10	0.09
c_{r_e}	Root chord of exposed tail surface, m (ft)	Table 2.1.1	0.871 (2.858)	1.575 (5.167)
S_w	Reference wing area, m^2 (ft^2)	Table 2.1.1	14.40 (155.0)	14.40 (155.0)
$(\Delta C_{D_o})_{h(f)}$	Interference drag of horizontal tail surface due to fuselage	Eq. (4.12.3.4)	0.00003	-
$(\Delta C_{D_o})_{v(f)}$	Interference drag of vertical tail surface due to fuselage	Eq. (4.12.3.4)	-	0.00001
$\overline{(C_{D_o})_h}$	Net zero-lift drag of horizontal tail in presence of fuselage	Eq. (4.12.3.6)	0.00224	-
$\overline{(C_{D_o})_v}$	Net zero-lift drag of vertical tail in presence of fuselage	Eq. (4.12.3.7)	-	0.00112

Table 4.12.3.3: Net zero-lift drag of nacelles in presence of wing

Symbol	Description	Reference	Magnitude
$(C_{D_o})_n$	Zero-lift drag of one isolated nacelle	Table 4.12.2.1	0.00614
$(C_{D_o})_w$	Zero-lift drag of isolated exposed wing panels	Table 4.12.1.2	0.00970
$(\Delta S_w)_n$	Wing area overlapped by one nacelle, m^2 (ft^2)	Figure 2.1.1	1.157 (12.45)
S_w	Reference wing area, m^2 (ft^2)	Table 2.1.1	14.40 (155.0)
$\overline{(C_{D_o})_{n(w)}}$	Net zero-lift drag of nacelles in presence of wing	Eq. (4.12.3.8)	0.01384

Table 4.12.4.1: Drag of wing and horizontal tail due to lift

Symbol	Description	Reference	Wing	Horizontal Tail
A	Aspect ratio	Table 2.1.1	10.32	4.75
θ	Twist angle, deg	Table 2.1	-3	0.
c_{ℓ_α}	Airfoil section lift curve slope, deg^{-1}	Table 4.12	0.115	-
C_{L_α}	Lift-curve slope of lifting surface, rad^{-1}	Table 4.2.1	5.090	3.878
λ	Taper ratio	Table 2.1.1	0.5	-
M	Mach number	-	0.081	0.081
β	$\sqrt{1 - M^2}$	-	0.9967	0.9967
βA	-	-	10.29	4.73
Λ_{le}	Leading edge sweep angle, deg	Table 2.1.1	3.67	0.
$\Lambda_{c/4}$	Quarter chord sweep angle, deg	Table 2.1.1	1.835	0
$\tan^{-1}\left(\frac{\tan\Lambda_{c/4}}{\beta}\right)$	-	-	1.841	0
v	Induced drag factor due to twist	Figure 4.12.4.1	0.00061	-
βw	Zero-lift drag factor due to twist	Figure 4.12.4.1	0.00221	-
w	$\beta w/\beta$	-	0.00222	-
$(N_{Re})_{MAC}$	Reynolds number based on $\bar{c}_w$	-	2.3×10^6	2.3×10^6
LER	Leading-edge-radius of airfoil, ratio of chord	-	0.06	0.1102
$\bar{c}/\bar{c}_w$	Ratio of mean aerodynamic chords	Table 2.1.1	1.	0.711
$(N_{Re})_{LER}\frac{\sqrt{1-M^2\cos^2\Lambda_{le}}}{\tan\Lambda_{le}}$	-	-	2.14×10^6	∞
$A\lambda/\cos\Lambda_{le}$	-	-	5.171	4.75
R	Leading-edge-suction parameter	Figure 4.12.4.3	0.961	0.959
e	Span-efficiency factor	Eq. (4.12.4.2)	0.9095	0.9850

Summary:

$$(C_{D_i})_w = \frac{C_{L_w}^2}{\pi Ae} + C_{L_w}\,\theta\,c_{\ell_\alpha}\,v + (\theta\,c_{\ell_\alpha})^2 w = \frac{C_{L_w}^2}{29.487} - 0.000210\,C_{L_w} + 0.000264 \text{ based on } S_w$$

$$(C_{D_i})_h = \frac{C_{L_h}^2}{14.6987} \text{ based on } S_h$$

Table 4.12.4.2: Summary induced drag of wing and horizontal tail

α, deg	$\alpha_w = \alpha + i_w$ deg	C_{L_w} Figure 4.2.4.1	$(C_{D_i})_w$ Eq.(4.12.4.4)	$\bar{\varepsilon}_h$, deg Figure 4.9.3.1	$\alpha_h = \alpha - \bar{\varepsilon}_h$ deg	C_{L_h} Figure 4.2.4.1	$(C_{D_i})_h$ Eq.(4.12.4.5)	$(C_{D_i})_h$ based on S_w
-4	-3.5	-0.0533	0.00037	-0.26	-3.74	-0.2531	0.00436	0.00109
-2	-1.5	0.1243	0.00075	0.56	-2.56	-0.1733	0.00204	0.00051
0	0.5	0.3019	0.00329	1.38	-1.38	-0.0934	0.00059	0.00015
2	2.5	0.4795	0.00796	2.19	-0.19	-0.0129	0.00001	≈ 0
4	4.5	0.6571	0.01476	2.99	1.01	0.0684	0.00032	0.00008
15.9	16.4	1.494	0.07565	7.24	8.66	0.5861	0.02337	0.00583

Table 4.12.5.1: Drag due to lift of fuselage and nacelles

α, deg	C_{L_f} Table 4.4.3.3	$(C_{D_i})_f$ Eq.(4.12.5.3)	C_{L_n} Table 4.4.3.3	$(C_{D_i})_n$ Eq.(4.12.5.4)
-4	-0.01503	0.00171	-0.00780	0.00055
-2	-0.01077	0.00085	-0.00398	0.00014
0	-0.00619	0.00027	0	0
2	-0.00128	0.00001	0.00414	0.00015
4	0.00395	0.00010	0.00844	0.00059
15.9	0.04171	0.00975	0.03737	0.01037

Table 4.12.8.1: Drag of the complete ATLIT airplane

α, deg	C_L Figure 4.4.3.1	C_{D_o} Eq.(4.12.8.1)	$(C_{D_i})_w$ Table 4.12.4.2	$(C_{D_i})_h$ Table 4.12.4.2	$(C_{D_i})_f$ Table 4.12.5.1	$(C_{D_i})_n$ Table 4.12.5.1	C_D Eq.(4.12.8.2)
-4	-0.1442	0.03352	0.00037	0.00109	0.00171	0.00055	0.03724
-2	0.0688	0.03352	0.00075	0.00051	0.00085	0.00014	0.03577
0	0.2822	0.03352	0.00329	0.00015	0.00027	0	0.03723
2	0.4963	0.03352	0.00796	0	0.00001	0.00015	0.04164
4	0.7111	0.03352	0.01476	0.00008	0.00010	0.00059	0.04906
15.9	1.7264	0.03352	0.07565	0.00583	0.00975	0.01037	0.13512

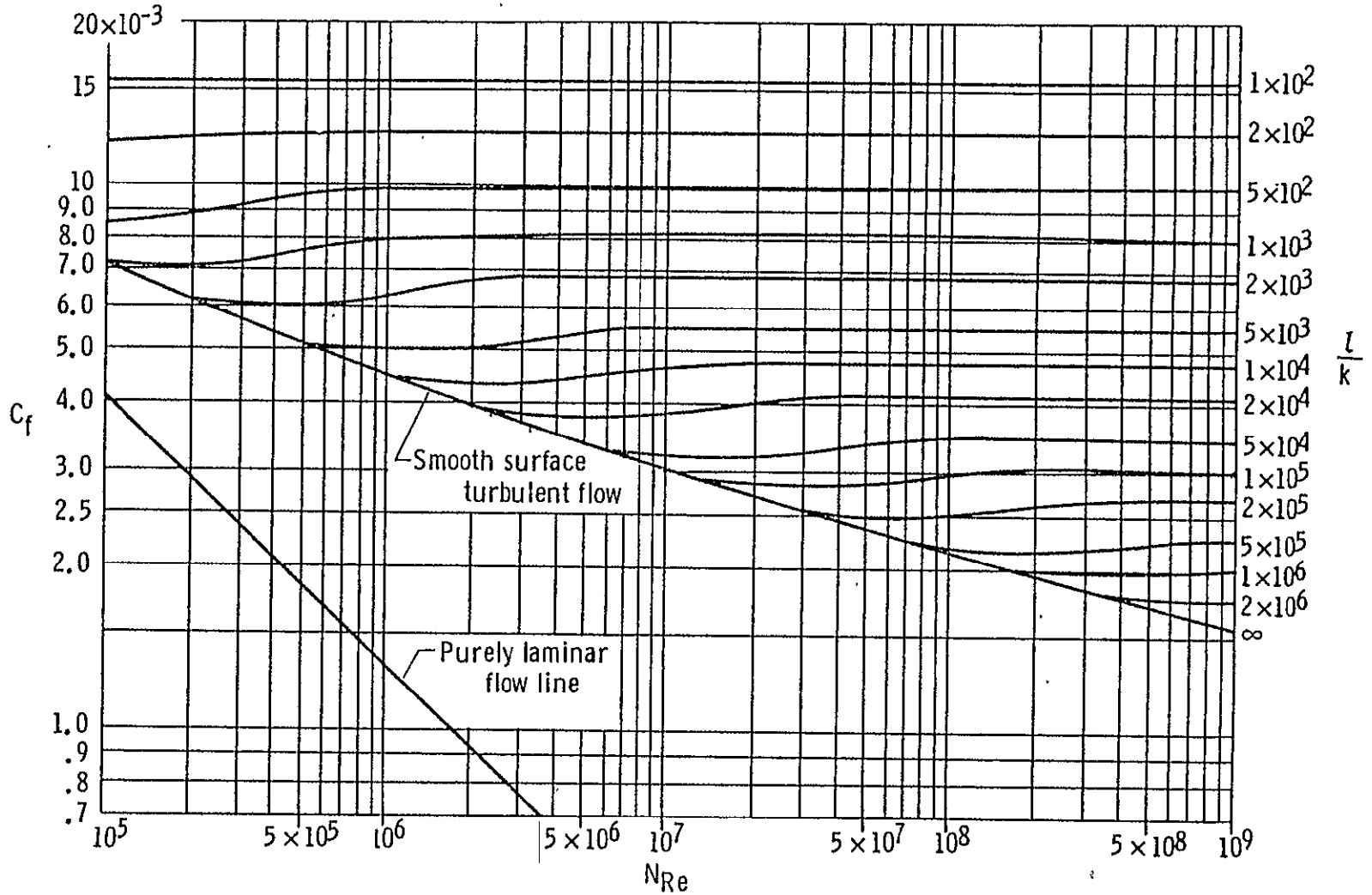

Figure 4.12.1.1: Incompressible skin friction coefficient of a flat plate (Reference 3)

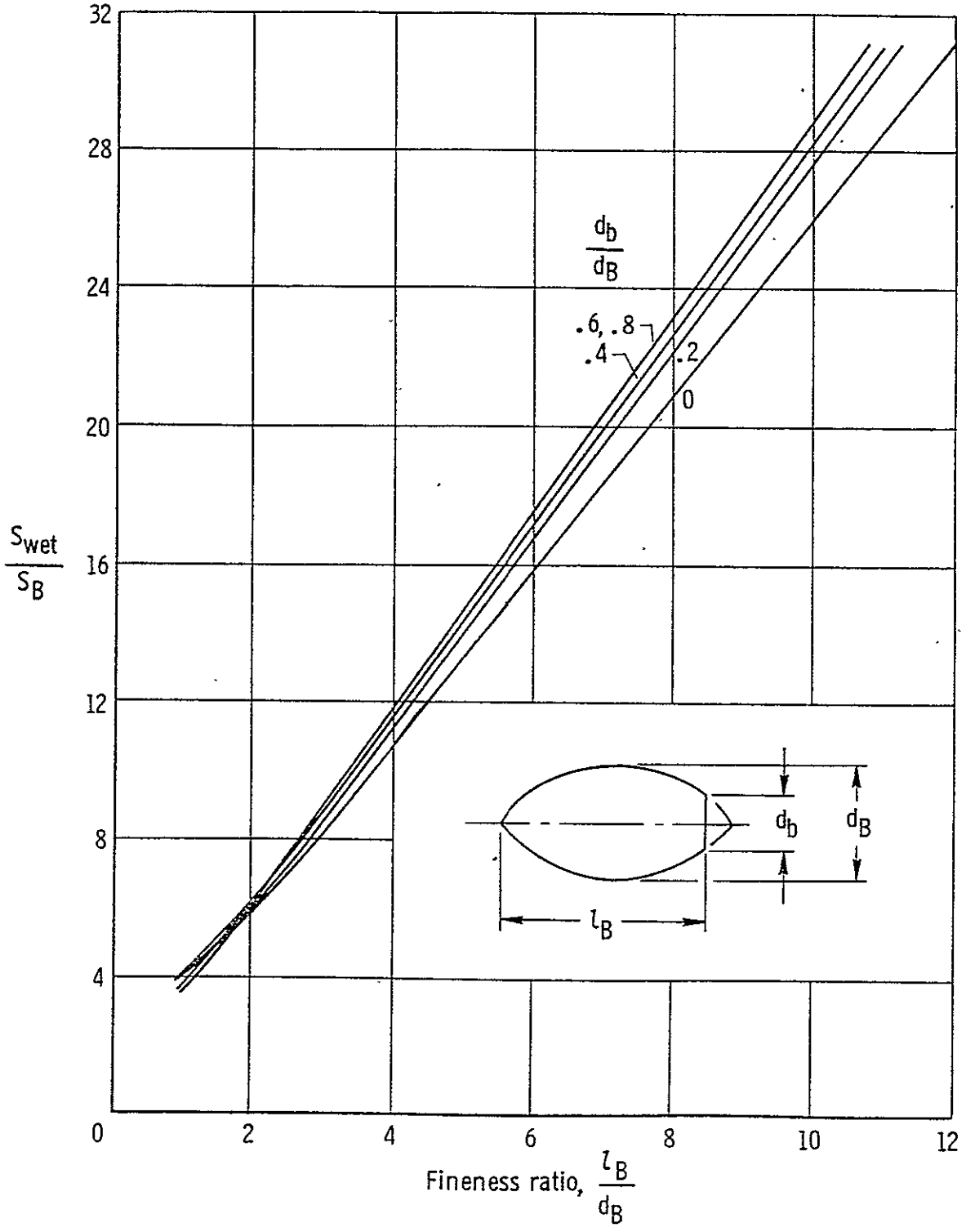

Figure 4.12.2.1: Wetted area of blunt base ogive bodies (Reference 3)

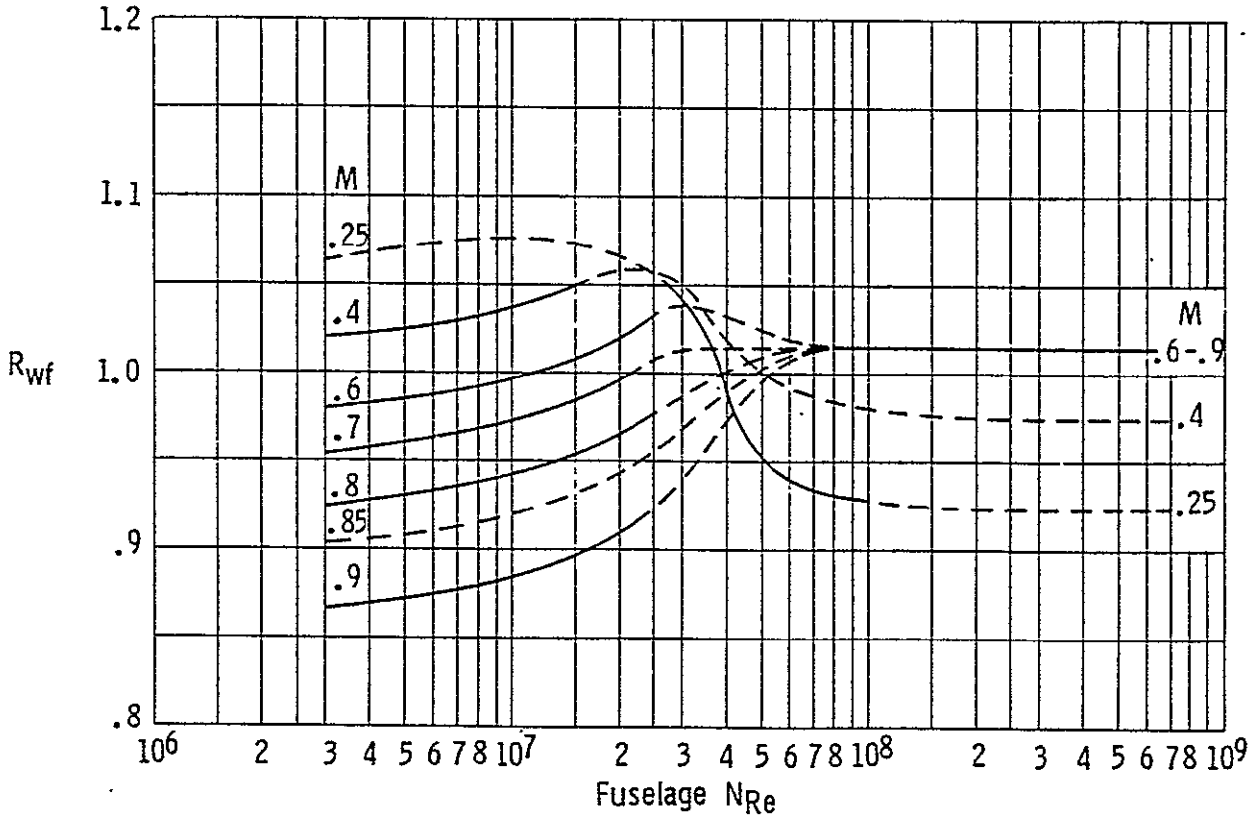

Figure 4.12.3.1: Wing-body interference correlation factor (Reference 3)

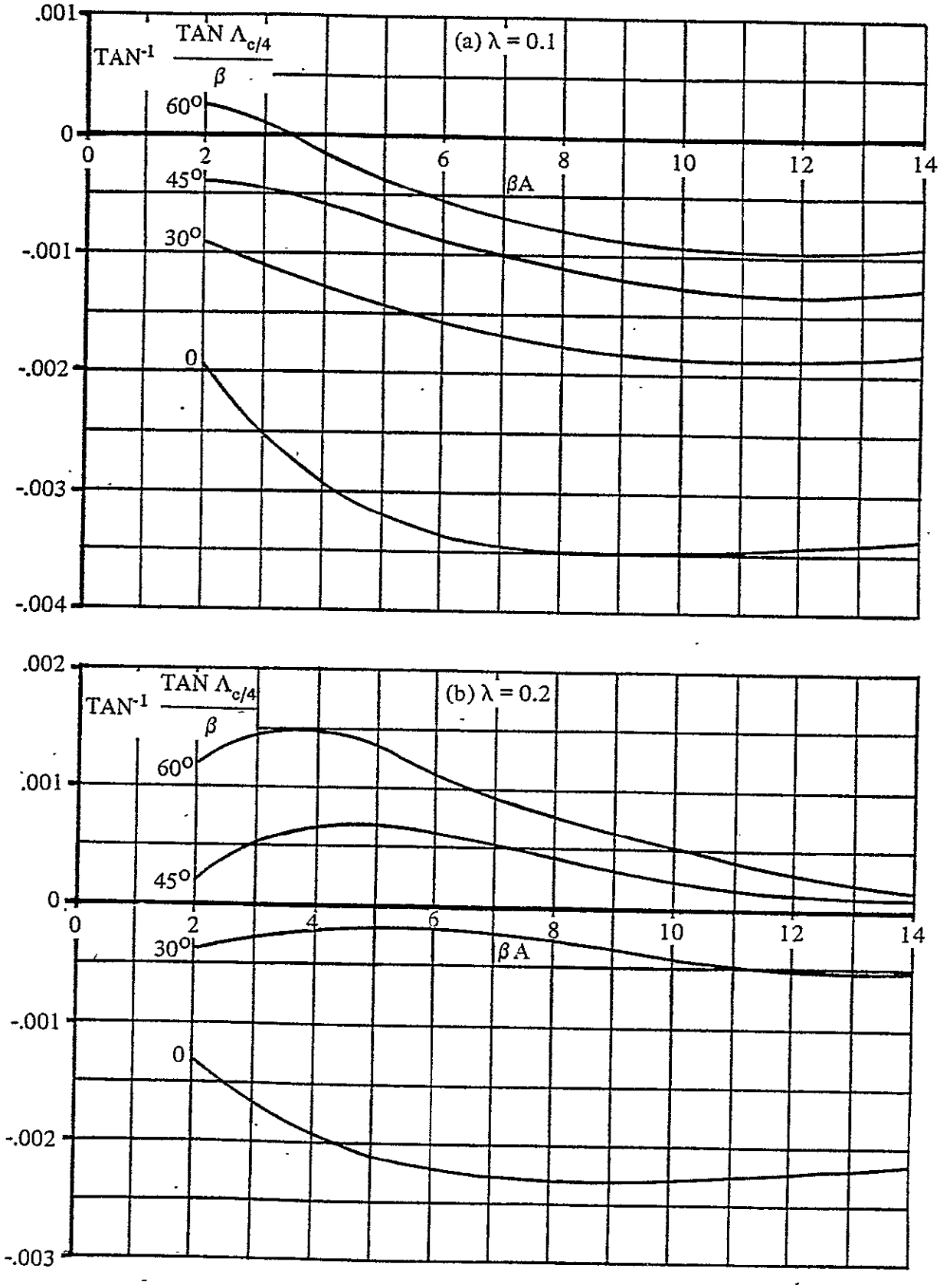

Figure 4.12.4.1: Lift dependent drag factor due to linear twist (Reference 4)

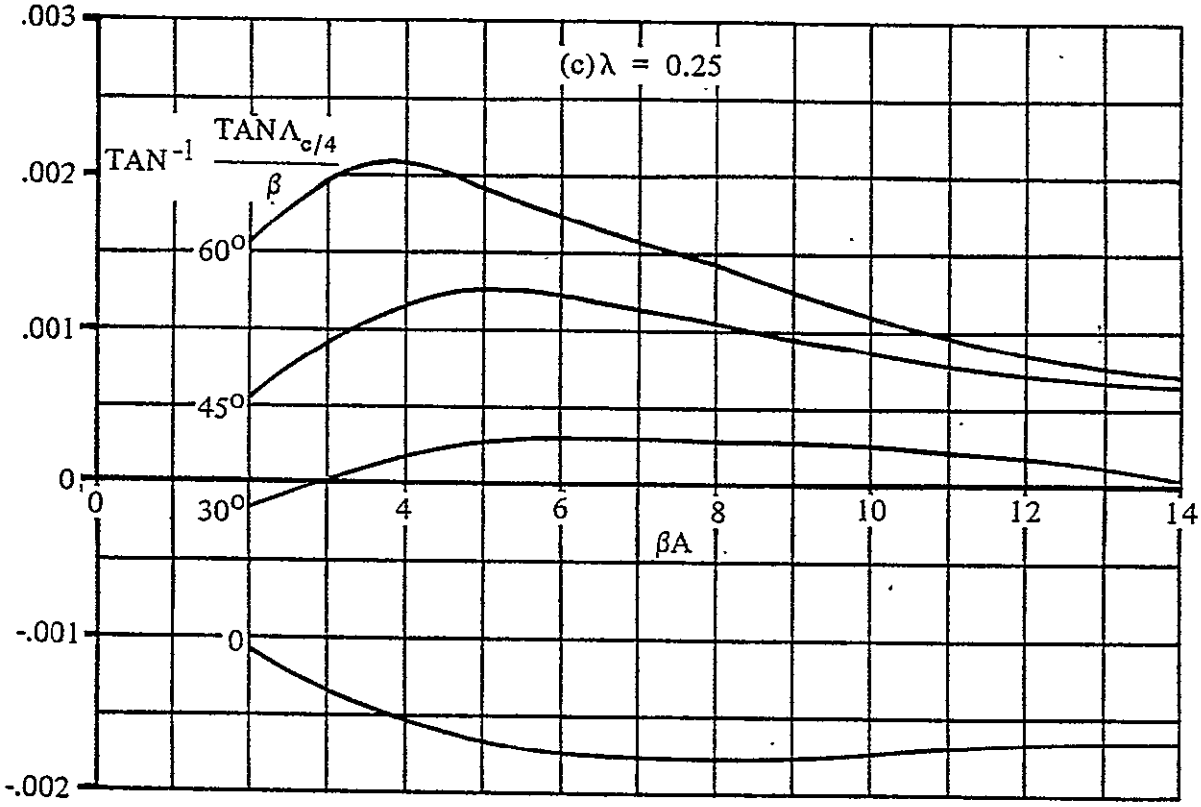

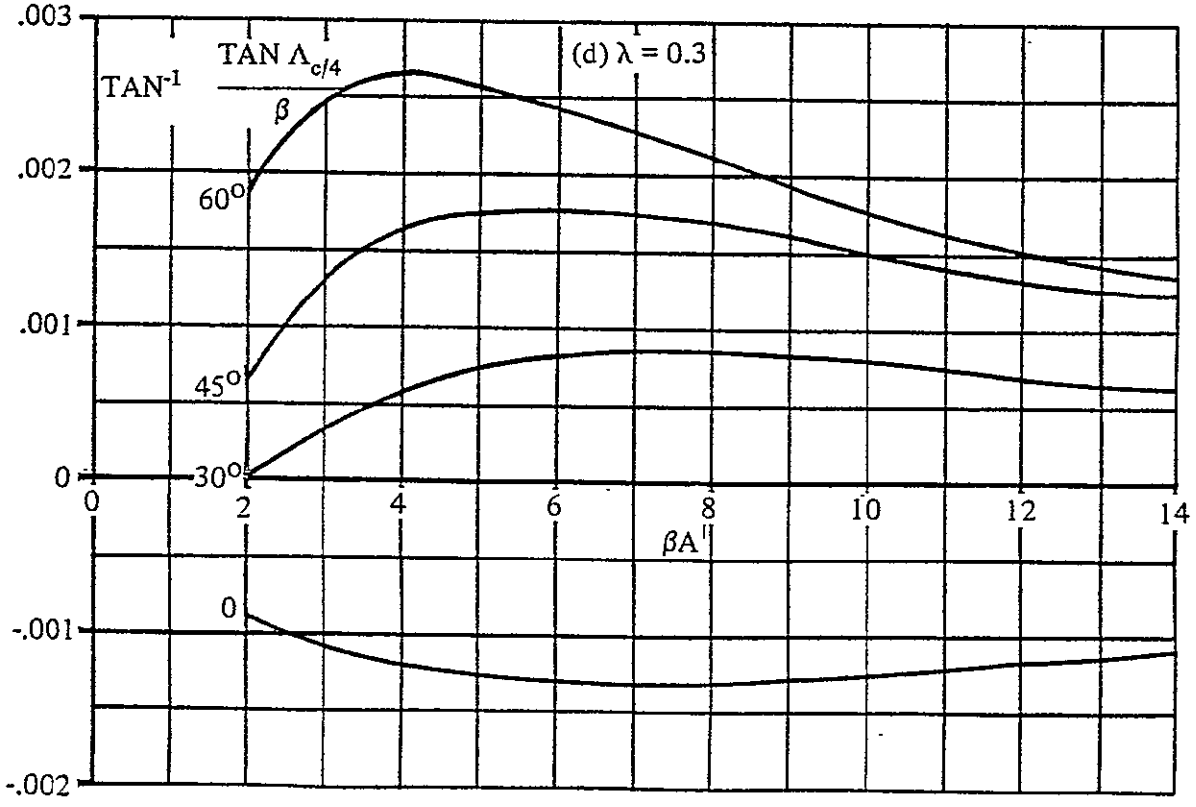

Figure 4.12.4.1: Continued

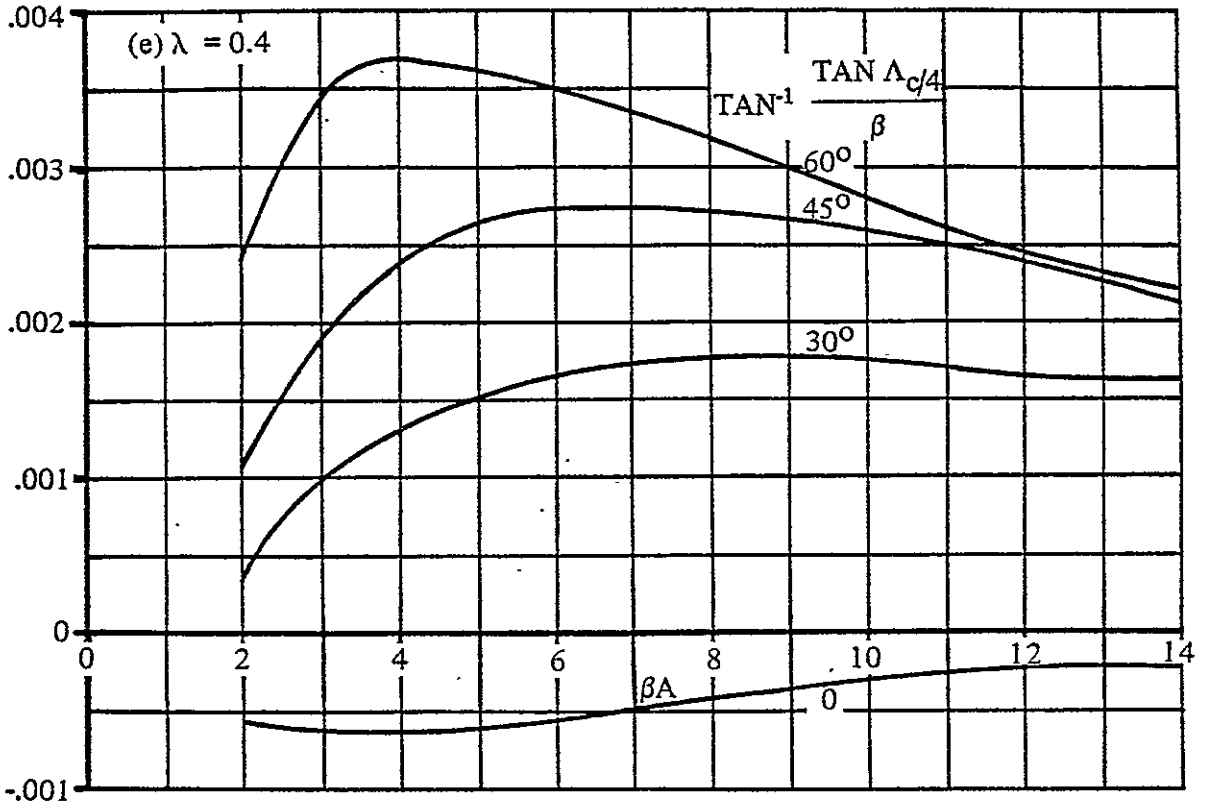

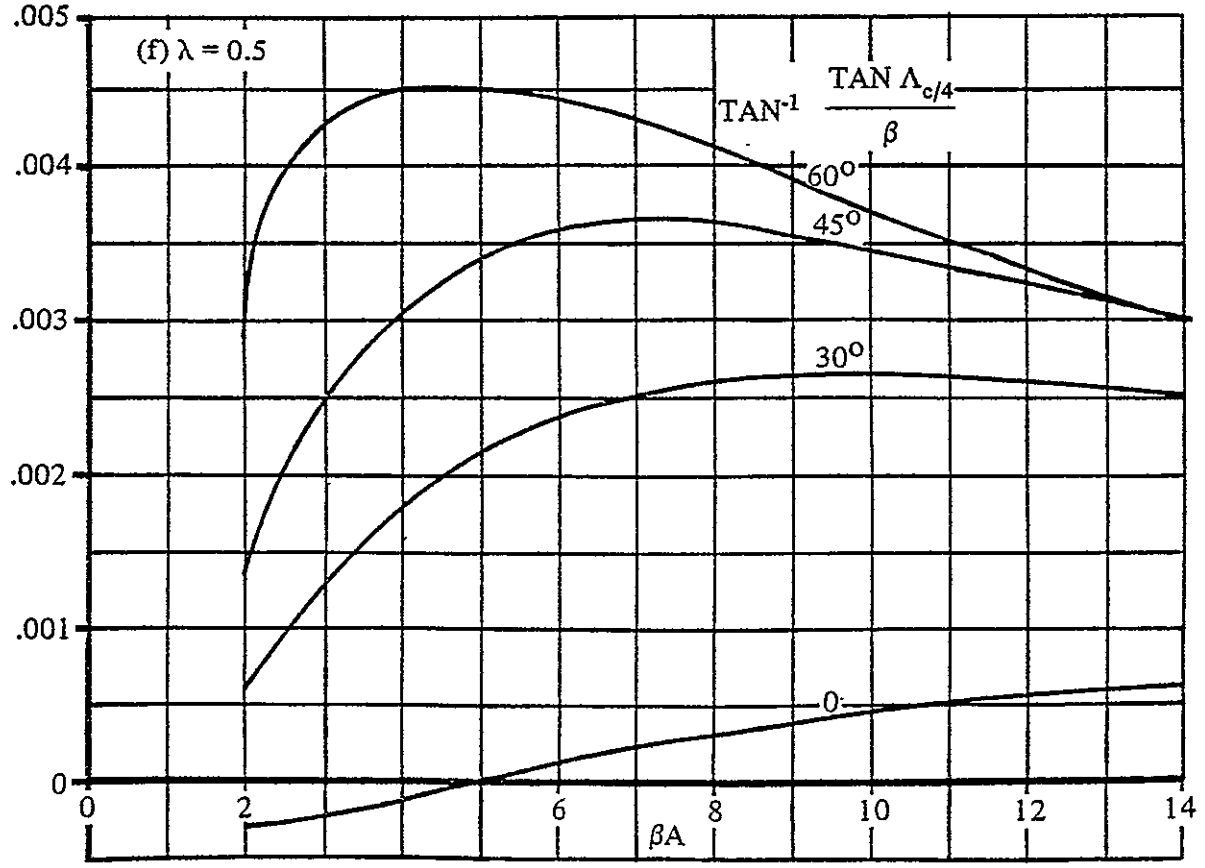

Figure 4.12.4.1: Continued

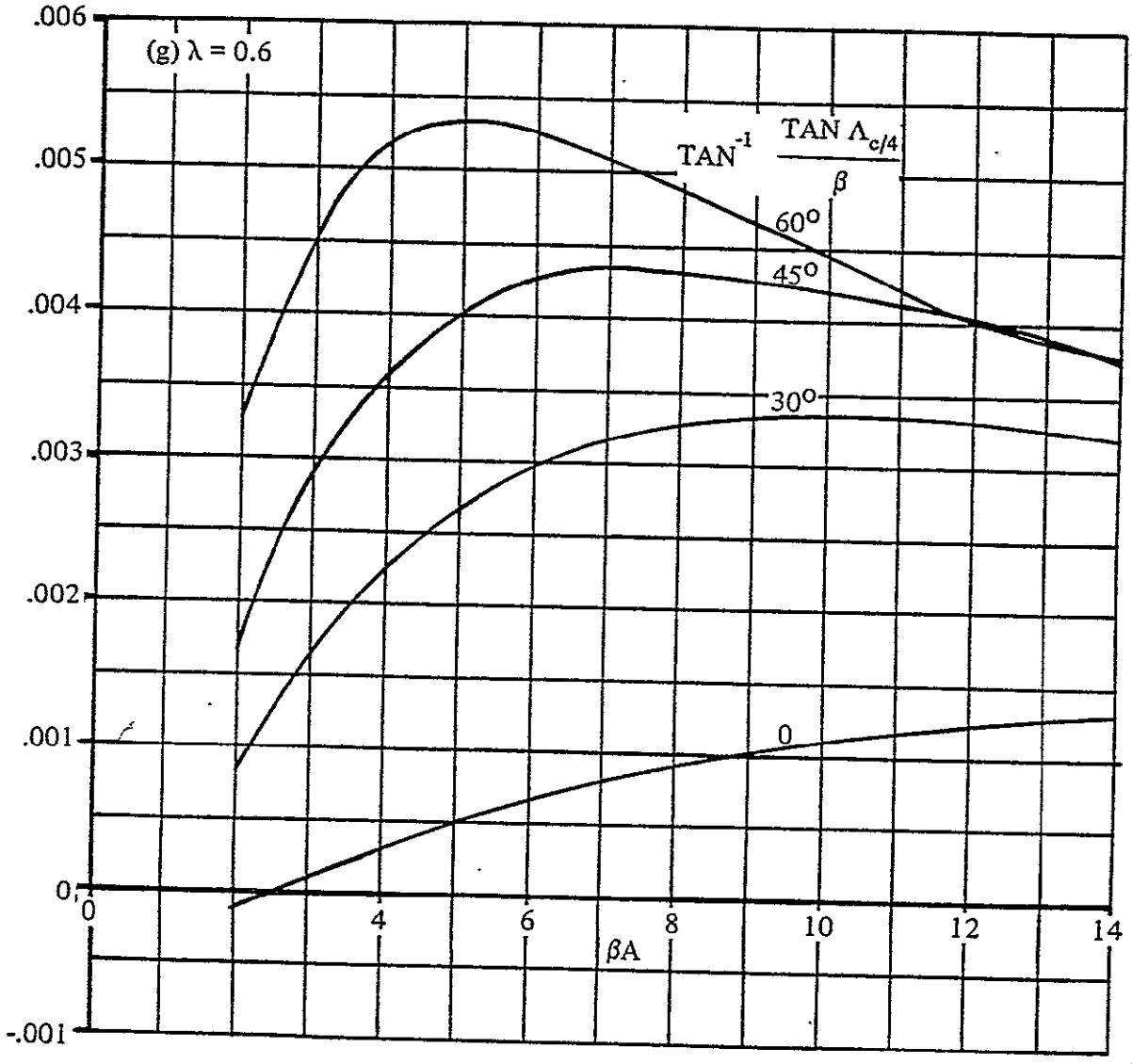

Figure 4.12.4.1: Continued

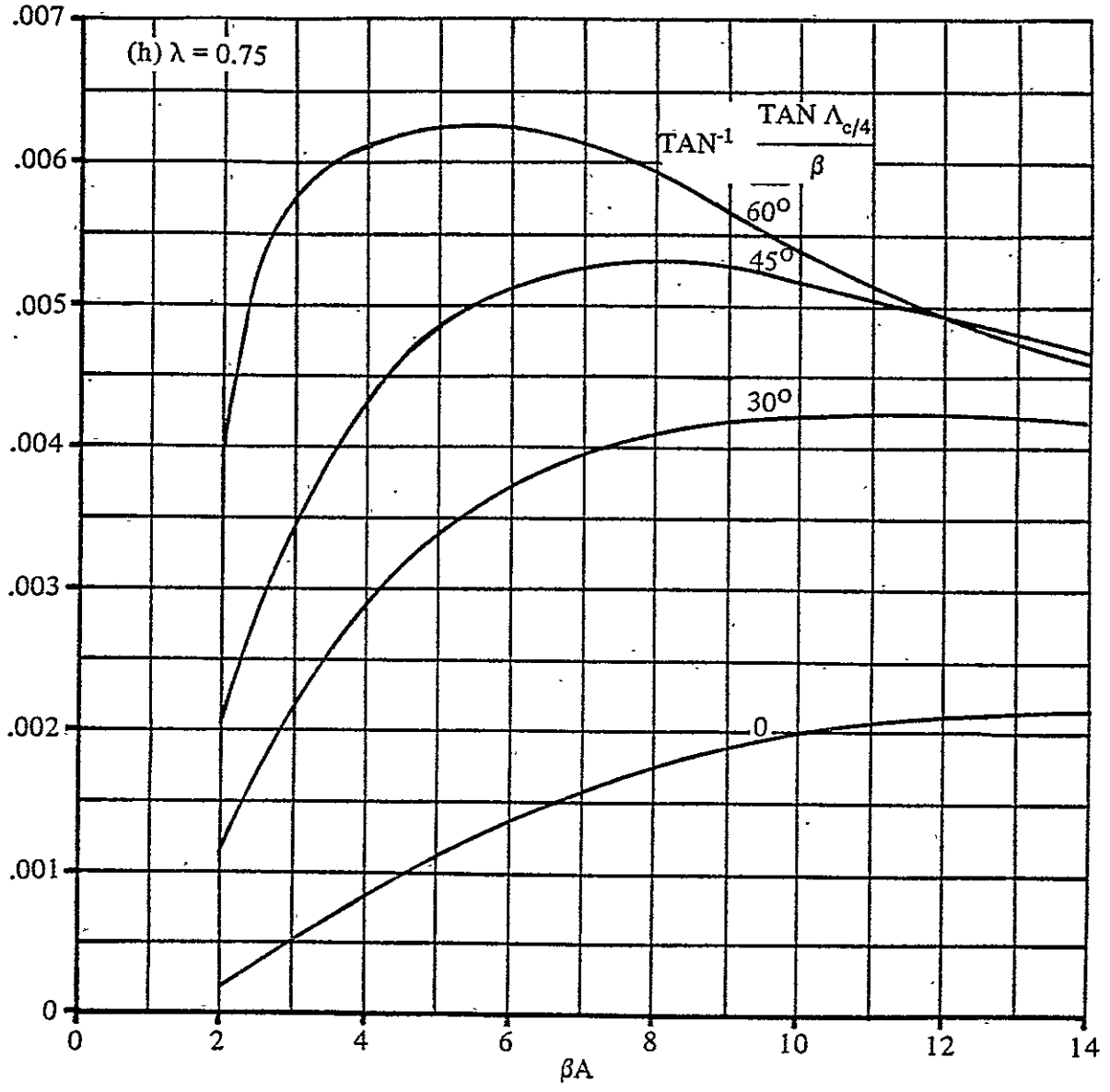

Figure 4.12.4.1: Continued

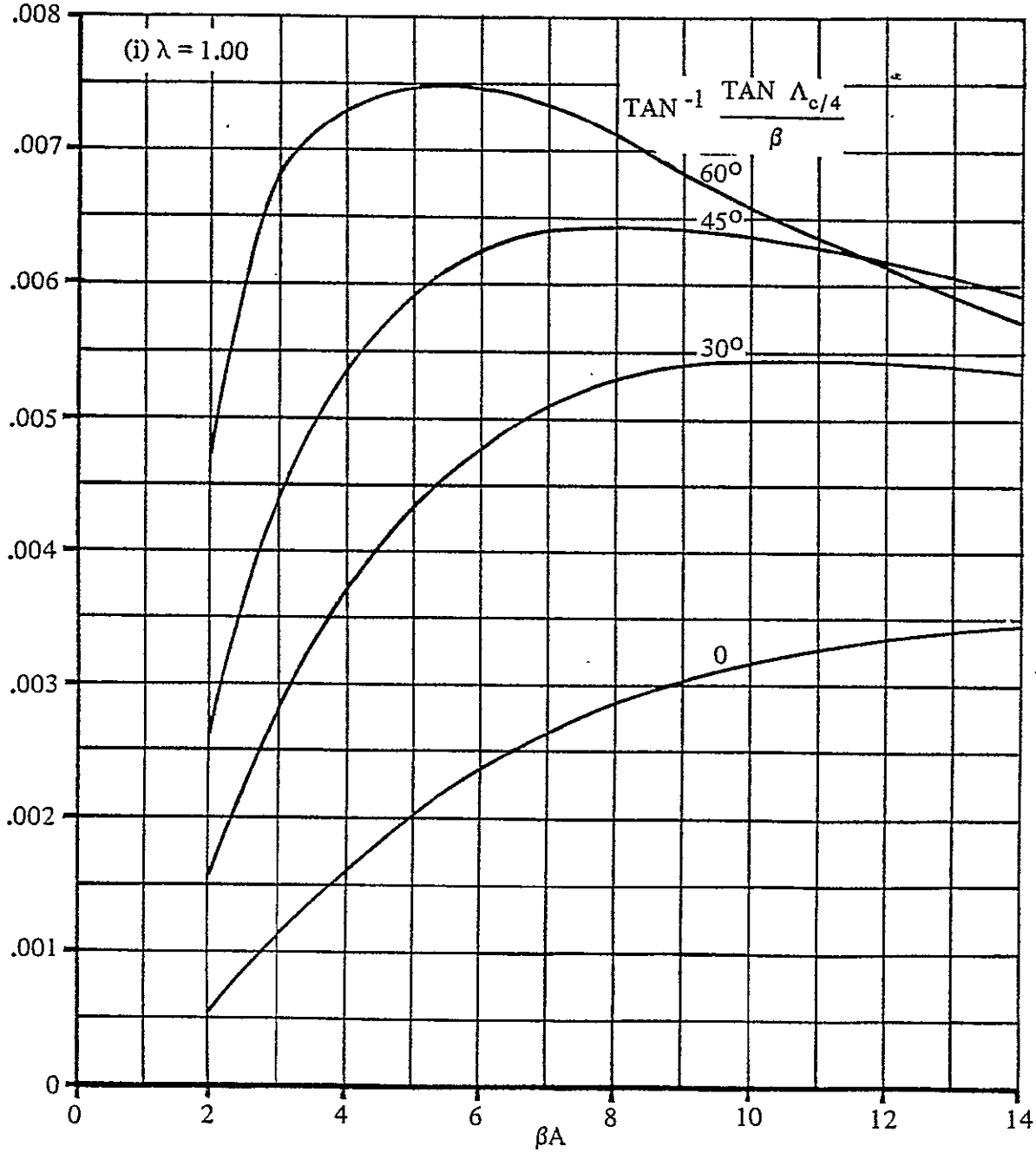

Figure 4.12.4.1: Concluded

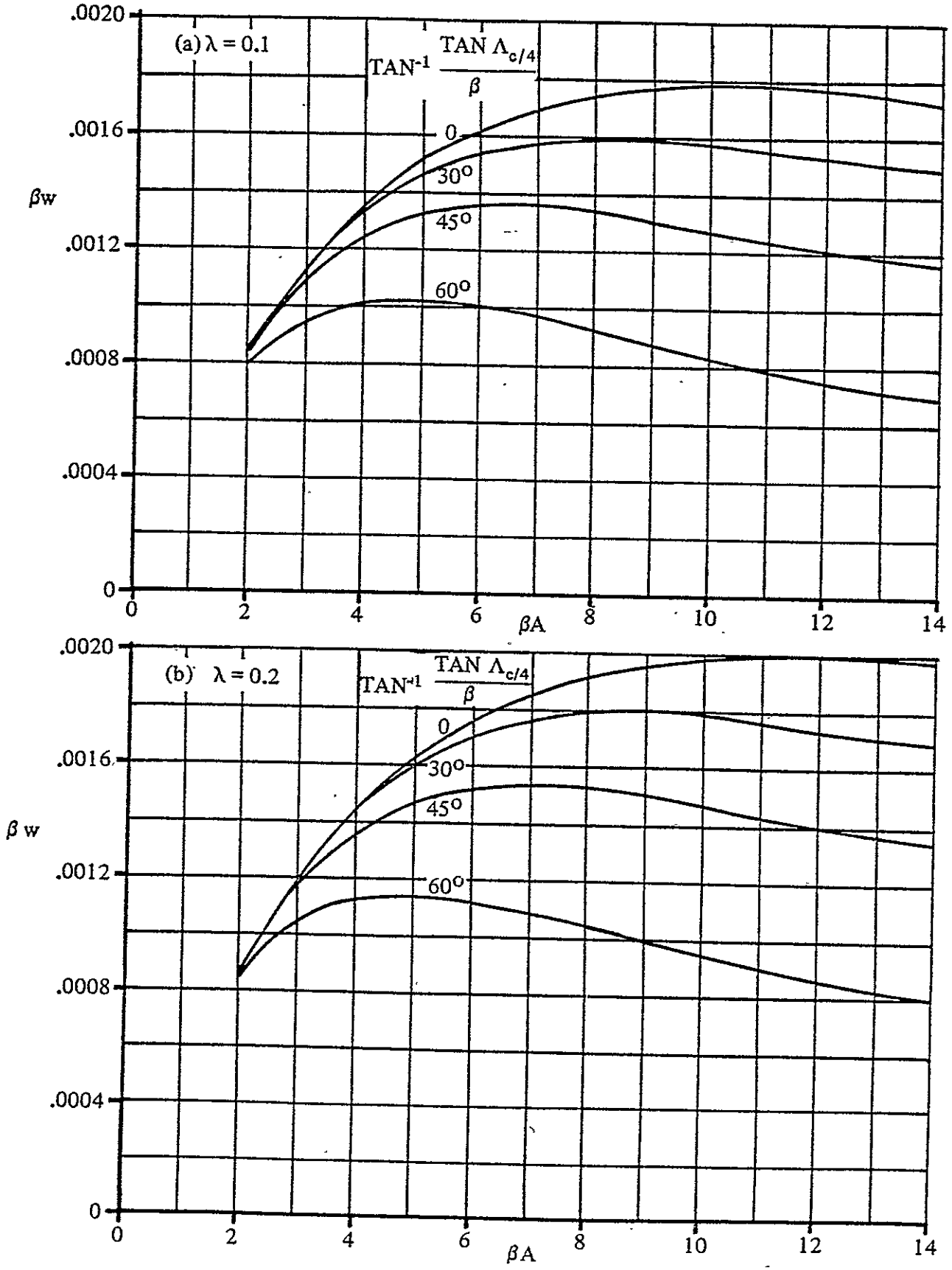

Figure 4.12.4.2: Zero-lift drag factor due to linear twist (Reference 4)

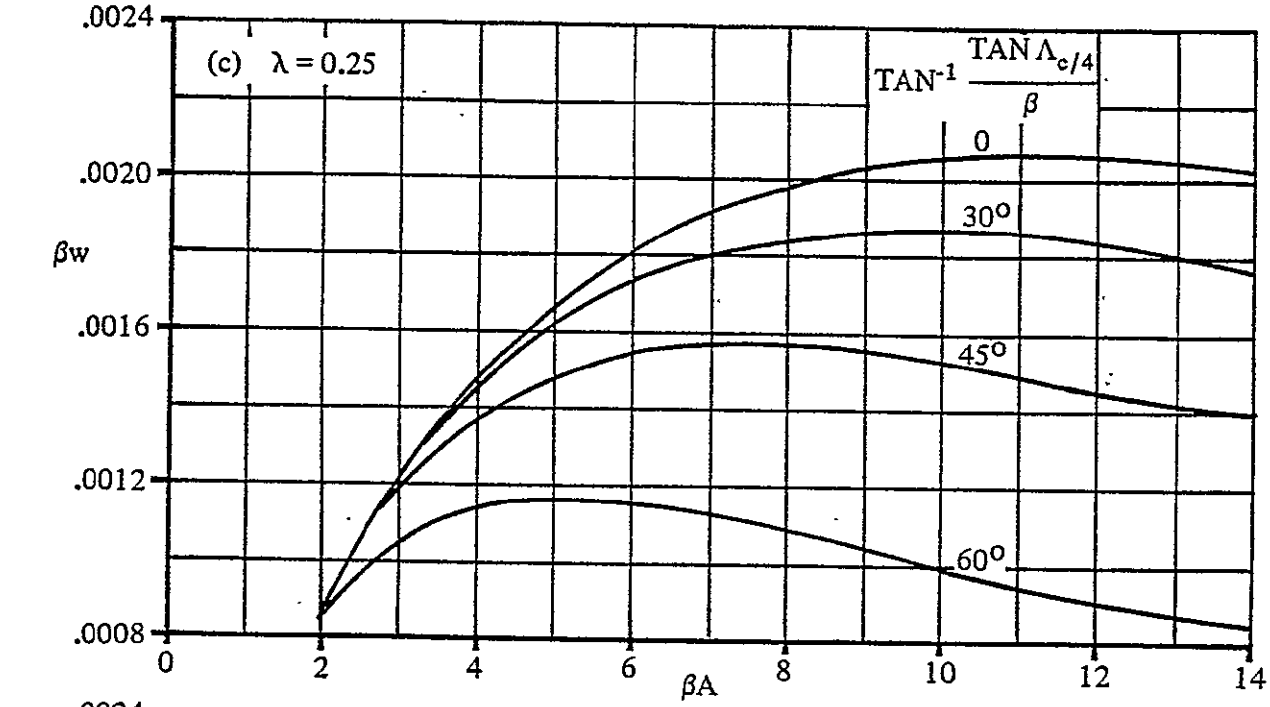

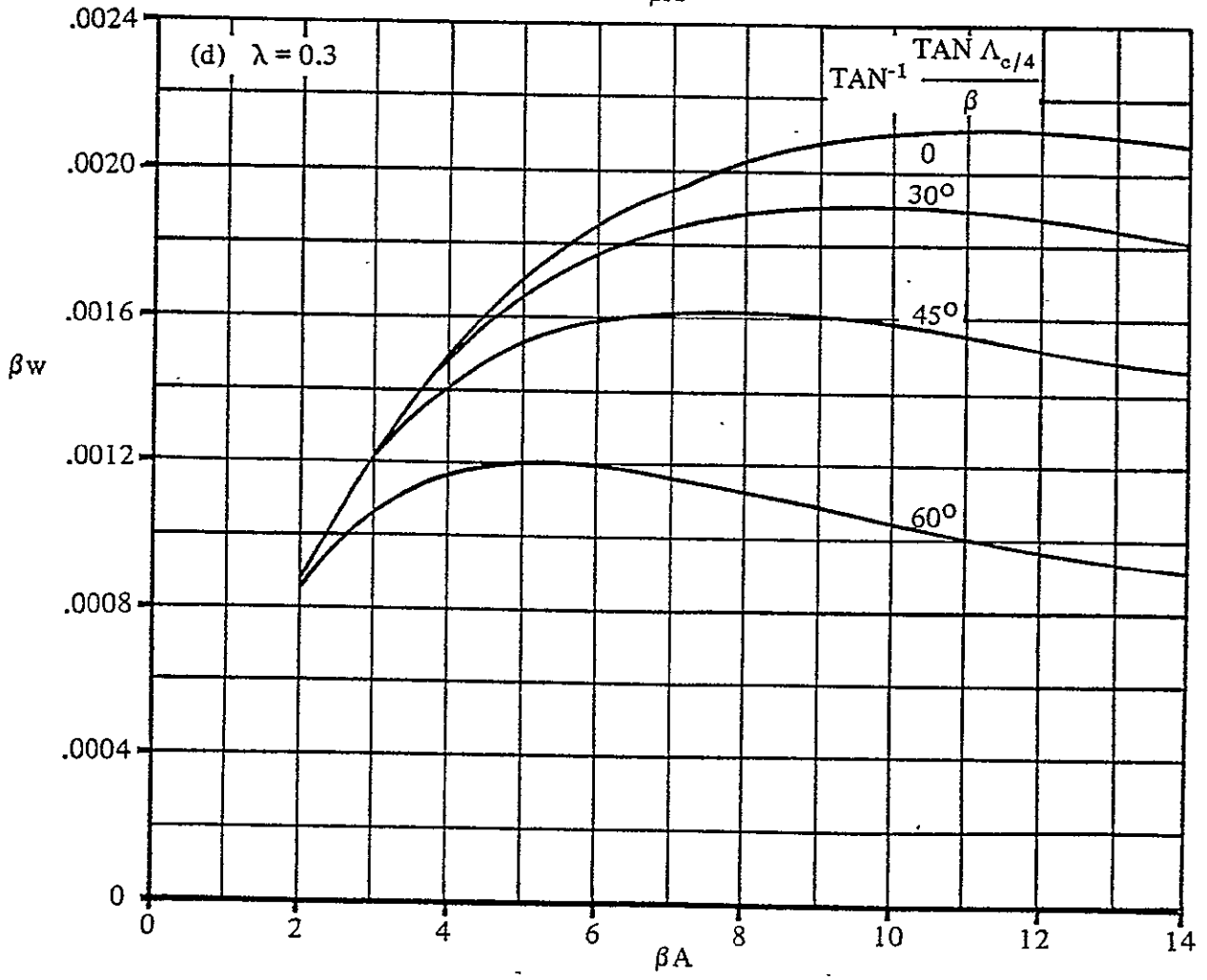

Figure 4.12.4.2: Continued

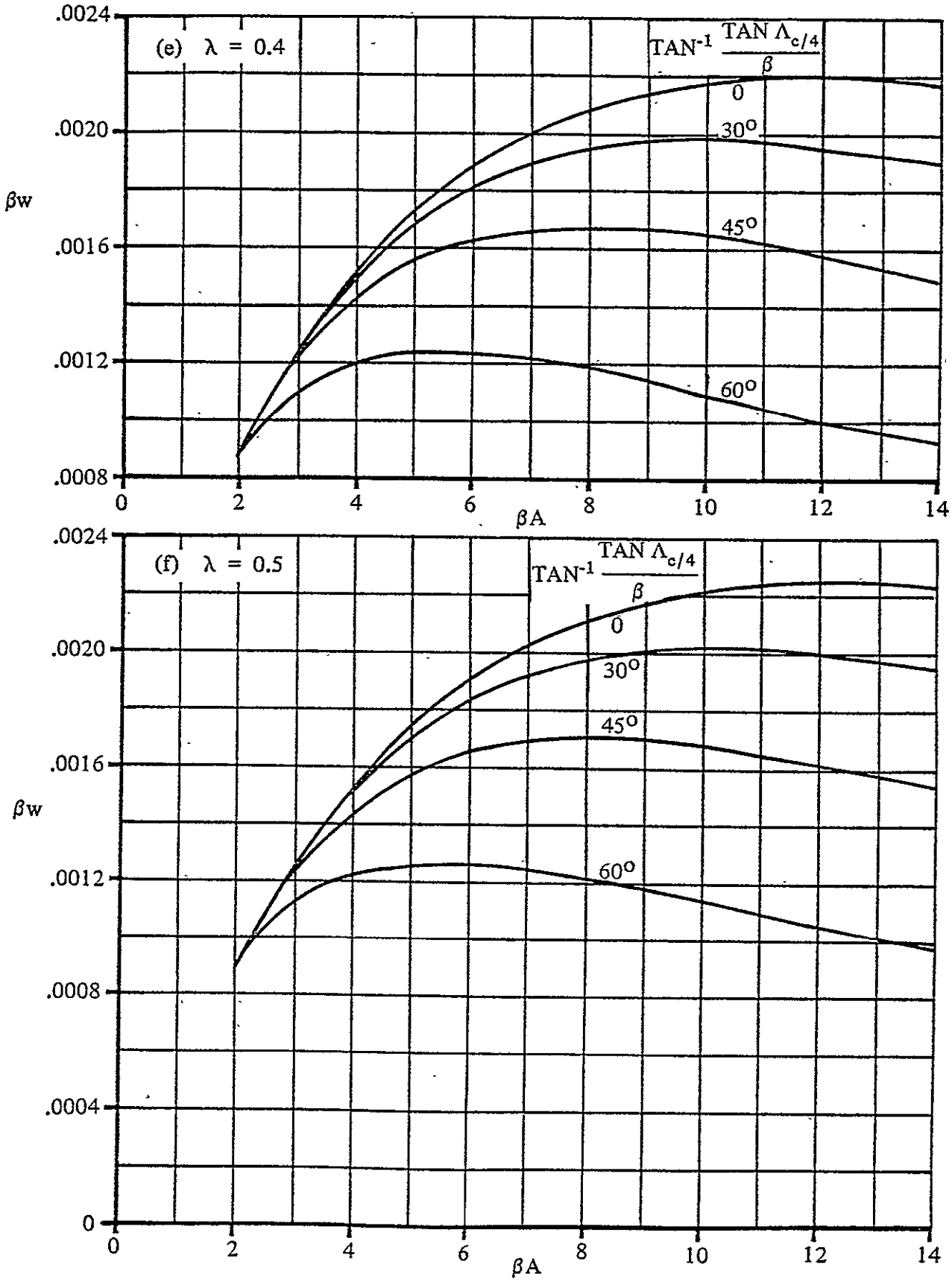

Figure 4.12.4.2: Continued

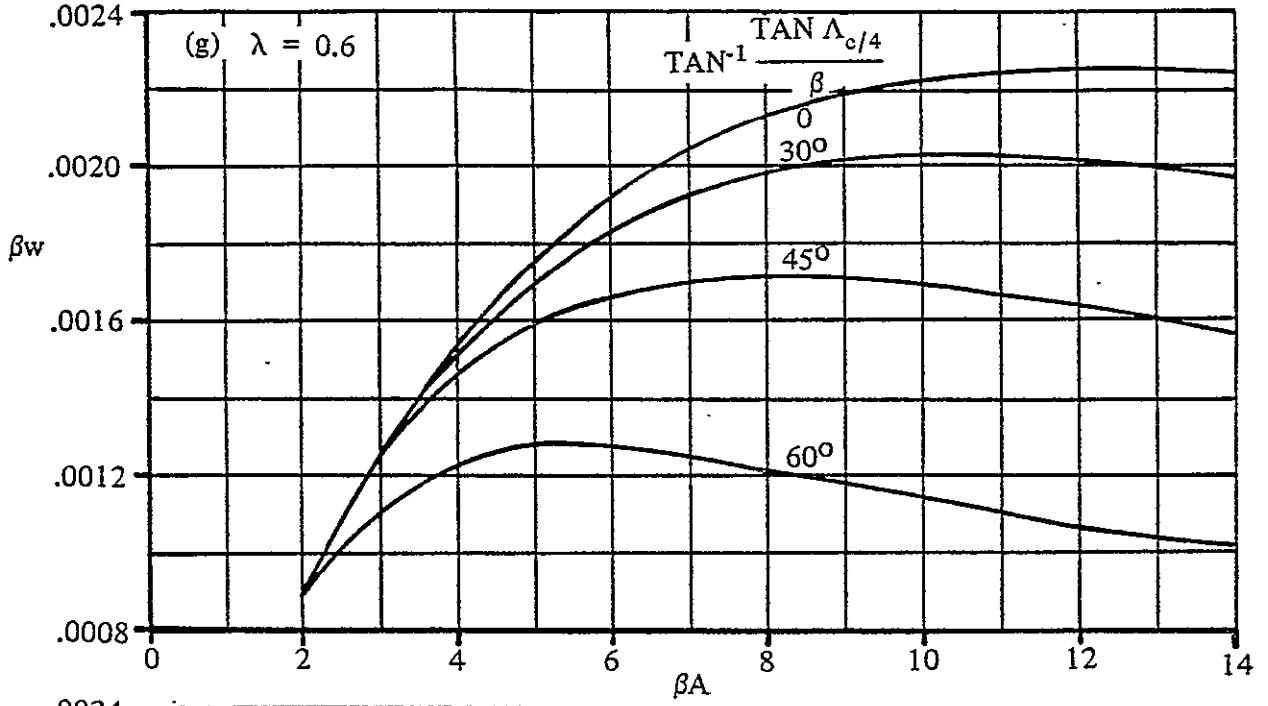

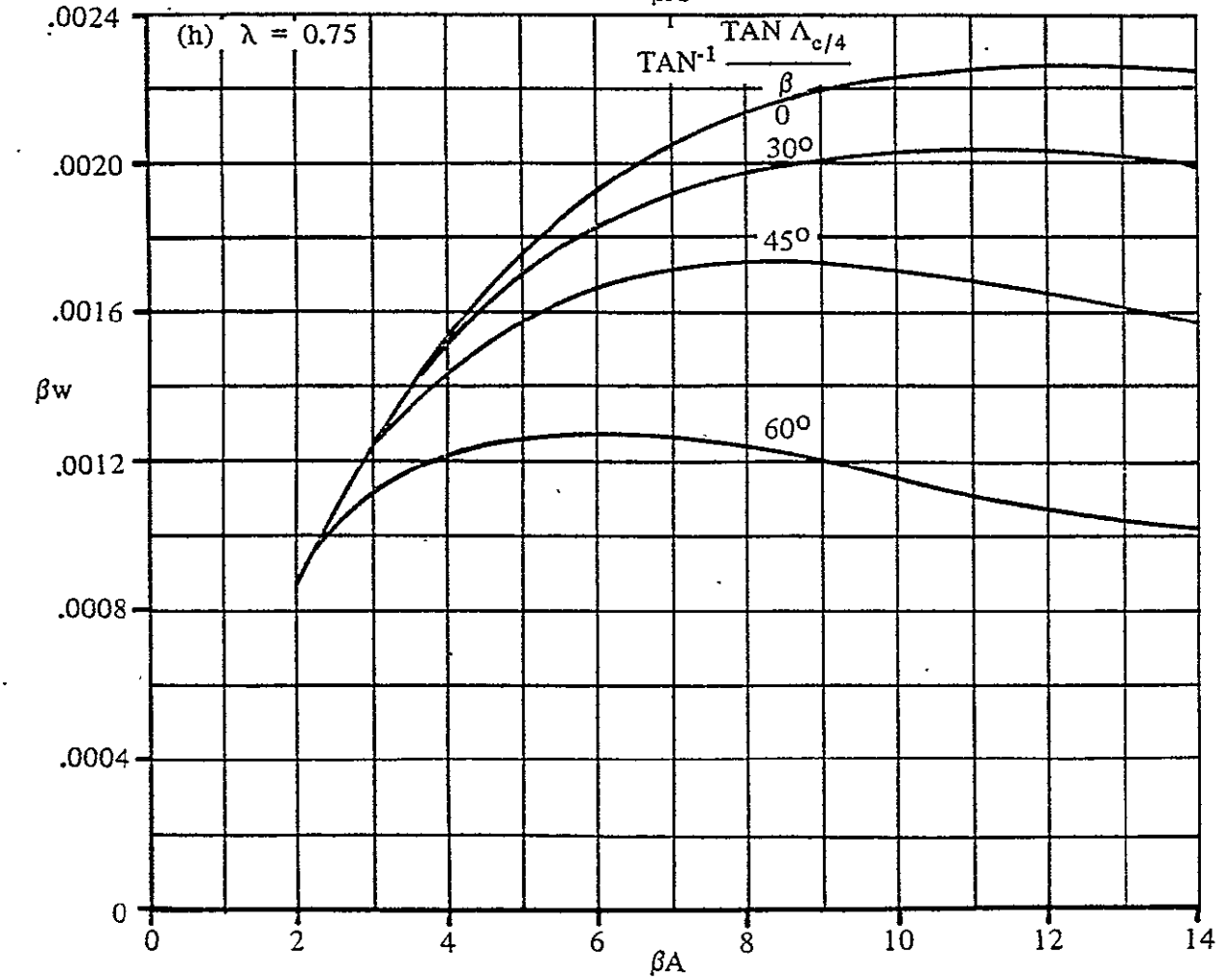

Figure 4.12.4.2: Continued

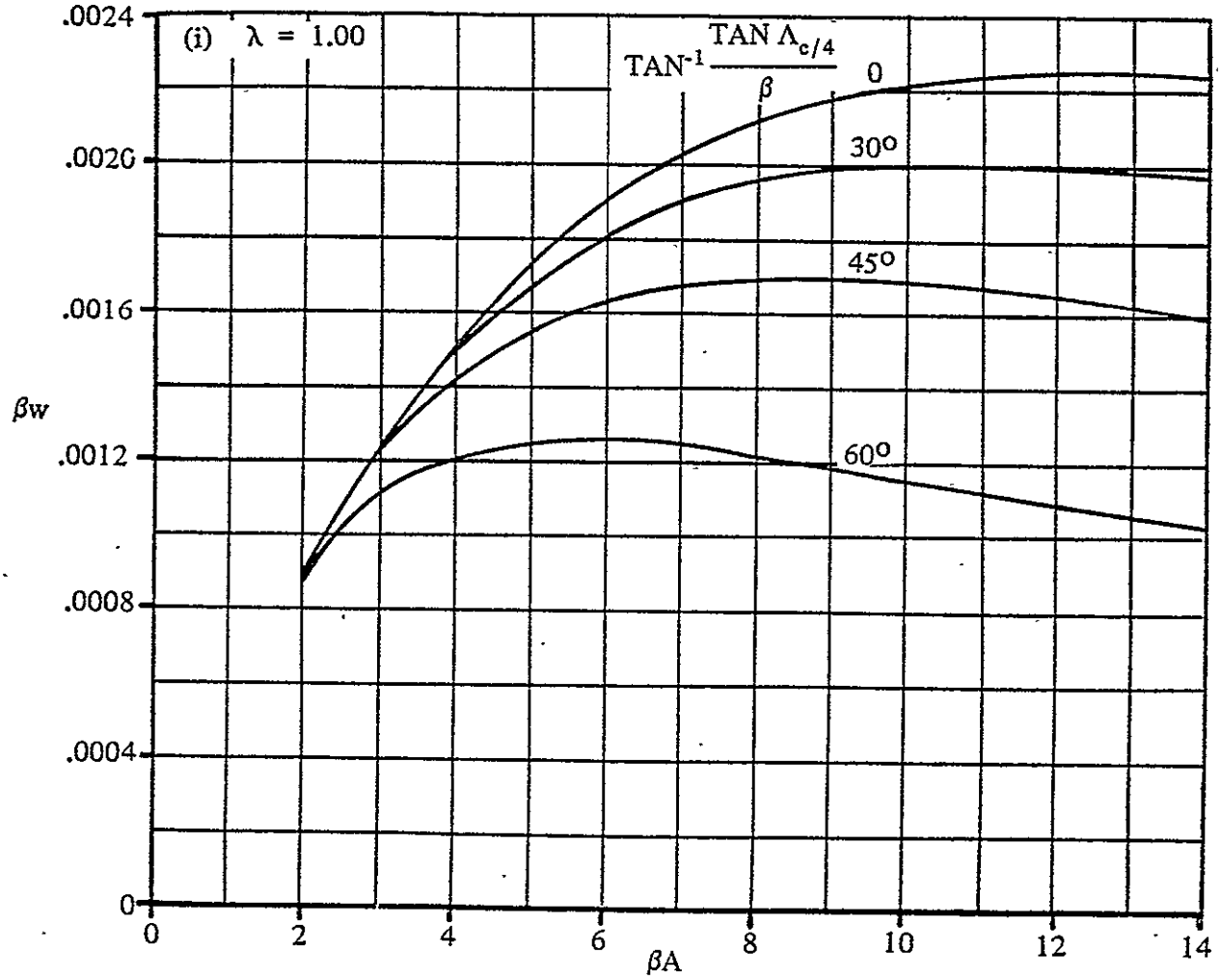

Figure 4.12.4.2: Concluded .

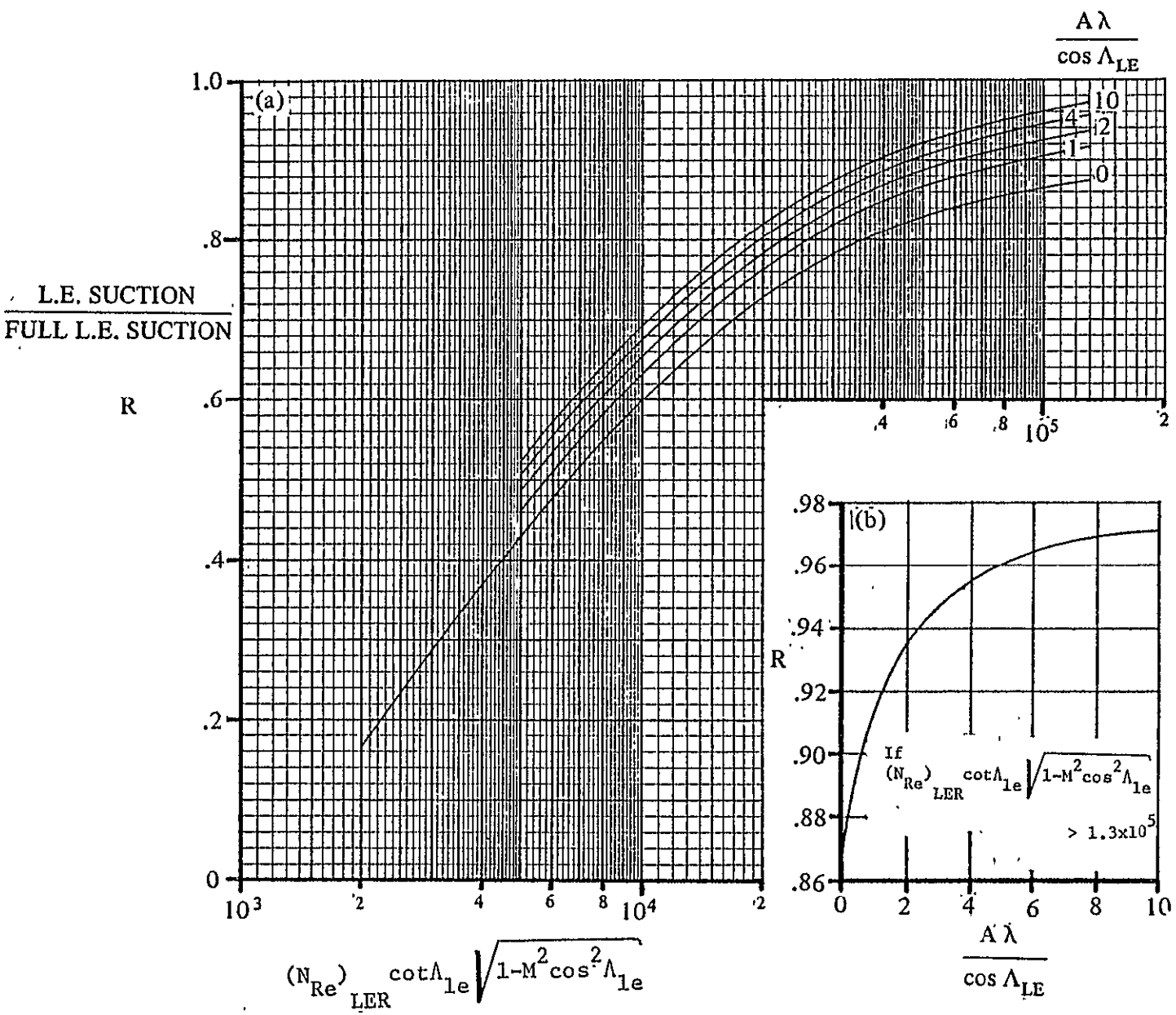

Figure 4.12.4.3: Leading-edge suction parameter at subsonic speeds (Reference 4)

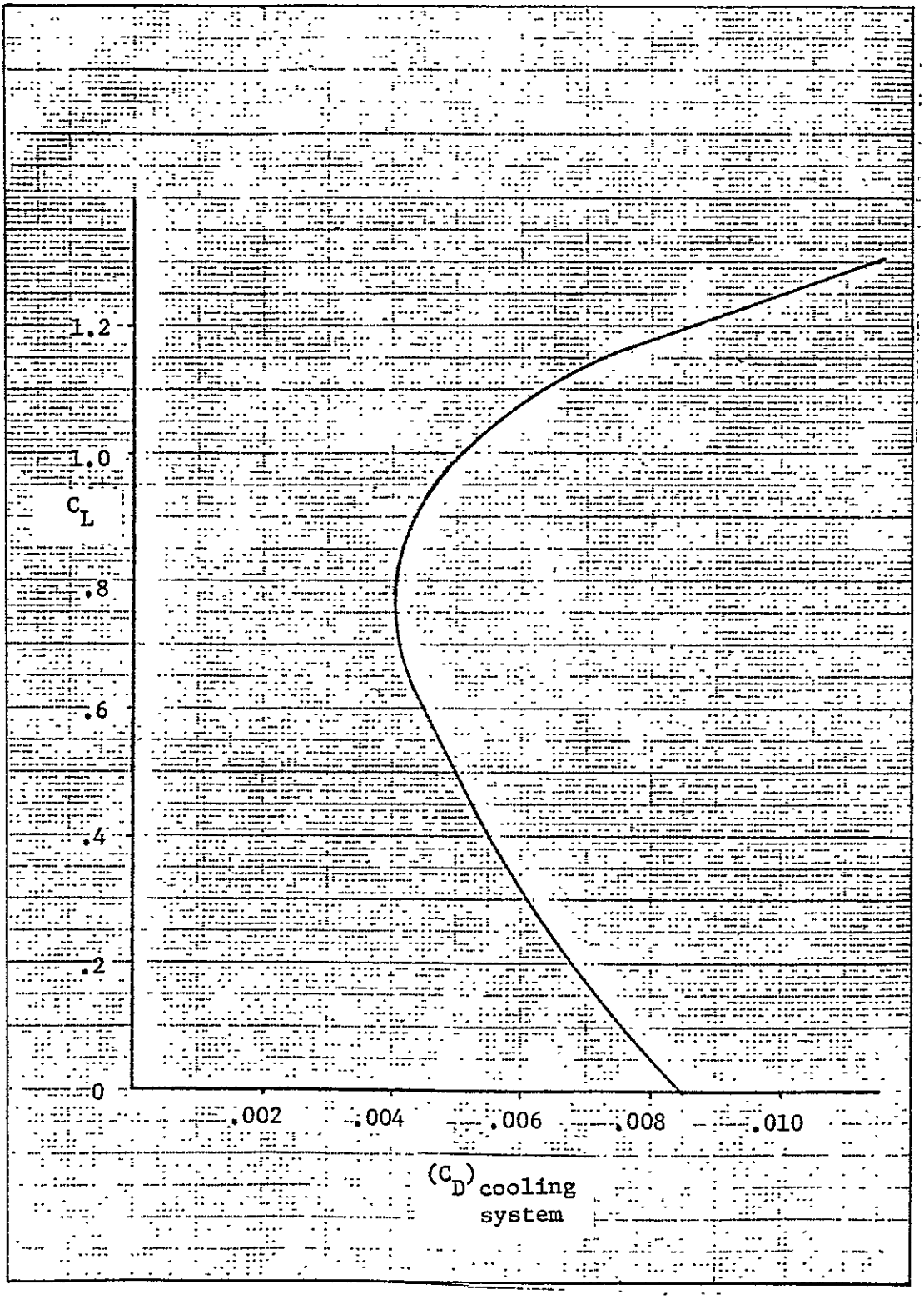

Figure 4.12.7.1: Full-scale wind tunnel data of increment in airplane drag due to open inlets and open cowl flaps (N_{Re} = 3.5 million)

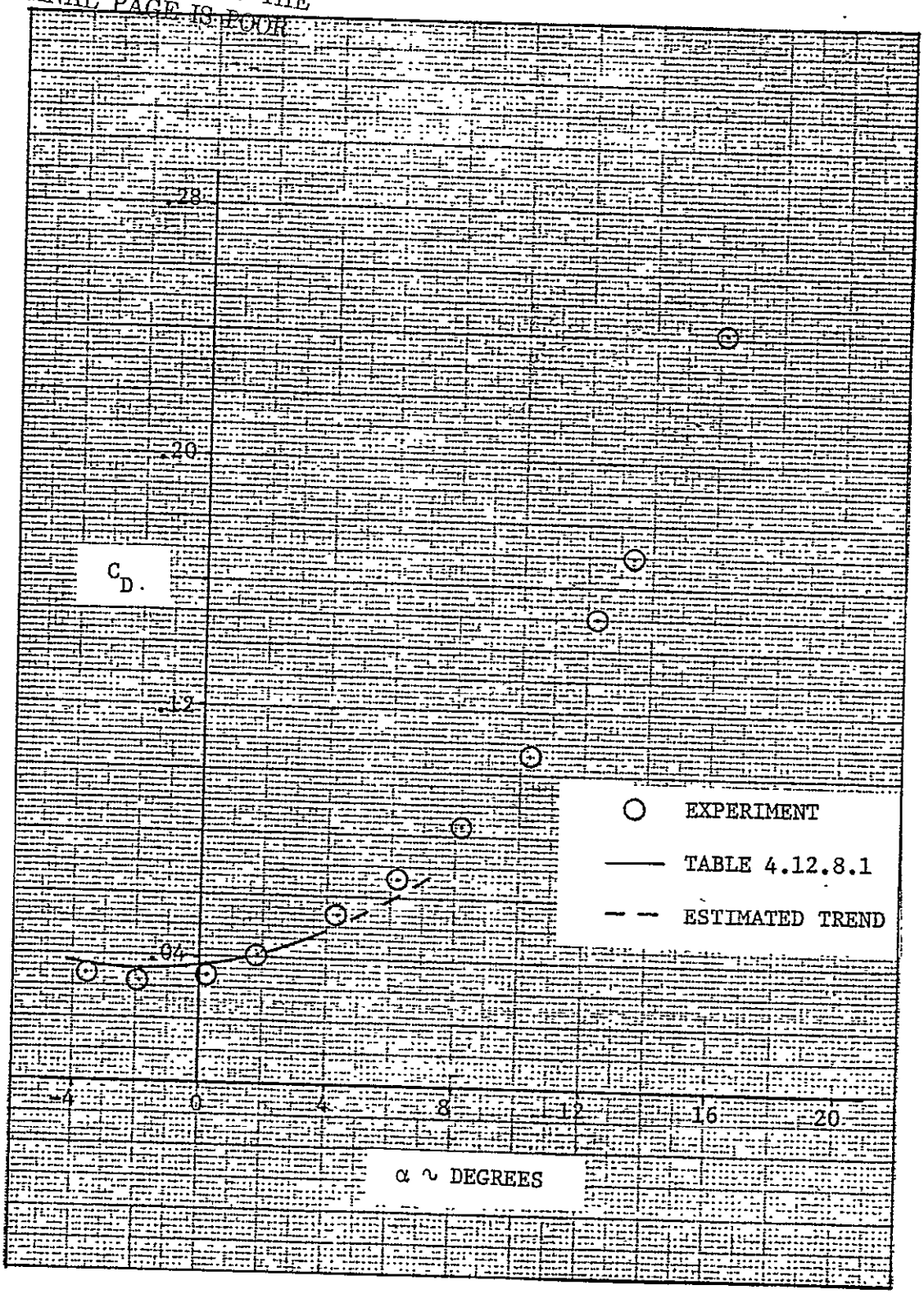

Figure 4.12.8.1: Comparison of predicted airplane drag with full-scale wind tunnel data (propellers removed, no engine cooling drag, N_{Re} = 2.3 million)

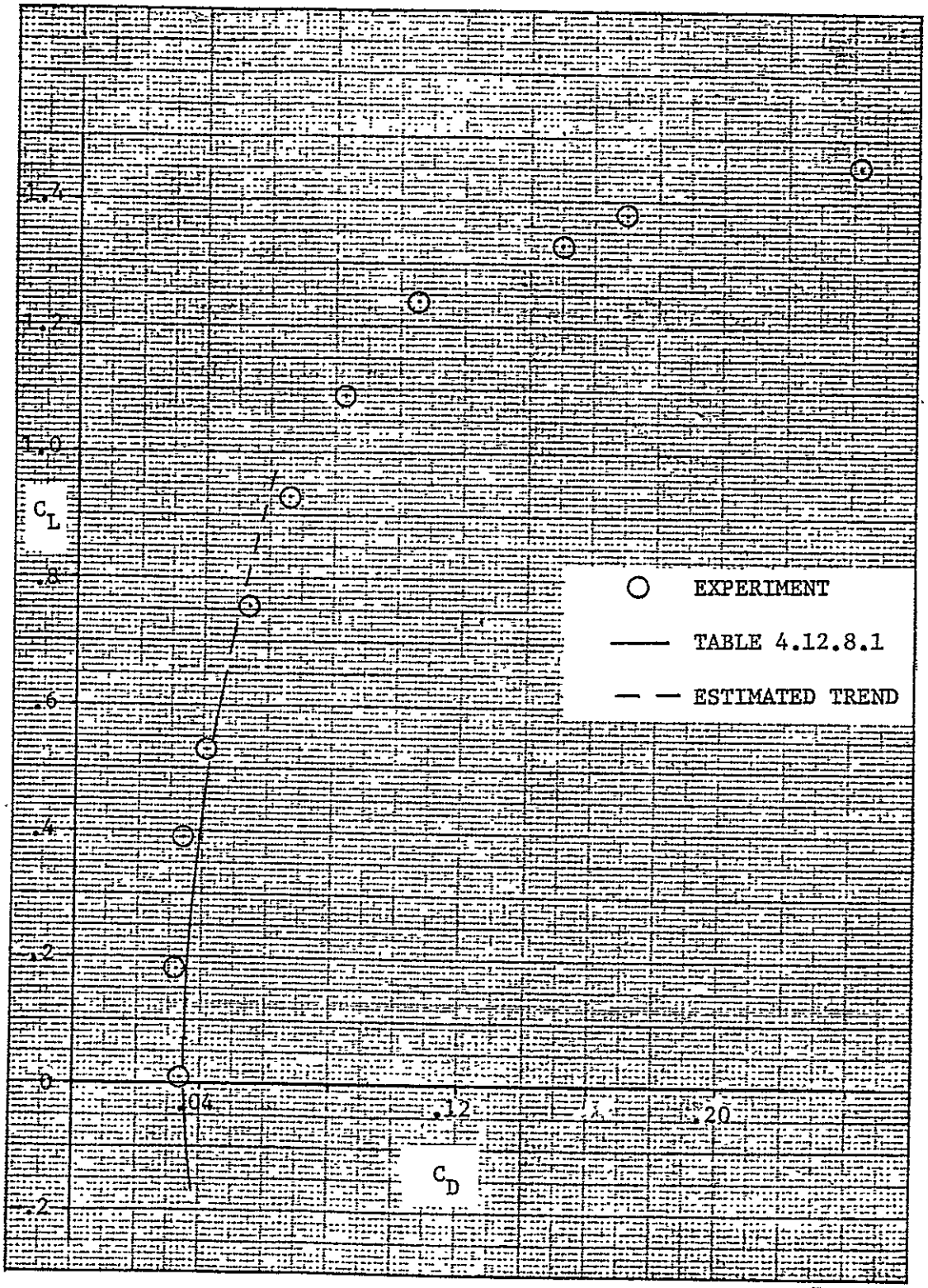

Figure 4.12.8.2: Comparison of predicted airplane drag with full-scale wind tunnel data (propellers removed, no engine cooling drag, N_{Re} = 2.3 million)

4.13 Effect of Horizontal Tail and Tab Deflection on Lift and Pitching Moments

The contributions of the horizontal tail to the lift and pitching moment were considered in Section 4.10 and 4.11, respectively, on the basis of a fixed tail at zero incidence setting. In this section the tail is considered as an all-moving surface with a geared tab.

4.13.1 Lift of the Horizontal Tail in the Linear Lift Range

The lift of an all-moving horizontal tail equipped with a tab is attributed to three superimposed sources:

(1) Lift due to angle of attack of the tail with the tail at zero incidence.

(2) Lift due to stabilizer deflection, i_h, from the zero incidence position.

(3) Lift due to tab deflection.

These three sources can also be found in the following expression which describes the tail lift in the presence of the fuselage; including carryover effects onto the fuselage, referenced to the reference wing area:

$$\bar{C}_{L_{h(hf)}} = \left[(C_{L_\alpha})_{h(hf)} (\alpha - \bar{\varepsilon}_h) + (C_{L_{i_h}})_{\delta_{tab}=0} i_h + C_{L_{\delta_{tab}}} \left(\frac{\delta_{tab}}{i_h}\right) i_h \right] \frac{\bar{q}_h}{\bar{q}_\infty} \frac{S_h}{S_w} \qquad (4.13.1.1)$$

Lift due to angle of attack of the tail with the tail at zero incidence: This lift can be represented as follows:

$$(C_{L_{h(hf)}})_{\substack{i_h=0 \\ \delta_{tab}=0}} = (C_{L_\alpha})_{h(hf)} \, (\alpha - \bar{\varepsilon}_h) \, \frac{\bar{q}_h}{\bar{q}_\infty} \, \frac{S_h}{S_w} \qquad (4.13.1.2)$$

where

$(C_{L_\alpha})_{h(hf)}$ is the horizontal tail lift curve slope in the presence of the fuselage, including the lift on the fuselage due to lift carry-over of the tail onto the fuselage, based on S_h.

$(\alpha - \bar{\varepsilon}_h)$ represents the angle of attack of the horizontal tail.

The calculations for the ATLIT airplane are summarized in Table 4.13.1.1 and the result is (referenced to S_w):

$$(C_{L_{h(hf)}})_{\substack{i_h=0 \\ \delta_{tab}=0}} = 0.0177(\alpha - \bar{\varepsilon}_h) \qquad (4.13.1.3)$$

where

$\bar{\varepsilon}_h$ can be obtained from Section 4.9 as a function of the angle of attack.

Lift due to stabilizer deflection from zero incidence position: The lift due to the stabilizer deflection, i_h, with $\delta_{tab} = 0$ degrees can be obtained in the same manner as the lift due to angle of attack of the tail in Section 4.10 or:

$$(\Delta C_L)_{i_h} = (C_{L_\alpha})_{h_e} \, (k_{h(f)} + k_{f(h)}) \, i_h \, \frac{\bar{q}_h}{\bar{q}_\infty} \, \frac{S_{h_e}}{S_w} \qquad (4.13.1.4)$$

where

$(C_{L_\alpha})_{h_e}$ is the lift curve slope of the exposed tail panels based on S_{h_e}.

S_{h_e} is the area of the exposed tail panels.

$k_{h(f)}$ is the ratio, due to the stabilizer deflection, i_h, of the lift on the stabilizer in the presence of the fuselage to the stabilizer alone obtained from Figure 4.13.1.1.

$k_{f(h)}$ is the ratio, due to the stabilizer-deflection, i_h, of the

stabilizer lift carryover onto the fuselage to the fuselage alone, obtained from Figure 4.13.1.1.

Applied to the ATLIT airplane and referenced to the reference wing area, S_w, Table 4.13.1.2 shows that:

$$(\Delta C_L)_{i_h} = 0.0156\, i_h \qquad (4.13.1.5)$$

where i_h represents the stabilizer deflection in degrees.

Lift due to tab deflection: In Reference 3 the following expression is given for the lift contribution of the tab:

$$C_{L_{\delta_{tab}}} = c_{\ell_{\delta_{tab}}} \frac{(C_{L_{\alpha\, h(f)}})}{(c_{\ell_{\alpha\, h}})} \left[\frac{(\alpha_{\delta_{tab}\, C_L})}{(\alpha_{\delta_{tab}\, c_\ell})} \right] K_b \qquad (4.13.1.6)$$

where

$(C_{L_{\alpha\, h(f)}})$ is the lift-curve slope of the horizontal tail surface alone in the presence of the fuselage based on S_h:

$$(C_{L_{\alpha\, h(f)}}) = (C_{L_{\alpha\, h_e}})\, k_{h(f)}\, \frac{S_{h_e}}{S_h} \qquad (4.13.1.7)$$

where

$(C_{L_{\alpha\, h_e}})$ is the lift-curve slope of the exposed horizontal tail panels based on S_{h_e}.

$k_{h(f)}$ is the ratio, due to the stabilizer deflection, i_h, of the lift on the stabilizer in the presence of the fuselage to the stabilizer alone, obtained from Figure 4.13.1.1.

$(c_{\ell_{\alpha\, h}})$ is the section lift-curve slope of the untabbed tail (δ_{tab} = 0 degrees) obtained from Section 4.1.

$(\alpha_{\delta_{tab}\, C_L})/(\alpha_{\delta_{tab}\, c_\ell})$ is the tab-chord factor obtained from Figure 4.13.1.2 as a function of the aspect ratio of the horizontal tail, A_h, and the parameter, $(\alpha_{\delta_{tab}\, c_\ell})$, which can be obtained from the insert in

Figure 4.13.1.2 as a function of c_{tab}/c_h. When $(\alpha_{\delta_{tab}})_{c_\ell}$ varies along the span, an average value of $(\alpha_{\delta_{tab}})_{c_\ell}$, based on an average value of c_{tab}/c_h, may be used.

K_b is the tab-span factor, obtained from Figure 4.13.1.2 as a function of the horizontal tail taper ratio, λ_h, and the span ratio, $\Delta\eta$, as defined in Figure 4.13.1.3.

$c_{\ell_{\delta_{tab}}}$ is the section lift effectiveness of the tab and may be obtained as follows:

$$c_{\ell_{\delta_{tab}}} = \frac{1}{\beta}\left[\frac{c_{\ell_{\delta_{tab}}}}{(c_{\ell_{\delta_{tab}}})_{theory}}\right](c_{\ell_{\delta_{tab}}})_{theory} K' \qquad (4.13.1.8)$$

where

β is equal to $\sqrt{1 - M^2}$ and

$(c_{\ell_{\delta_{tab}}})_{theory}$ is the theoretical lift effectiveness of the tab, obtained from Figure 4.13.1.4 as a function of c_{tab}/c_h and the thickness ratio of the horizontal tail, $(t/c)_h$

$c_{\ell_{\delta_{tab}}}/(c_{\ell_{\delta_{tab}}})_{theory}$ is an empirical correction factor based on experimental data obtained from Figure 4.13.1.5 as a function of c_{tab}/c_h and $(c_{\ell_\alpha})_{theory}$

$(c_{\ell_\alpha})_{theory}$ is the section lift curve of the untabbed tail:

$$(c_{\ell_\alpha})_{theory} = \frac{\pi}{180}[\,6.28 + 4.7\,(t/c)(1 + 0.00375\,\phi_{te})\,] \qquad (4.13.1.9)$$

K' is an empirical correction for lift effectiveness of the tab at large deflections, obtained from Figure 4.13.1.6

In Tables 4.13.1.3 and 4.13.1.4 the calculations are summarized and the lift effectiveness of the tab, referenced to the horizontal tail area, S_h, is:

$$C_{L_{\delta_{tab}}} = 0.0257 \text{ per degree for } \delta_{tab} = 6,\ 0,\ -6 \text{ and } -12 \text{ degrees}$$

$$C_{L_{\delta_{tab}}} = 0.0239 \text{ per degree for } \delta_{tab} = -18 \text{ degrees} \qquad (4.13.1.10)$$

Applied to the ATLIT airplane and referenced to the wing area, S_w:

$$(\Delta C_L)_{\delta_{tab}} = C_{L_{\delta_{tab}}} \left(\frac{\delta_{tab}}{i_h}\right) i_h \left(\frac{\bar{q}_h}{\bar{q}_\infty}\right) \frac{S_h}{S_w}$$

$$= 0.3745\ C_{L_{\delta_{tab}}}\ i_h \qquad (4.13.1.11)$$

This in the case of a tab-to-stabilizer gear ratio, δ_{tab}/i_h, of 1.5 and a dynamic pressure ratio at the tail, $\bar{q}_h/\bar{q}_\infty$, of 1.0.

In Table 4.13.1.5 the tail lift in the presence of the fuselage, referenced to the wing area, is presented as a function of the stabilizer deflection, i_h, and the angle of attack of the horizontal tail, α_h:

$$\bar{C}_{L_{h(hf)}} = (C_{L_{h(hf)}})_{\substack{i_h = 0 \\ \delta_{tab} = 0}} + (\Delta C_L)_{i_h} + (\Delta C_L)_{\delta_{tab}} \qquad (4.13.1.12)$$

4.13.2 Maximum Lift of the Horizontal Tail

The increment of the maximum lift coefficient due to trailing edge flaps can be determined with the following expression (based on the horizontal tail area, S_h):

$$(\Delta C_{L_{max}})_{\delta_{tab}} = (\Delta c_{\ell_{max}})_{tab} \frac{(S_h)_{tab}}{S_h} K_\Lambda \qquad (4.13.2.1)$$

where

$(S_h)_{tab}$ is the horizontal tail area in front of and including the tab

K_Λ is an empirically derived correction factor to account for the

effects of wing planform, obtained from Figure 4.13.2.1

$(\Delta c_{\ell_{max}})_{tab}$ represents the increment in airfoil maximum lift coefficient due to the tab and can be calculated as follows:

$$(\Delta c_{\ell_{max}})_{tab} = k_1 k_2 k_3 (\Delta c_{\ell_{max}})_{base} \qquad (4.13.2.2)$$

where

$(\Delta c_{\ell_{max}})_{base}$ is the section maximum lift increment for 25-percent chord flaps at a reference flap deflection angle of 60 degrees for plain flaps or tabs, obtained from Figure 4.13.2.2.

k_1 is the factor accounting for c_{tab}/c other than 0.25, obtained from Figure 4.13.2.3

k_2 is the factor accounting for a tab deflection angle other than 60 degrees, obtained from Figure 4.13.2.4

k_3 is the factor accounting for tab motion as a function of $\delta_{tab}/(\delta_{tab})_{reference}$, equal to 1 (one) for plain flaps or tabs.

The maximum lift coefficient for the horizontal tail may now be determined as follows:

$$(\overline{C_{L_{max}}})_{h(hf)} = [(C_{L_{max}})_{h(hf)}]_{\delta_{tab}=0} + (\Delta C_{L_{max}})_{\delta_{tab}} \qquad (4.13.2.3)$$

where

$[(C_{L_{max}})_{h(hf)}]_{\delta_{tab}=0}$ is the maximum lift coefficient of the untabbed tail based on the horizontal tail area and obtained from Section 4.10

The summary calculations for the maximum lift coefficient are presented in Tables 4.13.2.1 and 4.13.2.2.

4.13.3 Lift Curves of the Horizontal Tail through Stall

Because of net lift and pitching moment coefficients of an airplane

for different stabilizer (elevator) positions are dependent upon the tail lift characteristics and could involve the stall region of the tail, operational tail lift curves for the ATLIT airplane are plotted in Figure 4.13.3.1.

The following procedure was used in constructing the lift curve plots:

(1) Using the information from Table 4.13.1.5, draw the slope of the basic lift curve ($i_h = 0$) up to the limit of linearity (α_h^* can be obtained from Table 4.13.1.1).

(2) Spot the stall point for $i_h = 0$ degrees using the information of Table 4.13.2.2. Fair a curve similar to the fairing for the isolated tail in Figure 4.2.4.1 from the limit of linearity through the stall point.

(3) Using the information of Table 4.13.1.5, draw the slope of the other lift curves ($i_h = 4$, -4, -8 and -12 degrees) parallel to the basic lift curve.

(4) Using the maximum lift coefficients, $(\overline{C_{L_{max}}})_{h(hf)}$, of Table 4.13.2.2, draw horizontal lines to denote the different maximum lift values.

(5) Make a plot, to be used as an underlay in tracing of the non-linear part of the basic lift curve. Translate this underlay plot relative to the basic lift curve of the selected stabilizer setting and the corresponding maximum lift coefficient.

4.13.4 Lift and Pitching Moment Curves Including the Effect of Stabilizer Position

The lift and pitching moment characteristics of the ATLIT airplane

may now be determined as a function of angle of attack and stabilizer deflection as follows:

$$C_L = C_{L_{wfn}} + \overline{\overline{C_{L_{h(hf)}}}} \frac{S_h}{S_w} \tag{4.13.4.1}$$

$$C_m = C_{m_{wfn}} + \frac{x_{cg} - x_h}{\bar{c}_w} \overline{\overline{C_{L_{h(hf)}}}} \frac{S_h}{S_w} \tag{4.13.4.2}$$

where

$C_{L_{wfn}}$ is the tail-off lift coefficient which can be obtained from Section 4.4.

$C_{m_{wfn}}$ is the tail-off pitching moment coefficient obtained from Section 4.8

$\overline{\overline{C_{L_{h(hf)}}}}$ is the lift coefficient of the horizontal tail, referenced to the tail area, with tail-fuselage interaction effects, angle of attack, stabilizer deflection and tab deflection accounted for

$(x_{cg} - x_h)/\bar{c}_w$ is the distance from the center of gravity of the airplane to the quarter chord of the horizontal tail mean aerodynamic chord in chord lengths of the wing mean aerodynamic chord

The lift coefficient as a function of the angle of attack, α, and the stabilizer deflection, i_h, is calculated in Table 4.13.4.1. The pitching moment coefficient calculations are shown in Table 4.13.4.2. The results are compared with the full-scale wind tunnel data in Figures 4.13.4.1 through 4.13.4.3.

However, no wind tunnel data were available with the ATLIT airplane in the "fully clean" configuration. The effect of the stabilizer deflection was obtained in the same manner as the effect of the horizontal tail. (See Appendix D.) The incremental lift and pitching moment due to the stabilizer deflection are obtained

for the "power-off" condition for the airplane "as built" and then added to the results of the ATLIT airplane in the "fully clean" configuration (propellers removed) and a stabilizer setting of zero.

The predicted lift and pitching moment curves show poor agreement with the experimental data, especially in the cases i_h = -8 and -12 degrees. At low angles of attack, the experimental results reflect the tail stall when i_h = -8 and -12 degrees. The predicted curves, however, do not show this effect.

In Figure 3.13.4.4 the calculated incremental lift due to the stabilizer deflection has been added up to the experimental lift curve with a stabilizer setting of zero. This graph gives a better indication of the accuracy of the calculated stabilizer effectiveness. The comparison with the experimental results shows that the calculated lift effectiveness, $C_{L_{i_h}}$, is higher than indicated by the wind tunnel data. This has also its effect on the pitch control effectiveness, $C_{m_{i_h}}$, which is also higher than the experimental value as shown in Figure 4.14.4.2.

According to Reference 3, the factor $k_{f(h)}$, the ratio of the lift carry-over onto the fuselage to the lift of the stabilizer alone, causes the discrepancy. The value of this ratio, $k_{f(h)} = 0.10$, is too high for the type of tail-body configuration of the ATLIT airplane. In Reference 3 it is suggested that $k_{f(h)}$ be considered negligible for this type of tail-body configurations. By neglecting this factor, the calculated tail effectiveness, $C_{L_{i_h}}$, decreases by approximately 6 percent.

A second factor, which affects the change in lift due to stabilizer deflection, is the dynamic pressure ratio at the horizontal tail, $\bar{q}_h/\bar{q}_\infty$.

This ratio has been assumed to be equal to one. However, for the type of tail-body configuration of the ATLIT a value $\bar{q}_h/\bar{q}_\infty = 0.85$ seems to be more accurate (see Section 4.9). The decrease in dynamic pressure ratio will decrease the calculated lift effectiveness, $C_{L_{i_h}}$, and pitch-control effectiveness, $C_{m_{i_h}}$.

The above two changes will result in an improved agreement between the predicted results and the full-scale wind tunnel data.

Table 4.13.1.1: Lift contribution of the horizontal tail due to angle of attack ($i_h = \delta_{tab} = 0^o$)

Symbol	Description	Reference	Magnitude
$(C_{L_\alpha})_{h(hf)}$	Lift curve slope of tail with tail-fuselage intersection effects, referenced to S_h, deg^{-1}	Table 4.10.3.1	0.0709
$\alpha_h{}^*$	Limit of linearity, deg.	Table 4.10.3.1	12.2
$\bar{\varepsilon}_h$	Average downwash at the horizontal tail, deg.	Figure 4.9.3.1	Variable
$\bar{q}_h/\bar{q}_\infty$	Dynamic-pressure ratio at tail	Figure 4.9.3.2	1.0
S_h	Area of horizontal tail, $m^2(ft^2)$	Table 2.1.1	3.60 (38.7)
S_w	Reference wing area, $m^2(ft^2)$	Table 2.1.1	14.40 (155.0)

Summary: $(C_{L_{h(hf)}})_{\substack{i_h=0 \\ \delta_{tab}=0}} = (C_{L_\alpha})_{h(hf)} (\alpha - \bar{\varepsilon}_h) \frac{\bar{q}_h}{\bar{q}_\infty} \frac{S_h}{S_w}$

$= 0.0177 (\alpha - \bar{\varepsilon}_h)$ based on S_w and up to $\alpha_h{}^* = 12.2$ degrees

Table 4.13.1.2: Lift contribution due to stabilizer deflection ($\delta_{tab} = 0^{o}$)

Symbol	Description	Reference	Magnitude
$(d_f)_h$	Fuselage width at horizontal tail, m(ft)	Figure 2.1.2	0.405 (1.33)
b_h	Span of horizontal tail, m(ft)	Table 2.1.1	4.133 (13.56)
$(d_f/b)_h$	—	—	0.098
$k_{h(f)}$	Ratio of lift on movable tail in presence of body to tail alone	Figure 4.13.1.1	0.97
$k_{f(h)}$	Ratio of movable tail lift carryover on body to tail alone	Figure 4.13.1.1	0.10
$(C_{L_\alpha})_{h_e}$	Lift curve slope of exposed horizontal tail panels referenced to S_{h_e}, deg^{-1}	Table 4.2.4.1	0.0649
S_{h_e}	Area of exposed horizontal tail panels	Figure 2.1.1	3.25 (34.9)
S_w	Reference wing area	Table 2.1.1	14.40 (155.0)
$\bar{q}_h/\bar{q}_\infty$	Dynamic-pressure ratio at horizontal tail	Figure 4.9.3.2	1.0

Summary: $(\Delta C_L)_{i_h} = (C_{L_\alpha})_{h_e} (k_{h(f)} + k_{f(h)})\, i_h \frac{\bar{q}_h}{\bar{q}_\infty} \frac{S_{h_e}}{S_w}$

$= 0.0156\, i_h$ based on S_w

Table 4.13.1.3: Tab effectiveness of the ATLIT.

Symbol	Description	Reference	Magnitude
M	Mach number	—	0.081
β	$\sqrt{1 - M^2}$	—	0.9967
$(t/c)_h$	Thickness ratio of horizontal tail	Table 4.1.2	0.10
ϕ_{te}	Trailing edge angle of horizontal tail, deg.	Table 4.1.2	13.0
A_h	Aspect ratio of horizontal tail	Table 2.1.1	4.75
λ_h	Taper ratio of horizontal tail	Table 2.1.1	1.0
S_h	Area of horizontal tail, $m^2(ft^2)$	Table 2.1.1	3.60 (38.7)
S_{h_e}	Area of exposed horizontal tail panels, $m^2(ft^2)$	Table 2.1.1	3.25 (34.9)
S_w	Reference wing area, $m^2(ft^2)$	Table 2.1.1	14.40 (155.0)
c_{tab}/c_h	Ratio of tab chord to tail chord	Table 2.1	0.204
η_i	Distance from root chord of tail to inboard edge of tab as a fraction of tail semi-span	Figure 2.1.2	0
η_o	Distance from root chord of tail to outboard edge of tab as a fraction of tail semi-span	Figure 2.1.2	0.731
$(c_{\ell_\alpha})_h$	Section lift-curve slope of tail, deg^{-1}	Table 4.1.2	0.109
$(C_{L_\alpha})_{h_e}$	Lift-curve slope of exposed tail panels, based on S_{h_e}, deg^{-1}	Table 4.2.4.1	0.0649
$k_{h(f)}$	Ratio of lift on movable tail in presence of body to tail alone	Table 4.13.1.2	0.97
$(C_{L_\alpha})_{h(f)}$	Lift curve slope of tail surface alone in presence of fuselage, based on S_h, deg^{-1}	Eq. (4.13.1.7)	0.0568
$(\alpha_{\delta_{tab}})_{c_\ell}$	Section lift parameter	Figure 4.13.1.2	−0.556
$\frac{(\alpha_{\delta_{tab}})_{C_L}}{(\alpha_{\delta_{tab}})_{c_\ell}}$	Ratio of finite and section lift parameter	Figure 4.13.1.2	1.071
K_b	Span factor	Figure 4.13.1.3	0.83
$(c_{\ell_\alpha})_{theory}$	Theoretical section lift-curve slope of tail, deg^{-1}	Eq. (4.13.1.9)	0.1182
$\frac{(c_{\ell_\alpha})_h}{(c_{\ell_\alpha})_{theory}}$	—	—	0.922
$\frac{c_{\ell_{\delta_{tab}}}}{(c_{\ell_{\delta_{tab}}})_{theory}}$	Function of c_{tab}/c_h and $(c_{\ell_\alpha})_h/(c_{\ell_\alpha})_{theory}$	Figure 4.13.1.5	0.873
$(c_{\ell_{\delta_{tab}}})_{theory}$	Theoretical section effectiveness, deg^{-1}	Figure 4.13.1.4	0.0634

Summary: $$C_{L_{\delta_{tab}}} = \frac{1}{\beta}\left[\frac{c_{\ell_{\delta_{tab}}}}{(c_{\ell_{\delta_{tab}}})_{theory}}\right](c_{\ell_{\delta_{tab}}})_{theory} K' \frac{(C_{L_\alpha})_{h(f)}}{(c_{\ell_\alpha})_h}\left[\frac{(\alpha_{\delta_{tab}})_{C_L}}{(\alpha_{\delta_{tab}})_{c_\ell}}\right]K_b$$

$$= 0.0257\ K' \text{ based on } S_h$$

Table 4.13.1.4: Lift contribution due to tab deflection

δ_{tab}, deg.	K' Figure 4.13.1.6	$C_{L_{\delta_{tab}}}$ based on S_h, deg^{-1} Eq. (4.13.1.6)
6	1.0	0.0257
0	1.0	0.0257
-6	1.0	0.0257
-12	1.0	0.0257
-18	0.93	0.0239

Table 4.13.1.5: Lift contribution of the horizontal tail with $\delta_{tab}/i_h = 1.5$

i_h, deg.	δ_{tab}, deg.	$(C_{L_{h(hf)}})_{\substack{i_h=0 \\ \delta_{tab}=0}}$ Eq. (4.13.1.3)	$(\Delta C_L)_{i_h}$ Eq. (4.13.1.5)	$(\Delta C_L)_{\delta_{tab}}$ Eq. (4.13.1.11)	$\bar{C}_{L_{h(hf)}}$ based on S_w Eq. (4.13.1.12)	$\bar{C}_{L_{h(hf)}}$ based on S_h
4	6	$0.0177(\alpha - \bar{\varepsilon}_h)$	$0.0156 i_h$	$0.0096 i_h$	$0.0177(\alpha - \bar{\varepsilon}_h) + 0.0252 i_h$	$0.0709(\alpha - \bar{\varepsilon}_h) + 0.1009 i_h$
0	0					
-4	-6					
-8	-12					
-12	-18	$0.0177(\alpha - \bar{\varepsilon}_h)$	$0.0156 i_h$	$0.0090 i_h$	$0.0177(\alpha - \bar{\varepsilon}_h) + 0.0246 i_h$	$0.0709(\alpha - \bar{\varepsilon}_h) + 0.0985 i_h$

Table 4.13.2.1: Change in maximum lift coefficient of the horizontal tail due to tab deflection.

Symbol	Description	Reference	Magnitude
$(\Lambda_{c/4})_h$	Sweep of horizontal tail along c/4 line, deg.	Table 2.1.1	0
$(t/c)_h$	Section thickness ratio of horizontal tail	Table 4.1.2	0.10
c_{tab}/c_h	Tab chord as ratio of tail chord	Figure 2.1.2	0.204
$(S_h)_{tab}$	Area of horizontal tail in front of and including tab, $m^2(ft^2)$	Figure 2.1.2	3.40 (36.6)
S_h	Area of horizontal tail, $m^2(ft^2)$	Table 2.1.1	3.60 (38.7)
S_w	Reference wing area, $m^2(ft^2)$	Table 2.1.1	14.40 (155.0)
K_Λ	Correction factor for wing planform	Figure 4.13.2.1	0.92
$(\Delta c_{\ell_{max}})_{base}$	Section maximum lift increment for 25-percent chord tab	Figure 4.13.2.2	0.81
k_1	Factor accounting for c_{tab}/c_h other than 0.25	Figure 4.13.2.3	0.94
k_2	Factor accounting for tab deflection other than 60 degrees	Figure 4.13.2.4	Variable
k_3	Factor accounting for tab motion as a function of $\delta_{tab}/(\delta_{tab})_{reference}$	—	1.0
$[(C_{L_{max}})_{h(hf)}]_{\delta_{tab}=0}$	Horizontal tail maximum lift coefficient with $\delta_{tab} = 0^o$ in presence of fuselage based on S_h	Table 4.10.3.2	$\pm$ 1.214
$[(\alpha_{C_{L_{max}}})_{h(hf)}]_{\delta_{tab}=0}$	Horizontal tail angle of attack, deg.	Table 4.10.3.2	$\pm$ 19.3

Summary: $(\Delta C_{L_{max}})_{\delta_{tab}} = k_1\, k_2\, k_3\, (\Delta c_{\ell_{max}})_{base}\, \frac{(S_h)_{tab}}{S_h}\, K_\Lambda$

$= 0.6625\, k_2$ based on S_h

Table 4.13.2.2: Maximum lift coefficient of the horizontal tail

i_h, deg.	δ_{tab}, deg.	k_2 Figure 4.13.2.4	$(\Delta C_{L_{max}})_{\delta_{tab}}$ Eq. (4.13.2.1)	$(\bar{C}_{L_{max}})_{h(hf)}$ Eq. (4.13.2.3)	
				(a)	(b)
4	6	0.22	0.146	-1.068	1.360
0	0	0	0	-1.214	1.214
-4	-6	-0.22	-0.146	-1.360	1.068
-8	-12	-0.40	-0.265	-1.479	0.949
-12	-18	-0.53	-0.325	-1.566	0.862

(a) for negative α_h

(b) for positive α_h

Table 4.13.4.1: Lift coefficient of the ATLIT airplane (δ_{tab}/i_h=1.5)

α, deg	$\bar{\varepsilon}_h$, deg Figure 4.9.3.1	α_h, deg $\alpha - \bar{\varepsilon}_h$	$\bar{C}_{L_{h(hf)}}$ from Figure 4.13.4.1 based on S_h					$C_{L_{wfn}}$ Table 4.4.3.3	C_L with Eq. (4.13.4.1) based on S_w				
			i_h = 4°	i_h = 0°	i_h = -4°	i_h = -8°	i_h = -12°		i_h = 4°	i_h = 0°	i_h = -4°	i_h = -8°	i_h = -12°
-4	-0.26	-3.74	0.1384	-0.2652	-0.6688	-1.0724	-1.448	-0.0780	-0.0434	-0.1442	-0.2450	-0.3458	-0.4395
-2	0.564	-2.564	0.2218	-0.1818	-0.5854	-0.9890	-1.363	0.1141	0.1695	0.0687	-0.0321	-0.1328	-0.2262
0	1.377	-1.377	0.3060	-0.0976	-0.5012	-0.9048	-1.280	0.3066	0.3830	0.2822	0.1815	0.0807	-0.0130
2	2.192	-0.192	0.3900	-0.0136	-0.4172	-0.8208	-1.1956	0.4997	0.5971	0.4963	0.3955	0.2948	0.2012
4	2.990	1.010	0.4752	0.0716	-0.3320	-0.7356	-1.1104	0.6932	0.8118	0.7111	0.6103	0.5095	0.4160
15.9	7.238	8.662	1.0177	0.6141	0.2105	-0.1931	-0.5679	1.5731	1.8272	1.7264	1.6257	1.5249	1.4313

Table 4.13.4.2: Pitching moment of the ATLIT airplane (δ_{tab}/i_h=1.5).

α, deg	$\bar{\varepsilon}_h$, deg Figure 4.9.3.1	α_h, deg $\alpha - \bar{\varepsilon}_h$	$\bar{C}_{L_{h(hf)}} \left(\frac{x_{cg} - x_h}{\bar{c}_w}\right)^*$ from Table 4.13.4.1					$C_{m_{wfn}}$ Table 4.8.4.1	C_m with Eq. (4.13.4.2) based on S_w				
			i_h = 4°	i_h = 0°	i_h = -4°	i_h = -8°	i_h = -12°		i_h = 4°	i_h = 0°	i_h = -4°	i_h = -8°	i_h = -12°
-4	-0.26	-3.74	-0.5447	1.0438	2.6324	4.2210	5.699	-0.1256	-0.2616	0.1350	0.5317	0.9283	1.2973
-2	0.564	-2.564	-0.8730	0.7156	2.3041	3.8927	5.365	-0.0806	-0.2986	0.0981	0.4947	0.8913	1.2589
0	1.377	-1.377	-1.2044	0.3842	1.9727	3.5613	5.038	-0.0365	-0.3372	0.0594	0.4560	0.8527	1.2214
2	2.192	-0.192	-1.5350	0.0535	1.6421	3.2307	4.7059	0.0067	-0.3766	0.0201	0.4167	0.8133	1.1817
4	2.990	1.010	-1.8704	-0.2818	1.3068	2.8953	4.3705	0.0490	-0.4180	-0.0214	0.3753	0.7719	1.1402
15.9	7.238	8.662	-4.0057	-2.4171	-0.8285	0.7600	2.2353	0.1674	-0.8327	-0.4361	-0.0395	0.3572	0.7255

* $\frac{x_{cg} - x_h}{\bar{c}_w}$ = -3.936 obtained from Table 4.11.1

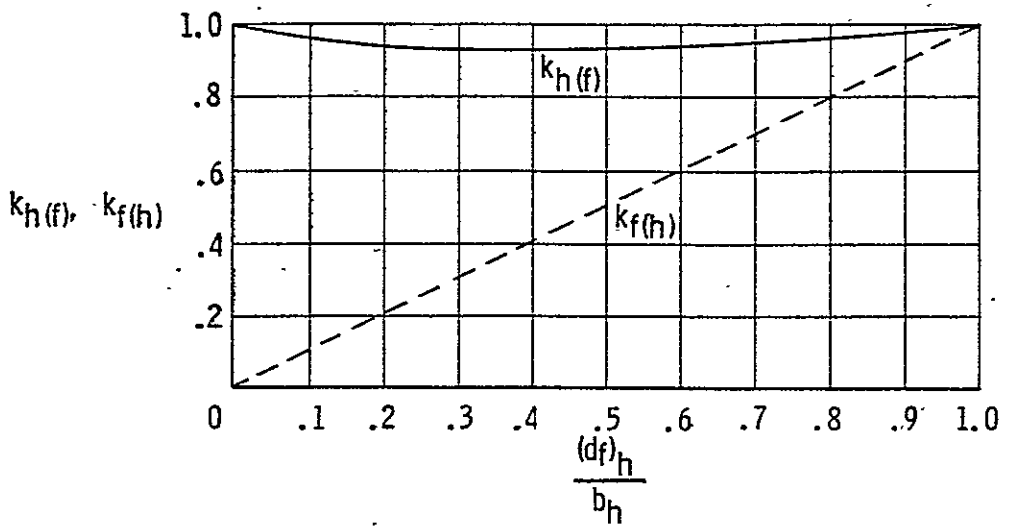

Figure 4.13.1.1: Lift ratios $k_{h(f)}$ and $k_{f(h)}$ (Reference 3)

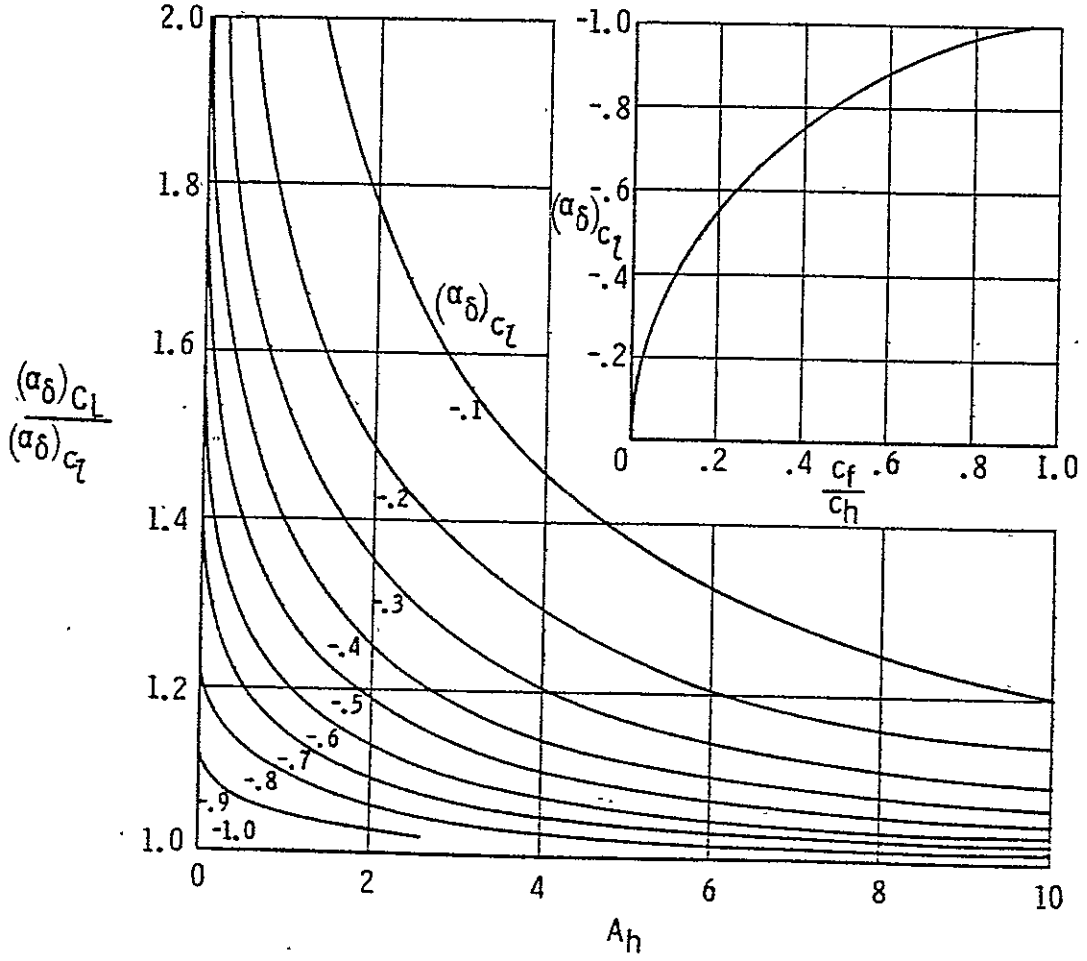

Figure 4.13.1.2: Tab chord factor with $c_f = c_{tab}$ (Reference 3)

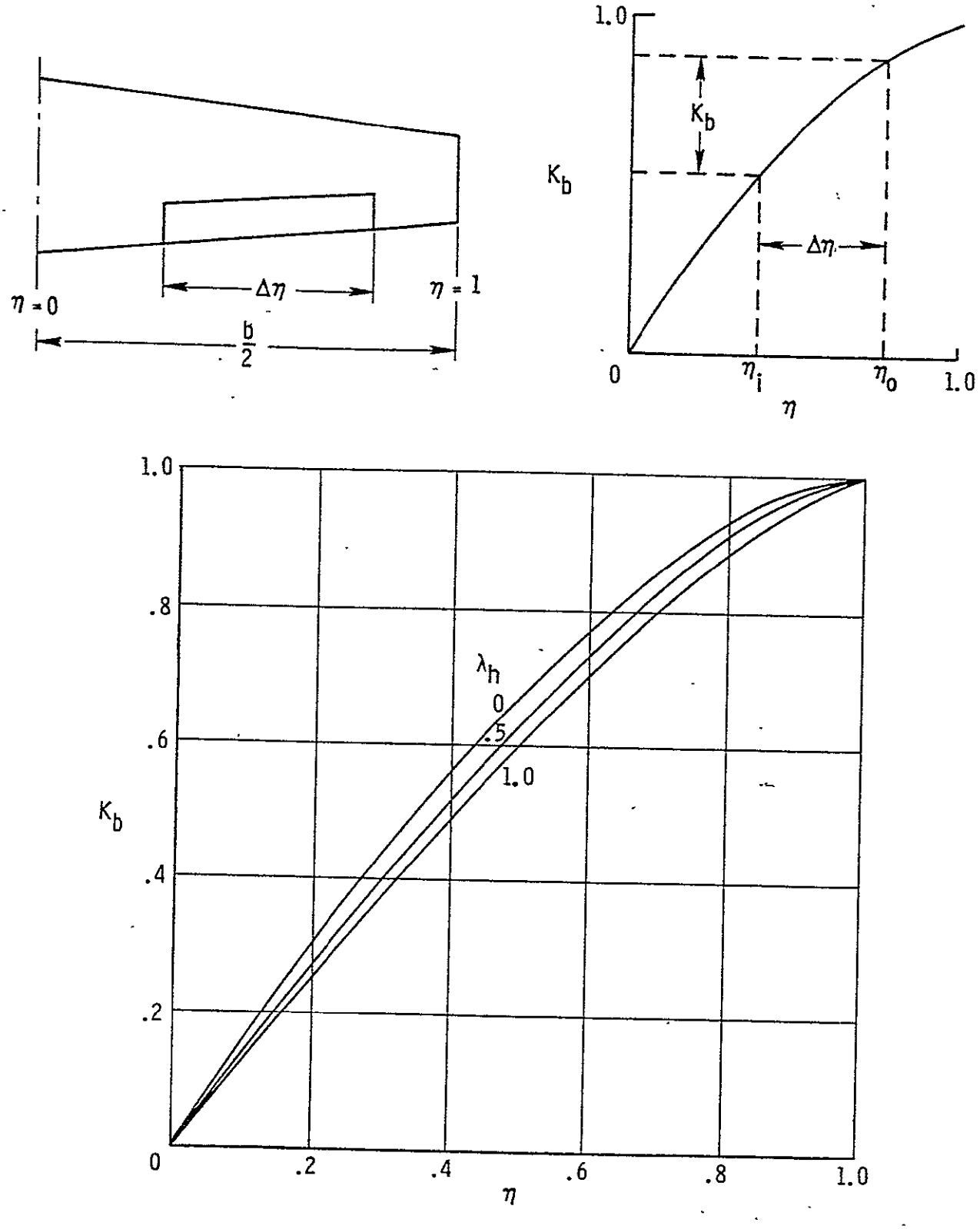

Figure 4.13.1.3: Span factor for inboard flaps (Reference 3)

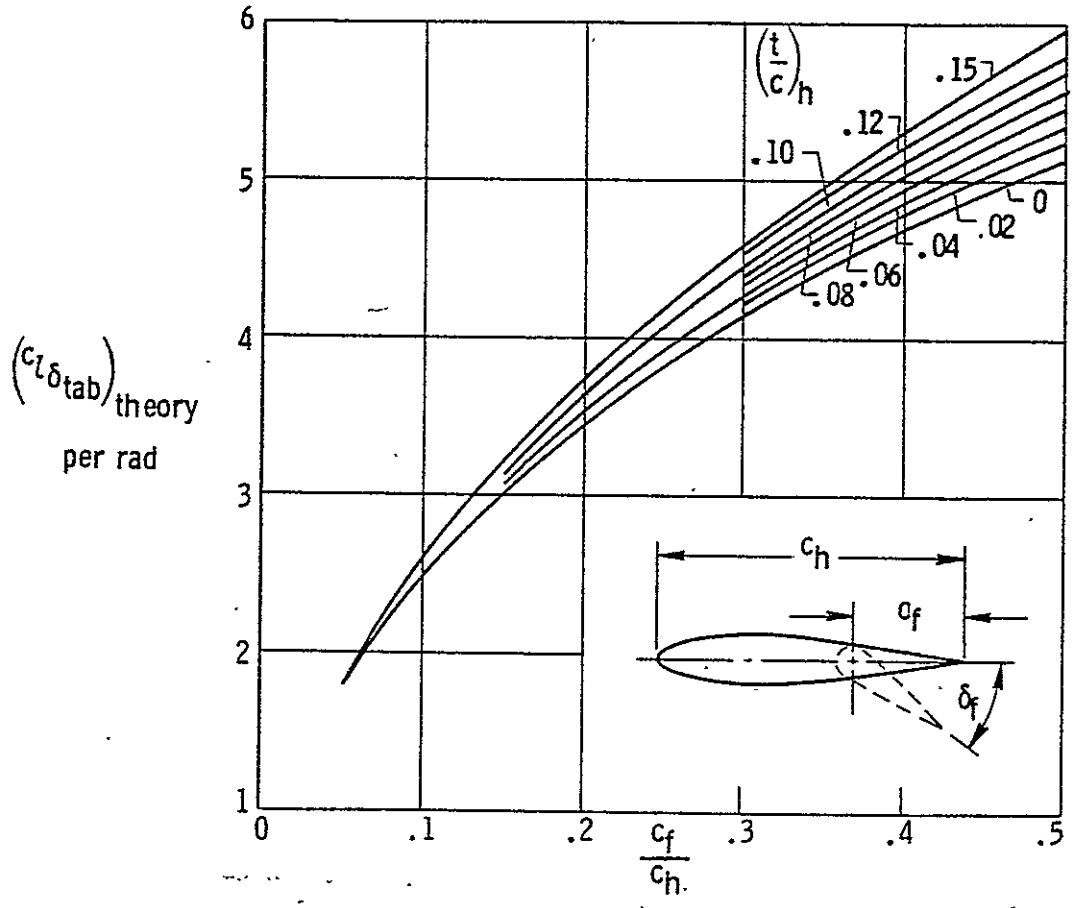

Figure 4.13.1.4: Theoretical lift effectiveness of plain trailing edge flap; $c_f = c_{tab}$ (Reference 3)

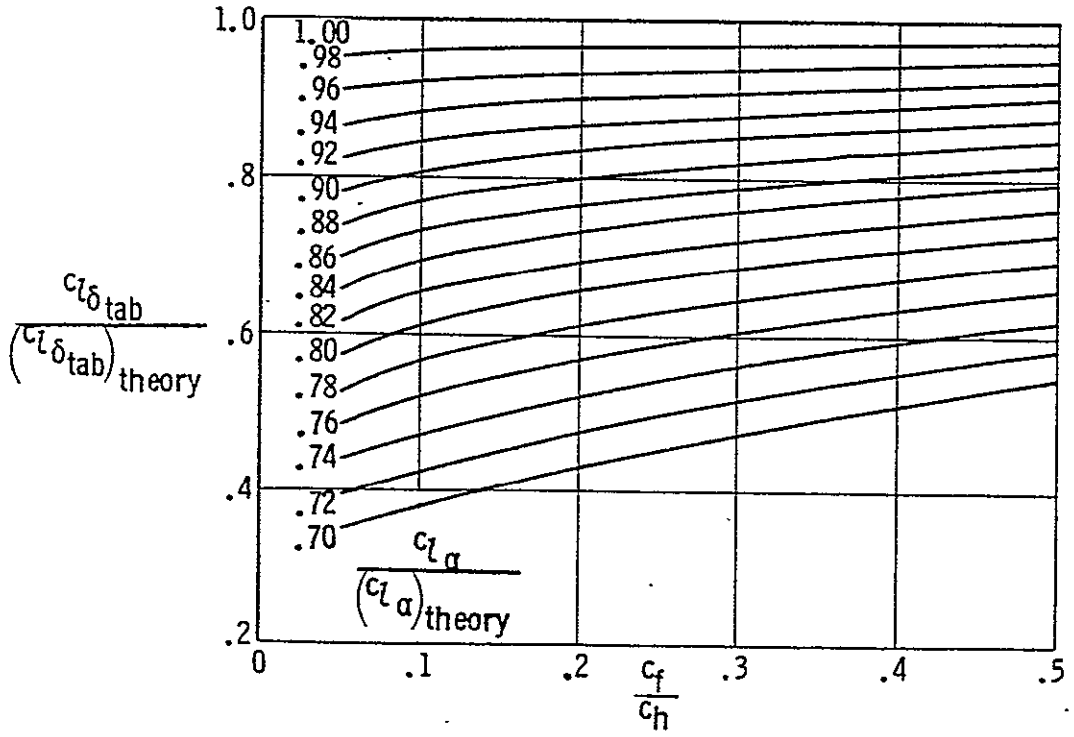

Figure 4.13.1.5: Empirical correction for lift effectiveness of plain trailing edge flaps; $c_f = c_{tab}$ (Reference 3)

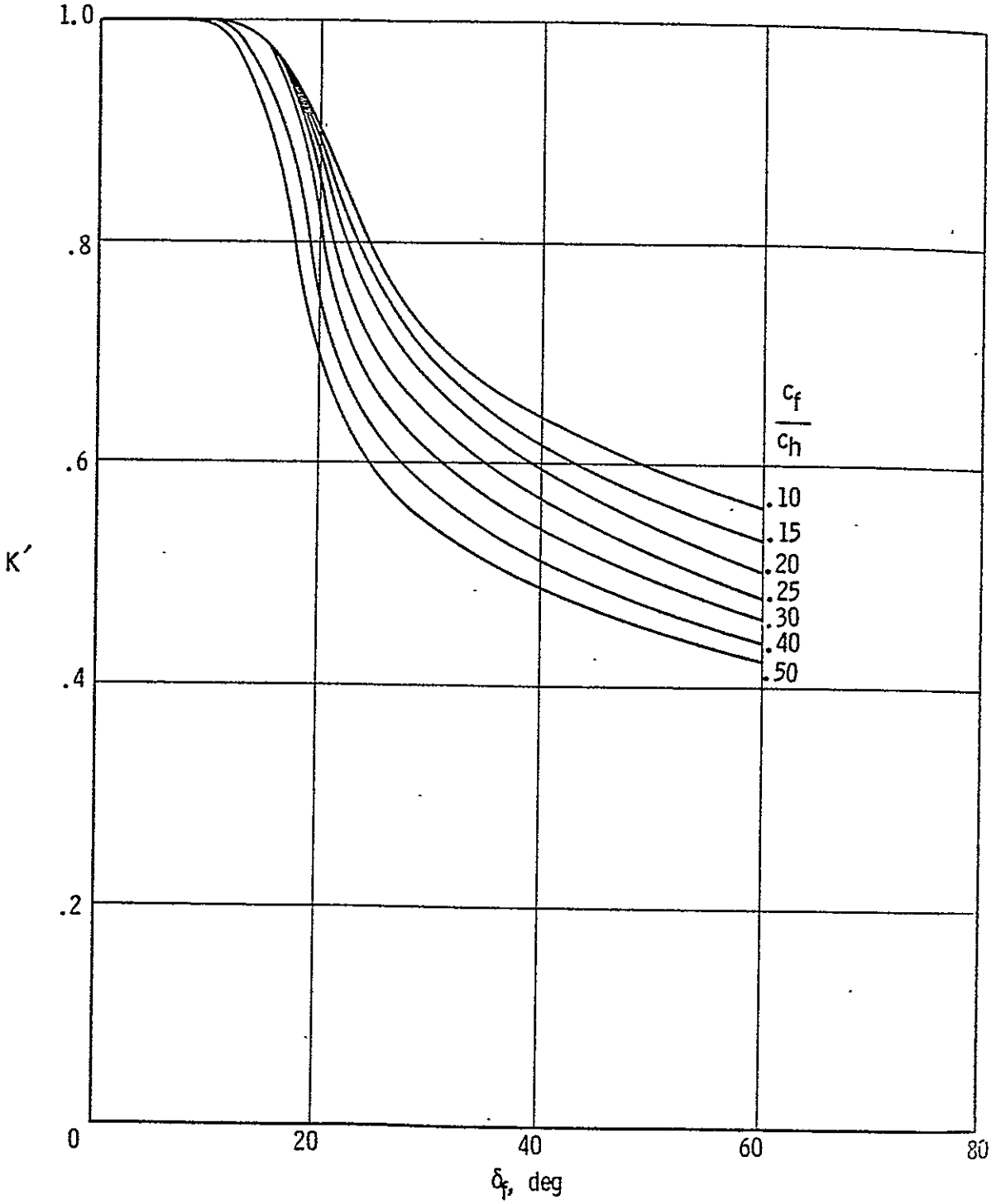

Figure 4.13.1.6: Empirical correction factor for lift effectiveness of plain trailing-edge flaps at high flap deflections; $\delta_f = \delta_{tab}$ and $c_f = c_{tab}$ (Reference 3)

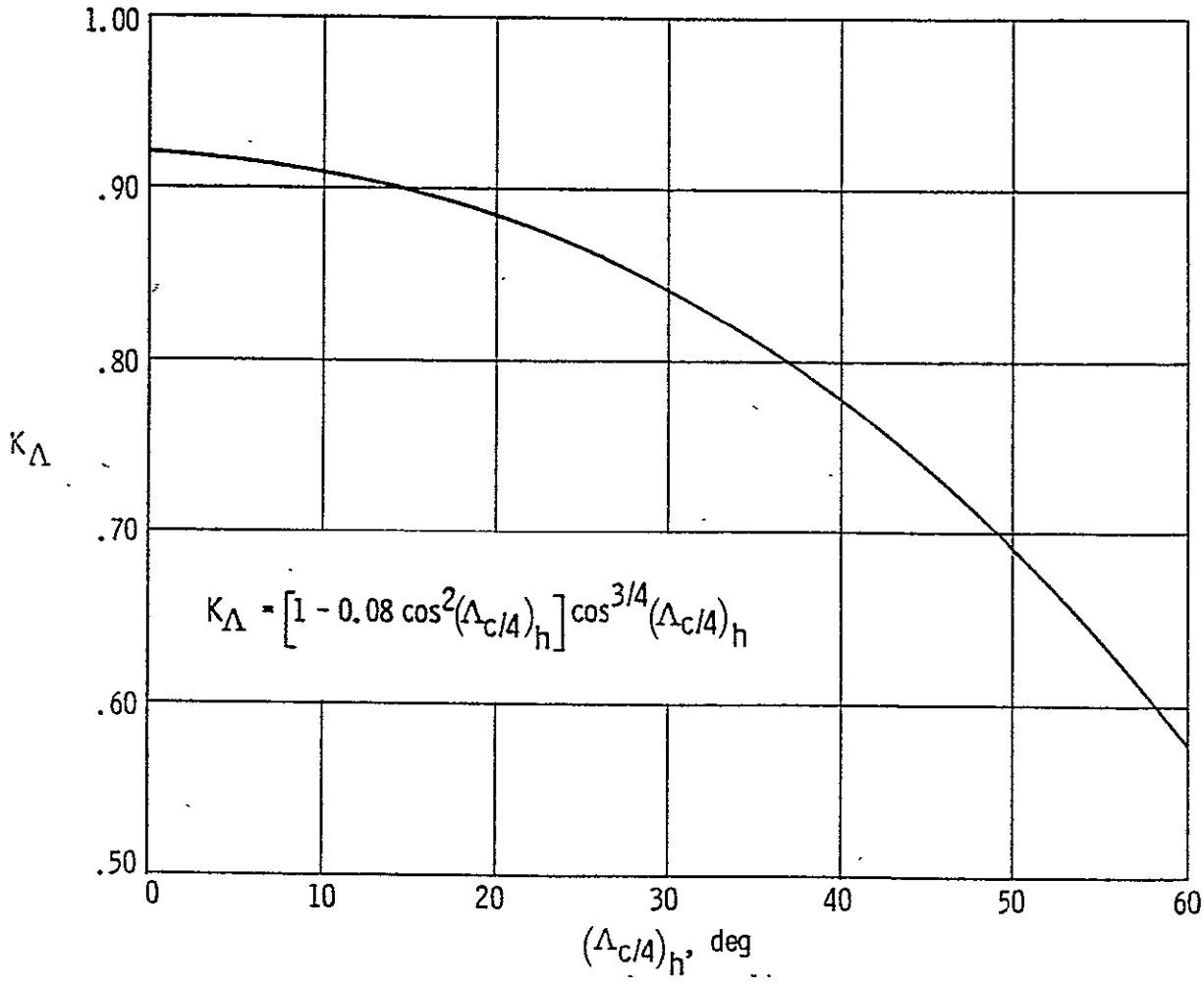

Figure 4.13.2.1: Correction factor for wing planform (Reference 3)

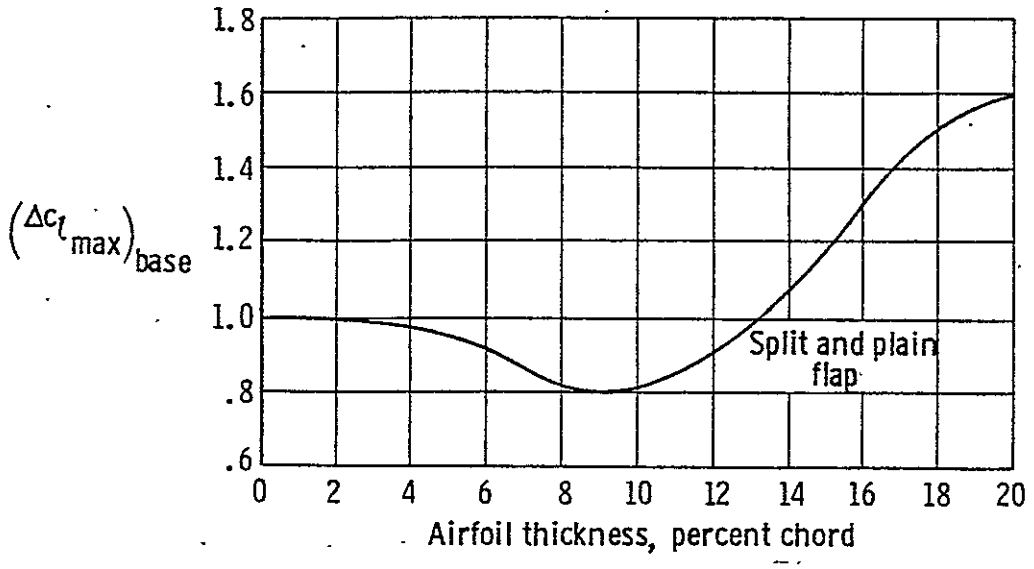

Figure 4.13.2.2: Section maximum lift increment for 25-percent chord tab at reference angle of 60 degrees (Reference 3)

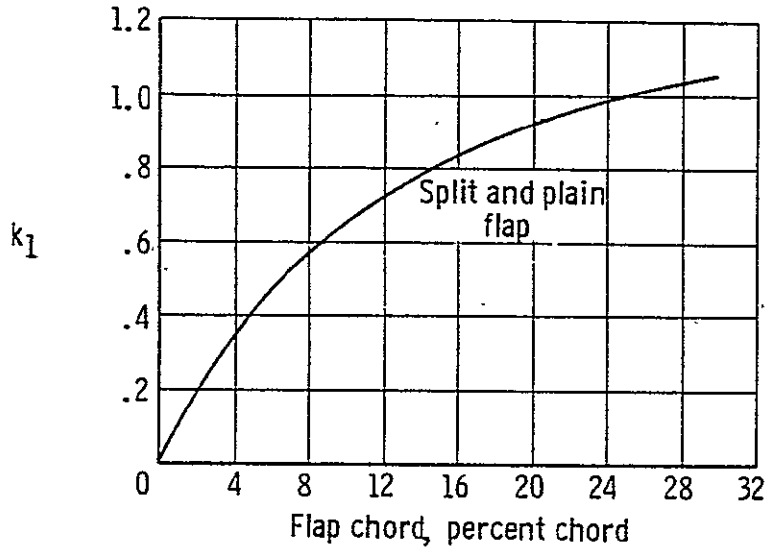

Figure 4.13.2.3: Factor accounting for tab chord other than 25-percent (Reference 3)

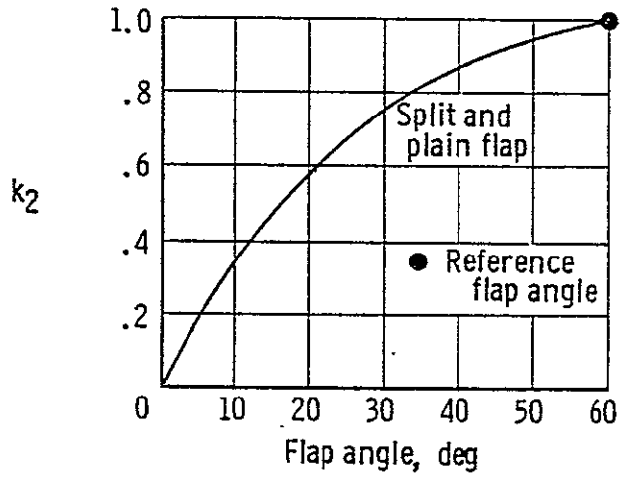

Figure 4.13.2.4: Factor accounting for tab deflection other than 60 degrees (Reference 3)

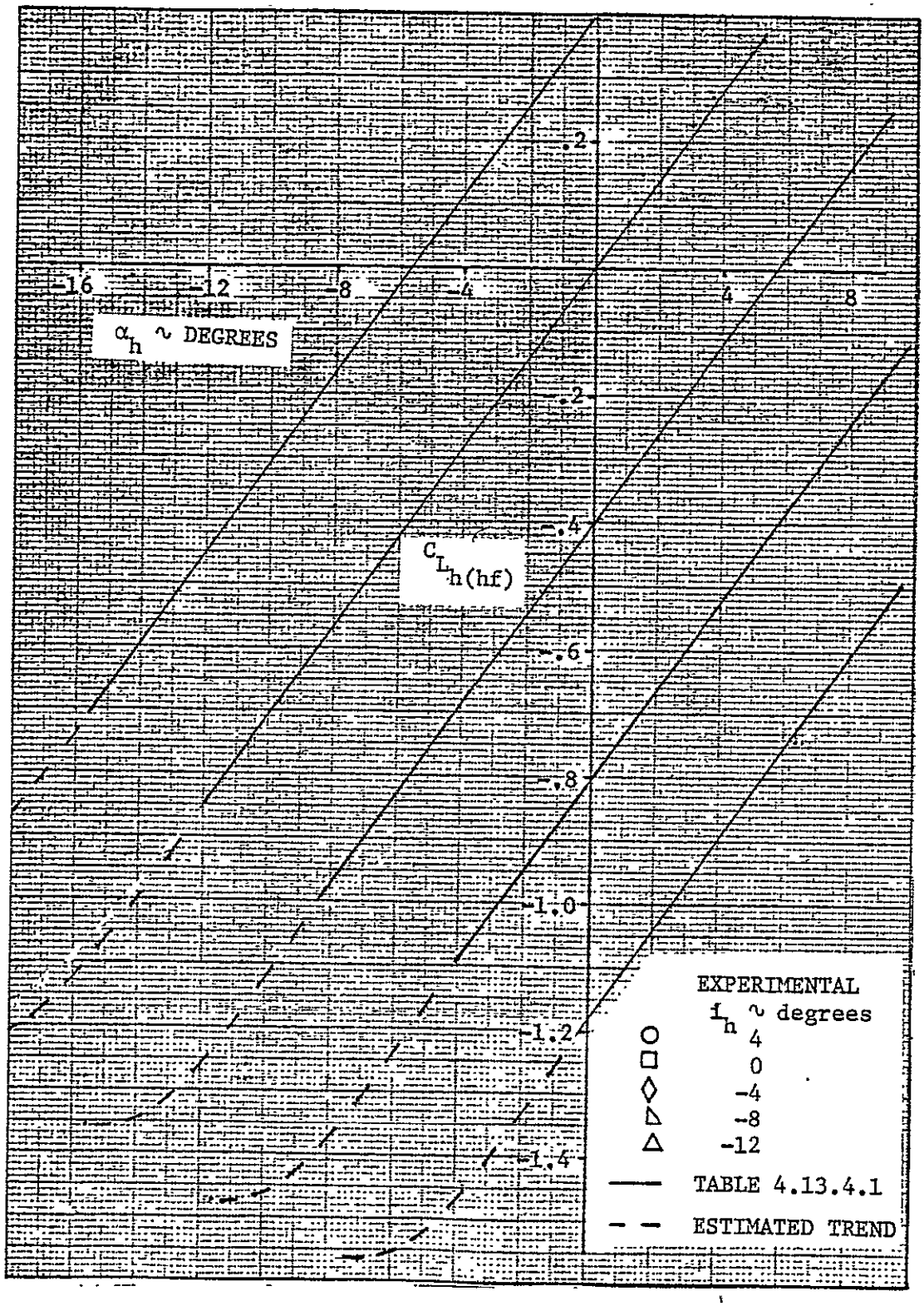

Figure 4.13.3.1: Calculated lift curves of the horizontal tail with tab geared to elevator, based on $S_h(\bar{q}_h/\bar{q}_\infty = 1.0$, $\delta_{tab}/i_h = 1.5$, $N_{Re} = 2.3$ million)

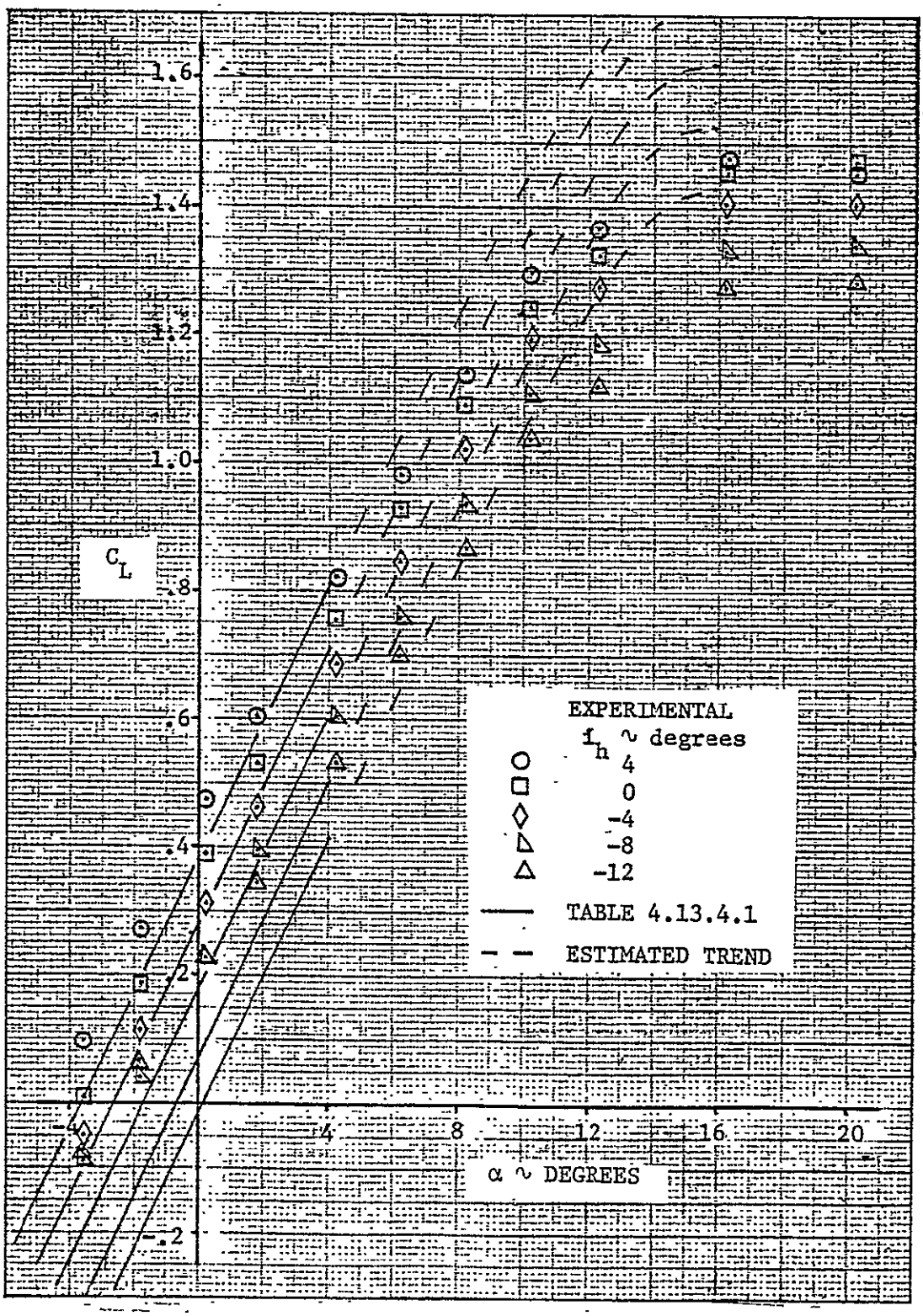

Figure 4.13.4.1: Comparison of predicted lift coefficient with full-scale wind tunnel data (propellers removed, N_{Re} = 2.3 million)

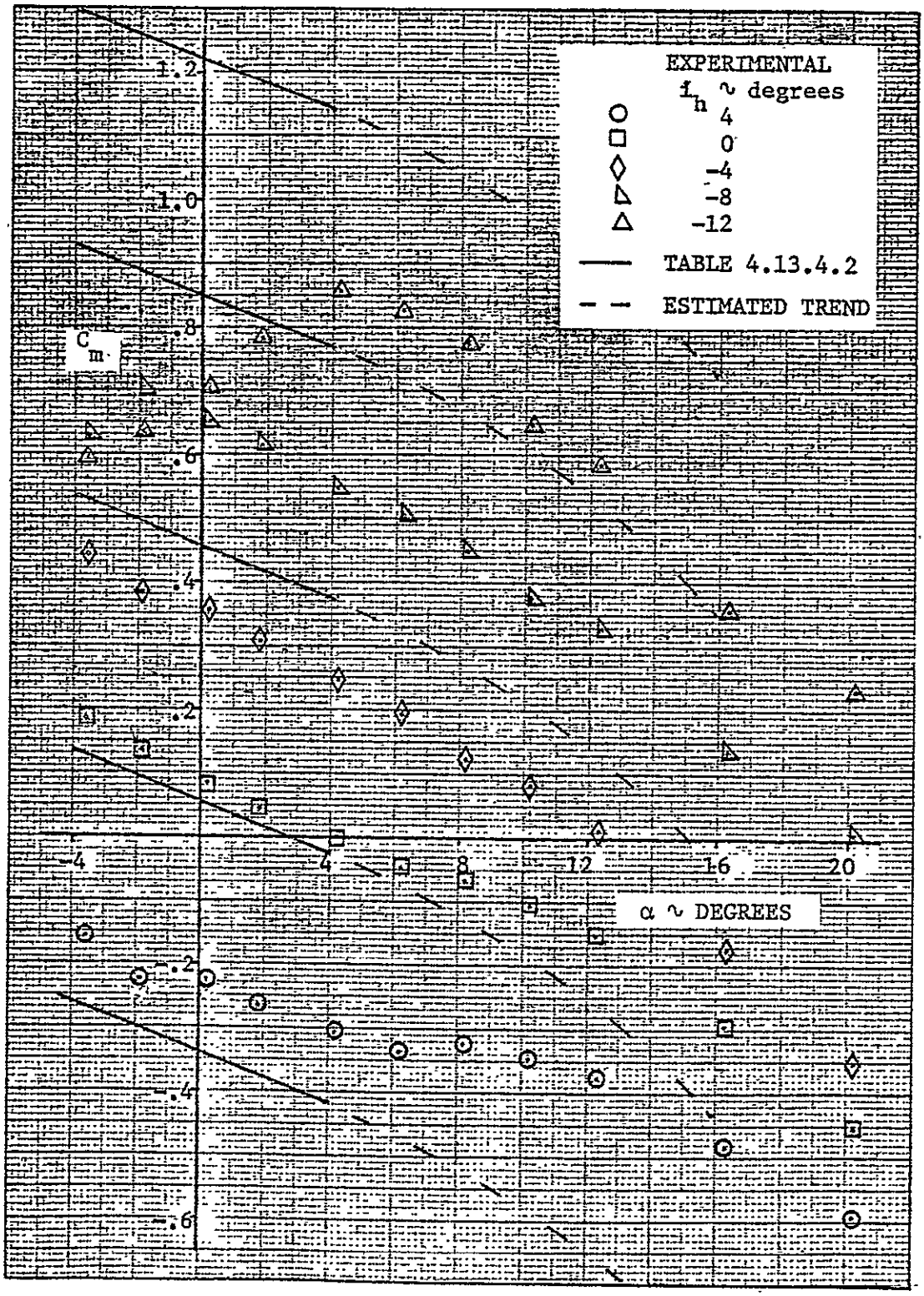

Figure 4.13.4.2: Comparison of predicted pitching moments with experimental results (propellers removed, N_{Re} = 2.3 million) .

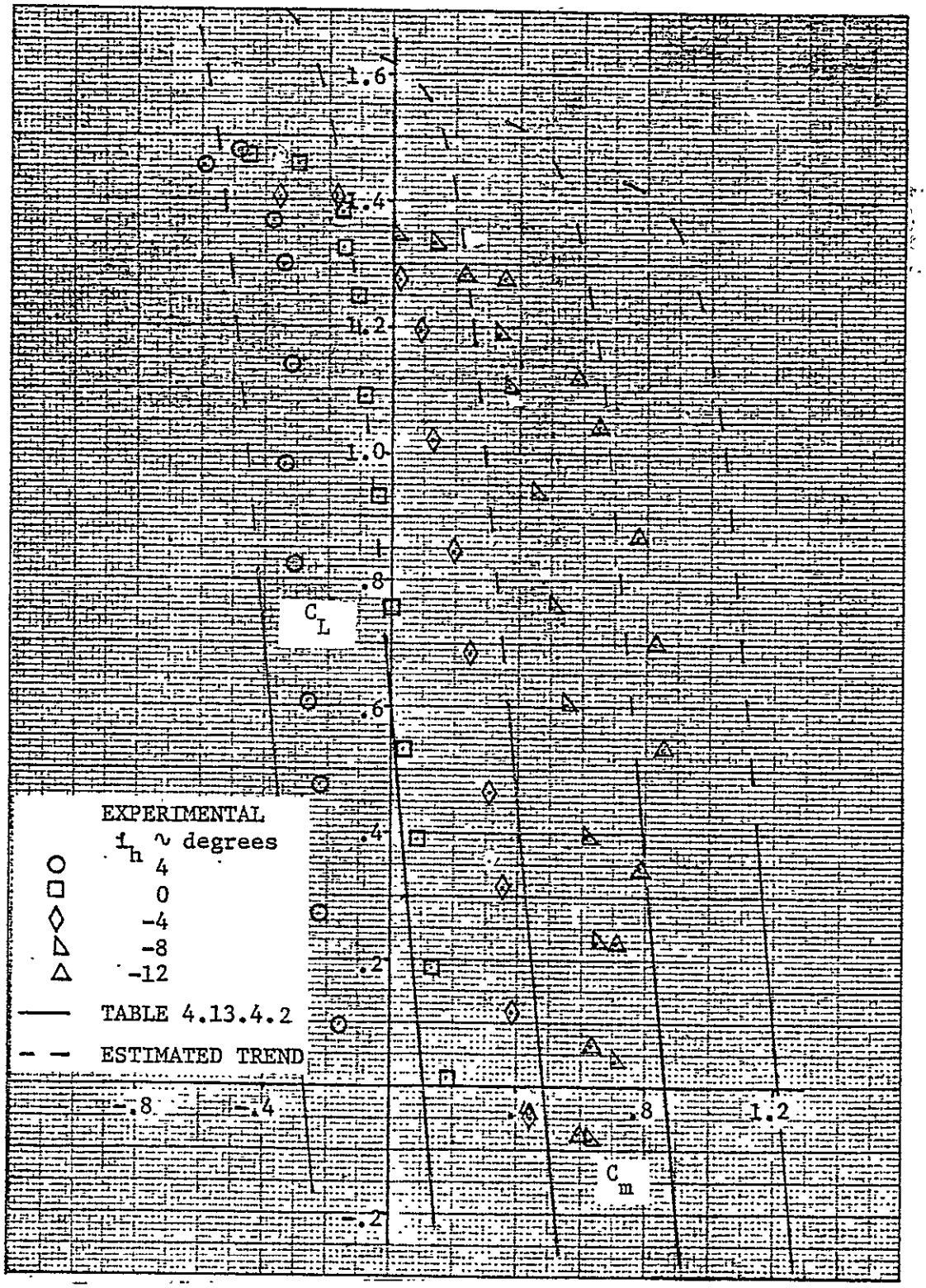

Figure 4.13.4.3: Comparison of calculated pitching moments with full-scale wind tunnel data (propellers removed, N_{Re} = 2.3 million)

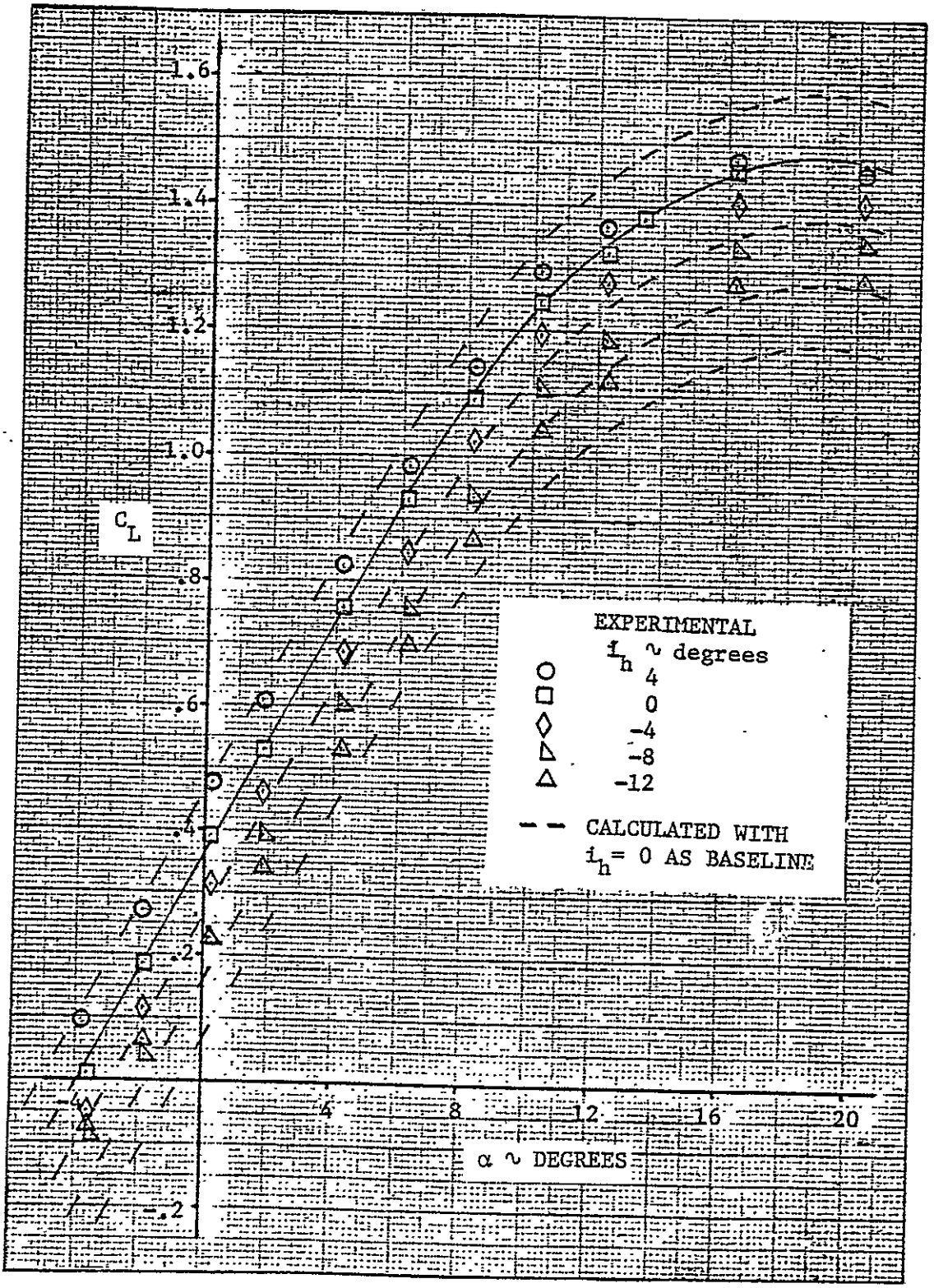

Figure 4.13.4.4: Comparison of predicted stabilizer effectiveness with experimental results (propellers removed, N_{Re} = 2.3 million)

CHAPTER 5

PREDICTION OF POWER-ON AERODYNAMIC CHARACTERISTICS

The effects of power from propeller operation are generally significant on the stability and control characteristics of an airplane. Unfortunately, because the propeller slipstream usually interacts with the flow around several airplane components, a number of separate effects must be accounted for. Although some of the effects have been accounted for by theoretical analysis, many are usually estimated by empirical methods.

In the following sections, the effects of power on lift, pitching moments, and drag are considered by the methods presented in Reference 3. In Figures 5.1 and 5.2 the parameters are defined, which are necessary to discuss power effects.

5.1 Propeller Power Effects on Lift

The effects of the propeller on the lift forces acting on the airplane may be divided into two groups, those due to the propeller forces and those due to the propeller slipstream. On this basis the lift of the airplane may be written as follows:

$$C_L = C_{L_{\text{prop off}}} + (\Delta C_L)_T + (\Delta C_L)_{N_p} + (\Delta C_L)_{\Delta \bar{q}_w} + (\Delta C_L)_{\varepsilon_p} + \\ + (\Delta C_{L_h})_{\Delta \bar{q}_h} + (\Delta C_{L_h})_{(\Delta \varepsilon_h)_{\text{power}}} \qquad (5.1.1)$$

where

$C_{L_{\text{prop off}}}$ is the lift coefficient of the airplane with the propellers removed, obtained from Section 4.13.

$(\Delta C_L)_T$ is the lift component of the thrust.

$(\Delta C_L)_{N_p}$ is the lift component of the propeller normal force.

$(\Delta C_L)_{\Delta\bar{q}_w}$ is the change in lift due to the change in dynamic pressure over the section of the wing in the propeller slipstream.

$(\Delta C_L)_{\varepsilon_p}$ is the change in lift of the section of the wing in the propeller slipstream due to a change in angle of attack from the propeller downwash.

$(\Delta C_{L_h})_{\Delta\bar{q}_h}$ is the change in lift contribution of the horizontal tail resulting from change in dynamic pressure at the tail due to power.

$(\Delta C_{L_h})_{(\Delta\varepsilon_h)_{power}}$ is the change in lift contribution of the horizontal tail resulting from change in downwash at the tail due to power.

In the following discussion of power effects on lift, the airplane will be considered initially on the basis of tail-off lift characteristics, followed by horizontal tail contributions to lift with tail-fuselage interaction effects included, or:

$$C_L = C_{L_{wfn}} + \bar{C}_{L_{h(hf)}} \tag{5.1.2}$$

where

$$C_{L_{wfn}} = (C_{L_{wfn}})_{prop\ off} + (\Delta C_L)_T + (\Delta C_L)_{N_p} +$$

$$+ (\Delta C_L)_{\Delta\bar{q}_w} + (\Delta C_L)_{\varepsilon_p} \tag{5.1.3}$$

5.1.1 Propeller Power Effects in Linear Lift Region

The above mentioned increments in lift can be determined by the following steps.

The lift component of the thrust, $(\Delta C_L)_T$, can be calculated as follows:

a) Calculate the angle of attack of the thrust axis measured from the free stream direction by:

$$\alpha_T = i_T + \alpha \qquad (5.1.1.1)$$

where

i_T is the incidence of the thrust line referenced to the X-body axis (Figure 5.2).

b) Calculate the thrust coefficient due to one propeller (if not given or assumed) by:

$$T_c'/\text{prop} = \frac{\text{Thrust/propeller}}{\bar{q}_\infty S_w} \qquad (5.1.1.2)$$

where the thrust per propeller is a given or chosen quantity.

c) Calculate the lift component of the thrust as follows:

$$(\Delta C_L)_T = n(T_c'/\text{prop}) \sin\alpha_T = T_c' \sin\alpha_T \qquad (5.1.1.3)$$

where

n represents the number of propellers

The lift component of the propeller normal force, $(\Delta C_L)_{N_p}$, can be obtained as follows:

a) Calculate the empirical normal force factor of the propeller by:

$$K_N = 262 \left(\frac{b_p}{R_p}\right)_{0.3R_p} + 262 \left(\frac{b_p}{R_p}\right)_{0.6R_p} + 135 \left(\frac{b_p}{R_p}\right)_{0.9R_p} \qquad (5.1.1.4)$$

where the subscripts indicates the radial position from the center of the propeller where the blade width, b_p, is to be evaluated.

b) From Figure 5.1.1.1 obtain a value for the propeller normal force coefficient, $[(C_{N_\alpha})_p]_{K_N=80.7}$, based on the propeller normal force factor, $K_N = 80.7$, as a function of propeller blade angle, β', and type of propeller.

c) Calculate the true propeller normal force coefficient, $(C_{N_\alpha})_p$, per radian by:

$$(C_{N_\alpha})_p = [(C_{N_\alpha})_p]_{K_N=80.7} \left[1 + 0.8 \left(\frac{K_N}{80.7} - 1\right)\right] \qquad (5.1.1.5)$$

d) Determine the propeller correlation parameter defined as:

$$\frac{S_w(T_c'/\text{prop})}{8 R_p^2} \qquad (5.1.1.6)$$

e) From Figure 5.1.1.2 obtain a value for the propeller inflow factor, f, as a function of the propeller correlation parameter, which can be obtained from Equation (5.1.1.6)

f) Calculate the propeller disc area by:

$$(S_p/\text{prop}) = \pi R_p^2 \qquad (5.1.1.7)$$

g) Determine the upwash gradient at the propeller, $-(\partial\varepsilon_u/\partial\alpha)$, from Figure 5.1.1.3 as a function of the wing aspect ratio, A_w, and the parameter, $x_p'/\bar{c}_i$, where x_p' is defined in Figure 5.2 and $\bar{c}_i$ in Figure 5.1

h) Calculate the local angle of attack of the propeller plane as follows:

$$\alpha_p = \alpha_T - \frac{\partial\varepsilon_u}{\partial\alpha}(\alpha_w - \alpha_{o_w}) \qquad (5.1.1.8)$$

where

α_w is the angle of attack of the wing obtained from:

$$\alpha_w = \alpha + i_w \tag{5.1.1.9}$$

i_w is the wing incidence, obtained from Section 4.4.

α_{o_w} is the wing zero-lift angle obtained from Section 4.2.

i) Calculate the lift component of the propeller normal force by:

$$(\Delta C_L)_{N_p} = n\, f\, (C_{N_\alpha})_p \, \frac{\alpha_p}{57.3} \, \frac{(S_p/\text{prop})}{S_w} \cos\alpha_T \tag{5.1.1.10}$$

The increment of lift due to the change in angle of attack on the wing induced by the propeller flow field, $(\Delta C_L)_{\varepsilon_p}$, can be obtained as follows:

a) Calculate the downwash gradient, $\partial\varepsilon_p/\partial\alpha_p$, by:

$$\frac{\partial\varepsilon_p}{\partial\alpha_p} = C_1 + C_2\, (C_{N_\alpha})_p \tag{5.1.1.11}$$

where

C_1 and C_2 are obtained from Figure 5.1.1.4.

$(C_{N_\alpha})_p$ is the true propeller normal force coefficient obtained from Equation (5.1.1.5).

b) Calculate the downwash behind the propeller, ε_p, by:

$$\varepsilon_p = \frac{\partial\varepsilon_p}{\partial\alpha_p}\, \alpha_p \tag{5.1.1.12}$$

where

α_p is the angle of attack of the propeller plane, obtained from Equation (5.1.1.8).

c) Calculate the change in angle of attack of the portion of the wing

immersed in the propeller slipstream, $(\Delta\alpha)_{S_i}$, as follows:

$$(\Delta\alpha)_{S_i} = - \frac{\varepsilon_p}{1 - \frac{\partial \varepsilon_u}{\partial \alpha}} \tag{5.1.1.13}$$

d) Calculate the upwash angle at the propeller, $-\varepsilon_u$, by:

$$-\varepsilon_u = - \frac{\partial \varepsilon_u}{\partial \alpha} (\alpha_w - \alpha_{o_w}) \tag{5.1.1.14}$$

e) Calculate the vertical distance, z_s, from the body X-axis to the centerline of the propeller slipstream at the longitudinal station of the quarter-chord of the mean aerodynamic chord of the immersed portion of the wing (Figure 5.2) by:

$$z_s = - \frac{x_p'}{57.3} (\alpha - \varepsilon_u - \varepsilon_p) + z_T \tag{5.1.1.15}$$

where

z_T is the vertical distance from the X-body axis to the thrust axis (Figure 5.2).

f) Calculate the span of the immersed wing, b_i/prop, by:

$$b_i/\text{prop} = 2\sqrt{R_p^2 - (z_s - z_w)^2} \tag{5.1.1.16}$$

where

$(z_s - z_w)$ is defined in Figure 5.1.

g) Calculate the immersed wing area, S_i/prop, by:

$$S_i/\text{prop} = (b_i/\text{prop})\bar{c}_i \tag{5.1.1.17}$$

h) Calculate the aspect ratio, A_i, of the immersed portion of the wing by:

$$A_i = \frac{b_i/\text{prop}}{\bar{c}_i} \tag{5.1.1.18}$$

i) Calculate the increase in dynamic pressure due to the propeller slipstream on the immersed portion of the wing as follows:

$$\frac{\Delta\bar{q}_w}{\bar{q}_\infty} = \frac{S_w\ (T_c'/\text{prop})}{\pi R_p^2} \qquad (5.1.1.19)$$

j) Calculate the change in wing lift due to change in angle of attack resulting from propeller downwash, ε_p, by:

$$(\Delta C_L)_{\varepsilon_p} = n\left(1 + \frac{\Delta\bar{q}_w}{\bar{q}_\infty}\right)\ (C_{L_\alpha})_{w_{\text{prop off}}}\ (\Delta\alpha)_{S_i}\ \frac{S_i/\text{prop}}{S_w} \qquad (5.1.1.20)$$

where

$(C_{L_\alpha})_{w_{\text{prop off}}}$ represents the lift curve slope of the wing with the propeller removed obtained from Section 4.2

The contribution of power to lift due to change in dynamic pressure on the immersed portion of the wing is obtained as follows:

a) From Figure 5.1.1.5 obtain a value for the empirical constant K_1 as a function of the wing aspect ratio, A_w, the immersed-wing aspect ratio, A_i, and the propeller correlation parameter obtained from Equation (5.1.1.6)

b) Calculate the increment of lift due to change in dynamic pressure on the immersed portion of the wing by:

$$(\Delta C_L)_{\Delta\bar{q}_w} = n\ K_1\ \frac{\Delta\bar{q}_w}{\bar{q}_\infty}\ (C_{L_w})_{\text{prop off}}\ \frac{(S_i/\text{prop})}{S_w} \qquad (5.1.1.21)$$

where

$(C_{L_w})_{\text{prop off}}$ is the lift coefficient of the wing obtained from Section 4.2 as function of the wing angle of attack, α_w.

The lift of the airplane without horizontal tail can be obtained with Equation (5.1.3) where $(C_{L_{wfn}})_{prop\ off}$ is the tail-off and propellers removed lift coefficient obtained from Section 4.4.

The contribution of the horizontal tail to the lift of the airplane may be obtained as follows:

a) From Figures 5.1.1.6 obtain a value for the downwash increment due to power, $(\Delta\varepsilon_h)_{power}$, as a function of the propeller correlation parameter, the downwash at the tail with propeller(s) removed, $(\bar{\varepsilon}_h)_{prop\ off}$, obtained from Section 4.9 and the parameter $z_{h_T}/2R_p$ where z_{h_T} is defined in Figure 5.2.

b) Calculate the effective distance, $z_{h_{eff}}$, parallel to the z-body axis, from the quarter chord of the horizontal-tail mean aerodynamic chord to the centerline of the propeller slipstream by:

$$z_{h_{eff}} = z_s - \frac{\ell_h'}{57.3}\left[\alpha - \varepsilon_u - \varepsilon_p - (\bar{\varepsilon}_h)_{prop\ off} - (\Delta\varepsilon_h)_{power}\right] - z_h \qquad (5.1.1.22)$$

where

ℓ_h' is the distance from the quarter chord of the mean aerodynamic chord of the immersed portion of the wing to the quarter chord of the horizontal tail mean aerodynamic chord (see Figure 5.2).

z_h is the distance, parallel to the z-body axis, from the X-body axis to the quarter chord of the horizontal tail mean aerodynamic chord, obtained from Figure 5.2.

c) From Figure 5.1.1.7 obtain a value for the power-induced increment in dynamic-pressure ratio at the tail, $\Delta\bar{q}_h/\bar{q}_\infty$, as a function of the propeller correlation parameter, the ratio of horizontal tail immersed area and horizontal tail area, S_{h_i}/S_h, and the parameter $z_{h_{eff}}/R_p$. When

the increment obtained is negative, it can be assumed to be zero.

d) Calculate the angle of attack of the horizontal tail by:

$$\alpha_h = \alpha - (\bar{\varepsilon}_h)_{\text{prop off}} - (\Delta\varepsilon_h)_{\text{power}} \qquad (5.1.1.23)$$

c) From Section 4.13 obtain a value for the lift, $(\bar{C}_{L_{h(hf)}})'_{S_h, \bar{q}_h, \bar{q}_\infty=1.0}$, of the horizontal tail referenced to the horizontal tail area, S_h, and a dynamic pressure ratio, $\bar{q}_h / \bar{q}_\infty$, equal to one.

f) Calculate the contribution of the horizontal tail to the lift of the airplane by:

$$\bar{C}_{L_{h(hf)}} = [(\bar{C}_{L_{h(hf)}})'_{S_h, \bar{q}_h, \bar{q}_\infty=1.0}] \frac{S_h}{S_w} [(\frac{\bar{q}_h}{\bar{q}_\infty})_{\text{prop off}} + \frac{\Delta\bar{q}_h}{\bar{q}_\infty}] \qquad (5.1.1.24)$$

where

$(\bar{q}_h/\bar{q}_\infty)_{\text{prop off}}$ follows from Section 4.9.

The total lift of the airplane can be obtained with Equation (5.1.2).

5.1.2 Propeller Power Effects on Maximum Lift

Over the linear lift-curve slope, increases in lift due to propeller power result from the factors discussed above. However, near or at maximum lift an additional increase in lift occurs because the angle of attack for stall increases with power. This effect depends primarily upon the ratio of the immersed wing area to the total area, S_i/S_w. The propeller power effect on maximum lift can be obtained as follows:

a) From Figure 5.1.2.1 obtain a value for the empirical constant, K, as a function of the ratio of immersed wing area to the total wing area, S_i/S_w.

b) Calculate the increment in tail-off lift due to power, $(\Delta C_L)'_{power}$, at the propeller off angle of attack for maximum lift:

$$(\Delta C_L)'_{power} = (\Delta C_L)_T + (\Delta C_L)_{N_p} + (\Delta C_L)_{\Delta \bar{q}_w} + (\Delta C_L)_{\varepsilon_p} \qquad (5.1.2.1)$$

c) Calculate the increment of maximum lift due to propeller power by:

$$\Delta C_{L_{max}} = K(\Delta C_L)'_{power} \qquad (5.1.2.2)$$

The complete power-on tail-off lift curve is constructed as follows:

a) Plot the linear portion of the power-on lift curve.

b) Draw a horizontal line representing the power-on tail-off maximum lift coefficient.

c) Translate the non-linear propeller-off portion of the lift curve to a tangency with a) and b). This construction not only shapes the power-on lift curve but also fixes the power-on stall angle. The construction of the power-on tail-off lift curve is also demonstrated in Figure 5.1.2.2.

The power-on lift curve of the complete airplane can be obtained by adding the horizontal tail lift to the tail-off lift curve as shown by Equation (5.1.2).

5.1.3 Lift Characteristics of the ATLIT Airplane

In Tables 5.1.3.1 through 5.1.3.5 the calculations are summarized which lead to the lift curve of the airplane including power effects. The results for two power settings are shown in Figures 5.1.3.2 and 5.1.3.3 and compared with experimental data from Reference 2.

The predictions have been performed for a Reynolds number of 2.3 million. However, no power-on wind tunnel data were available of the

ATLIT in the "fully clean" configuration at a Reynolds number of 2.3 million. Data were available for a Reynolds number of 3.5 million. As is shown in Reference 2, a change in Reynolds number of this magnitude has an almost negligible effect on the lift of the airplane.

The vertical position of the center of gravity of the ATLIT airplane, used in this study, is situated at a distance of 0.333 m. (13.1 in.) above the wing root chord.

The predicted lift curves show fair agreement with the wind tunnel data. However, when the predicted increment in lift due to power is added to the experimental lift curve obtained with propellers removed, cowl flaps open, and engine inlets open, good agreement is obtained with the wind tunnel data of Reference 2. The increment in lift due to power can be written as follows:

$$(\Delta C_L)_{power} = C_L - (C_L)_{prop\ off} \qquad (5.1.3.1)$$

where

C_L is the predicted lift coefficient of the airplane including power effects, obtained from Table 5.1.3.4.

$(C_L)_{prop\ off}$ is the predicted lift coefficient of the airplane with propellers removed, obtained from Section 4.10.

The effect of engine cooling on the lift of the airplane is briefly discussed in Section 4.10.

Table 5.1.3.1: Lift due to direct action of the propeller forces.

Symbol	Description	Reference	Magnitude
i_T	Incidence of thrust line to reference X_b-axis, deg	Figure 5.2	0
α_T	Angle of attack of thrust axis, deg	Eq.(5.1.1.1)	α
T_c'/prop	Thrust coefficient	-	Variable
n	Number of propellers	Figure 5.1	2
$(\Delta C_L)_T$	Lift component of the thrust	Eq.(5.1.1.3)	$2(T_c'/\text{prop})\ \sin\alpha$

Table 5.1.3.1: Continued.

Symbol	Description	Reference	Magnitude
b_p	Width of propeller blade, m (ft)	—	.127 (.417) at .3R_p .157 (.515) at .6R_p .108 (.354) at .9R_p
R_p	Propeller radius, m (ft	Table 2.1	.97 (3.17)
K_N	Propeller normal force factor	Eq.(5.1.1.4)	92.22
β'	Propeller blade angle, deg	—	Variable
$[(C_{N_\alpha})_p]_{K_N=80.7}$	Propeller normal force parameter, rad^{-1}	Figure 5.1.1.1	Variable
$(C_{N_\alpha})_p$	Propeller normal force derivative, rad^{-1}	Eq.(5.1.1.5)	$1.114[(C_{N_\alpha})_p]_{K_N=80.7}$
S_w	Reference wing area, m^2 (ft^2)	Table 2.1.1	14.40 (155.0)
$\frac{S_w(T_c'/prop)}{8R_p^2}$	Propeller correlation parameter	Eq.(5.1.1.6)	$1.93(T_c'/prop)$
f	Propeller inflow parameter	Figure 5.1.1.2	Variable
$S_p/prop$	Propeller disc area, m^2 (ft^2)	Eq.(5.1.1.7)	2.93 (31.57)
A_w	Wing aspect ratio	Table 2.1.1	10.32
x_p'	Distance of propeller forward of $\bar{c}_i/4$, m (ft)	Figure 5.2	1.95 (6.41)
$\bar{c}_i$	Mean aerodynamic chord of immersed wing area, m (ft)	Figure 5.1	1.34 (4.38)
$-(\partial\epsilon_u/\partial\alpha)$	Upwash gradient at propeller	Figure 5.1.1.3	.155
i_w	Wing incidence at root, deg	Table 2.1	0.5
α_w	Wing angle of attack, deg	Eq.(5.1.1.9)	$\alpha + 0.5$
α_{o_w}	Wing zero-lift angle of attack relative to wing chord, deg	Table 4.2.4.1	-2.89
α_T	Angle of attack of thrust line, deg	Table 4.1.3.1	α
α_p	Angle of attack of propeller plane, deg	Eq.(5.1.1.8)	$1.155\alpha + 0.525$

Table 5.1.3.1: Continued.

T_c'/prop	$\frac{S_w (T_c'/prop)}{8 R_p^2}$ Eq. (5.1.1.6)	f Figure 5.1.1.2	β', deg Appendix G	$[(C_{N_\alpha})_p]_{K_N = 80.7}$ Figure 5.1.1.1	$(C_{N_\alpha})_p$ Eq. (5.1.1.5)
0	0	0	18	.090	.10
.0458	.0882	1.075	18	.090	.10
.0985	.1900	1.154	18	.090	.10

Table 5.1.3.1: Concluded

α, deg	$(\Delta C_L)_T$; Table 5.1.3.1 T_c'			α_p, deg Eq.(5.1.1.8)	$(\Delta C_L)_{N_p}$; Eq. (5.1.1.10) T_c'		
	0	0.0915	0.1970		0	0.0915	0.1970
-4	0	-0.0064	-0.0137	-4.09	-0.0029	-0.0031	-0.0033
-2	0	-0.0032	-0.0069	-1.78	-0.0013	-0.0014	-0.0015
0	0	0	0	0.53	0.0004	0.0004	0.0004
2	0	0.0032	0.0069	2.84	0.0020	0.0022	0.0024
4	0	0.0064	0.0137	5.15	0.0036	0.0039	0.0042
15.9	0	0.0251	0.0540	18.90	0.0129	0.0139	0.0149

Table 5.1.3.2: Wing lift increments due to propeller slipstream effects

Symbol	Description	Reference	Magnitude
$\frac{S_w(T_c'/\text{prop})}{8 R_p^2}$	Propeller correlation parameter	Eq.(5.1.1.6)	1.93 (T_c'/prop)
C_1	Factor for determining propeller downwash	Figure 5.1.1.4	Variable
C_2	Factor for determining propeller downwash	Figure 5.1.1.4	Variable
$(C_{N_\alpha})_p$	Propeller normal force factor	Table 5.1.3.3	0.10
$\partial\epsilon_p/\partial\alpha_p$	Downwash gradient behind propeller	Eq.(5.1.1.11)	$C_1 + 0.10C_2$
α_p	Angle of attack of propeller plane, deg	Eq.(5.1.1.8)	$1.155\alpha + 0.525$
ϵ_p	Propeller downwash behind propeller, deg	Eq.(5.1.1.12)	Variable
$(\Delta\alpha)_{S_i}$	Change in angle of attack of immersed wing, deg	Eq.(5.1.1.13)	$-\epsilon_p/1.55$
$-\epsilon_u$	Wing upwash at propeller plane, deg	Eq.(5.1.1.14)	$0.155\ (\alpha + 3.39)$
x_p'	Distance of propeller forward of $\bar{c}_i/4$, m (ft)	Figure 5.2	1.95 (6.41)
z_T	Distance from X-body axis to thrust line, m (ft)	Figure 5.2	-0.128 (-0.417)
z_s	Defined in Figure 5.2	Eq.(5.1.1.15)	Variable
z_w	Distance from X-axis to quarter chord immersed wing mean aerodynamic shord, m (ft)	Figure 5.1	0.100 (0.329)
b_i/prop	Immersed span per propeller	Eq.(5.1.1.16)	Variable
$\bar{c}_i$	Mean aerodynamic chord of immersed wing area, m (ft)	Figure 5.1	1.34 (4.38)
S_i/prop	Immersed area per propeller, m^2 (ft^2)	Eq.(5.1.1.17)	Variable
A_i	Aspect ratio of immersed portion of wing	Eq.(5.1.1.18)	Variable
$\frac{\Delta\bar{q}_w}{\bar{q}_\infty}$	Change in dynamic pressure ratio on immersed wing	Eq.(5.1.1.19)	Variable
$(C_{L_\alpha})_{w_{\text{prop off}}}$	Lift curve slope of wing, rad^{-1} (deg^{-1})	Table 4.2.4.1	5.090 (0.0888)
K_1	Correlation parameter for added lift due to power	Figure 5.1.1.5	Variable
$(C_{L_w})_{\text{prop off}}$	Lift coefficient of wing	Figure 4.2.4.1	Variable

Table 5.1.3.2: Continued

T_c'	$\frac{S_w(T_c'/prop)}{8R_p^2}$	C_1 Figure 4.1.1.4	C_2 Figure 4.1.1.4	$\frac{\partial \varepsilon_p}{\partial \alpha}$ Eq.(5.1.1.11)	$\frac{\Delta \bar{q}_w}{\bar{q}_\infty}$ Eq.(5.1.1.19)
0	0	0	0.25	0.025	0
0.0915	0.0882	0.0783	0.25	0.1033	0.2246
0.1970	0.1900	0.1304	0.25	0.1554	0.4836

Table 5.1.3.2: Concluded

α, deg	α_p, deg Table 5.1.3.1	$-\epsilon_u$, deg Eq.(5.1.1.14)	ϵ_p, deg; Eq.(5.1.1.12) T_c'			$(\Delta\alpha)_{S_f}$, deg; Eq.(5.1.1.13) T_c'			z_s, ft; Eq. (5.1.1.15) T_c'		
			0	0.0915	0.1970	0	0.0915	0.1970	0	0.0915	0.1970
-4	-4.09	-0.095	-0.1023	-0.4217	-0.6348	0.0886	0.3651	0.5496	0.0080	-0.006	-0.0295
-2	-1.78	0.216	-0.0445	-0.1835	-0.2763	0.0385	0.1589	0.2392	-0.2224	-0.2380	-0.2481
0	0.53	0.526	0.0133	0.0546	0.0823	-0.0115	-0.0473	-0.0713	-0.4743	-0.4697	-0.4666
2	2.84	0.836	0.0710	0.2928	0.4408	-0.0615	-0.2535	-0.3816	-0.7263	-0.7018	-0.6852
4	5.15	1.146	0.1288	0.5310	0.7993	-0.1115	-0.4597	-0.6920	-0.9782	-0.9338	-0.9038
15.9	18.90	2.990	0.4725	1.9486	2.9333	-0.4091	-1.6871	-2.5397	-2.4773	-2.3122	-2.2020

$z_s - z_w$, ft T_c'			b_f/prop, ft; Eq. (5.1.1.16) T_c'			S_f/prop, ft^2; Eq. (5.1.1.17) T_c'			$(\Delta C_L)_{\epsilon_p}$, Eq. (5.1.1.20) T_c'		
0	0.0915	0.1970	0	0.0915	0.1970	0	0.0915	0.1970	0	0.0915	0.1970
-0.3210	-0.3350	-0.3585	6.3074	6.3045	6.2993	27.626	27.614	27.591	0.0028	0.0141	0.0258
-0.5514	-0.5670	-0.5771	6.2434	6.2378	6.2341	27.346	27.322	27.305	0.0012	0.0061	0.0111
-0.8033	-0.7987	-0.7956	6.1331	6.1355	6.1371	26.863	26.873	26.880	-0.0004	-0.0018	-0.0033
-1.0553	-1.0308	-1.0142	5.9784	5.9954	6.0068	26.185	26.260	26.310	-0.0018	-0.0093	-0.0171
-1.3072	-1.2628	-1.2328	5.7759	5.8152	5.8409	25.298	25.471	25.583	-0.0032	-0.0164	-0.0301
-2.8063	-2.6412	-2.5310	2.9486	3.5060	3.8173	12.915	15.356	16.720	-0.0061	-0.0364	-0.0722

A_f; Eq. (5.1.1.18) T_c'			K_f; Figure 5.1.1.5 T_c'			$(C_{L_w})_{\text{prop off}}$ Figure 4.2.4.1	$(\Delta C_L)_{\Delta q_w}$; Eq. (5.1.1.21) T_c'		
0	0.0915	0.1970	0	0.0915	0.1970		0	0.0915	0.1970
-	1.439	1.439	-	1.0	0.96	-0.0533	0	-0.0043	-0.0088
-	1.424	1.423	-	1.0	0.96	0.1243	0	0.0098	0.0203
-	1.401	1.401	-	1.0	0.96	0.3019	0	0.0235	0.0486
-	1.369	1.371	-	1.0	0.96	0.4795	0	0.0365	0.0756
-	1.328	1.334	-	1.0	0.96	0.6571	0	0.0485	0.1007
-	0.800	0.872	-	0.98	0.94	1.494	0	0.0652	0.1465

Table 5.1.3.3: Tail-off lift characteristics with power-on of the ATLIT airplane.

α, deg	$(C_{L_{wfn}})_{prop\ off}$ Figure 4.4.3.1	$(\Delta C_L)_T$; Table 5.1.3.1			$(\Delta C_L)_{N_p}$; Table 5.1.3.1		
		T_c'			T_c'		
		0	0.0915	0.1970	0	0.0915	0.1970
-4	-0.0780	0	-0.0064	-0.0137	-0.0029	-0.0031	-0.0033
-2	0.1141	0	-0.0032	-0.0069	-0.0013	-0.0014	-0.0015
0	0.3066	0	0	0	0.0004	0.0004	0.0004
2	0.4997	0	0.0032	0.0069	0.0020	0.0022	0.0024
4	0.6932	0	0.0064	0.0137	0.0036	0.0039	0.0042
15.9	1.5731	0	0.0251	0.0540	0.0129	0.0139	0.0149

$(\Delta C_L)_{\Delta\bar{q}_w}$; Table 5.1.3.2			$(\Delta C_L)_{\varepsilon_p}$; Table 5.1.3.2			$C_{L_{wfn}}$; Eq.(5.1.3)		
T_c'			T_c'			T_c'		
0	0.0915	0.1970	0	0.0915	0.1970	0	0.0915	0.1970
0	-0.0043	-0.0088	0.0028	0.0141	0.0258	-0.0781	-0.0777	-0.0780
0	0.0098	0.0203	0.0012	0.0061	0.0111	0.1140	0.1254	0.1371
0	0.0235	0.0486	-0.0004	-0.0018	-0.0033	0.3066	0.3287	0.3523
0	0.0365	0.0756	-0.0018	-0.0093	-0.0171	0.4999	0.5323	0.5675
0	0.0482	0.1007	-0.0032	-0.0164	-0.0301	0.6936	0.7356	0.7817
0	0.0652	0.1465	-0.0061	-0.0364	-0.0722	1.5799	1.6409	1.7163

Table 5.1.3.4: Power effects on horizontal tail lift and total lift of the ATLIT airplane.

Symbol	Description	Reference	Magnitude
S_w	Reference wing area, $m^2(ft^2)$	Table 2.1.1	14.40 (155.0)
S_h	Horizontal tail area, $m^2(ft^2)$	Table 2.1.1	3.60 (38.7)
z_{h_T}	Vertical distance from thrust line to horizontal tail, m(ft)	Figure 5.2	-0.127(-0.417)
R_p	Propeller radius, m(ft)	Table 2.1	0.97 (3.17)
$z_{h_T}/2R_p$	—	—	-0.066
$(\bar{\varepsilon}_h)_{prop\ off}$	Downwash at horizontal tail with propeller removed, deg	Figure 4.9.3.1	Variable
$(\Delta\varepsilon_h)_{power}$	Downwash increment at horizontal tail due to power, deg	Figure 5.1.1.6	Variable
$\alpha - \varepsilon_u - \varepsilon_p$	Inclination of slipstream centerline behind propeller relative to X-body axis	Table 5.1.3.2	Variable
S_{h_i}/S_h	—	Figure 5.1	0.50
z_s	Defined in Figure 5.2	Table 5.1.3.2	Variable
z_h	Vertical distance from X-body axis to horizontal tail, m(ft)	Figure 5.2	-0.28 (-0.92)
ℓ_h'	Distance along X-body axis from $\bar{c}_i/4$ to $\bar{c}_h/4$, m(ft)	Figure 5.2	4.87 (15.99)
$z_{h_{eff}}$	Vertical distance from $\bar{c}_h/4$ to slipstream centerline, m(ft)	Eq. (5.1.1.21)	Variable
$\Delta\bar{q}_h/\bar{q}_\infty$	Increment in dynamic-pressure ratio at horizontal tail	Figure 5.1.1.7	Variable
α_h	Angle of attack at horizontal tail	Eq.(5.1.1.22)	Variable
$(\bar{q}_h/\bar{q}_\infty)_{prop\ off}$	Propeller-off dynamic pressure ratio at horizontal tail	Figure 4.9.3.2	1.0
$(\bar{C}_{L_{h(hf)}})^t_{S_h, \frac{\bar{q}_h}{\bar{q}_\infty}=1.0}$	C_L of tail referenced to tail area and a dynamic pressure ratio of 1.0	Figure 4.13.3.1	Variable
$C_{L_{wfn}}$	Tail-off C_L with power on referenced to S_w	Table 5.1.3.9	Variable

Table 5.1.3.4: Concluded.

α, deg	$\alpha - \epsilon_u - \epsilon_p$, deg; Table 5.1.3.2			$(\bar{\epsilon}_h)_{prop\ off}$, deg	$(\Delta\epsilon_h)_{power}$, deg; Figure 5.1.1.6			z_s, ft; Table 5.1.3.2		
	T_c'				T_c'			T_c'		
	0	0.0915	0.1970	Figure 4.9.3.1	0	0.0915	0.1970	0	0.0915	0.1970
-4	-3.9927	-3.6733	-3.4602	-0.26	0	0	0	0.0080	-0.006	-0.0295
-2	-1.7395	-1.6005	-1.5077	0.564	0	0.20	0.45	-0.2224	-0.2380	-0.2481
0	0.5127	0.4714	0.4437	1.377	0	0.50	1.0	-0.4743	-0.4697	-0.4666
2	2.765	2.5432	2.3952	2.192	0	0.70	1.25	-0.7263	-0.7018	-0.6852
4	5.0172	4.6150	4.3467	2.990	0	1.0	1.75	-0.9782	-0.9338	-0.9038

$z_{h_{eff}}/R_p$; Eq. (5.1.1.21)			$\Delta\bar{q}_h/\bar{q}_\infty$; Figure 5.1.1.7			α_h, deg; Eq. (5.1.3.22)			$(\bar{C}_{L_{h(hf)}})_{S_h}$, $\bar{q}_h/\bar{q}_\infty$=1.0; Figure 4.13.3.1		
T_c'			T_c'			T_c'			T_c'		
0	0.0915	0.1970	0	0.0915	0.1970	0	0.0915	0.1970	0	0.0915	0.1970
0.6213	0.5888	0.5626	0	.03	.10	-3.740	-3.740	-3.740	-0.2652	-0.2652	-0.2652
0.4228	0.4233	0.4339	0	.035	.12	-2.654	-2.764	-3.014	-0.1818	-0.1970	-0.2137
0.2167	0.2658	0.3132	0	.04	.12	-1.377	-1.877	-2.377	-0.0976	-0.1331	-0.1685
0.0107	0.0995	0.1662	0	.045	.13	-0.192	-0.892	-1.442	-0.0136	-0.0632	-0.1022
-0.1968	-0.0594	0.0397	0	.05	.15	1.010	0.010	-0.740	0.0716	0.0007	-0.0525

$\bar{C}_{L_{h(hf)}}$; Eq. (5.1.1.23)			$C_{L_{wfn}}$; Table 5.1.3.3			C_L; Eq. (5.1.2)		
T_c'			T_c'			T_c'		
0	0.0915	0.1970	0	0.0915	0.1970	0	0.0915	0.1970
-0.0662	-0.0682	-0.0728	-0.0781	-0.0777	-0.0780	-0.1443	-0.1459	-0.1508
-0.0454	-0.0504	-0.0598	0.1140	0.1254	0.1371	0.0686	0.0750	0.0773
-0.0244	-0.0346	-0.0471	0.3066	0.3287	0.3523	0.2822	0.2941	0.3052
-0.0034	-0.0165	-0.0288	0.4999	0.5323	0.5675	0.4965	0.5158	0.5387
0.0179	0.0002	-0.0151	0.6936	0.7356	0.7817	0.7115	0.7358	0.7666

Table 5.1.3.5: Power effects on maximum lift.

Symbol	Description	Reference	Magnitude
K	Correlation factor	Figure 5.1.2.1	Variable
S_i/S_w	Ratio of total immersed wing area to S_w at propellers-off $(C_{L_{wfn}})_{max}$	Table 5.1.3.2	Variable
$(\Delta C_L)'_{power}$	Increment in lift due to power at propeller-off $(C_{L_{wfn}})_{max}$	Table 5.1.3.3	Variable

T_c'	$\frac{S_i}{S_w} = 2\left(\frac{S_i/prop}{S_w}\right)$ Table 5.1.3.2	K Figure 5.1.2.1	$(\Delta C_L)'_{power}$ Eq.(5.1.2.1)	$\Delta C_{L_{max}}$ Eq.(5.1.2.2)
0	0.1666	1.065	0.0068	0.0072
0.0915	0.1981	1.097	0.0678	0.0744
0.1970	0.2157	1.110	0.1432	0.1590

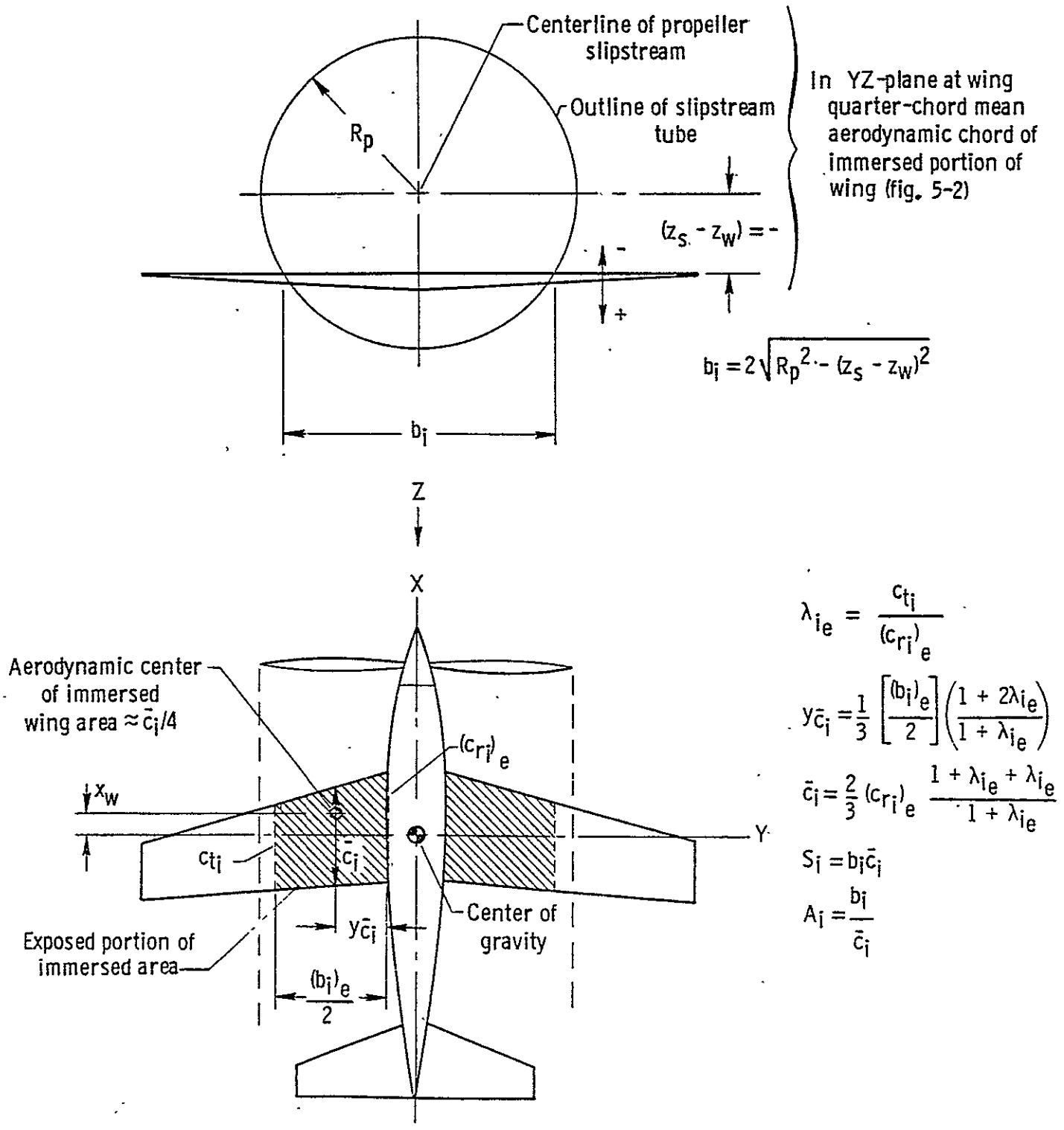

Figure 5.1: Definition sketches for calculation of immersed areas.

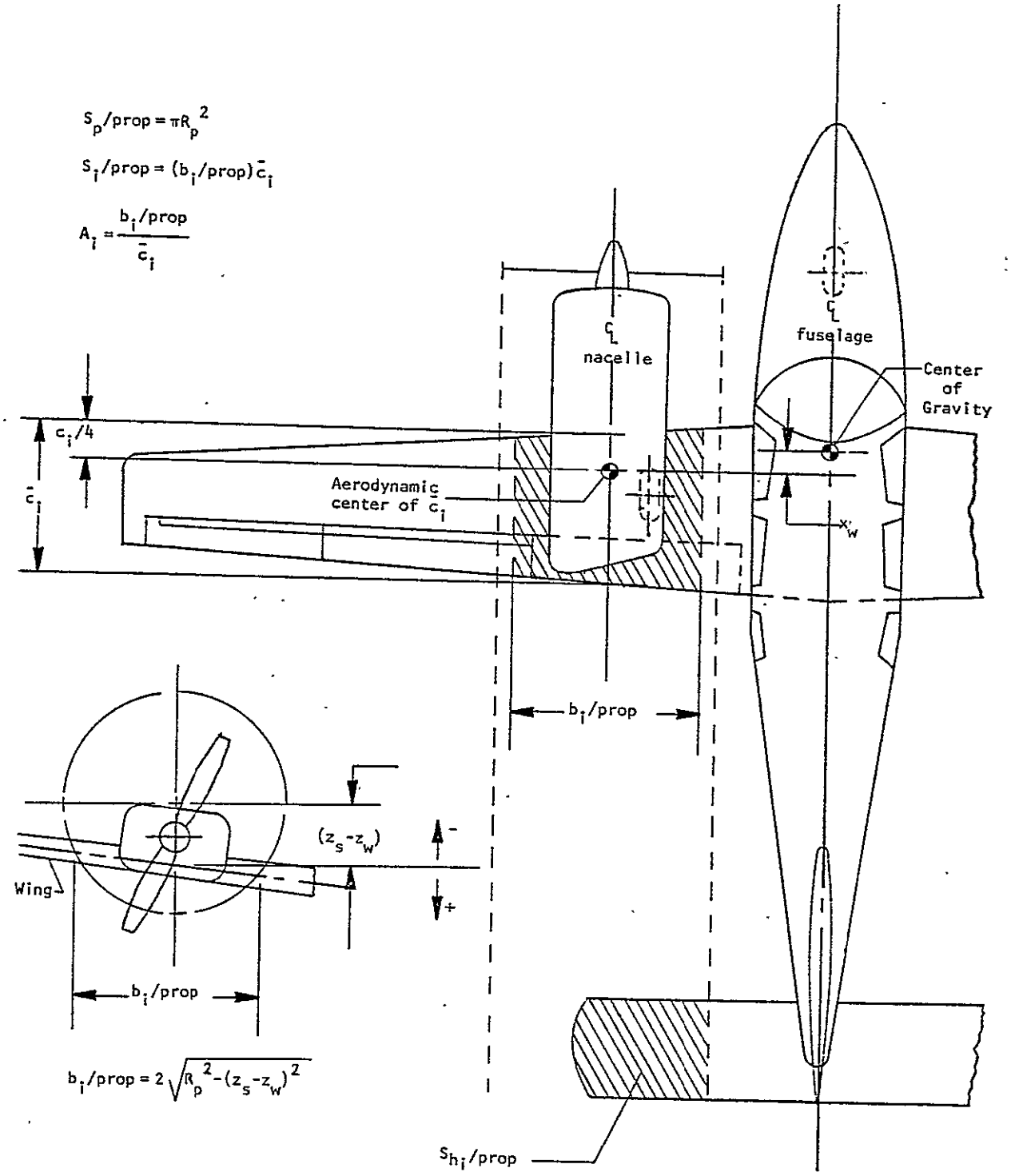

Figure 5.1: Concluded

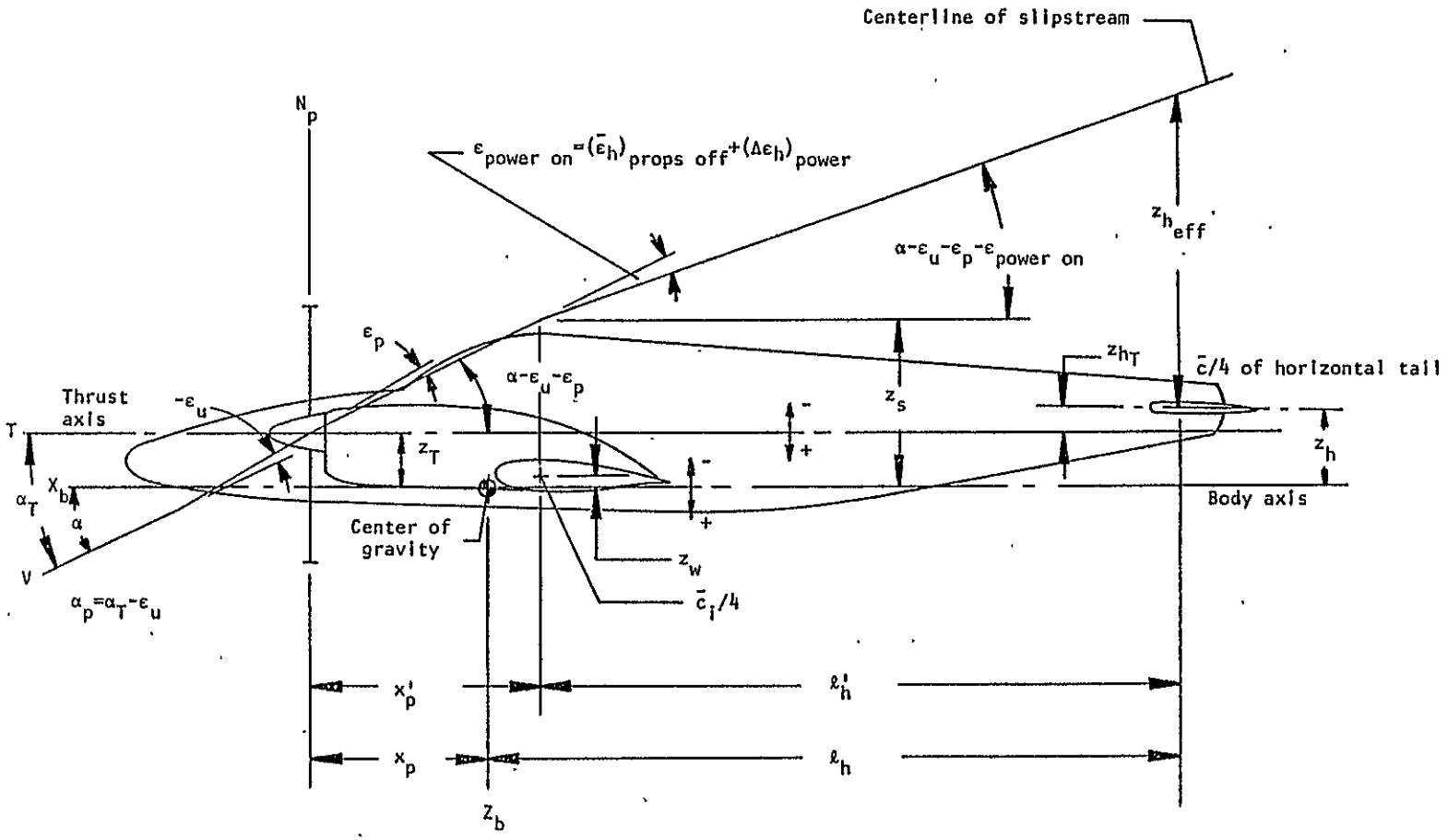

Figure 5.2: Definition sketch for calculation of propeller power effects

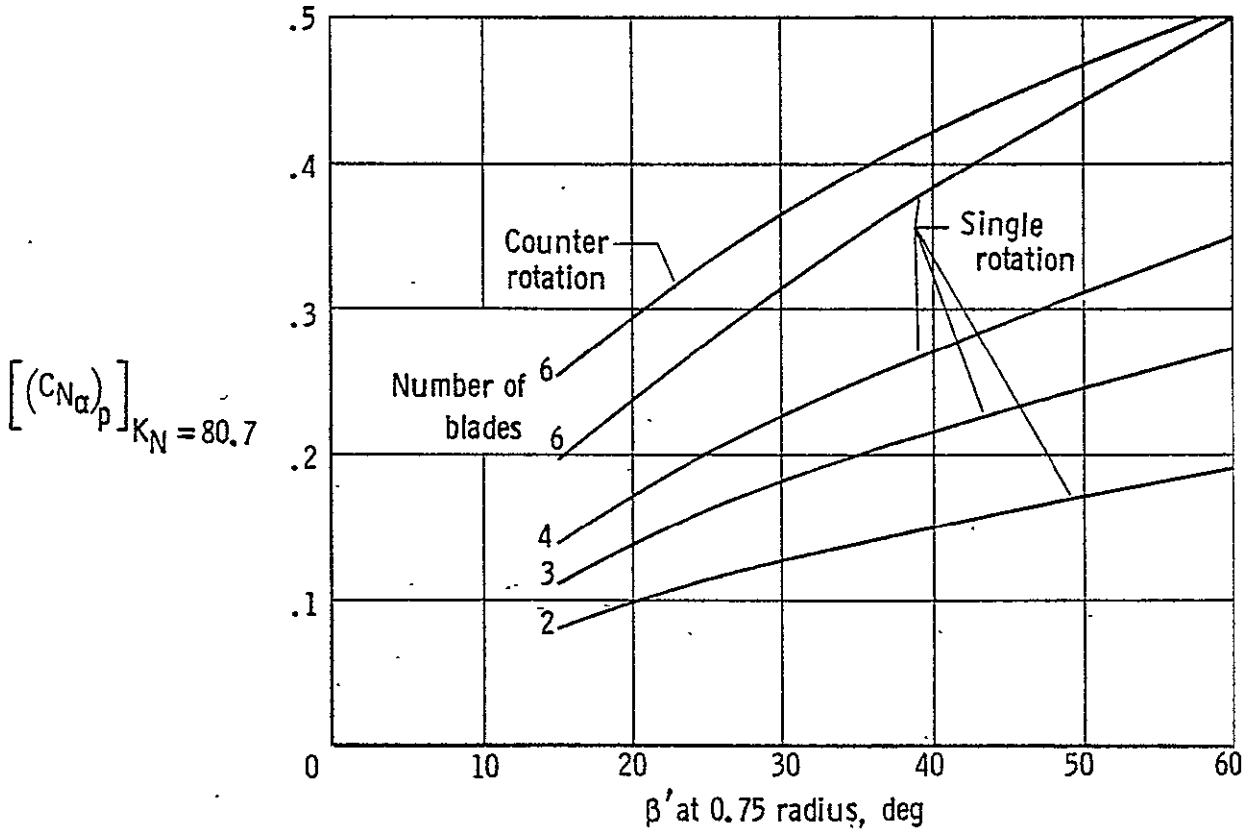

Figure 5.1.1.1: Propeller normal force parameter (Reference 3)

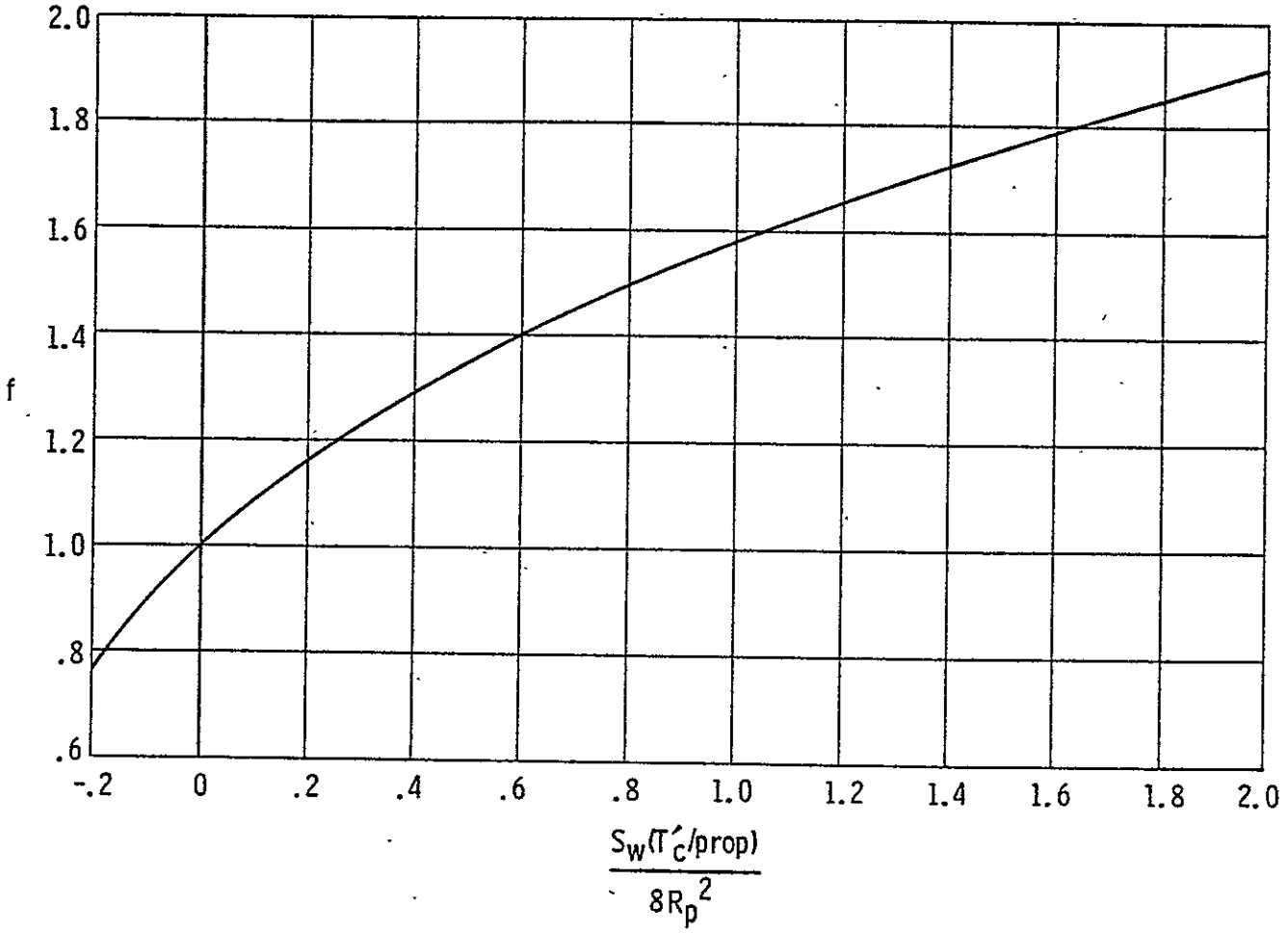

Figure 5.1.1.2: Propeller inflow factor (Reference 3)

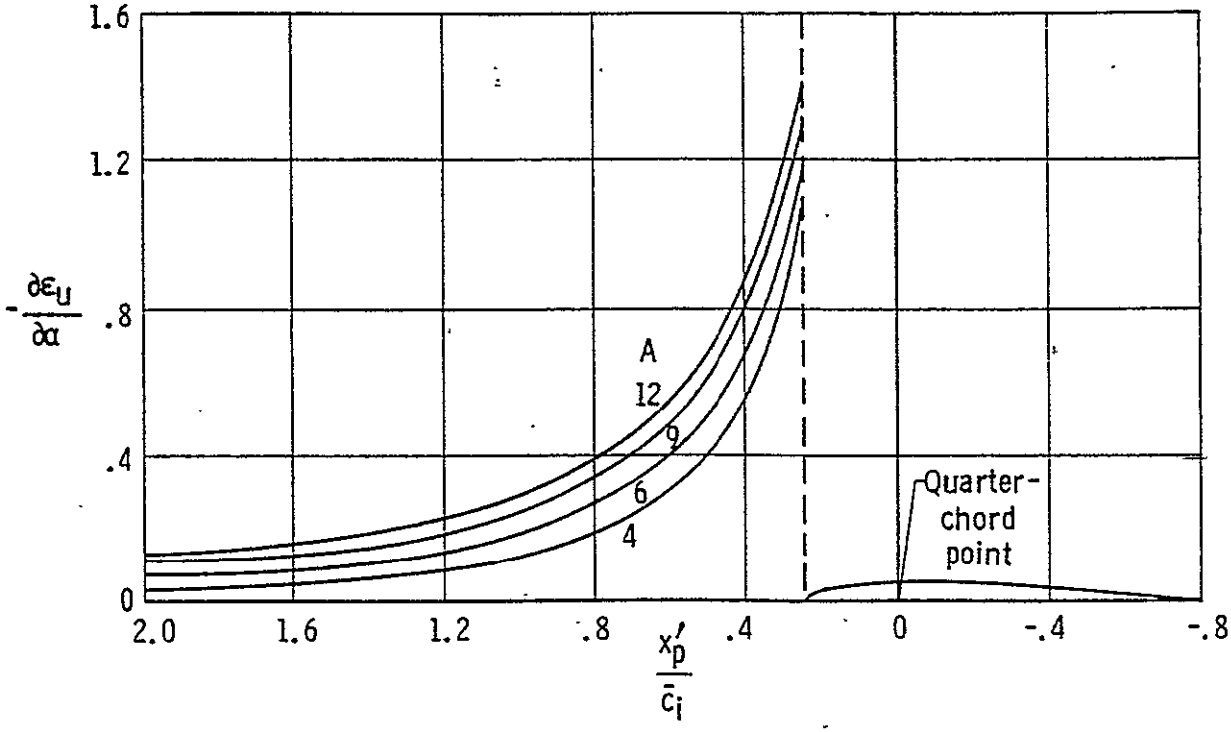

Figure 5.1.1.3: Upwash gradient at plane of symmetry for unswept wings (Reference 3)

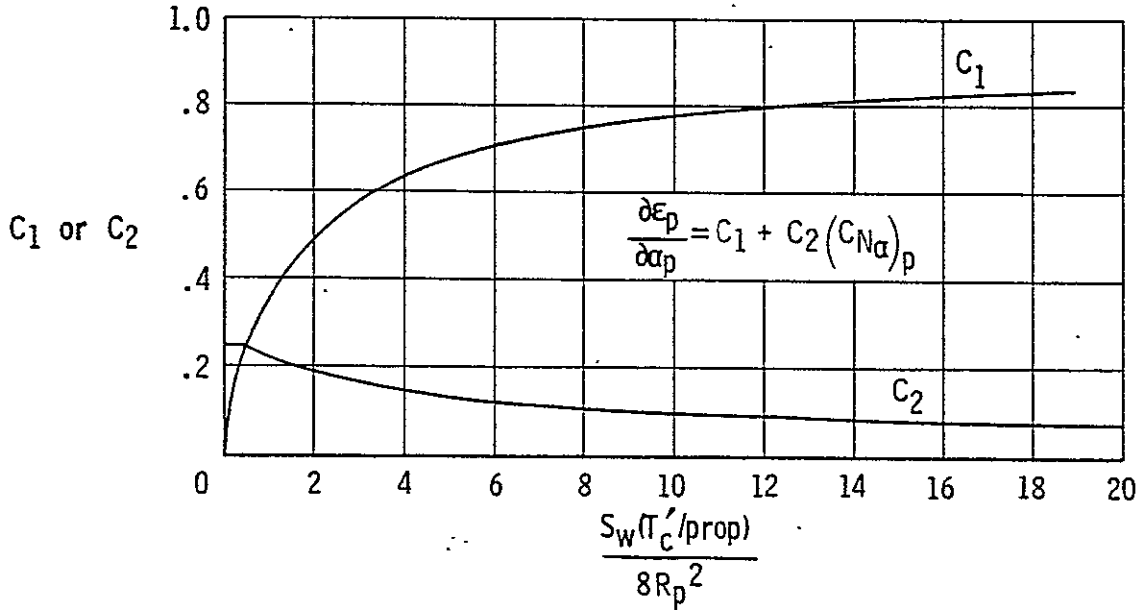

Figure 5.1.1.4: Factors for determining propeller downwash (Reference 3)

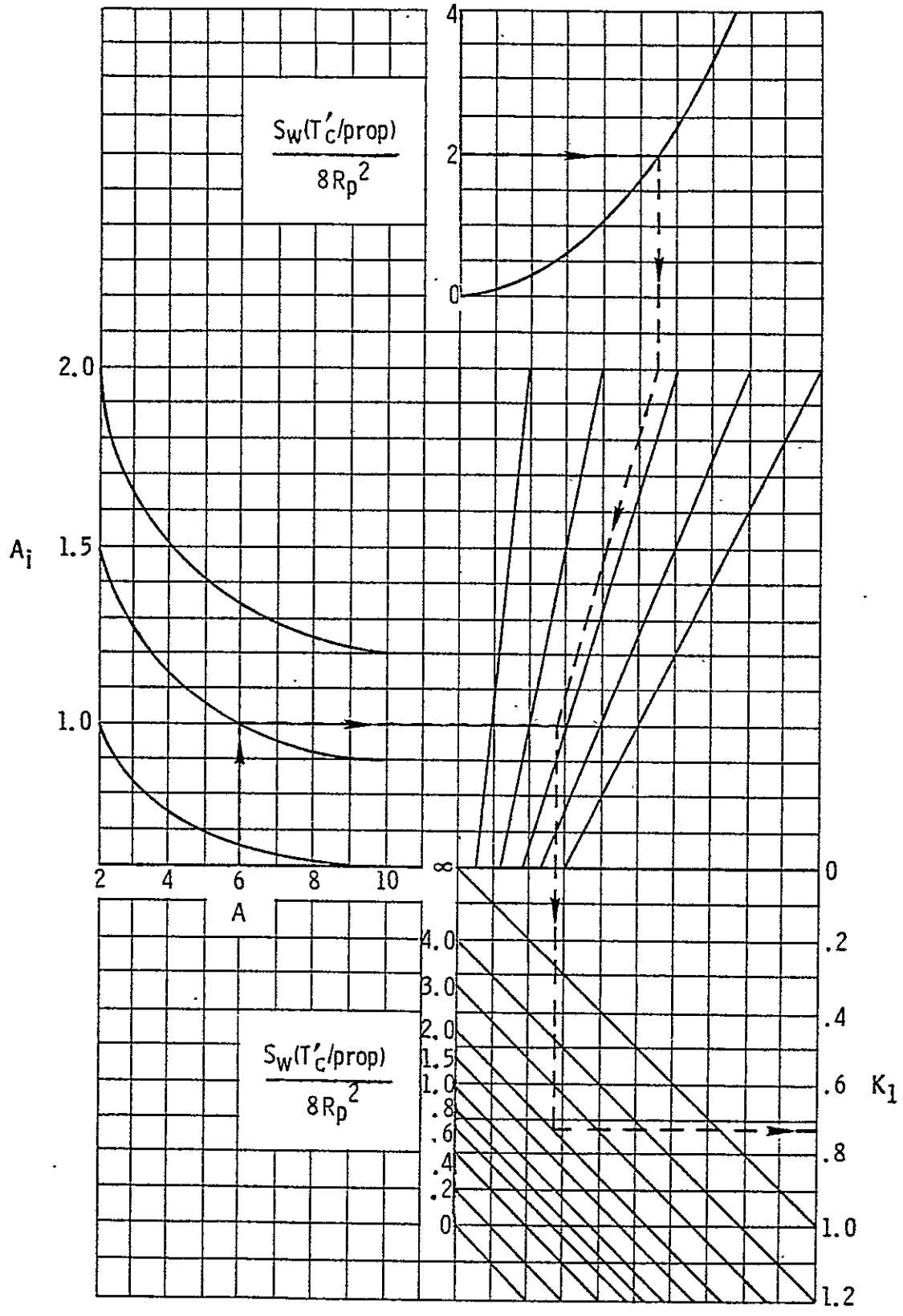

Figure 5.1.1.5: Correlation parameter for additional wing lift due to propeller power (Reference 3)

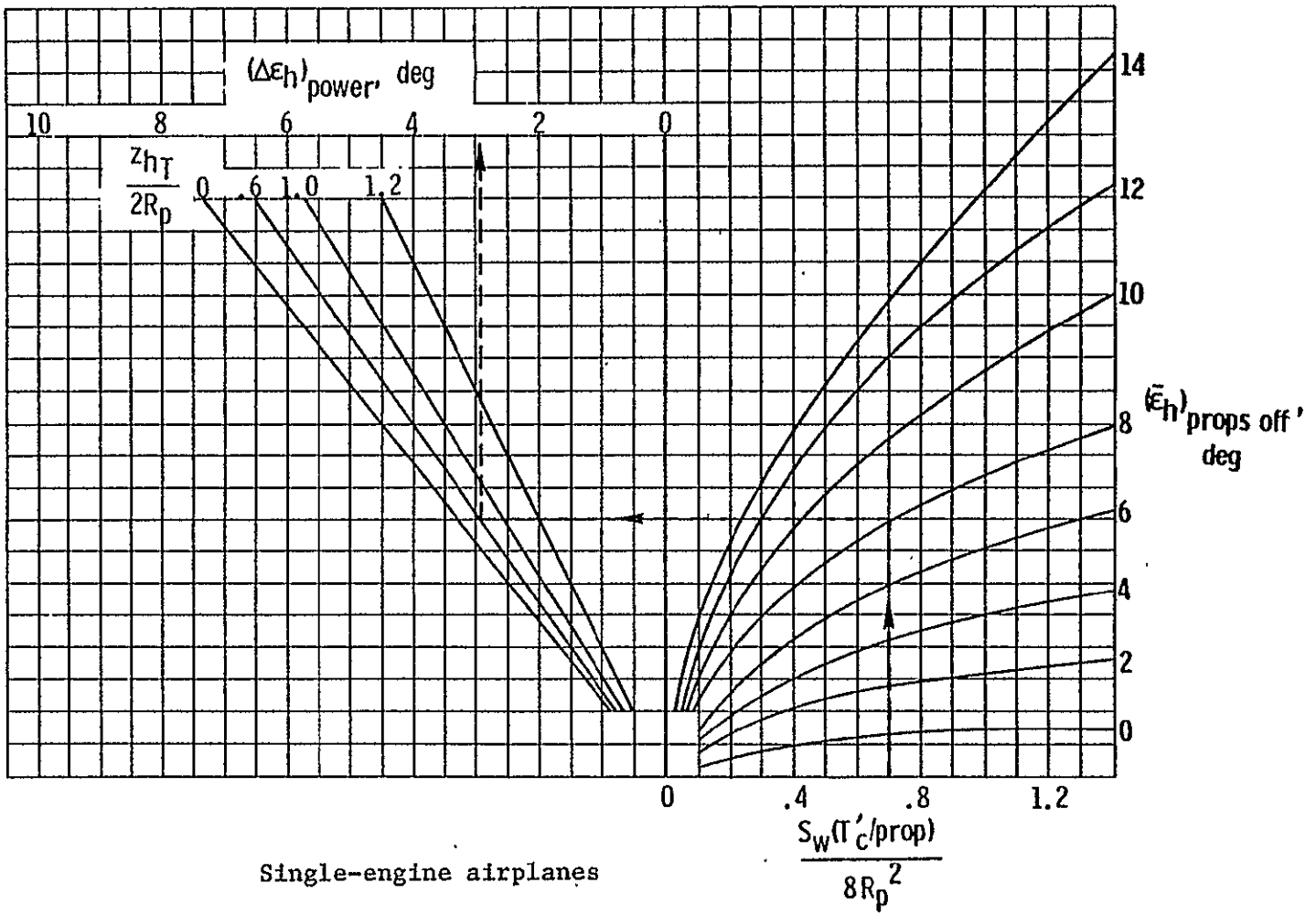

Figure 5.1.1.6: Increment in downwash due to propeller power (Reference 3)

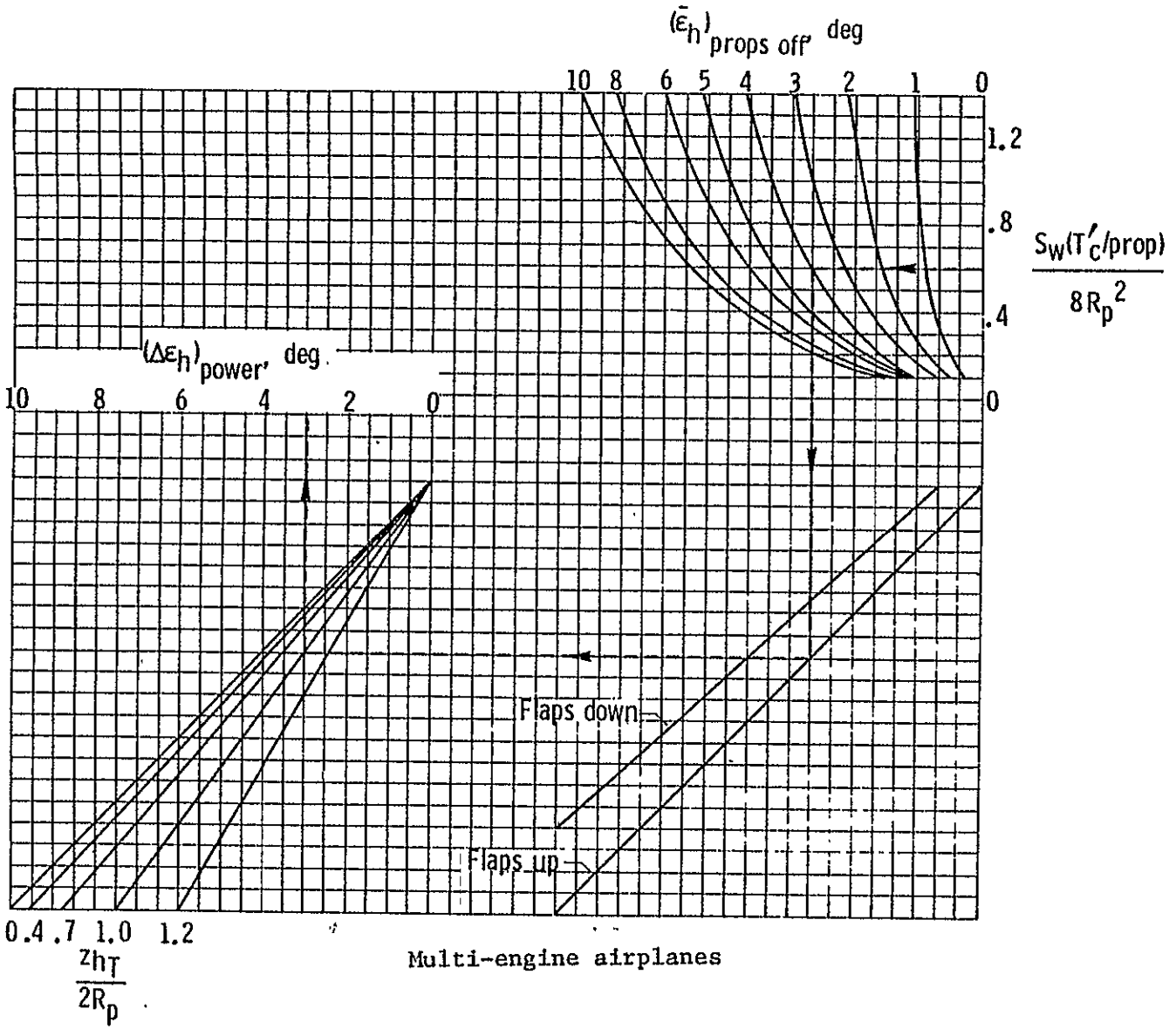

Multi-engine airplanes

Figure 5.1.1.6: Concluded

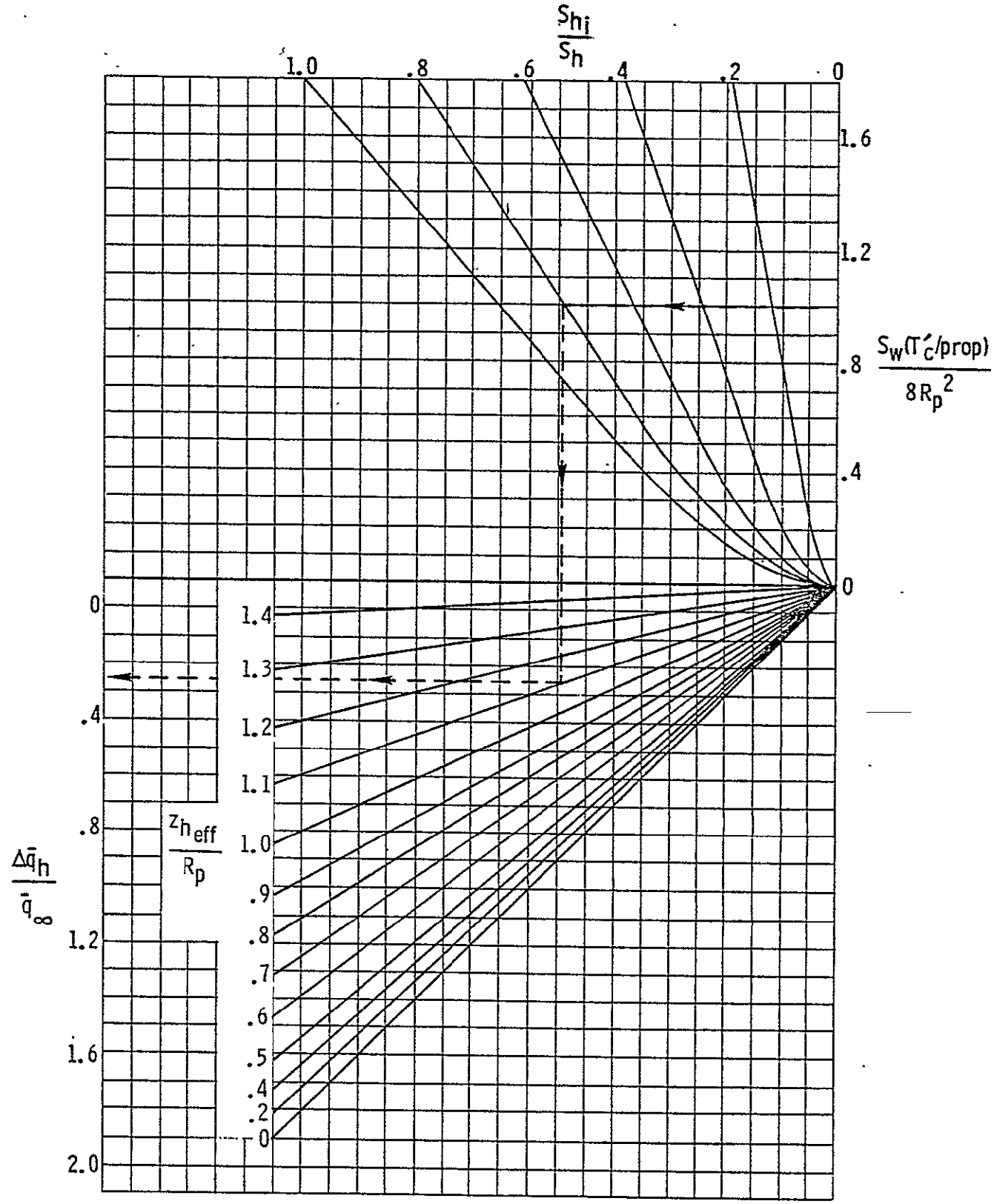

Figure 5.1.1.7: Effect of propeller power on the dynamic pressure ratio at horizontal tail (Reference 3)

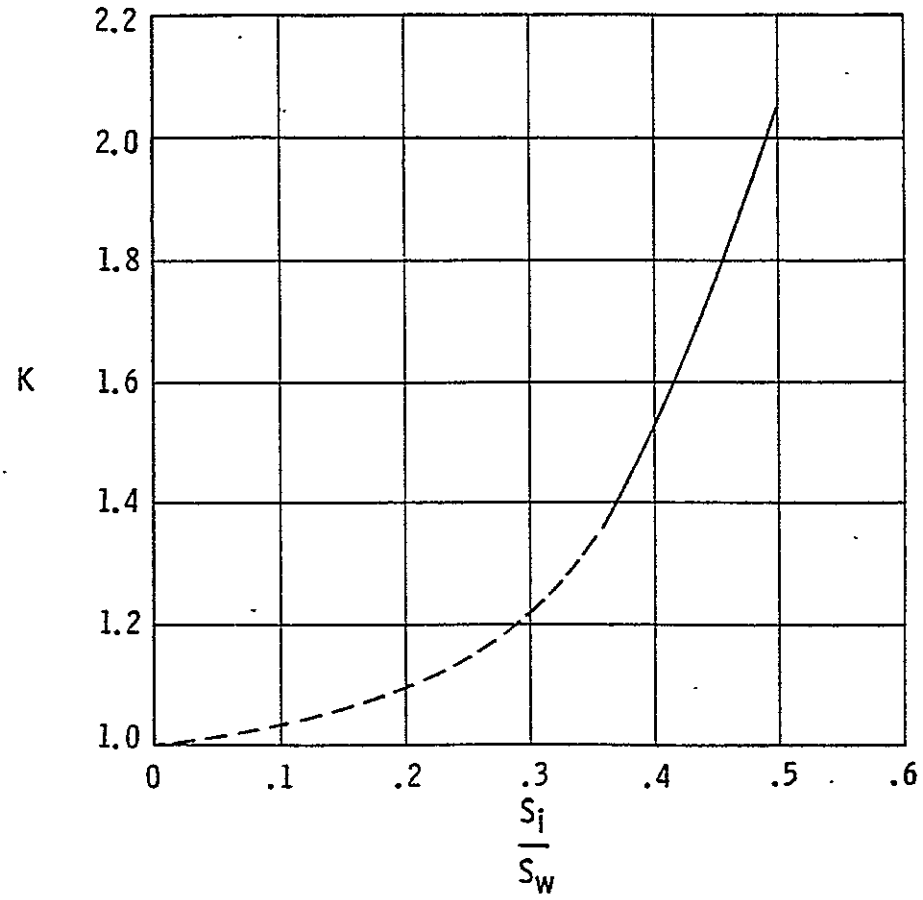

Figure 5.1.2.1: Correlation factor for maximum lift due to power (Reference 3)

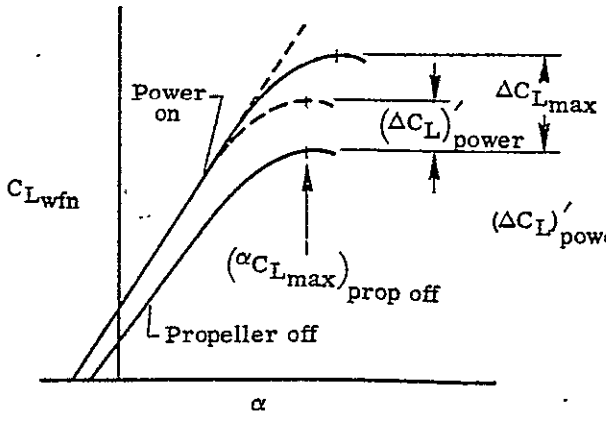

$$(\Delta C_L)'_{power} = (\Delta C_L)_T + (\Delta C_L)_{N_p} + (\Delta C_L)_{\Delta \bar{q}_w} + (\Delta C_L)_{\epsilon_p}$$

Figure 5.1.2.2: Construction of the power-on tail-off lift curve

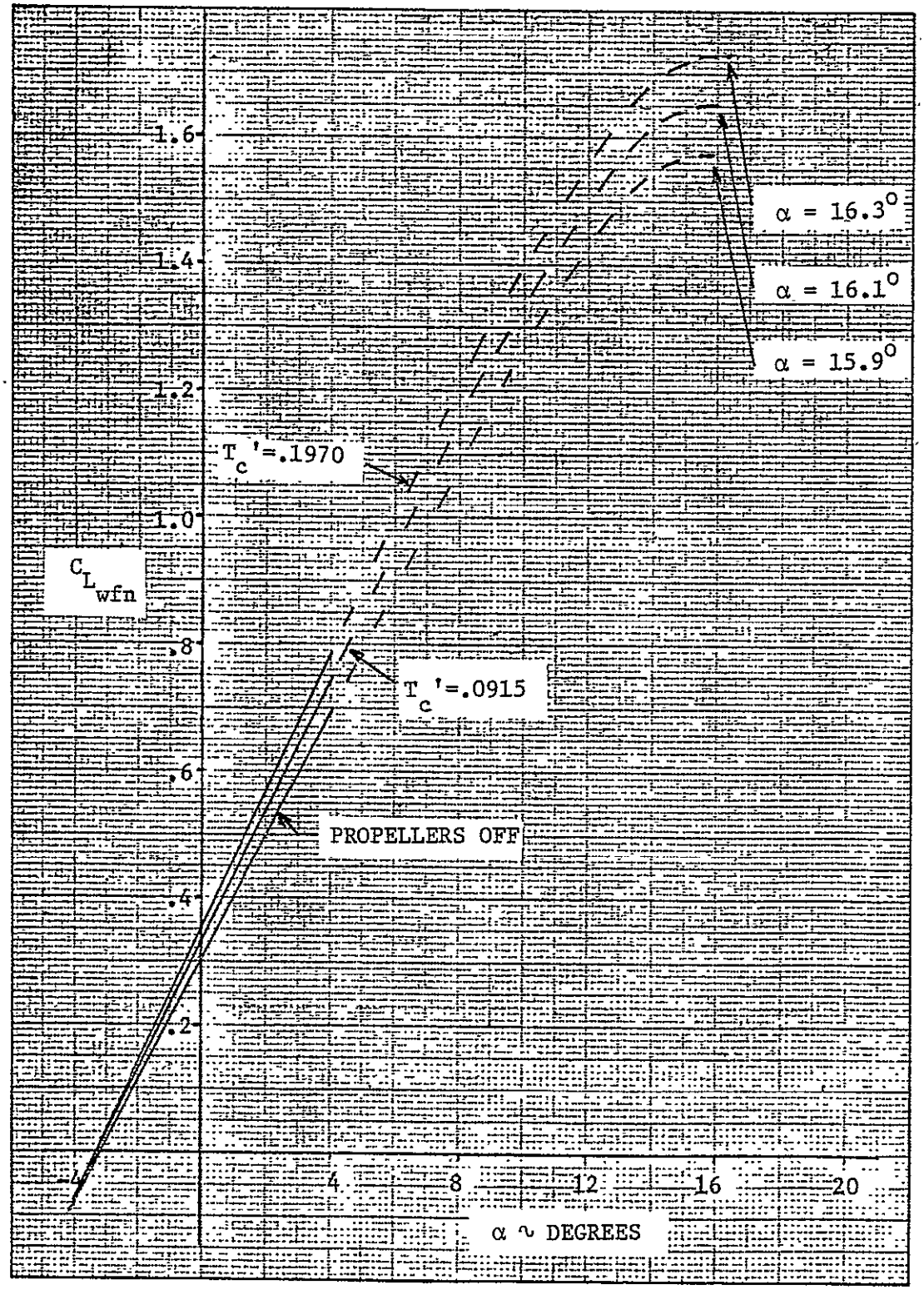

Figure 5.1.3.1: Tail-off lift characteristics of the ATLIT airplane for different power settings. $\Delta C_{L_{max}}$ obtained from Table 5.1.3.5 (N_{Re} = 2.3 million)

C-4

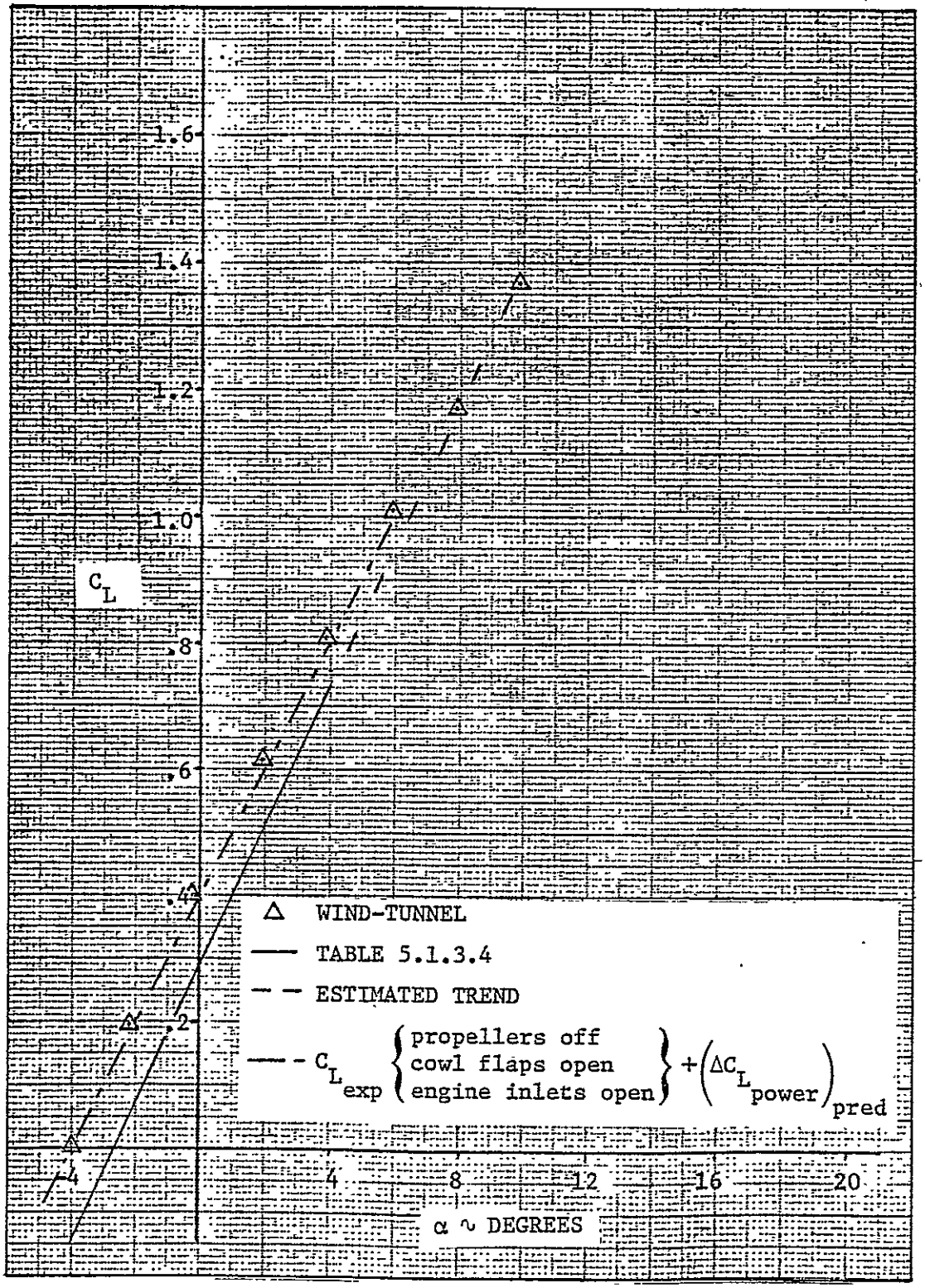

Figure 5.1.3.2: Comparison of predicted lift curve with full-scale wind tunnel data (T_c' = 0.0915, no stabilizer deflection)

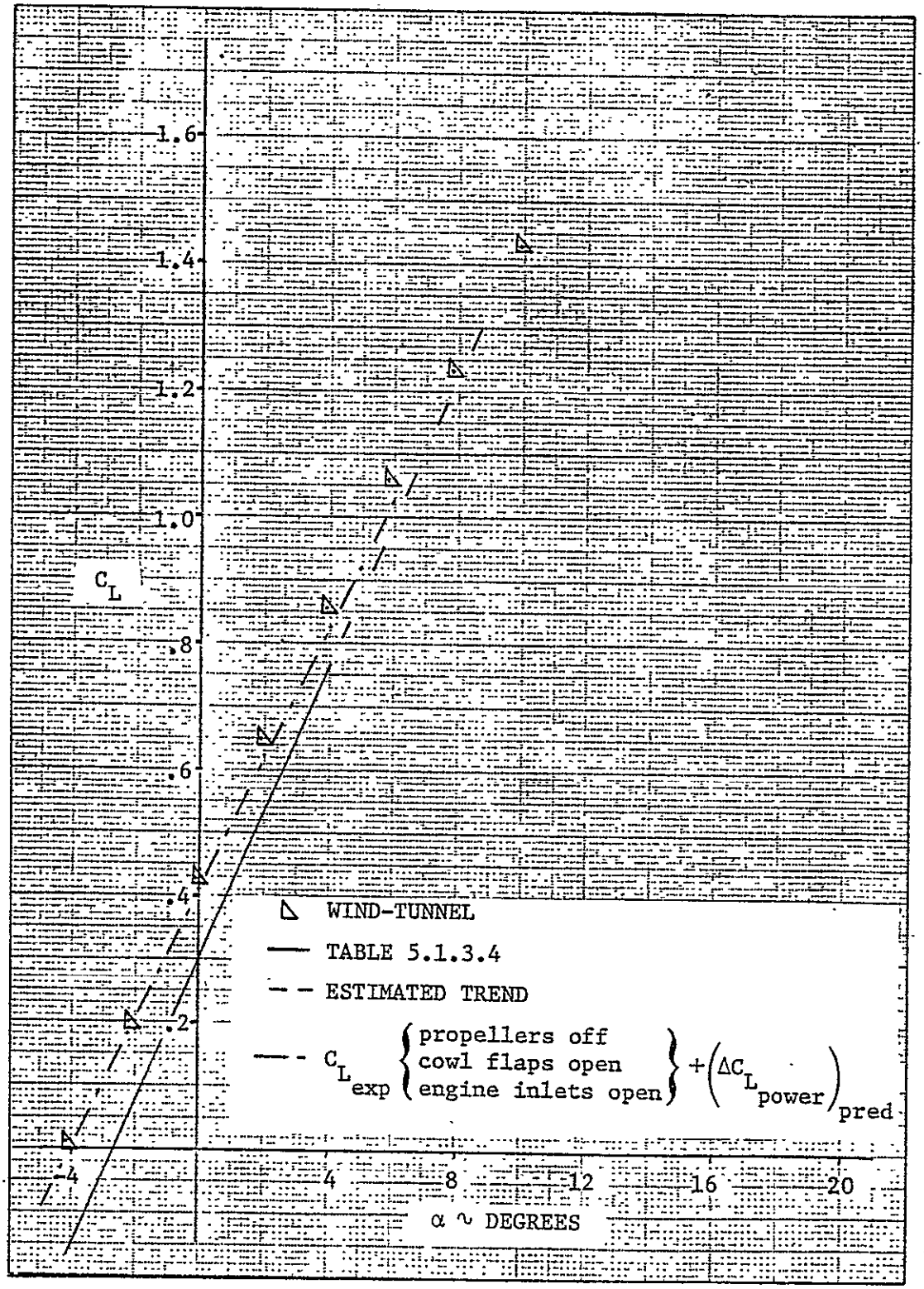

Figure 5.1.3.3: Comparison of predicted lift curve with full-scale wind tunnel data ($T_c' = 0.1970$, no stabilizer deflection)

5.2 Propeller Power Effects on Pitching Moment

Power effects of propellers introduce increments of pitching moment due to direct action of the propeller forces offset from the center of gravity and propeller induced slipstream effects on the wing, nacelles (or fuselage), and the horizontal tail. Although all the increments of lift due to power (Section 5.1) contribute to power induced increments of pitching moment, several additional contributions must be considered. These contributions include the propeller slipstream dynamic pressure effect on C_{m_o} and nacelle (or fuselage) free moments.

The pitching moment of the complete airplane can be considered as follows:

$$C_m = (C_m)_{\text{prop off}} + (\Delta C_m)_T + (\Delta C_m)_{N_p} + (\Delta C_{m_o})_{\Delta\bar{q}_w} + (\Delta C_m)_{\Delta\bar{q}_w} + (\Delta C_m)_{\varepsilon_p} + (\Delta C_m)_{B_p} + (\Delta C_m)_{\Delta\bar{q}_h} + (\Delta C_m)_{(\Delta\varepsilon_h)_{\text{power}}} \quad (5.2:1)$$

where

$(C_m)_{\text{prop off}}$ is the propeller-off pitching moment obtained from Section 4.13.

$(\Delta C_m)_T$ is the pitching moment due to offset of the thrust from the center of gravity.

$(\Delta C_m)_{N_p}$ is the pitching moment due to offset of propeller normal force from the center of gravity.

$(\Delta C_{m_o})_{\Delta\bar{q}_w}$ is the effect of propeller slipstream dynamic pressure increment on zero-lift pitching.

$(\Delta C_m)_{\Delta\bar{q}_w}$ is the effect on pitching moment due to change in wing lift resulting from change in propeller-induced dynamic pressure.

$(\Delta C_m)_{\varepsilon_p}$ is the pitching moment due to change in wing angle of attack resulting from propeller slipstream.

$(\Delta C_m)_{B_p}$ is the effect of propeller slipstream on body (nacelle or fuselage) free moments.

$(\Delta C_m)_{\Delta \bar{q}_h}$ is the pitching moment due to change in dynamic pressure acting on the horizontal tail.

$(\Delta C_m)_{(\Delta \varepsilon_h)_{power}}$ is the pitching moment due to change in angle of attack at the horizontal tail.

In the following discussion of power effects on pitching moment the pitching moment of the complete airplane will be considered as follows:

$$C_m = (C_{m_{wfn}})_{prop\ off} + (\Delta C_m)_T + (\Delta C_m)_{N_p} + (\Delta C_{m_o})_{\Delta \bar{q}_w} + (\Delta C_m)_{W_L} + (\Delta C_m)_{B_p} + \bar{C}_{m_{h(hf)}} \tag{5.2.2}$$

where

$(C_{m_{wfn}})_{prop\ off}$ is the propeller-off, tail-off pitching moment obtained from Section 4.8.

$(\Delta C_m)_{W_L}$ is the net effect on pitching moment due to change in wing lift resulting from propeller slipstream induced dynamic pressure and angle of attack changes on the wing, or:

$$(\Delta C_m)_{W_L} = (\Delta C_m)_{\Delta \bar{q}_w} + (\Delta C_m)_{\varepsilon_p} \tag{5.2.3}$$

$\bar{C}_{m_{h(hf)}}$ is the net pitching moment contribution of the horizontal tail for power-on conditions, which can be obtained as follows:

$$\bar{C}_{m_{h(hf)}} = (\bar{C}_{m_{h(hf)}})_{prop\ off} + (\Delta C_m)_h \tag{5.2.4}$$

The above mentioned increments in pitching moment can be determined by the following steps.

The pitching moment increment, $(\Delta C_m)_T$ due to propeller thrust is obtained from:

$$(\Delta C_m)_T = n(T_c'/\text{prop}) \frac{z_T}{\bar{c}_w} \tag{5.2.5}$$

where

n is the number of propellers.

z_T is the moment arm of the thrust relative to the center of gravity, obtained from Figure 5.2.

$\bar{c}_w$ is the wing mean aerodynamic (geometric) chord.

T_c'/prop is the thrust coefficient due to one propeller obtained from Section 5.1.

The pitching moment increment, $(\Delta C_m)_{N_p}$, due to propeller normal force can be determined as follows:

$$(\Delta C_m)_{N_p} = (\Delta C_L)_{N_p} \frac{x_p}{\bar{c}_w} \frac{1}{\cos\alpha_T} \tag{5.2.6}$$

where

$(\Delta C_L)_{N_p}$ is the increment in lift due to the normal force of the propeller, obtained from Section 5.1.

x_p is the moment arm of the propeller force relative to the center of gravity, obtained from Figure 5.2.

α_T is the angle of attack of the thrust axis, obtained from Section 5.1.

The zero-lift pitching moment increment, $(\Delta C_{m_o})_{\Delta \bar{q}_w}$, due to propeller slipstream effects on immersed portions of the wing-body or wing-nacelles at zero-lift condition can be obtained as follows:

a) Calculate the zero-lift pitching moment coefficient of those components of the tail-off configuration that are not immersed by the propeller slipstream as follows:

$$(C_{m_o})_{\substack{\text{area not} \\ \text{immersed}}} = (C_{m_o})_{w_{\text{prop off}}} \frac{S_w - S_i}{S_w} \frac{S_w - S_i}{(b_w - b_i)\bar{c}_w} \qquad (5.2.7)$$

where

$(C_{m_o})_{w_{\text{prop off}}}$ is the C_{m_o} of the wing with the propellers removed, obtained from Section 4.5.

b) Calculate the zero-lift pitching moment coefficient, $(C_{m_o})_{i_{\text{prop off}}}$, of those components of the tail-off configuration immersed by the propeller slipstream as follows:

$$(C_{m_o})_{i_{\text{prop off}}} = (C_{m_o})_{wB_{\text{prop off}}} - (C_{m_o})_{\substack{\text{area not} \\ \text{immersed}}} \qquad (5.2.8)$$

where

$(C_{m_o})_{wB_{\text{prop off}}}$ is the propeller-off C_{m_o} of the wing and nacelles, $(C_{m_o})_{wn_{\text{prop off}}}$, for a multi-engine airplane and the propeller-off C_{m_o} of the wing and fuselage, $(C_{m_o})_{wf_{\text{prop off}}}$, for a single-engine airplane, obtained from Section 4.6.

c) Calculate the zero-lift pitching moment due to the change in slipstream dynamic pressure by:

$$(\Delta C_{m_o})_{\Delta \bar{q}_w} = \frac{\Delta \bar{q}_w}{\bar{q}_\infty} \frac{S_i}{S_w} \frac{\bar{c}_i}{\bar{c}_w} (C_{m_o})_{i_{\text{prop off}}} \qquad (5.2.9)$$

where

$\Delta\bar{q}_w/\bar{q}_\infty$ is the increase in dynamic-pressure ratio of the immersed portion of the wing, obtained from Section 5.1.

The pitching moment encrement, $(\Delta C_m)_{w_L}$, due to change in the lift of the wing resulting from power effects, is obtained as follows:

$$(\Delta C_m)_{w_L} = - \left[(\Delta C_L)_{\Delta\bar{q}_w} + (\Delta C_L)_{\varepsilon_p} \right] \frac{x_w}{\bar{c}_w} \tag{5.2.10}$$

where

x_w is the distance from the aerodynamic center of the immersed wing area to the center of gravity, obtained from Figure 5.1.

$(\Delta C_L)_{\Delta\bar{q}_w}$ and $(\Delta C_L)_{\varepsilon_p}$ are obtained from Section 5.1.

The pitching moment increment, $(\Delta C_m)_{B_p}$, due to propeller slipstream effects on the nacelle free moments (for multi-engine configurations) or on the fuselage free moments (for single-engine airplanes), is accounted for by calculation similar to those in Section 4.8 which considered the free moments due to wing induced flows with the propellers removed. The following expression indicates the nacelle free moments increment:

$$(\Delta C_m)_{n_p} = - \frac{n\ (\varepsilon_p + \varepsilon_u)}{36.5\ S_w\ \bar{c}_w} \left(1 + \frac{\Delta\bar{q}_w}{\bar{q}_\infty} \right) \int w_n^{\,2}\ dx \tag{5.2.11}$$

where

ε_p and $-\varepsilon_u$ are propeller induced changes in flow inclination on the nacelle obtained from Section 5.1.

$\Delta\bar{q}_w/\bar{q}_\infty$ can be obtained from Section 5.1.

$\int w_n^{\,2}\ dx$ of the nacelle is obtained from Section 4.8.

For single-engine airplanes the effect of power on the free moments

of the fuselage should be accounted for. The procedure is identical to the one above.

The net pitching moment contribution of the horizontal tail for power-on conditions, $\bar{C}_{m_{h(hf)}}$, is:

$$\bar{C}_{m_{h(hf)}} = -\frac{\ell_h}{\bar{c}_w} \bar{C}_{L_{h(hf)}} \tag{5.2.12}$$

where

ℓ_h is the distance from the center of gravity to the quarter chord of the mean aerodynamic chord of the horizontal tail, obtained from Figure 5.1.

$\bar{C}_{L_{h(hf)}}$ is the lift coefficient of the horizontal tail obtained from Section 5.1.

5.2.1 Pitching Moment Characteristics of the ATLIT Airplane

Tables 5.2.1.1 to 5.2.1.4 account for the pitching moment increments due to the direct propeller forces and power induced slipstream effects on the wing and nacelles. These increments are summarized and added to the propeller-off, tail-off pitching moments in Table 5.2.1.5 to provide power-on, tail-off characteristics. These characteristics are added to the power-on horizontal tail contributions (in Table 5.2.1.5) to provide the pitching moment characteristics of the complete ATLIT airplane.

The results of Table 5.2.1.5 are plotted in Figures 5.2.1.1 and 5.2.1.2 for $T_c' = 0.0915$, while the results for $T_c' = 0.1970$ are shown in Figures 5.2.1.3 and 5.2.1.4.

The predictions have been performed for a Reynolds number of 2.3

million. No power-on wind tunnel data, however, were available for the ATLIT in the "fully clean" configuration at a Reynolds number of 2.3 million. Data were available for a Reynolds number of 3.5 million. In the case of the ATLIT, this increase in Reynolds number will result in an increase in pitching moment, $(\Delta C_m)_{N_{Re}} \approx 0.03$, in the linear lift region. The predicted pitching moment, including the Reynolds number correction, is also shown in Figures 5.2.1.1 through 5.2.1.4.

The predicted pitching moment curves show fair agreement with the power-on full-scale wind tunnel data. The discrepancy between the predicted and experimental curves is caused mainly by the pitching moment contribution of the engine cooling system. The prediction method does not take into account the pitching moment due to the engine cooling, while from the wind tunnel data (see Section 4.11) it follows that the contribution is significant.

When the predicted increment in pitching moment due to power is added to the experimental pitching moment curve obtained with propellers removed, cowl flaps open, and engine inlets open, good agreement is obtained with the power-on wind tunnel data of Reference 2. The increment in pitching moment due to power can be obtained as follows:

$$(\Delta C_m)_{power} = C_m - (C_m)_{prop\ off} \qquad (5.2.1.1)$$

where

C_m is the predicted pitching moment coefficient of the airplane including power effects, obtained from Table 5.2.1.5.

$(C_m)_{prop\ off}$ is the predicted pitching moment coefficient of the airplane with propellers removed, obtained from Section 4.11.

Table 5.2.1.1: Pitching moment increment due to propeller forces

Symbol	Description	Reference	Magnitude
n	Number of propellers	Figure 5.1	2
$\bar{c}_w$	Wing mean aerodynamic chord, m (ft)	Table 2.1.1	1.225 (4.018)
z_T	Distance from X-body axis to thrust line, m (ft)	Figure 5.2	-0.128 (-0.417)
x_p	Distance from propeller plane to center of gravity, m (ft)	Figure 5.2	2.01 (6.59)
α_T	Angle of attack of thrust axis	Eq.(5.1.1.1)	α
T_c'/prop	Thrust coefficient per propeller	-	Variable
$(\Delta C_L)_{N_p}$	Normal force coefficient of the propellers	Table 5.1.3.1	Variable

α, deg	$(\Delta C_L)_{N_p}$; Table 5.1.3.1			$(\Delta C_m)_T$; Eq. (5.2.5)			$(\Delta C_m)_{N_p}$; Eq. (5.2.6)		
	T_c'			T_c'			T_c'		
	0	0.0915	0.1970	0	0.0915	0.1970	0	0.0915	0.1970
-4	-0.0029	-0.0031	-0.0033	0	-0.0095	-0.0204	-0.0047	-0.0051	-0.0054
-2	-0.0013	-0.0014	-0.0015	0	-0.0095	-0.0204	-0.0022	-0.0023	-0.0025
0	0.0004	0.0004	0.0004	0	-0.0095	-0.0204	0.0006	0.0006	0.0006
2	0.0020	0.0022	0.0024	0	-0.0095	-0.0204	0.0033	0.0036	0.0039
4	0.0036	0.0039	0.0042	0	-0.0095	-0.0204	0.0060	0.0064	0.0069

Table 5.2.1.2: Zero-lift pitching moment increment due to propeller power.

Symbol	Description	Reference	Magnitude
n	Number of propellers	Figure 5.1	2
R_p	Propeller radius, m (ft)	Table 2.1	0.97 (3.17)
S_w	Reference wing area, m^2 (ft^2)	Table 2.1.1	14.4 (155.0)
b_w	Wing span, m (ft)	Table 2.1.1	12.19 (40.0)
$\bar{c}_w$	Wing mean aerodynamic chord, m (ft)	Table 2.1.1	1.225 (4.018)
S_i	Total immersed wing area, m^2 (ft^2)	Table 5.1.3.2	Variable
$n(b_i/\text{prop})$	Total immersed span, m (ft)	Table 5.1.3.2	Variable
$\bar{c}_i$	Chord of immersed wing area, m (ft)	Figure 5.1	1.34 (4.38)
$(C_{m_o})_{w_{\text{prop off}}}$	Zero-lift pitching moment of wing, propellers off	Table 4.5.1	-0.0783
$(C_{m_o})_{wn_{\text{prop off}}}$	Zero-lift pitching moment of wing plus nacelles, propellers off	Table 4.6.1	-0.0783
$\Delta\bar{q}_w/\bar{q}_\infty$	Change in dynamic pressure ratio on immersed wing	Table 5.1.3.2	4.9098 (T_c'/prop)

Table 5.2.1.2: Concluded

α, deg	S_i/S_w; Table 5.1.3.2			b_w-b_i, ft; Table 5.1.3.2			$(C_{m_o})_{\text{area not immersed}}$; Eq.(5.2.7)		
	T_c'			T_c'			T_c'		
	0	0.0915	0.1970	0	0.0915	0.1970	0	0.0915	0.1970
-4	0.3565	0.3563	0.3560	27.385	27.391	27.401	-0.0457	-0.0457	-0.0457
-2	0.3529	0.3525	0.3523	27.513	27.524	27.532	-0.0460	-0.0460	-0.0460
0	0.3466	0.3467	0.3468	27.734	27.729	27.726	-0.0465	-0.0465	-0.0465
2	0.3379	0.3388	0.3395	28.043	28.009	27.986	-0.0472	-0.0471	-0.0471
4	0.3264	0.3287	0.3301	28.448	28.370	28.318	-0.0482	-0.0480	-0.0479

$(C_{m_o})_{\text{prop off}}$; Eq.(5.2.8)			$(\Delta C_{m_o})_{\Delta\tilde{q}_w}$; Eq. (5.2.9)		
T_c'			T_c'		
0	0.0915	0.1976	0	0.0915	0.1970
-0.0326	-0.0326	-0.0326	0	-0.0028	-0.0061
-0.0323	-0.0323	-0.0323	0	-0.0028	-0.0060
-0.0318	-0.0318	-0.0318	0	-0.0027	-0.0058
-0.0311	-0.0312	-0.0312	0	-0.0026	-0.0056
-0.0301	-0.0303	-0.0304	0	-0.0024	-0.0053

Table 5.2.1.3: Pitching moment increment due to power induced change in wing lift

Symbol	Description	Reference	Magnitude
x_w	Distance from $\bar{c}_i/4$ to center of gravity, m (ft)	Figure 5.2	0.026 (0.086)
$\bar{c}_w$	Wing mean aerodynamic chord, m (ft)	Table 2.1.1	1.225 (4.018)
$(\Delta C_L)_{\Delta \bar{q}_w}$	Change in wing lift due to power induced change in dynamic pressure on wing	Table 5.1.3.2	Variable
$(\Delta C_L)_{\varepsilon_p}$	Change in wing lift due to power induced change in flow direction on wing	Table 5.1.3.2	Variable

α, deg	$(\Delta C_L)_{\Delta \bar{q}_w}$; Table 5.1.3.2			$(\Delta C_L)_{\varepsilon_p}$; Table 5.1.3.2			$(\Delta C_m)_{w_L}$; Eq. (5.2.10)		
	T_c'			T_c'			T_c'		
	0	0.0915	0.1970	0	0.0915	0.1970	0	0.0915	0.1970
-4	0	-0.0043	-0.0088	0.0028	0.0141	0.0258	-0.0001	-0.0002	-0.0004
-2	0	0.0098	0.0203	0.0012	0.0061	0.0111	-0.	-0.0003	-0.0007
0	0	0.0235	0.0486	-0.0004	-0.0018	-0.0033	0.	-0.0005	-0.0010
2	0	0.0365	0.0756	-0.0018	-0.0093	-0.0171	0.	-0.0006	-0.0013
4	0	0.0485	0.1007	-0.0032	-0.0164	-0.0301	0.0001	-0.0007	-0.0015

Table 5.2.1.4: Pitching moment increment due to power effect on nacelle free moments

Symbol	Description	Reference	Magnitude
n	Number of nacelles	Figure 5.1	2
S_w	Reference wing area, $m^2(ft^2)$	Table 2.1.1	14.4 (155.0)
$\bar{c}_w$	Wing mean aerodynamic chord, m(ft)	Table 2.1.1	1.225 (4.018)
$-\epsilon_u$	Upwash at propeller, deg	Table 5.1.3.2	Variable
ϵ_p	Propeller induced downwash behind propeller, deg.	Table 5.1.3.2	Variable
$\Delta\bar{q}_w/\bar{q}_\infty$	Change in dynamic pressure ratio on immersed wing	Table 5.1.3.2	4.9098 (T_c'/prop)
$\int w_n^2\, dx$	Integral of square of mean width of nacelle planform segments of Δx length, $m^3(ft^3)$	Table 4.8.1.2	1.15 (40.69) per nacelle

α, deg	ϵ_p, deg; Table 5.1.3.2			ϵ_u, deg	$(\Delta C_m)_{n_p}$; Eq. (5.2.11)		
	T_c'			Table 5.1.3.2	T_c'		
	0	0.0915	0.1970		0	0.0915	0.1970
-4	-0.1023	-0.4217	-0.6348	0.0946	0	0.0014	0.0029
-2	-0.0445	-0.1835	-0.2763	-0.2155	0.0009	0.0017	0.0026
0	0.0133	0.0546	0.0823	-0.5255	0.0018	0.0021	0.0024
2	0.0710	0.2928	0.4408	-0.8355	0.0027	0.0024	0.0021
4	0.1288	0.5310	0.7993	-1.1455	0.0036	0.0027	0.0018

Table 5.2.1.5: Pitching moment characteristics with tail-off and tail-on with power on

α, deg	$(\Delta C_m)_T$; Table 5.2.1.1			$(\Delta C_m)_{N_p}$; Table 5.2.1.1			$(\Delta C_{m_o})_{\Delta\bar{q}_w}$; Table 5.2.1.2			$(\Delta C_m)_{w_L}$; Table 5.2.1.3		
	T_c'			T_c'			T_c'			T_c'		
	0	0.0915	0.1970	0	0.0915	0.1970	0	0.0915	0.1970	0	0.0915	0.1970
-4	0	-0.0095	-0.0204	-0.0047	-0.0051	-0.0054	0	-0.0028	-0.0061	-0.0001	-0.0002	-0.0004
-2	0	-0.0095	-0.0204	-0.0022	-0.0023	-0.0025	0	-0.0028	-0.0060	0	-0.0003	-0.0007
0	0	-0.0095	-0.0204	0.0006	0.0006	0.0006	0	-0.0027	-0.0058	0	-0.0005	-0.0010
2	0	-0.0095	-0.0204	0.0033	0.0036	0.0039	0	-0.0026	-0.0056	0	-0.0006	-0.0013
4	0	-0.0095	-0.0204	0.0060	0.0064	0.0069	0	-0.0024	-0.0053	0.0001	-0.0007	-0.0015

$(\Delta C_m)_{n_p}$; Table 5.2.1.4			$(C_{m_{wfn}})_{prop\ off}$	$C_{m_{wfn}}$; Eq. (5.2.2)			$\bar{C}_{L_{h(hf)}}$; Table 5.1.3.4			$\bar{C}_{m_{h(hf)}}$; Eq. (5.2.12)		
T_c'			Table 4.8.4.1	T_c'			T_c'			T_c'		
0	0.0915	0.1970		0	0.0915	0.1970	0	0.0915	0.1970	0	0.0915	0.1970
0.	0.0014	0.0029	-0.1256	-0.1304	-0.1418	-0.1550	-0.0662	-0.0682	-0.0728	0.2606	0.2684	0.2865
0.0009	0.0017	0.0026	-0.0806	-0.0819	-0.0938	-0.1076	-0.0454	-0.0504	-0.0598	0.1787	0.1983	0.2353
0.0018	0.0021	0.0024	-0.0365	-0.0341	-0.0465	-0.0607	-0.0244	-0.0346	-0.0471	0.0960	0.1361	0.1853
0.0027	0.0024	0.0021	0.0067	0.0127	0.	-0.0146	-0.0034	-0.0165	-0.0288	0.0134	0.0649	0.1133
0.0036	0.0027	0.0018	0.0490	0.0587	0.0455	0.0305	0.0179	0.0002	-0.0151	-0.0704	-0.0008	0.0594

C_m; Eq. (5.2.2)		
T_c'		
0	0.0915	0.1970
0.1302	0.1266	0.1317
0.0968	0.1045	0.1277
0.0619	0.0896	0.1246
0.0261	0.0649	0.0987
-0.0118	0.0447	0.0899

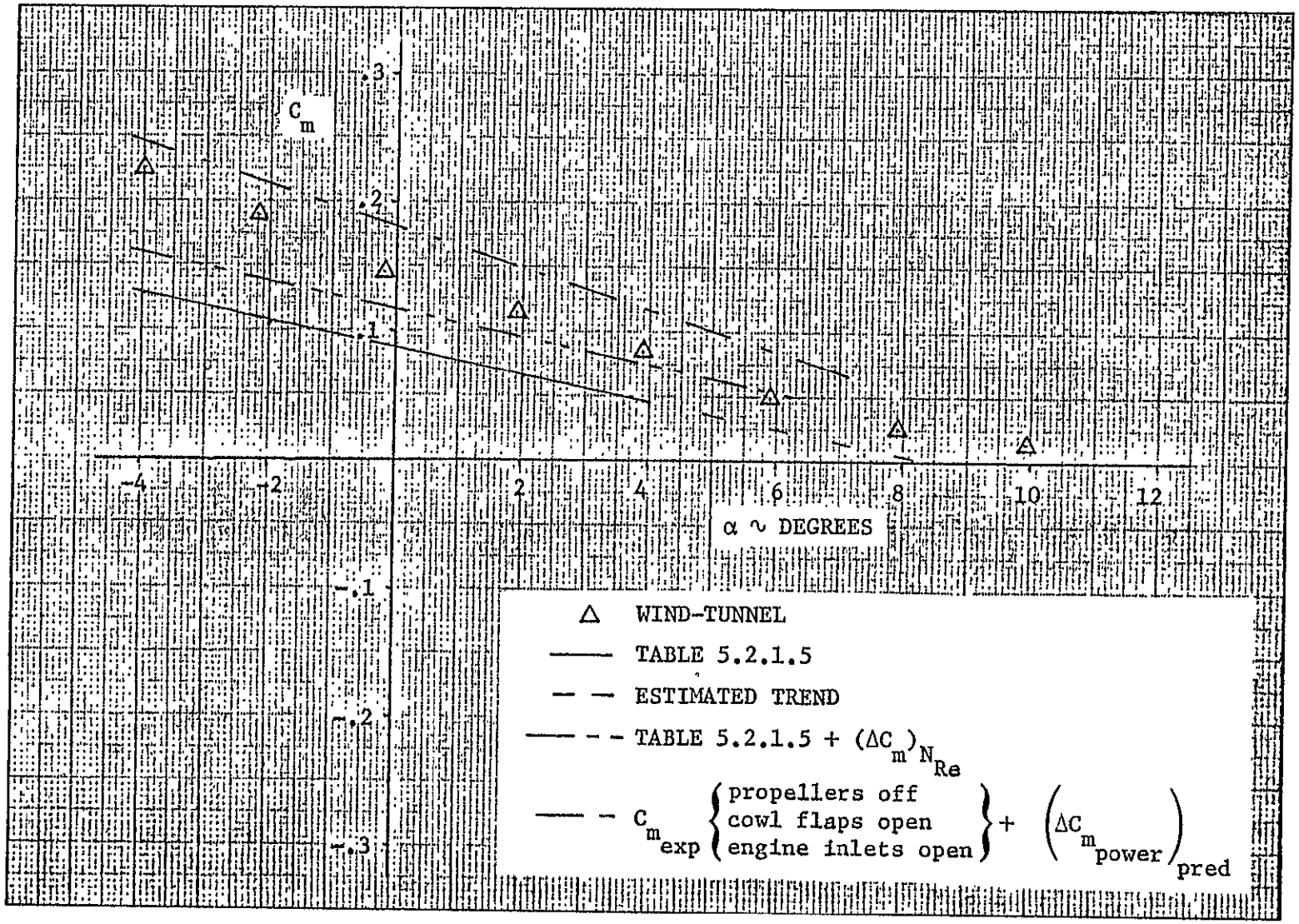

Figure 5.2.1.1: Comparison of predicted pitching moments with full-scale wind-tunnel data ($T_c' = 0.0915$, no stabilizer deflection)

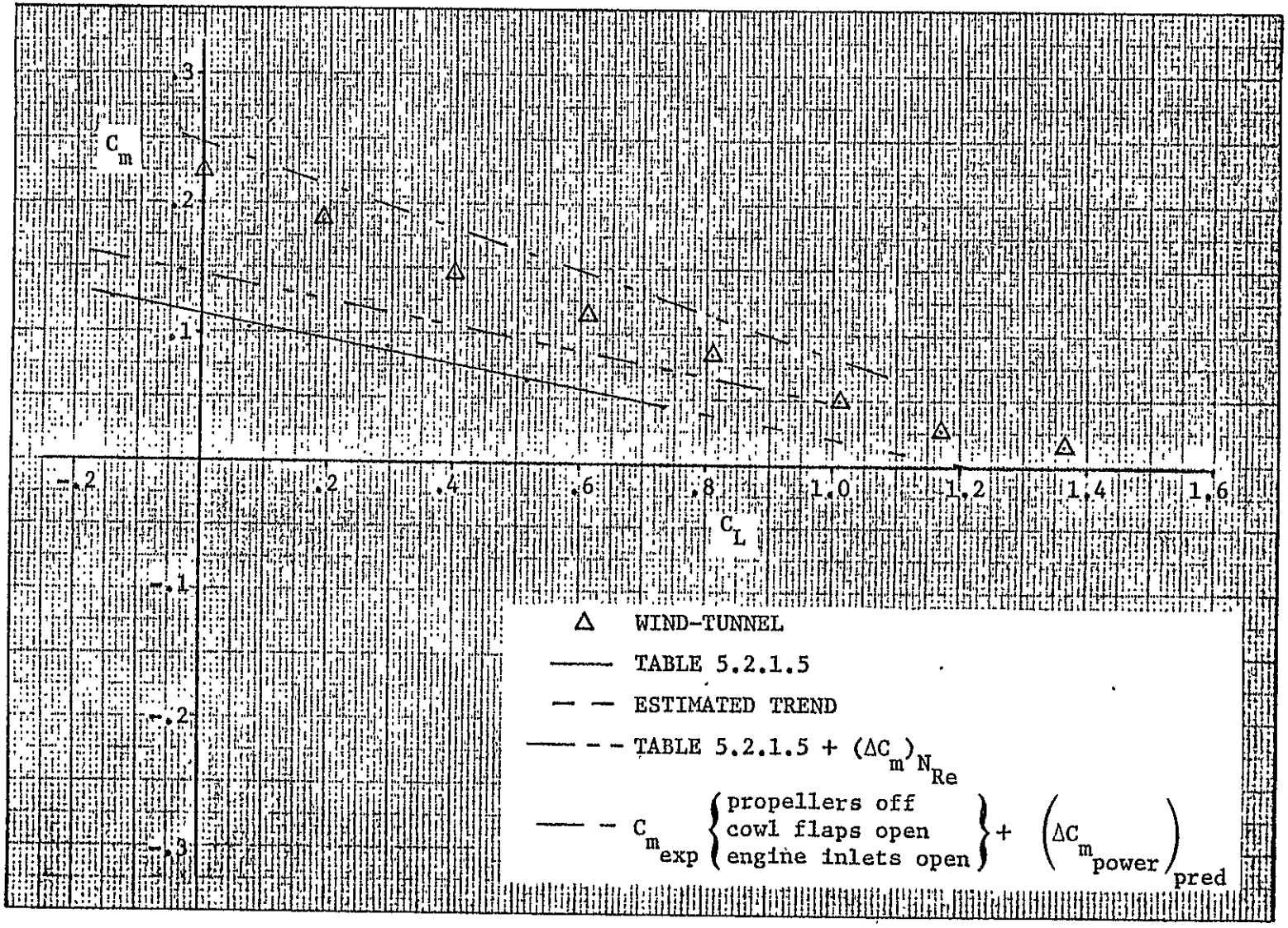

Figure 5.2.1.2: Comparison of predicted pitching moments with wind tunnel results ($T_c' = 0.0915$, no stabilizer deflection)

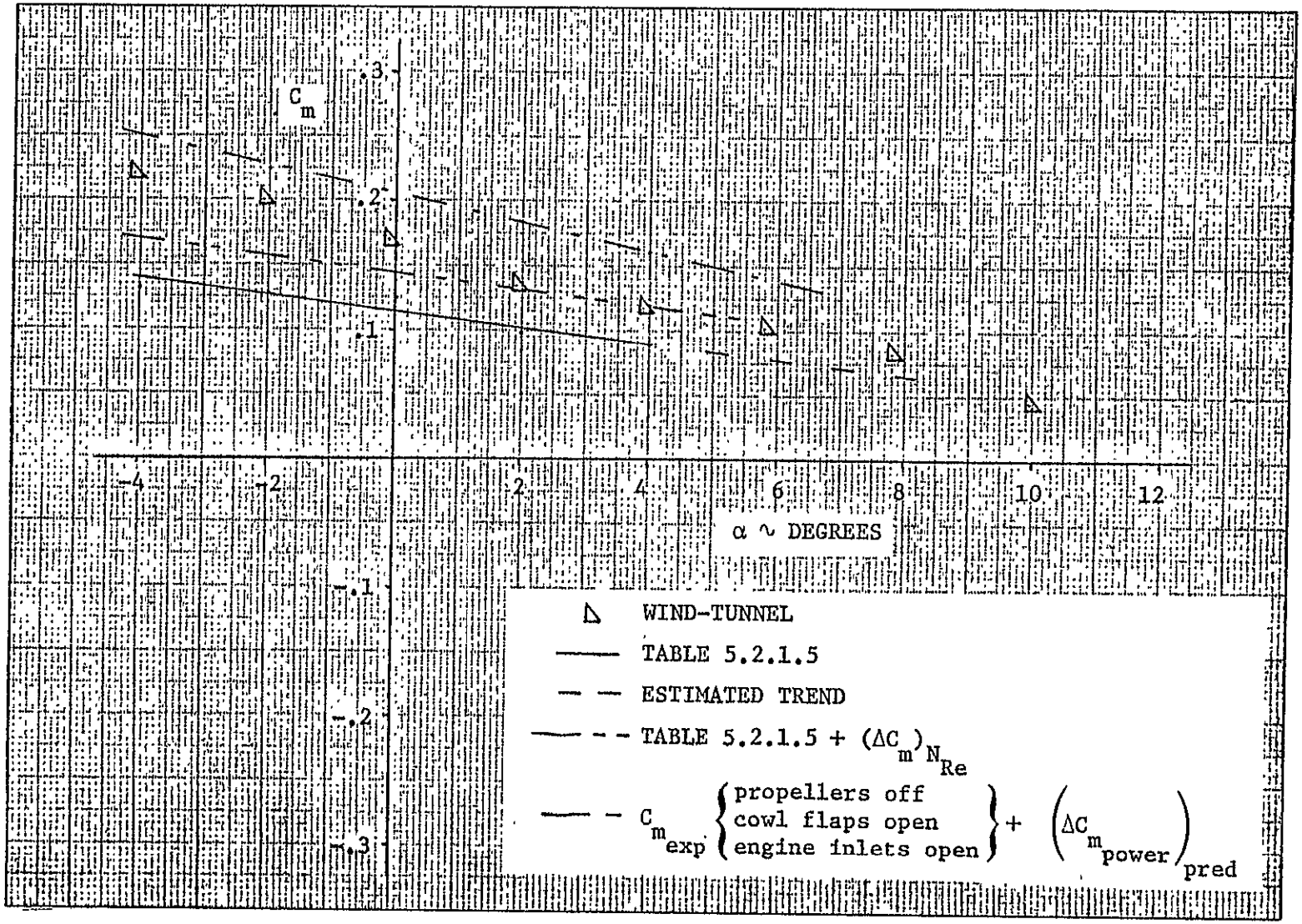

Figure 5.2.1.3: Comparison of calculated pitching moment with full-scale wind tunnel results (T_c' = 0.1970, no stabilizer deflection)

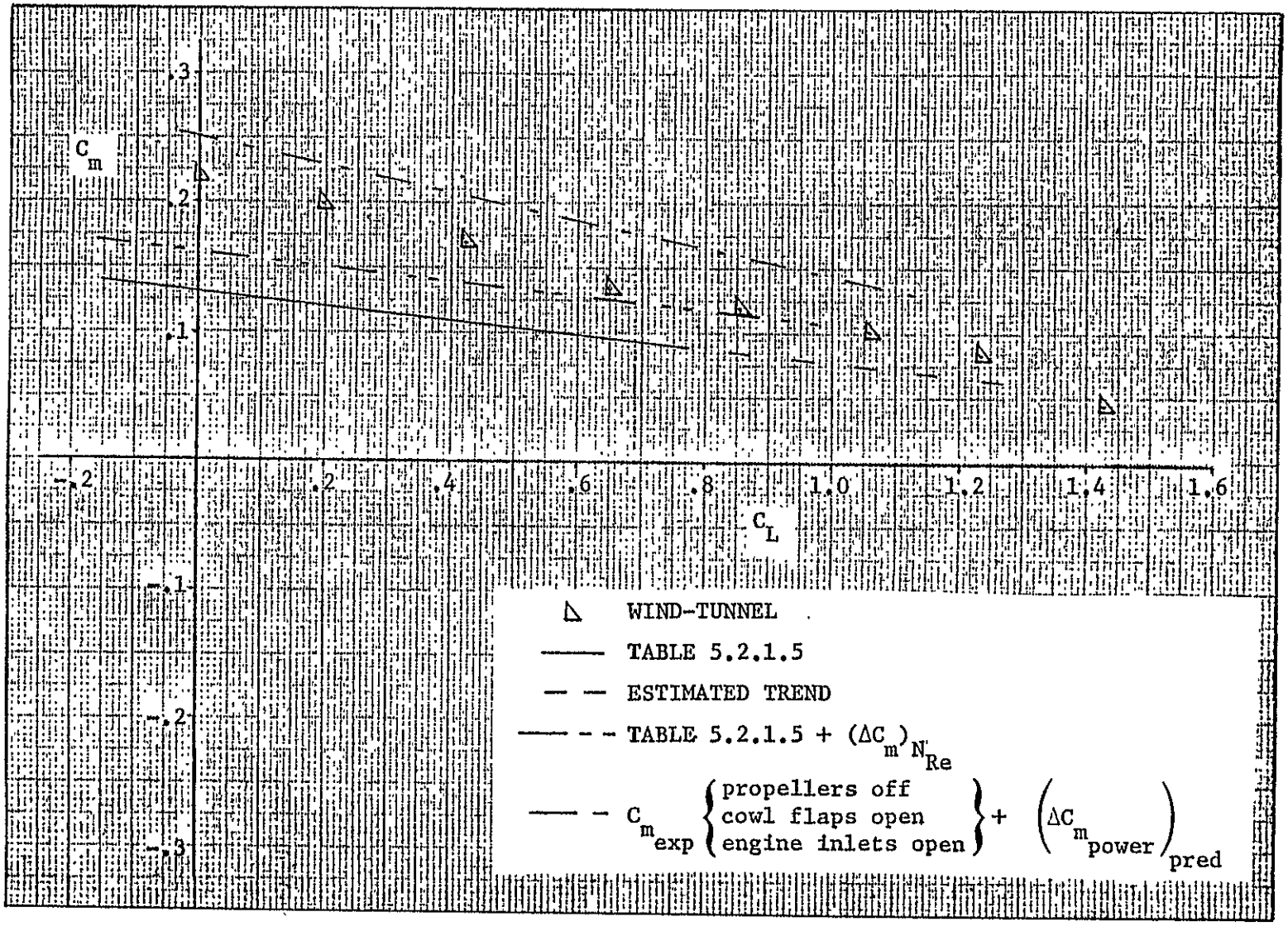

Figure 5.2.1.4: Comparison of predicted pitching moments with experimental results (T_c' = 0.1970, no stabilizer deflection)

5.3 Propeller Power Effects on Drag

The net drag change of the airplane due to propeller power results from:

1) the component of the propeller thrust parallel to the X-stability axis

2) the change in zero-lift drag due to slipstream dynamic pressure of those portions of the aircraft immersed in the propeller slipstream

3) the change in induced drag due to the lift component of the direct propeller forces and the change in angle of attack of the immersed portions of the wing

4) the change in cooling drag due to the power induced change in dynamic pressure acting on the immersed cooling system.

For the subject airplane, where the propeller slipstream immerses the nacelle as well as a portion of the wing and horizontal tail, the drag with power on can be written as follows:

$$C_D = C_{D_{\text{prop off}}} + (\Delta C_D)_T + (\Delta C_{D_o})_w + (\Delta C_{D_o})_h + (\Delta \bar{C}_{D_o})_n + \Delta C_{D_i} + (\Delta C_D)_{\substack{\text{cooling} \\ \text{system}}} \tag{5.3.1}$$

where

$(C_D)_{\text{prop off}}$ is the propeller-off drag of the complete airplane, obtained from Section 4.12

$(\Delta C_D)_T$ is the component of the total thrust parallel to the velocity vector, a positive thrust is equal to a negative drag contribution.

$(\Delta C_{D_o})_w$ is the change in profile drag due to power effects on the wing.

$(\Delta C_{D_o})_h$ is the change in profile drag due to power effects on the horizontal tail.

$(\Delta \bar{C}_{D_o})_n$ is the change in zero-lift drag of the nacelles (including nacelle-wing interference effects).

ΔC_{D_i} is the change in induced drag of the wing due to power effects.

$(\Delta C_D)_{\substack{\text{cooling} \\ \text{system}}}$ is the change in cooling system drag due to power.

The component of the total thrust parallel to the velocity vector, $(\Delta C_D)_T$, can be calculated as follows:

$$(\Delta C_D)_T = -n(T_c'/\text{prop}) \cos\alpha_T \tag{5.3.2}$$

where

n indicates the number of propellers.

T_c'/prop is the thrust coefficient due to one propeller, obtained from Section 5.1.

α_T is the angle of attack of the thrust axis, obtained from Section 5.1.

The change in profile drag, $(\Delta C_{D_o})_w$, due to power effects on the wing can be obtained as follows:

$$(\Delta C_{D_o})_w = n(C_{D_o})_{w_{\text{prop off}}} \frac{S_i/\text{prop}}{S_w} \frac{\Delta \bar{q}_w}{\bar{q}_\infty} \tag{5.3.3}$$

where

$(C_{D_o})_{w_{\text{prop off}}}$ is the propeller-off zero-lift drag coefficient of the wing obtained from Section 4.12.

S_i/prop is the immersed wing area per propeller, obtained from Section 5.1.

$\Delta\bar{q}_w/\bar{q}_\infty$ is the increment in dynamic pressure ratio, due to power, at the wing, obtained from Section 5.1.

The change in profile drag, $(\Delta C_{D_o})_h$, due to power effects on the horizontal tail is:

$$(\Delta C_{D_o})_h = n(C_{D_o})_{h_{prop\ off}} \frac{S_{h_i}/prop}{S_w} \frac{\Delta\bar{q}_h}{\bar{q}_\infty} \qquad (5.3.4)$$

where

$(C_{D_o})_{h_{prop\ off}}$ is the propeller-off zero-lift drag coefficient of the horizontal tail, obtained from Section 5.1.

S_{h_i}/prop is the immersed horizontal tail area per propeller, obtained from Figure 5.2.

$\Delta\bar{q}_h/\bar{q}_\infty$ is the increment in dynamic pressure, due to power, at the horizontal tail, obtained from Section 5.1.

The change in profile drag coefficient, $(\Delta\bar{C}_{D_o})_n$, due to power effects on the nacelles with nacelle-wing interference effects included is:

$$(\Delta\bar{C}_{D_o})_n = (\bar{C}_{D_o})_{n(w)_{prop\ off}} \frac{\Delta\bar{q}_w}{\bar{q}_\infty} \qquad (5.3.5)$$

where

$(\bar{C}_{D_o})_{n(w)_{prop\ off}}$ is the propeller-off zero-lift drag coefficient of the two nacelles with nacelle wing interference effects included, obtained from Section 4.12.

The induced drag increment, ΔC_{D_i}, of the wing due to propeller slipstream modification of the downwash over portions of the wing can be accounted for as follows:

1) Calculate the lift coefficient, C_L'', as follows:

$$C_L'' = C_{L_{w_{\text{prop off}}}} + (\Delta C_L)_T/\text{prop} + (\Delta C_L)_{N_p}/\text{prop} \qquad (5.3.6)$$

where

$(\Delta C_L)_T/\text{prop}$ is the lift component of the thrust per propeller, obtained from Section 5.1 on a per propeller basis.

$(\Delta C_L)_{N_p}/\text{prop}$ is the lift component of the propeller normal force per propeller, obtained from Section 5.1 on a per propeller basis.

$C_{L_{w_{\text{prop off}}}}$ is the lift coefficient of the wing alone with the propeller removed, having stall angles extended to power-on stall angles (see Section 5.1.2).

2) From Figure 5.3.1 obtain a value for the propeller drag factor, K_D, as a function of the propeller correlation parameter.

3) From Figure 5.3.2 obtain a value for the average propeller downwash, $(\bar{\varepsilon}/\varepsilon_p)$, as a function of the propeller correlation parameter and the ratio, R_p/b_w.

4) Calculate the effective propeller downwash angle, $\bar{\varepsilon}$, average over the entire wing by:

$$\bar{\varepsilon} = \left(\frac{\bar{\varepsilon}}{\varepsilon_p}\right)\left(\frac{\partial \varepsilon_p}{\partial \alpha_p}\right)\alpha_T \qquad (5.3.7)$$

where

$\partial \varepsilon_p/\partial \alpha_p$ is obtained from Section 5.1.

5) Calculate the induced drag increment ratio on a per propeller basis by:

$$\frac{[(C_{D_i})_w/\text{prop}]_{\text{power on}}}{(C_{D_i})_{w_{\text{prop off}}}} = \left(\frac{C_{L_{w_{\text{prop off}}}}}{C_L''}\right)^2 \left[1 + \frac{\pi^2 A_w \bar{\varepsilon}}{180 C_{L_{w_{\text{prop off}}}}}\right] + \left[\frac{b_w}{2R_p}\left(\frac{(\Delta C_L)_T/\text{prop} + (\Delta C_L)_{N_p}/\text{prop}}{C_L''}\right)\right]^2 K_D \qquad (5.3.8)$$

where

$C_{L_{w_{\text{prop off}}}}$ is the lift coefficient of the wing alone with propeller removed, having stall angles extended to power-on stall angles (see Section 5.1.2).

6) Calculate the induced drag increment, ΔC_{D_i}, of the wing due to propeller slipstream modification of the downwash over portions of the wing by:

$$C_{D_i} = (C_{D_i})_{w_{\text{prop off}}} n \left[\frac{[(C_{D_i})_w/\text{prop}]_{\text{power on}}}{(C_{D_i})_{w_{\text{prop off}}}} - 1\right] \qquad (5.3.9)$$

where

$(C_{D_i})_{w_{\text{prop off}}}$ is the propeller-off induced drag of the wing, obtained from Section 4.12.

The change in drag coefficient of the cooling system, $(\Delta C_D)_{\text{cooling system}}$, due to power induced changes in dynamic pressure behind the propeller acting on the cooling system immersed in the propeller slipstream is estimated by:

$$(\Delta C_D)_{\text{cooling system}} = (C_{D_{\text{cooling system}}})_{\text{prop off}} \frac{\Delta \bar{q}_w}{\bar{q}_\infty} \qquad (5.3.10)$$

where

$(C_{D_{\text{cooling system}}})_{\text{prop off}}$ is obtained from Section 4.12.

With Equation (5.3.1) the drag coefficient of the airplane including power effects can be calculated.

5.3.1 Drag Characteristics of the ATLIT Airplane

Calculations for power-on net-drag characteristics of the ATLIT airplane are summarized in Tables 5.3.1.1 to 5.3.1.4 as functions of the angle of attack, α, and the thrust coefficient, T_c'. Table 5.3.1.1 summarizes the zero-lift increments of drag due to power, Table 5.3.1.2 the induced drag increments due to power, and Table 5.3.1.3 the change in cooling-system drag due to power. Table 5.3.1.4 summarizes all the power effects on drag and lists the power-on net drag.

The results of Table 5.3.1.4 are plotted in Figures 5.3.1.1 and 5.3.1.2 and they show good agreement with the experimental results of Reference 2. The predicted results do not include a Reynolds number correction. The predictions have been performed for a Reynolds number of 2.3 million, while power-on wind-tunnel data for the $\overline{\text{ATLIT}}$ in the "fully clean" configuration were only available for a Reynolds number of 3.5 million. For the ATLIT an increase in Reynolds number of this magnitude will result in a slight decrease in drag, $(\Delta C_D)_{N_{Re}} \approx 0$ to -0.0002. Adding this correction to the predicted drag will result in an even better agreement with the wind tunnel data.

Table 5.3.1.1: Zero-lift drag increments due to power

Symbol	Description	Reference	Magnitude
n	Number of propellers	Figure 5.1	2
S_w	Reference wing area, m^2 (ft^2)	Table 2.1.1	14.40 (155.0)
$\Delta\bar{q}_w/\bar{q}_\infty$	Change in dynamic pressure ratio at the wing due to power	Table 5.1.3.2	4.9098 (T_c'/prop)
S_i/prop	Immersed wing area per propeller, m^2(ft^2)	Table 5.1.3.2	Variable
$(C_{D_o})_{w_{prop\ off}}$	Propeller-off zero-lift drag of wing	Table 4.12.1.2	0.00970
$(C_{D_o})_{h_{prop\ off}}$	Propeller-off zero-lift drag of horizontal tail referenced to tail area	Table 4.12.1.2	0.00885
$\Delta\bar{q}_h/\bar{q}_\infty$	Change in dynamic pressure ratio at the horizontal tail due to power	Table 5.1.3.4	Variable
S_{h_i}/prop	Immersed horizontal tail area per propeller, m^2 (ft^2)	Table 5.1.3.4	2.95 (9.68)
$(\bar{C}_{D_o})_{n(w)_{prop\ off}}$	Propeller-off zero-lift drag of both nacelles with wing-nacelle interference included, referenced to wing area	Table 4.12.3.3	0.01384

α, deg	S_i/prop, ft^2; Table 5.1.3.2			$(\Delta C_{D_o})_w$; Eq.(5.3.3)			$\Delta\bar{q}_h/\bar{q}_\infty$; Table 5.1.3.4		
	T_c'			T_c'			T_c'		
	0	0.0915	0.1970	0	0.0915	0.1970	0	0.0915	0.1970
-4	27.626	27.614	27.591	0	0.00078	0.00167	0	0.030	0.10
-2	27.346	27.322	27.305	0	0.00077	0.00165	0	0.035	0.12
0	26.863	26.873	26.880	0	0.00076	0.00163	0	0.040	0.12
2	26.185	26.260	26.310	0	0.00074	0.00159	0	0.045	0.13
4	25.298	25.471	25.583	0	0.00072	0.00155	0	0.050	0.15

$(\Delta C_{D_o})_h$; Eq. (5.3.4)			$(\Delta C_{D_o})_n$; Eq. (5.3.5)			$\Delta C_{D_o} = (\Delta C_{D_o})_w + (\Delta C_{D_o})_h + (\Delta C_{D_o})_n$		
T_c'			T_c'			T_c'		
0	0.0915	0.1970	0	0.0195	0.1970	0	0.0915	0.1970
0	0.00003	0.00011	0	0.00311	0.00669	0	0.00392	0.00847
0	0.00004	0.00013	0	0.00311	0.00669	0	0.00392	0.00847
0	0.00004	0.00013	0	0.00311	0.00669	0	0.00391	0.00845
0	0.00005	0.00014	0	0.00311	0.00669	0	0.00390	0.00842
0	0.00006	0.00017	0	0.00311	0.00669	0	0.00389	0.00841

Table 5.3.1.2: Induced drag increment due to power

Symbol	Description	Reference	Magnitude
n	Number of propellers	Figure 5.1	2
b_w	Wing Span, m (ft)	Table 2.1.1	12.19 (40.0)
α_T	Angle of attack of thrust axis, deg	Figure 5.1	α
A_w	Wing aspect ratio	Table 2.1.1	10.32
R_p	Propeller radius, m (ft)	Table 2.1	0.966 (3.17)
$(C_D)_{prop\ off}$	Drag of airplane with propellers off	Table 4.12.8.1	Variable
ΔC_{D_o}	Zero-lift drag increment due to power	Table 5.3.1.1	Variable
$(C_{D_i})_{w_{prop\ off}}$	Induced wing drag with propellers off	Table 4.12.4.2	Variable
$C_{L_{w_{prop\ off}}}$	Lift coefficient of wing alone with propellers off and stall angles extended to power-on stall angles	Table 4.2.4.1	Variable
C_L''	-	Eq. (5.3.6)	Variable
$\partial\epsilon_p/\partial\alpha_p$	Rate of change of propeller downwash with propeller angle of attack	Table 5.1.3.2	Variable
$\bar{\epsilon}/\epsilon_p$	Averaged propeller downwash over wing span as a ratio of propeller downwash behind propeller	Figure 5.3.2	Variable
$\bar{\epsilon}$	Effective propeller downwash averaged over wing, deg	Eq. (5.3.7)	Variable
K_D	Propeller drag factor	Figure 5.3.1	Variable

T_c'	$\frac{S_w(T_c'/prop)}{R_p^2}$	R_p/b_w	K_D Figure 5.3.1	$\partial\epsilon_p/\partial\alpha_p$ Table 5.1.3.2	$\bar{\epsilon}/\epsilon_p$ Figure 5.3.2	$\bar{\epsilon}$, deg Eq. (5.3.7)
0	0	0.0793	4.0	0.0250	0	0
0.0915	0.7056	0.0793	3.76	0.1033	0.114	0.01178α
0.1970	1.520	0.0793	3.54	0.1554	0.168	0.02611α

Table 5.3.1.2: Concluded

α, deg	$C_{L_{w_{prop\ off}}}$ Table 4.2.4.1	$(\Delta C_L)_T$/prop + $(\Delta C_L)_{N_p}$/prop; Table 5.1.3.1			C_L''; Eq. (5.3.6)		
		T_c'			T_c'		
		0	0.0915	0.1970	0	0.0915	0.1970
-4	-0.0533	-0.0015	-0.0048	-0.0085	-0.0548	-0.0581	-0.0618
-2	0.1243	-0.0007	-0.0023	-0.0042	0.1237	0.1220	0.1201
0	0.3019	0.0002	0.0002	0.0002	0.3021	0.3021	0.3021
2	0.4795	0.0010	0.0027	0.0047	0.4805	0.4822	0.4842
4	0.6571	0.0018	0.0052	0.0090	0.6589	0.6623	0.6661

$\bar{\epsilon}$, deg; Eq. (5.3.7)			$[(C_{D_i})_w/\text{prop}]_{\text{power on}}/[(C_{D_i})_{w_{prop\ off}}]$; Eq. (5.3.8)			$(C_{D_i})_{w_{prop\ off}}$ Table 4.12.4.2	ΔC_{D_i}; Eq. (5.3.9)		
T_c'			T_c'				T_c'		
0	0.0915	0.1970	0	0.0915	0.1970		0	0.0915	0.1970
0	-0.0471	-0.1044	1.0653	2.2827	4.2339	0.00037	0.00005	0.00095	0.00239
0	-0.0236	-0.0522	1.0148	0.9797	0.9834	0.00075	0.00002	-0.00003	-0.00002
0	0	0	0.9987	0.9987	0.9987	0.00329	-0.00001	-0.00001	-0.00001
0	0.0236	0.0522	0.9965	1.0211	1.0544	0.00796	-0.00006	0.00034	0.00087
0	0.0471	0.1044	0.9957	1.0335	1.0864	0.01476	-0.00013	0.00099	0.00255

Table 5.3.1.3: Change in cooling-system drag due to power

Symbol	Description	Reference	Magnitude
$(C_{D_{cooling\ system}})_{prop\ off}$	Cooling drag coefficient with propellers off	Figure 4.12.7.1	Variable
S_w	Wing reference area, m^2 (ft^2)	Table 2.1.1	14.40 (155.0)
R_p	Propeller radius, m (ft)	Table 2.1	0.966 (3.17)
$\Delta\bar{q}_w/\bar{q}_\infty$	Change in dynamic pressure ratio at wing due to power	Table 5.1.3.2	4.9098 (T_c'/prop)

α, deg	$(C_{D_{cooling\ system}})_{prop\ off}$ Figure 4.12.7.1	$(\Delta C_D)_{cooling\ system}$; Eq. (5.3.10)		
		T_c'		
		0	0.0915	0.1970
-4	0.0083	0	0.00186	0.00401
-2	0.0067	0	0.00150	0.00324
0	0.0055	0	0.00124	0.00266
2	0.0045	0	0.00101	0.00218
4	0.0040	0	0.00090	0.00193

Table 5.3.1.4: Power-on drag of complete airplane

α, deg	$(\Delta C_D)_T$; Eq. (5.3.2)			ΔC_{D_o}; Table 5.3.1.1			ΔC_{D_i}; Table 5.3.1.2		
	T_c'			T_c'			T_c'		
	0	0.0915	0.1970	0	0.0915	0.1970	0	0.0915	0.1970
-4	0	-0.09128	-0.19652	0	0.00392	0.00847	0.00005	0.00095	0.00239
-2	0	-0.09144	-0.19688	0	0.00392	0.00847	0.00002	-0.00003	-0.00002
0	0	-0.09150	-0.19700	0	0.00391	0.00845	-0.00001	-0.00001	-0.00001
2	0	-0.09144	-0.19688	0	0.00390	0.00842	-0.00006	0.00034	0.00087
4	0	-0.09128	-0.19652	0	0.00389	0.00841	-0.00013	0.00099	0.00255

$(\Delta C_D)_{cooling\ system}$; Table 5.3.1.3			$(\Delta C_D)_{power}$			$(C_D)_{prop\ off}$	$(C_D)_{power\ on}$; Eq. (5.3.1)		
T_c'			T_c'			Table 4.12.8.1	T_c'		
0	0.0915	0.1970	0	0.0915	0.1970		0	0.0915	0.1970
0	0.00186	0.00401	0.00005	-0.08455	-0.18165	0.03724	0.03729	-0.04731	-0.14441
0	0.00150	0.00324	0.00002	-0.08605	-0.18519	0.03577	0.03579	-0.05028	-0.14942
0	0.00124	0.00266	-0.00001	-0.08636	-0.18590	0.03723	0.03722	-0.04913	-0.14867
0	0.00101	0.00218	-0.00006	-0.08619	-0.18541	0.04164	0.04158	-0.04455	-0.14377
0	0.00090	0.00193	-0.00013	-0.08550	-0.18363	0.04906	0.04893	-0.03644	-0.13457

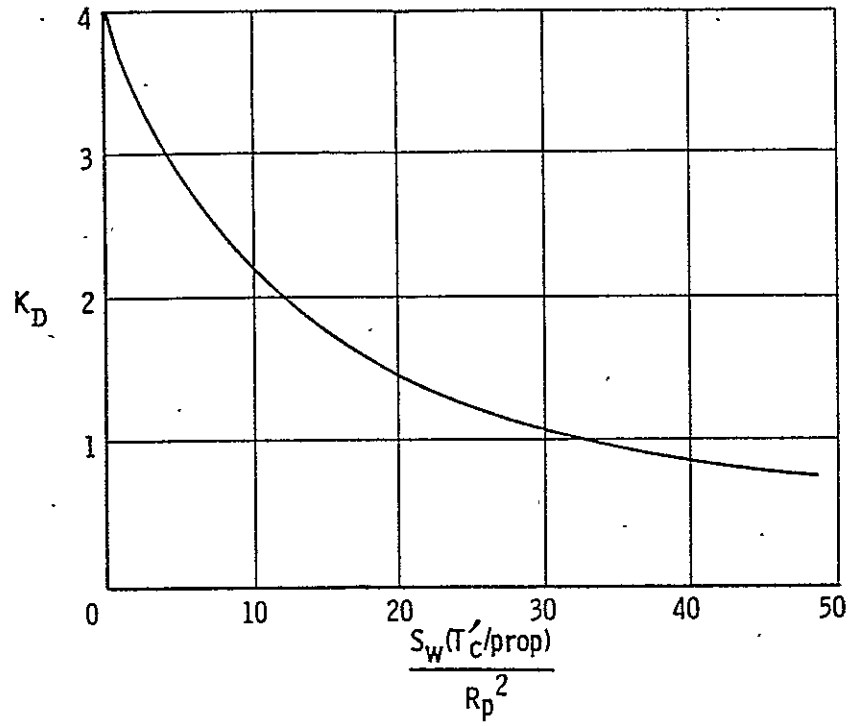

Figure 5.3.1: Propeller drag factor (Reference 3)

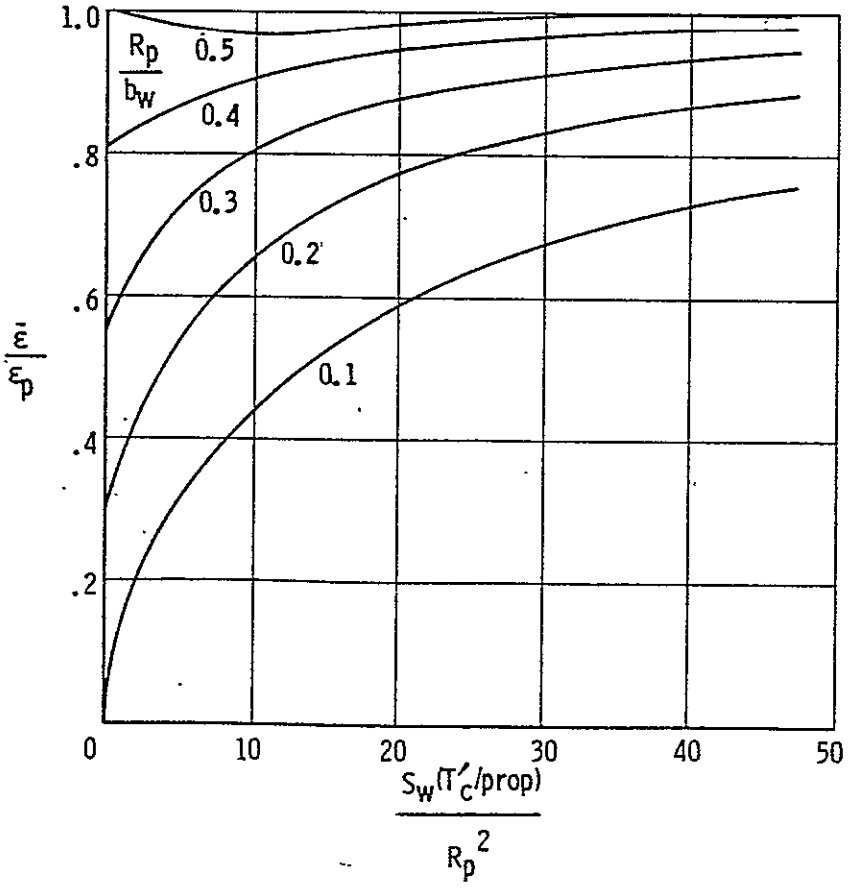

Figure 5.3.2: Average propeller downwash (Reference 3)

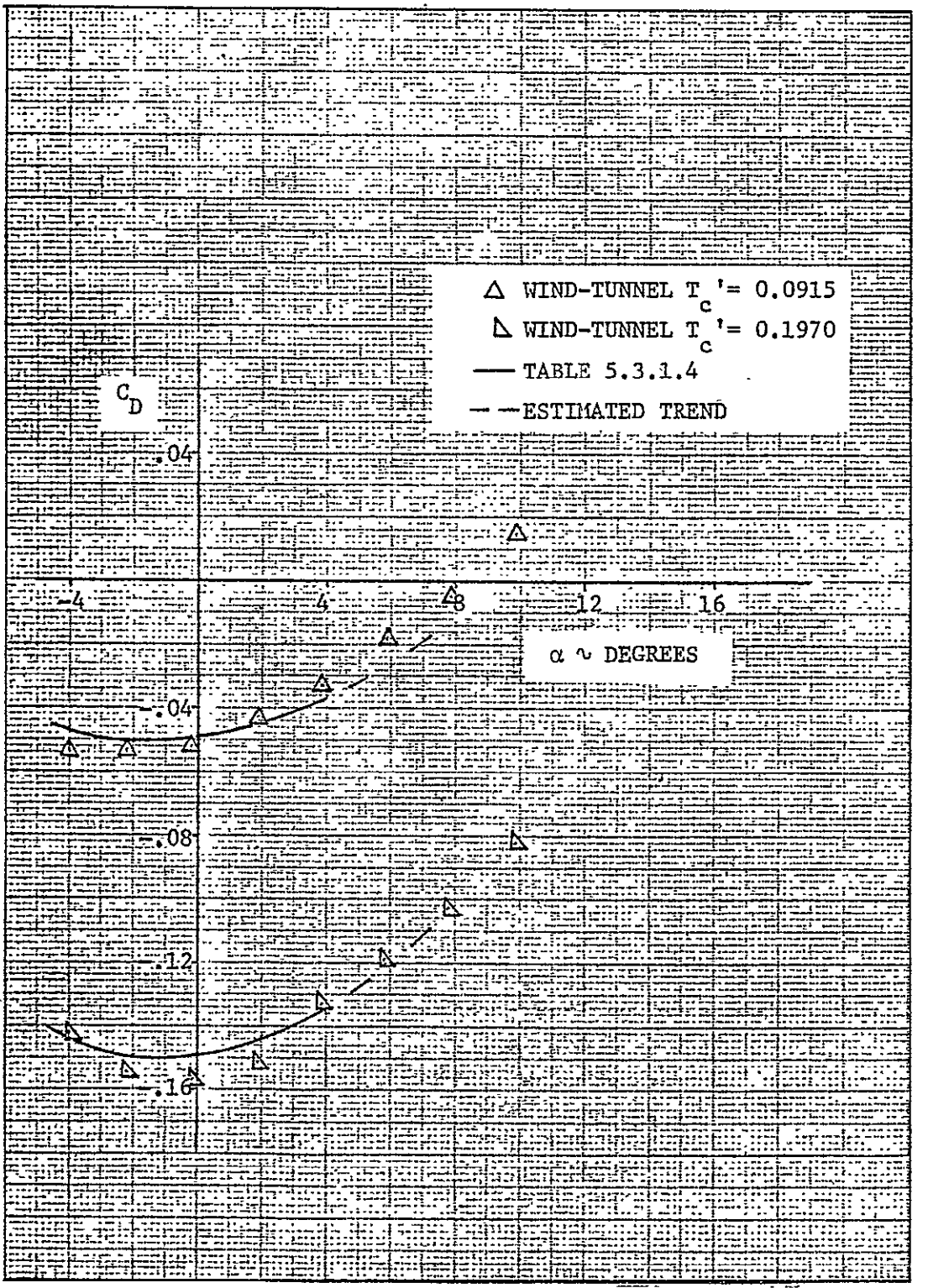

Figure 5.3.1.1: Comparison of calculated and wind-tunnel-determined drag at different power conditions

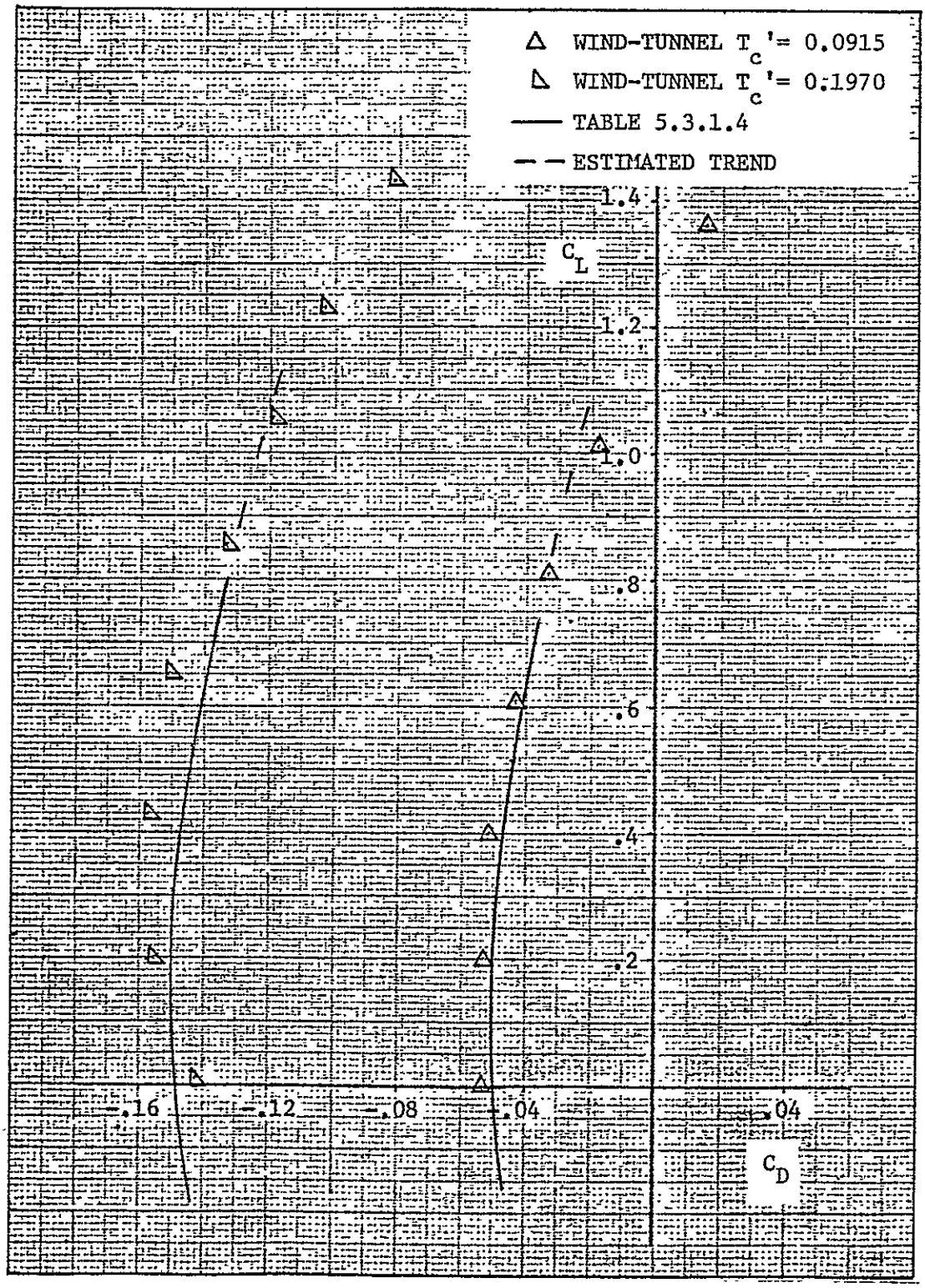

Figure 5.3.1.2: Comparison of predicted drag with full-scale wind tunnel data at different power conditions

CHAPTER 6

CONCLUSIONS AND RECOMMENDATIONS

In this report an analytical method is presented for predicting lift, pitching moment and drag of light, twin-engine, propeller-driven airplanes. The method is applied to the Advanced Technology Light Twin-Engine (ATLIT) airplane and the calculated characteristics are compared with the full-scale wind tunnel data.

The following conclusions can be made:

1. The calculated lift curves show fair agreement with the wind tunnel results. However, the accuracy can be improved as is indicated by the good agreement of the results obtained with the lifting surface programs of Reference 4 and 5 with the experimental data.
2. The calculated pitching moment coefficients agree well with the wind tunnel results.
3. In Section 4.12 the drag of the ATLIT airplane is predicted. The predicted drag shows good agreement with the wind tunnel data of Reference 2.
4. The calculated lift and pitching moment for the airplane with deflected stabilizer show poor agreement with the experimental results.
5. In Chapter 5 the prediction of power-on aerodynamic characteristics is presented. The predicted power effects agree well with the wind tunnel results.

The following recommendations are made to improve the accuracy of the predicted results:

1. In Section 4.2 the factor, K_{Pol}, has been presented. This factor describes the error in the wing lift curve slope, C_{L_α}, obtained with the Polhamus formula when compared with the value for C_{L_α} obtained with the lifting surface method of Reference 5. A similar factor, K_{α_o}, is suggested for the wing angle of attack for zero-lift. Use of such a factor will greatly increase the lift coefficient prediction.

2. The lifting line theory overestimates the wing maximum lift coefficient, $C_{L_{max}}$. A study is suggested which would result in a correction factor, $K_{C_{L_{max}}}$, as function of wing configuration and wing planform.

3. In Reference 3 and 4 the dynamic pressure ratio at the horizontal tail, $\bar{q}_h/\bar{q}_\infty$, is assumed to be equal to one, as long as the tail is not situated in the wake. It is suggested to use $\bar{q}_h/\bar{q}_\infty = 1.0$ only in the case of a T-tail, while $\bar{q}_h/\bar{q}_\infty$ may be assumed equal to 0.85 for a fuselage mounted stabilizer (ATLIT) and 0.95 for a fin mounted stabilizer. This change will result in a better agreement of the calculated "stabilizer deflected" results with the wind tunnel data.

4. The wetted areas of the fuselage and nacelle have to be determined exactly to obtain an accurate prediction of the zero-lift drag coefficient of the airplane. Instead of using Figure 4.12.2.1 to predict the wetted area of a body, the method described in Appendix F is recommended.

5. The computer program of Reference 5 does not take engine nacelles into consideration. Inclusion of the nacelle will improve the

results obtained with this program considerably. This will result in predicted characteristics which show good agreement with the wind tunnel data and with the data obtained with the program of Reference 6. However, the program uses much less computer time than the program of Reference 6.

6. The engine cooling system appears to affect the drag and pitching moment of the airplane considerably. A study is suggested to make it possible to incorporate this effect into the prediction of the aerodynamic characteristics.

REFERENCES

1. Holmes, B. J., "Flight Evaluation of an Advanced Technology Light Twin-Engine Airplane (ATLIT)," NASA CR-2832, July 1977.
2. Hassell, J. L., Jr., "Full-Scale Wind Tunnel Investigation of an Advanced Technology Light Twin-Engine Airplane (ATLIT)," Proposed NASA TP, 1979.
3. Wolowicz, C. H., and Yancey, R. B., "Longitudinal Aerodynamic Characteristics of Light, Twin-Engine, Propeller-Driven Airplanes," NASA TN D-6800, June 1972.
4. Finck, R. D., and Hoak, D. E., "USAF Stability and Control DATCOM," Air Force Flight Dynamics Laboratory, Wright-Patterson Air Force Base, Ohio, October 1960 (Revised January 1975).
5. Lan, C. E., "A Quasi Vortex Lattice Method in Thin Wing Theory," Journal of Aircraft, Vol. 11, No. 9, September 1974, pp. 518-527.
6. Hess, J. L., "Calculation of Potential Flow about Arbitrary Three-Dimensional Lifting Bodies," MDC - J 5679/01, NASC, October 1972.
7. Smetana, F. O., "Comparison of Predicted with Measured Aerodynamic Characteristics of the ATLIT Airplane," SAE-770449, Wichita, Kansas, March 29 - April 1, 1977.
8. Torenbeek, E., Synthesis of Subsonic Airplane Design, Delft University Press, Delft, Netherlands, 1976.
9. McGhee, R. J., and Beasley, W. D., "Low-Speed Aerodynamic Characteristics of a 17-Percent Thick Airfoil Section Designed for General Aviation Applications," NASA TN D-7428, December 1973.
10. Roskam, J., and van Keppel, B., et al., "A Study of Commuter Airplane Design Optimization," KU-FRL-313-5, University of Kansas, May 1978.

11. Weber, J., "The Calculation of the Pressure Distribution over the Surface of Two-Dimensional and Swept Wings with Symmetrical Aerofoil Sections," ARC R&M 2918, 1953.

12. Weber, J., "The Calculation of the Pressure Distribution on the Surface of Thick Cambered Wings and the Design of Wings with Given Pressure Distribution," ARC R&M 3026, 1955.

13. Hess, J. L., and Smith, A. M. O., "Calculation of Potential Flow about Arbitrary Bodies," Progress in Aeronautical Sciences, Vol. 8, 1966.

14. Giesing, J. P., "Potential Flow about Two-Dimensional Airfoils," Douglas Aircraft Company, Report No. LB31946, 1968.

15. Oellers, H. J., "Die Inkompressible Potentialströmung in der Ebenen Gitterstufe," Jahrbuch WGL, 1962, pp. 349-353.

16. Ormsbee, A. I., and Chen, A. W., "Multiple Element Airfoils Optimized for Maximum Lift Coefficient," AIAA Journal, Vol. 10, No. 12, December 1972, pp. 1620-1624.

17. Stevens, W. A., Goradia, S. H., and Braden, J. A., "Mathematical Model for Two-Dimensional Multi-Component Airfoils in Viscous Flow," NASA CR-1843, July 1971.

BLANK PAGE

APPENDIX A

CALCULATION OF THE SHIFT IN ANGLE OF ATTACK FOR ZERO-LIFT PER UNIT WING TWIST IN THE CASE OF PARABOLIC TWIST

APPENDIX A

CALCULATION OF THE SHIFT IN ANGLE OF ATTACK FOR ZERO-LIFT PER UNIT WING TWIST IN THE CASE OF PARABOLIC TWIST

According to Reference 8, the shift in angle of attack for zero-lift per degree of wing twist can be written as follows:

$$\frac{\Delta\alpha_o}{\theta} = -\int_0^1 \frac{\varepsilon}{\theta}\{C_1 \frac{c}{c_g} + C_2 \frac{4}{\pi}\sqrt{1-\eta^2} + C_3 f\}d\eta \qquad (A.1)$$

where

$\eta = 2y/b$ is the non-dimensional spanwise station

C_1 through C_3 can be obtained from Figure 4.2.3.4

f is the lift distribution function obtained from Figure 4.2.3.5.

For parabolic twist the following expression can be written:

$$\frac{\varepsilon}{\theta} = a\eta^2 + b\eta + d \qquad (A.2)$$

At the wing root ($\eta = 0$) the ratio $\varepsilon/\theta = 0$, while at the wing tip ($\eta = 1$) $\varepsilon/\theta = 1$. Substituting this information into Equation (A.2) leads to the following result:

$$\frac{\varepsilon}{\theta} = a\eta^2 + (1-a)\eta \qquad (A.3)$$

The chord, c, at wing station, η, can be calculated by:

$$c = (c_t - c_r)\eta + c_r \qquad (A.4)$$

The standard mean chord for straight tapered wings is:

$$c_g = c_r \frac{1+\lambda}{2} \qquad (A.5)$$

Substituting Equations (A.3) through (A.5) into Equation (A.1) results in the following expression:

$$\frac{\Delta\alpha_o}{\theta} = -\int_0^1 \{a\eta^2 + (1-a)\eta\}\left[\left\{\frac{2(\lambda-1)\eta}{\lambda+1} + \frac{2}{\lambda+1}\right\} C_1 + C_2 \frac{4}{\pi}\sqrt{1-\eta^2} + C_3 f\right] d\eta \qquad (A.6)$$

or:

$$\frac{\Delta\alpha_o}{\theta} = -\int_0^1 \left[\frac{2(\lambda-1)}{\lambda+1} C_1 \{a\eta^3 + (1-a)\eta^2\} + \left(\frac{2C_1}{\lambda+1} + C_3 f\right)\{a\eta^2 + (1-a)\eta\} + C_2 \frac{4}{\pi}\{a\eta^2\sqrt{1-\eta^2} + (1-a)\eta\sqrt{1-\eta^2}\}\right] d\eta \qquad (A.7)$$

For unswept wings ($\Lambda_{c/4} = 0$) the lift distribution function, f, is elliptical:

$$f = \frac{4}{\pi}\sqrt{1-\eta^2} \qquad (A.8)$$

In this case Equation (A.7) can be written as:

$$\frac{\Delta\alpha_o}{\theta} = -\int_0^1 \left[\frac{2(\lambda-1)}{\lambda+1} C_1 \{a\eta^3 + (1-a)\eta^2\} + \frac{2C_1}{\lambda+1}\{a\eta^2 + (1-a)\eta\} + (C_2 + C_3)\frac{4}{\pi}\{a\eta^2\sqrt{1-\eta^2} + (1-a)\eta\sqrt{1-\eta^2}\}\right] d\eta \qquad (A.9)$$

From Equation (A.9) follows:

$$-\frac{\Delta\alpha_o}{\theta} = \left[\frac{2(\lambda-1)}{\lambda+1} C_1 \left\{\frac{1}{4}a\eta^4 + \frac{1}{3}(1-a)\eta^3\right\} + 2\frac{C_1}{\lambda+1}\left\{\frac{1}{3}a\eta^3 + \frac{1}{2}(1-a)\eta^2\right\} + (C_2 + C_3)\frac{4}{\pi}a\left\{-\frac{\eta}{4}\sqrt{(1-\eta^2)^3} + \right.\right.$$

$$\left.\left. + \frac{1}{8}(\eta\sqrt{1-\eta^2} + \arcsin\eta)\right\} + (C_2 + C_3)\frac{4}{\pi}(1-a)\left\{-\frac{1}{3}\sqrt{(1-\eta^2)^3}\right\}\right]_0^1 \qquad (A.10)$$

This expression may be written as:

$$-\frac{\Delta\alpha_o}{\theta} = \frac{2C_1}{\lambda+1}\left\{\lambda\left(-\frac{a}{12} + \frac{1}{3}\right) + \left(\frac{1}{6} - \frac{a}{12}\right)\right\} + (C_2 + C_3)\frac{4}{\pi}\left\{a\left(\frac{\pi}{16} - \frac{1}{3}\right) + \frac{1}{3}\right\} \qquad (A.11)$$

To determine the parameter, a, a third point of the twist distribution line has to be known. In the case of the ATLIT:

$$\eta = 0.395 \qquad \varepsilon/\theta = 0.1667 \qquad (A.12)$$

From Equation (A.3) follows:

$$a = 0.9554 \qquad (A.13)$$

The following data are known for the ATLIT:

$$\frac{2\pi A}{c'_{\ell_\alpha} \cos\Lambda_{c/4}} = 9.846 \qquad (A.14)$$

$$\lambda = 0.5$$

From Figure 4.2.3.4 follows:

$$C_1 = 0.462$$
$$C_2 = 0.179 \qquad (A.15)$$
$$C_3 = 0.359$$

Using the information from Equations (A.13), (A.14) and (A.15) in Equation (A.11) leads to the following result:

$$\frac{\Delta\alpha_o}{\theta} = -0.2705 \qquad (A.16)$$

Because the sweep angle of the quarter-chord of the ATLIT is very small ($\Lambda_{c/4} < 2°$), the wing of the ATLIT may be assumed to be unswept.

APPENDIX B

CALCULATION OF MAXIMUM LIFT COEFFICIENT FOR STRAIGHT TWISTED WINGS

APPENDIX B

CALCULATION OF MAXIMUM LIFT COEFFICIENT FOR STRAIGHT TWISTED WINGS

The method described in Section 4.2.3 is discussed in more detail in Reference 8. According to Section 4.2.3, the additional lift coefficient for $C_L = 1$ is:

$$c_{\ell_a} = C_1 + \frac{C_2}{c/c_g}\frac{4}{\pi}\sqrt{1-\eta^2} + \frac{C_3 f}{c/c_g} \tag{B.1}$$

and the basic lift coefficient is:

$$c_{\ell_b} = c_{\ell_a}\,\theta\, c_{\ell_\alpha} C_4 \left(\frac{\varepsilon}{\theta} + \frac{\Delta\alpha_o}{\theta}\right)\cos\Lambda_\beta \tag{B.2}$$

The ratio of the wing chord at spanwise wing station, η, to the mean geometric chord is, according to Appendix A:

$$\frac{c}{c_g} = \frac{2}{\lambda+1}(\lambda\eta - \eta + 1) \tag{B.3}$$

In the case of linear twist the twist ratio can be written as:

$$\frac{\varepsilon}{\theta} = \eta \tag{B.4}$$

However, the ATLIT airplane has a parabolic twist distribution, as discussed in Appendix A. For the ATLIT the following twist ratio is valid:

$$\frac{\varepsilon}{\theta} = 0.9554\eta^2 + 0.0446\eta \tag{B.5}$$

The following data are known for the ATLIT wing:

$$\frac{2\pi A}{c_{\ell_\alpha}\cos\Lambda_{c/4}} = 9.846$$

$$c_{\ell_\alpha} = 0.115\ \text{deg}^{-1} \qquad \text{(Table 4.1.2)}$$

$$c_{\ell_{max}} = 1.59 \qquad \text{(Table 4.1.2)}$$

$$\theta = -3 \text{ deg} \qquad \text{(Table 2.1)}$$

$$\frac{\Delta\alpha_o}{\theta} = -0.2705 \qquad \text{(Appendix A)}$$

Then, from Figure 4.2.3.4 follows:

$$\begin{aligned} C_1 &= 0.462 \\ C_2 &= 0.179 \\ C_3 &= 0.359 \\ C_4 &= 0.560 \end{aligned} \qquad \text{(B.6)}$$

The quarter chord sweep angle, $\Lambda_{c/4}$, of the ATLIT wing is nearly zero. In that case, the lift distribution function is:

$$f = \frac{4}{\pi}\sqrt{1-\eta^2} \qquad \text{(B.7)}$$

and Equation (B.1) can be written as:

$$c_{\ell_a} = C_1 + \frac{(C_2 + C_3)}{c/c_g}\frac{4}{\pi}\sqrt{1-\eta^2} \qquad \text{(B.8)}$$

Table B.1 summarizes the calculations which lead to the value of the maximum wing lift coefficient. From this table follows that the minimum value of the ratio of $(c_{\ell_{max}} - c_{\ell_b})$ to c_{ℓ_a} at $C_L = 1$ is:

$$\frac{c_{\ell_{max}} - c_{\ell_b}}{c_{\ell_a}} = 1.494 = (C_{L_{max}})_w \qquad \text{(B.9)}$$

The minimum value of this ratio is considered to be the maximum lift coefficient of the wing.

Table B.1: Maximum wing lift coefficient prediction

η	c/c_g Eq. (B.3)	c_{ℓ_a} Eq. (B.8)	ε/θ Eq. (B.5)	c_{ℓ_b} Eq. (B.2)	$\frac{c_{\ell_{max}} - c_{\ell_b}}{c_{\ell_a}}$
0	1.333	0.9758	0	0.0510	1.577
0.1	1.267	0.9999	0.0140	0.0496	1.541
0.2	1.200	1.0213	0.0471	0.0441	1.514
0.3	1.133	1.0386	0.0994	0.0343	1.498
0.35	1.1	1.0453	0.1326	0.0278	1.494
0.4	1.067	1.0506	0.1707	0.0203	1.494
0.45	1.033	0.0540	0.2135	0.0116	1.498
0.5	1.0	1.0552	0.2612	0.0019	1.505
0.6	0.933	1.0492	0.3707	-0.0203	1.535
0.7	0.867	1.0264	0.4994	-0.0454	1.593
0.8	0.8	0.9758	0.6471	-0.0710	1.702
0.9	0.733	0.8693	0.8140	-0.0913	1.934
1.0	0.667	0.4620	1.0	-0.0651	3.582

APPENDIX C

COMPARISON OF EXPERIMENTAL GA(W)-1 SECTION AIRFOIL CHARACTERISTICS WITH THIN AIRFOIL THEORY AND THICK AIRFOIL THEORY PREDICTIONS

APPENDIX C

COMPARISON OF EXPERIMENTAL GA(W)-1 SECTION AIRFOIL CHARACTERISTICS WITH THIN AIRFOIL THEORY AND THICK AIRFOIL THEORY PREDICTIONS

In this study Reference 4 and Reference 5 have been used to predict the longitudinal aerodynamic characteristics of the ATLIT airplane. Reference 4 is based on the thin wing theory, while Reference 5 is based on the thick wing theory of Douglas Neumann. In this appendix a comparison will be shown between experimental results (Reference 9) and results obtained with the thin airfoil theory and the thick airfoil theory, respectively.

In the thin airfoil theory the airfoil is represented by its mean camber line, z_c. According to the thin airfoil theory, the lift coefficient is:

$$c_\ell = 2\pi(\alpha-\alpha_o) \tag{C.1}$$

where α is the angle of attack with respect to the airfoil chord in radians and α_o is the angle of zero lift in radians:

$$\alpha_o = \frac{1}{\pi}\int_o^\pi \frac{dz_c}{dx}(1-\cos\theta)\,d\theta \tag{C.2}$$

where:

$$x = \frac{1}{2}(1-\cos\theta) \tag{C.3}$$

In the thin airfoil theory, the thickness has been found to have no effect on c_ℓ and c_m. In reality, the thickness does affect slightly both c_ℓ and c_m. An improved thin airfoil theory is Weber's method (References 11 and 12). This method shows that for thin airfoils and for small angles of attack the lift coefficient can be represented as follows:

$$c_\ell = 2\pi(1+0.8\frac{t}{c})(\alpha-\alpha_o) \qquad (C.4)$$

The thick airfoil theory takes the complete airfoil into account. The first method is the Douglas Neumann method (References 13 and 14), which uses a surface source distribution. The second method replaces the airfoil surface by a vortex sheet instead of a source distribution (References 15 and 16). The results of both methods, however, have been proven to be similar.

In Table C.1 the airfoil coordinates of the GA(W)-1 airfoil are presented. The mean camber line of this airfoil can be represented by the following expression:

$$z_c = \sum_{n=0}^{10} a_n x^n \qquad (C.5)$$

where:

$$\begin{aligned}
a_0 &= 0. \\
a_1 &= 0.22690069 \\
a_2 &= -1.09038423 \\
a_3 &= -0.94538563 \\
a_4 &= 35.87784264 \\
a_5 &= -176.70961777 \\
a_6 &= 442.91119511 \\
a_7 &= -647.63095699 \\
a_8 &= 558.01744471 \\
a_9 &= -263.04762768 \\
a_{10} &= 52.38631204
\end{aligned} \qquad (C.6)$$

To calculate the angle of zero-lift, the slope of the mean camber line has to be determined:

$$\frac{dz_c}{dx} = \sum_{n=1}^{10} n a_n x^{(n-1)} \tag{C.7}$$

Substitution of Equation (C.3) into Equation (C.7) results in:

$$\frac{dz_c}{dx} = \sum_{n=0}^{9} b_n \cos^n \theta \tag{C.8}$$

where:

$$\begin{aligned} b_0 &= 0.00734851 \\ b_1 &= -0.00172714 \\ b_2 &= 0.01065684 \\ b_3 &= 0.44789152 \\ b_4 &= -0.27322050 \\ b_5 &= -1.48035280 \\ b_6 &= 0.30678088 \\ b_7 &= 2.27192933 \\ b_8 &= -0.03923674 \\ b_9 &= -1.02317016 \end{aligned} \tag{C.9}$$

Substitution of Equations (C.8) and (C.9) into Equation (C.2) leads to the following result:

$$\alpha_o = -0.07856 \text{ rad} = -4.5012 \text{ deg} \tag{C.10}$$

With Equations (C.1) and (C.10) the lift coefficient of the GA(W)-1 airfoil can be predicted and the result is plotted in Figure C.1.

In Figure C.1 the lift coefficient obtained with the thick airfoil theory method of Reference 17 is also shown. In the linear lift region the lift coefficient predictions of the thin airfoil theory and the thick airfoil theory are almost identical, and they show good agreement with

the experimental lift curve. The lift curve slope of the "thick airfoil" is steeper than the slope of the "thin airfoil" lift curve. This difference is caused by the thickness effect as shown by Weber's method.

Table C.1: NASA GA(W)-1 airfoil coordinates

x/c	$(z/c)_{upper}$	$(z/c)_{lower}$	$(z/c)_{camber\ line}$
0.0	0.0	0.0	0.0
.002	.01300	-.00974	.001630
.005	.02035	-.01444	.002955
.0125	.03069	-.02052	.005085
.025	.04165	-.02691	.007370
.0375	.04974	-.03191	.008915
.05	.05600	-.03569	.010155
.075	.06561	-.04209	.011760
.100	.07309	-.04700	.013045
.125	.07909	-.05087	.014110
.150	.08413	-.05426	.014935
.175	.08848	-.05700	.015740
.20	.09209	-.05926	.016415
.25	.09778	-.06265	.017565
.30	.10169	-.06448	.018605
.35	.10409	-.06517	.019460
.40	.10500	-.06483	.020085
.45	.10456	-.06344	.020560
.50	.10269	-.06091	.020890
.55	.09917	-.05683	.021170
.575	.09674	-.05396	.021390
.60	.09374	-.05061	.021565
.625	.09013	-.04678	.021675
.65	.08604	-.04265	.021695
.675	.08144	-.03830	.021570
.700	.07639	-.03383	.021280
.725	.07096	-.02930	.020830
.750	.06517	-.02461	.020280
.775	.05913	-.02030	.019415
.800	.05291	-.01587	.018520
.825	.04644	-.01191	.017265
.850	.03983	-.00852	.015655
.875	.03313	-.00565	.013740
.900	.02639	-.00352	.011435
.925	.01965	-.00248	.008585
.950	.01287	-.00257	.005150
.975	.00604	-.00396	.001040
1.0	-.00074	-.00783	-.004285

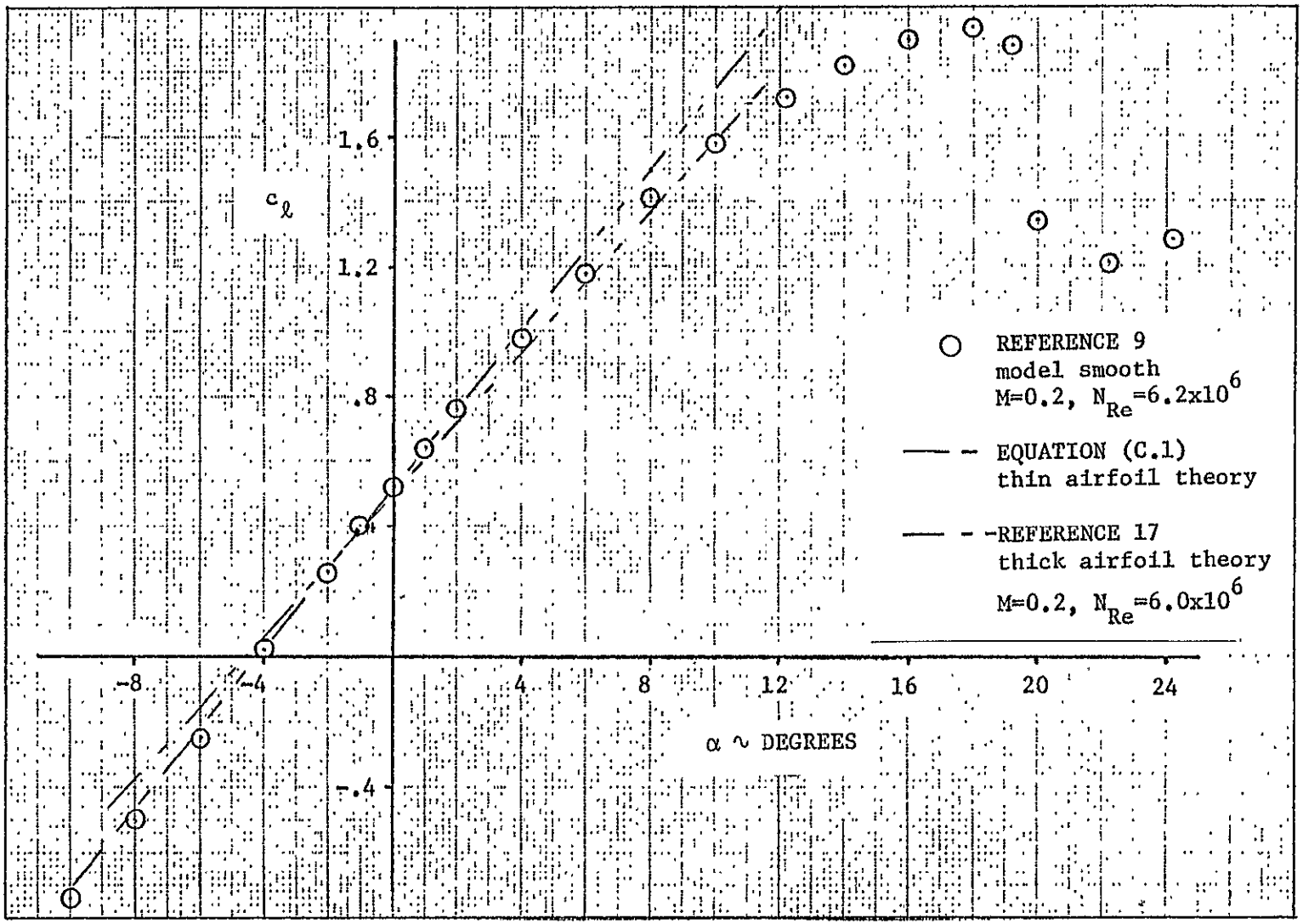

Figure C.1: Comparison of experimental GA(W)-1 section airfoil lift with predicted results

BLANK PAGE

APPENDIX D

DETERMINATION OF LIFT AND PITCHING MOMENT COEFFICIENT FOR THE ATLIT WITHOUT HORIZONTAL TAIL IN THE "FULLY CLEAN" CONFIGURATION

PAGE 304 INTENTIONALLY BLANK

APPENDIX D

DETERMINATION OF LIFT AND PITCHING MOMENT COEFFICIENT FOR THE ATLIT WITHOUT HORIZONTAL TAIL IN THE "FULLY CLEAN" CONFIGURATION

During the ATLIT drag clean-up investigation several factors were established which affected the lift curve slope, C_{L_α}, and the induced drag, C_{D_i}, of the ATLIT. The two most important factors were:

1. leakage through the spoiler-Fowler flap region along the wing trailing edge
2. premature flow separation on the wing upper surface between the fuselage and the nacelles.

The highest experimentally determined lift-curve slope was obtained with trailing-edge leakage eliminated and fillets installed at the wing-fuselage juncture. Therefore, in this study, any comparison with theory will be based on experimental data which includes these two fixes. However, these fixes were present on the ATLIT airplane only during the early phase of wind-tunnel testing. No data were obtained with horizontal tail removed until near the end of the test program.

The effect of the horizontal tail on the airplane lift curve was established for the "power-off" condition for the airplane "as built" at a Reynolds number of 2.3 million. The curves are shown in Figure D.1 and the incremental tail lift is established from these data. Next the tail lift can be subtracted from the lift curve of the ATLIT airplane in the "fully clean" configuration with the horizontal tail on. This procedure is shown in Figure D.2.

The same method can be used to determine the pitching moment coefficient of the airplane without horizontal tail in the "fully clean" configuration. In Figure D.3 the pitching moment increment due to the horizontal tail is determined. Figure D.4 shows the pitching moment curves of the complete airplane "fully clean" and also the pitching moment curve of the airplane without horizontal tail in the "fully clean" configuration.

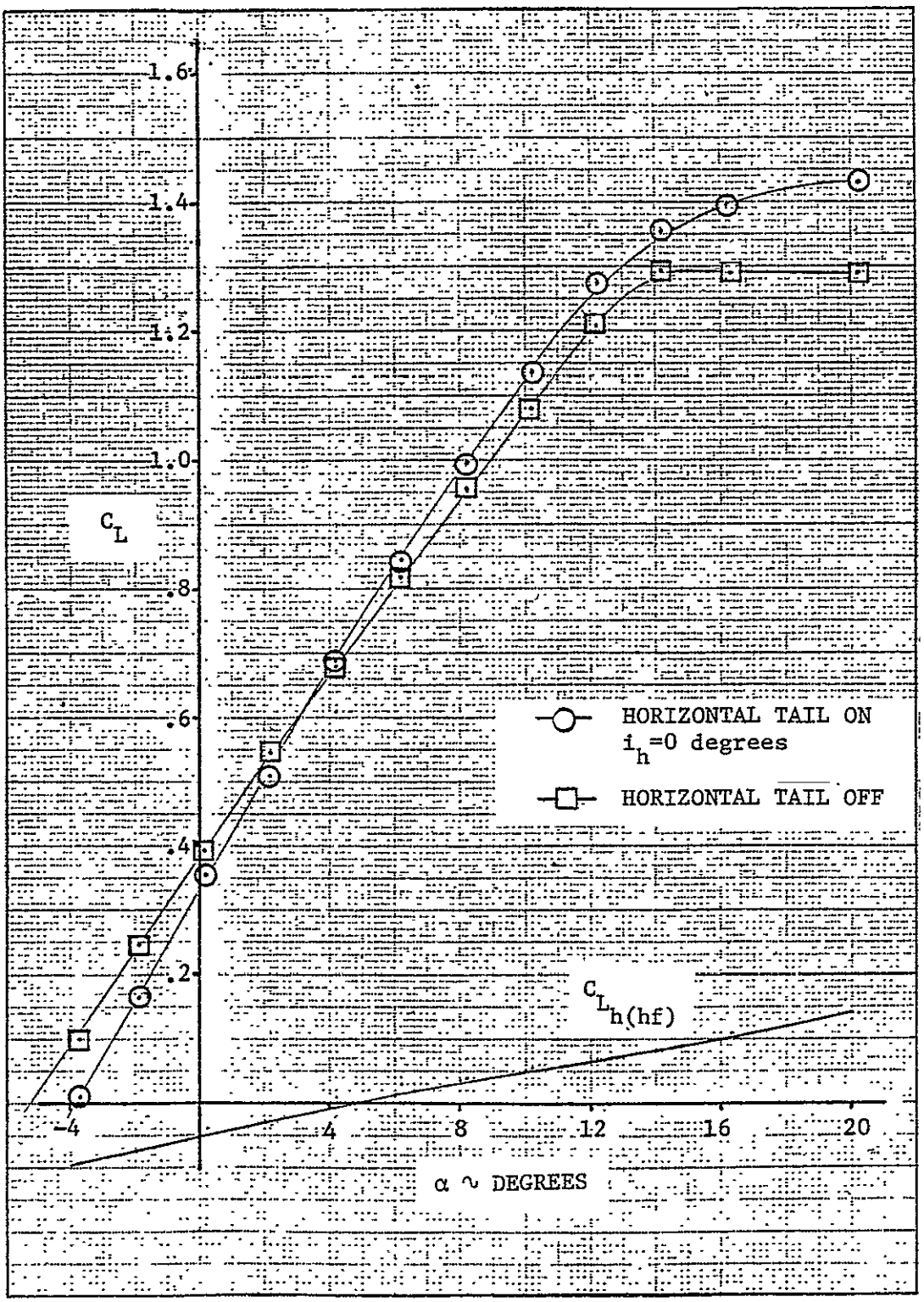

Figure D.1: Determination of horizontal tail increment to lift (Airplane "as built," propellers stopped, $N_{Re}=2.3\times10^6$)

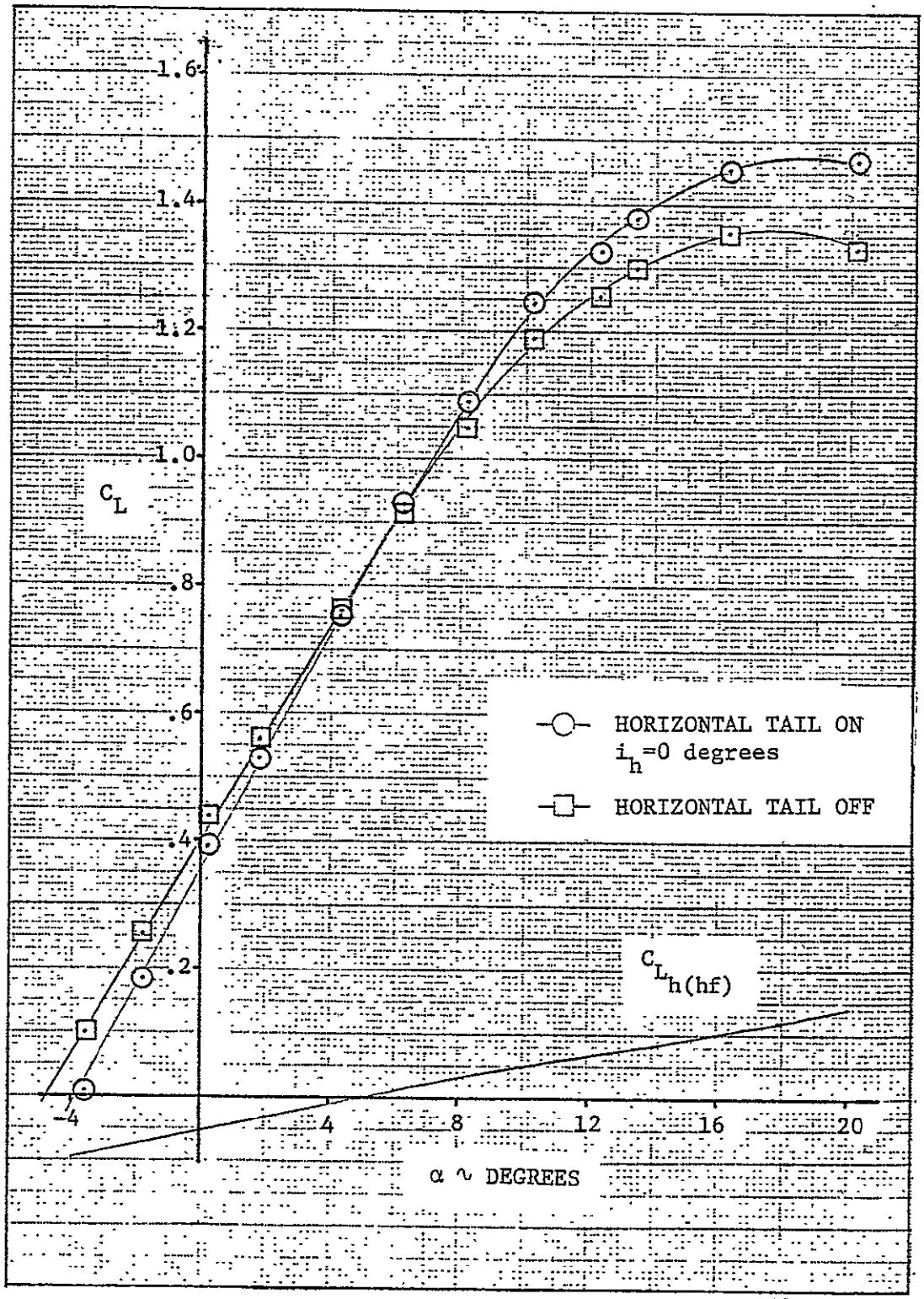

Figure D.2: Determination of horizontal tail off lift curve (Airplane "fully clean," $N_{Re}=2.3\times10^6$)

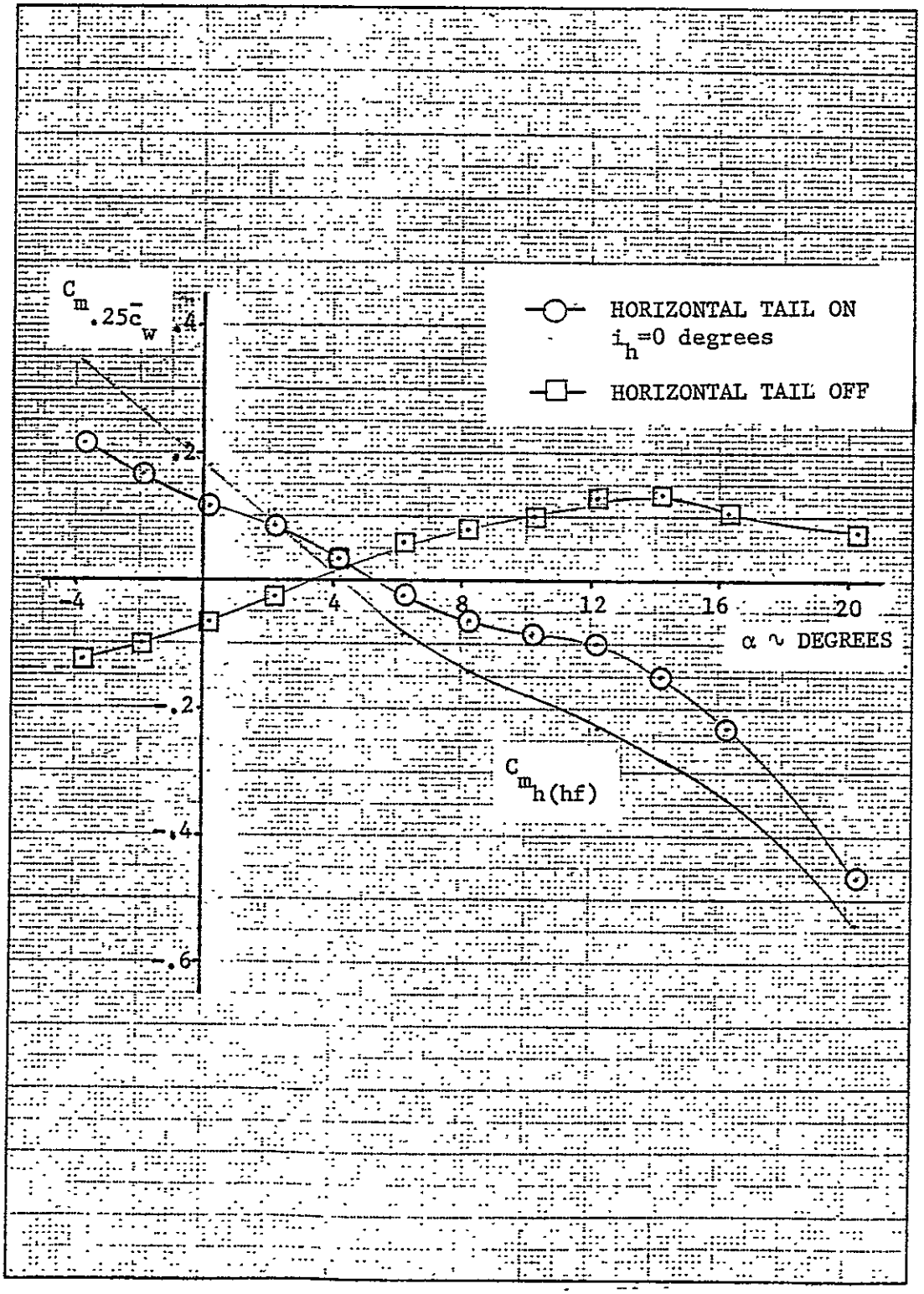

Figure D.3: Determination of horizontal tail increment to the pitching moment (Airplane "as built," propellers stopped, $N_{Re}=2.3\times10^6$)

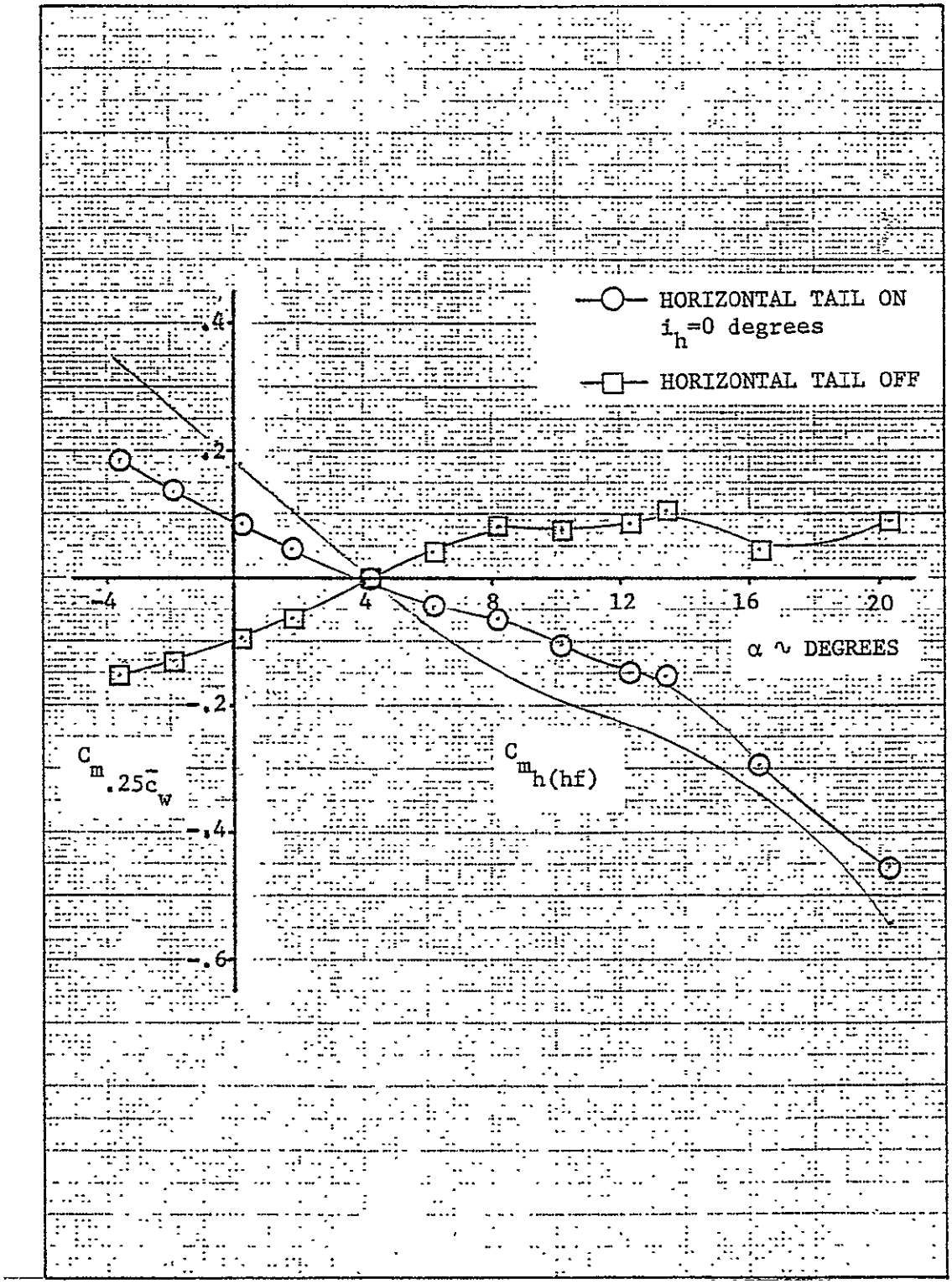

Figure D.4: Determination of pitching moment coefficient with horizontal tail off (Airplane "fully clean," $N_{Re}=2.3\times10^6$)

BLANK PAGE

APPENDIX E

DERIVATION OF THE DOWNWASH AT THE HORIZONTAL TAIL FROM THE FULL-SCALE WIND TUNNEL DATA

APPENDIX E

DERIVATION OF THE DOWNWASH AT THE HORIZONTAL TAIL FROM THE FULL-SCALE WIND TUNNEL DATA

In Reference 2 no experimental downwash results at the horizontal tail are shown. However, the average downwash at the horizontal tail, $\bar{\varepsilon}_h$, as a function of the angle of attack, α, can be derived from the graphs shown in Reference 2.

In Appendix D the horizontal tail lift including tail-fuselage interactions, wing downwash and dynamic-pressure effects, has been derived from the experimental data as a function of the angle of attack. The lift of the horizontal tail, based on the reference wing area, can be written as follows:

$$C_{L_{h(hf)}} = (C_{L_\alpha})_{h(hf)} \left(\alpha - \bar{\varepsilon}_h + i_h \right) \qquad \text{(E.1)}$$

In Section 3.10 the lift of the horizontal tail has been calculated ($i_h = 0$) and the result was:

$$C_{L_{h(hf)}} = 0.0177 \left(\alpha - \bar{\varepsilon}_h \right) \qquad \text{(E.2)}$$

based on the reference wing area, S_w, a dynamic pressure ratio, $\bar{q}_h / \bar{q}_\infty$, equal to unity and valid up to $\alpha_h^* = 12.2$ degrees.

With Figure D.1 and Equation (E.2) the average downwash at the horizontal tail, $\bar{\varepsilon}_h$, can be calculated. The results of the calculations are summarized in Table E.1.

Table E.1: Average downwash over the horizontal tail of the ATLIT airplane (N_{Re}= 2.3 million, no flap deflection)

α, deg.	$C_{L_{h(hf)}}$ Figure D.1	$\alpha - \bar{\varepsilon}_h$, deg. Eq. (E.2)	$\bar{\varepsilon}_h$, deg.
-4	-0.098	-5.54	1.54
-2	-0.075	-4.24	2.24
0	-0.052	-2.94	2.94
2	-0.028	-1.58	3.58
4	-0.005	-0.28	4.28
6	0.018	1.02	4.98
8	0.034	1.92	6.08
10	0.051	2.88	7.12
12	0.067	3.79	8.21
14	0.084	4.75	9.25
16	0.100	5.65	10.35
18	0.120	6.78	11.22
20	0.140	7.91	12.09

BLANK PAGE

APPENDIX F

CALCULATION OF THE WETTED AREA FOR FUSELAGE AND NACELLE

APPENDIX F

CALCULATION OF THE WETTED AREA FOR FUSELAGE AND NACELLE

In this appendix the wetted area of the fuselage and nacelle will be estimated in a manner different from the method described in Section 4.12. The accuracy of the fuselage and nacelle wetted area estimation must be high to obtain good agreement between the predicted value of the airplane zero-lift drag coefficient and the experimental result.

The wetted area of a body (fuselage or nacelle) will be calculated as follows:

1. Determine the circumference, C_x, of the cross section of the body at a distance, x, from the nose. Repeat this n times, as is shown in Figure F.1.

2. Plot the circumference, C_x, as a function of the distance, x, from the nose, as is demonstrated in Figure F.2.

3. Integrate the circumference, C_x, over the distance, $\overline{x}$, from the nose to obtain the uncorrected wetted area of the body. This integration can be performed with Simpson's approximation as follows:

$$S_{wet} = \sum_{i=0}^{n} C_{x_i} \Delta x_i \qquad (F.1)$$

where C_{x_i} represents the circumference of the cross section at the center of the interval Δx_i.

4. Determine the area of overlap between body and lifting surface(s). The area of a wing section can be estimated as follows (Reference 8):

$$A = 0.68(t.c) = 0.68(t/c)c^2 \qquad (F.2)$$

where c is the exposed root chord of the lifting surface. t/c is the thickness to chord ratio of the exposed root chord.

5. Subtract the total area of overlap between body and lifting surfaces from the uncorrected wetted area to obtain the actual wetted area of the body.

The fuselage was broken into eight segments. The cross-sectional circumference was determined at nine stations: four nose sections, one windshield section, two cabin sections and two tail cone sections. The corrected wetted area of the fuselage appears to be:

$$(S_{wet})_f = 23.32m^2 = 251.0ft^2 \qquad (F.3)$$

The wetted area (including spinner) of one nacelle is:

$$(S_{wet})_n = 5.55m^2 = 59.7ft^2 \qquad (F.4)$$

while the 8 inch extended nacelle has a wetted area:

$$(S_{wet})_n = 6.08m^2 = 65.4ft^2 \qquad (F.5)$$

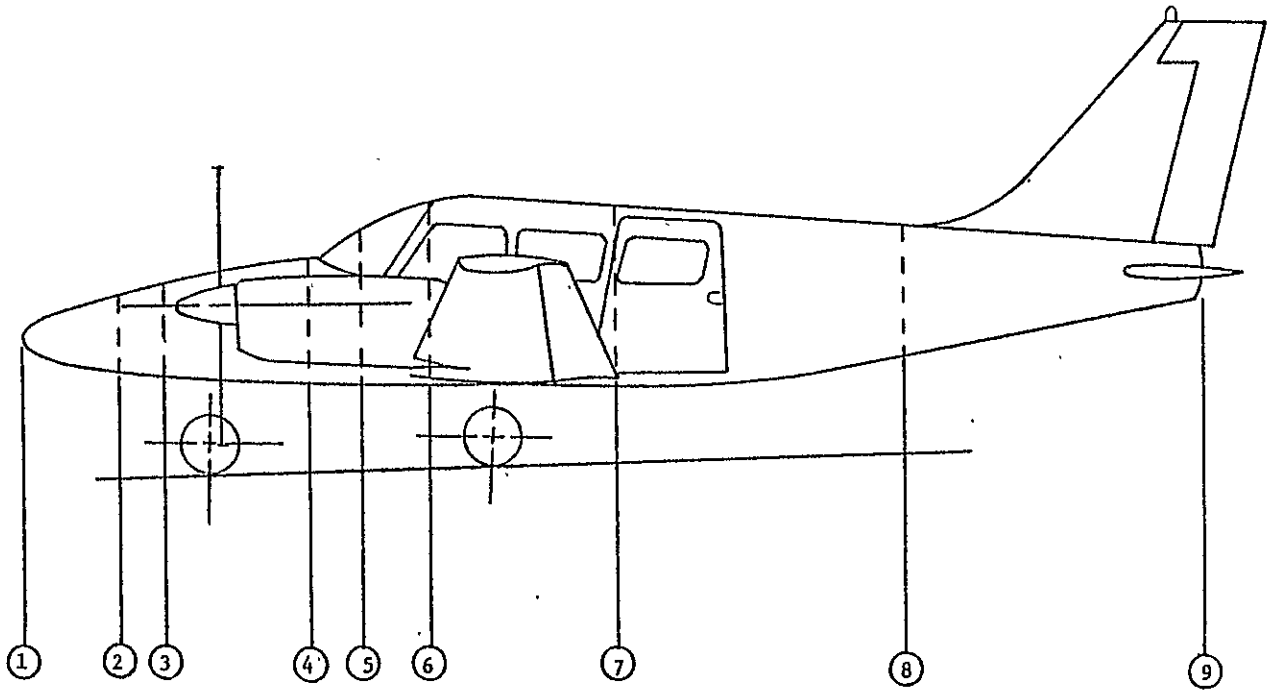

Figure F.1: Stations at which cross-sectional circumference is determined

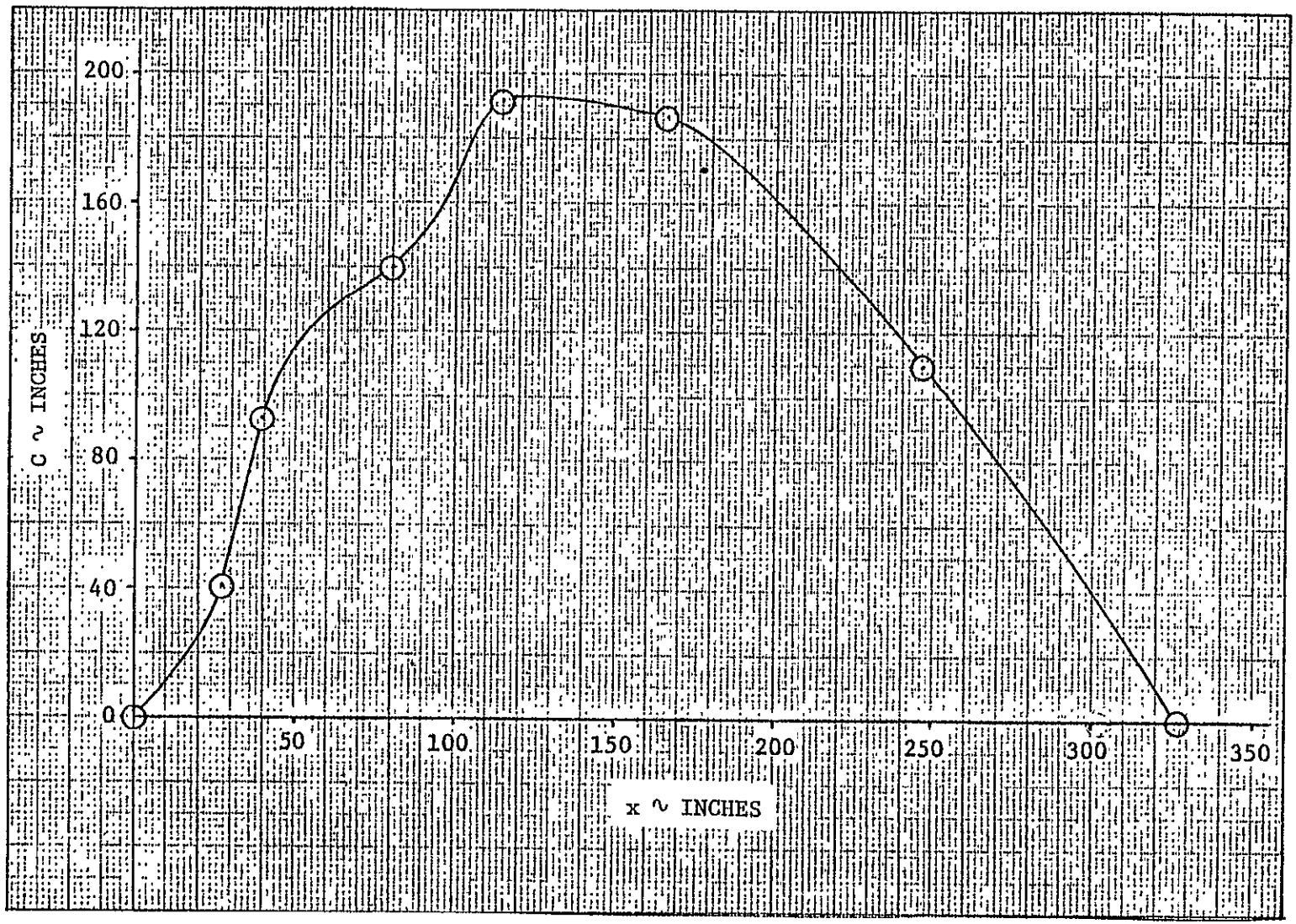

Figure F.2: Circumference of fuselage cross-section at different longitudinal stations

BLANK PAGE

CRINC